MARTIN MARIETTA ENERGY SYSTEMS LIBRARIES
3 4456 0361483 6

188.

CENTRAL RESEARCH LIBRARY
DOCUMENT COLLECTION

ORNL-2929
UC-81 - Reactors-Power

GAS-COOLED REACTOR PROJECT

QUARTERLY PROGRESS REPORT

FOR PERIOD ENDING MARCH 31, 1960

CENTRAL RESEARCH LIBRARY
DOCUMENT COLLECTION
LIBRARY LOAN COPY
DO NOT TRANSFER TO ANOTHER PERSON
If you wish someone else to see this document, send in name with document and the library will arrange a loan.

OAK RIDGE NATIONAL LABORATORY
operated by
UNION CARBIDE CORPORATION
for the
U.S. ATOMIC ENERGY COMMISSION

Printed in USA. Price $3.50. Available from the

Office of Technical Services
Department of Commerce
Washington 25, D.C.

LEGAL NOTICE

This report was prepared as an account of Government sponsored work. Neither the United States, nor the Commission, nor any person acting on behalf of the Commission:

A. Makes any warranty or representation, expressed or implied, with respect to the accuracy, completeness, or usefulness of the information contained in this report, or that the use of any information, apparatus, method, or process disclosed in this report may not infringe privately owned rights; or

B. Assumes any liabilities with respect to the use of, or for damages resulting from the use of any information, apparatus, method, or process disclosed in this report.

As used in the above, "person acting on behalf of the Commission" includes any employee or contractor of the Commission, or employee of such contractor, to the extent that such employee or contractor of the Commission, or employee of such contractor prepares, disseminates, or provides access to, any information pursuant to his employment or contract with the Commission, or his employment with such contractor.

ORNL-2929

Reactors — Power
TID-4500 (15th ed.)

Contract No. W-7405-eng-26

GAS-COOLED REACTOR PROJECT
QUARTERLY PROGRESS REPORT
For Period Ending March 31, 1960

Staff
Oak Ridge National Laboratory

DATE ISSUED

JUN 14 1960

OAK RIDGE NATIONAL LABORATORY
Oak Ridge, Tennessee
operated by
UNION CARBIDE CORPORATION
for the
U. S. ATOMIC ENERGY COMMISSION

MARTIN MARIETTA ENERGY SYSTEMS LIBRARIES

3 4456 0361483 6

CONTENTS

SUMMARY vii

PART 1. DESIGN INVESTIGATIONS

1. REACTOR PHYSICS 3

Energy Deposition in Graphite of EGCR 3

Worth of EGCR Control Rod Bank 3

Perturbations Produced in the EGCR by a Half-Empty Fuel Channel 5

Protactinium Losses in a BeO-Moderated Reactor 6

Comparison of Conversion Ratios of Blanket Materials 8

Comparison of Nuclear Characteristics of BeO-Moderated Cores and Graphite-Moderated Cores 10

2. REACTOR DESIGN STUDIES 16

EGCR Fuel Assemblies 16

Mechanical Design 16

Flow Distribution 16

Fission-Gas Pressure Buildup in EGCR Fuel Elements ... 21

Thermal Analysis 22

EGCR Control Rod Design 24

Structural Investigations 27

Study of Fuel Element Cladding Behavior Under Arbitrary Temperature Distributions 27

Thermal Stress Equations for a Thick-Walled Cylinder of Anisotropic Material 38

Seismic Analysis of the EGCR 43

Decontamination of EGCR Charge and Service Machines 53

Helium Purification System for EGCR 54

GCR Hazards Study 55

Fission-Product Release from UO_2 57

Parametric Study of Fission-Product Contamination 61

Graphite Oxidation in the EGCR 63

3. EXPERIMENTAL INVESTIGATIONS OF HEAT TRANSFER AND FLUID FLOW 65

Resistance-Heated-Tube Heat Transfer Experiment 65

Mass-Transfer Measurements 70

Velocity Distribution in Septafoil Channels 77

PART 2. MATERIALS RESEARCH AND TESTING

4. METALLURGICAL INVESTIGATIONS 85

Fuel and Moderator Materials Development 85

Fabrication of UO_2 85

UO_2 Process Development 85

Thermal Conductivity of UO_2 87

Mechanical Behavior of Encapsulated UO_2 87

Fission-Product Release Studies 92

Graphite Fabrication 95

Reactions of UO_2 with Graphite 98

Mechanical Properties of Graphite 100

Fabrication Development of BeO and BeO-UO_2 Bodies 100

Evolution of Lithium from BeO 101

Structural Materials Evaluation 102

Creep Tests in Various Environments 102

Reactions of Type 304 Stainless Steel with CO and CO_2 112

Mechanical Property Studies of Structural Materials .. 115

Pressure-Vessel Steel Investigations 118

Manufacturing and Inspection Methods 123

Fabrication of EGCR Fuel Elements 123

Reactor Vessel Penetrations 132

Welding of Austenitic to Stainless Steel 135

Beryllium Investigations 136

Reactions of Beryllium with CO_2 136

Compatibility Tests of Beryllium-NaK-Type 304 Stainless Steel Systems 137

Procurement of Beryllium Tubing 138

Beryllium-Tubing Evaluation 139
Joining of Beryllium 140
Thermal-Cycling Tests on Beryllium 145

5. IN-PILE TESTING OF COMPONENTS AND MATERIALS 148
Fuel Element Irradiation Program 148
Full-Diameter Prototype EGCR Fuel Capsules 148
Miniature Capsule Fission-Gas-Release Experiments ... 151
Advanced Fuel Element Testing 155
Examination of Irradiated Capsules 157
ORR- and ETR-Irradiated Full-Diameter Capsules 157
Measurements of Fission-Gas Pressure at EGCR Operating Temperature 159
LITR-Irradiated Miniature Capsules 163
GETR-Irradiated Capsules 164
Instantaneous Fission-Gas-Release Experiment 173
Fission-Gas-Release Measurements 173
Equipment Modifications 178
UO_2 Thermal Conductivity Determinations 178
Radiation Effects on Structural Metals 179
Steel 179
Beryllium 179
Inconel 184

6. OUT-OF-PILE TESTING OF MATERIALS AND COMPONENTS 187
Materials Compatibility Tests 187
Isothermal Tests of Graphite and Structural Materials in Static Helium 187
Thermal-Convection Loop Tests of Graphite and Structural Materials in High-Pressure Helium 190
Effect of Gas Impurities on Metal Specimens 193
Low-Pressure Thermal-Convection Loop Tests with Helium Containing Controlled Amounts of Impurities 195
Forced-Convection Loop Test of Gas Purification System 196
Evolution of Gases from Graphite 196

Transport of Gases Through Graphite 201
Permeability Studies 201
Constant-Pressure Diffusion Experiments 206
Chemical Behavior of Fission Products in Fissioning UO_2 .. 209
Measurement of High Temperature 211
Measurement of Surface Temperatures in High-Velocity Cooling Gas 211
Stability of Rhenium-Tungsten Thermocouples 217
Effects of Radiation on Thermocouples 217
Tests of Chromel-Alumel Thermocouples in Various Atmospheres 217
Purification of Cooling Gases 221
Determination of Impurities in Helium 223
Determination of Oxygen-to-Uranium Ratios in UO_2 Pellets .. 226

7. DEVELOPMENT OF TEST LOOPS AND COMPONENTS 228
ORR Gas-Cooled In-Pile Loops 228
GCR-ORR Loop No. 1 228
GCR-ORR Loop No. 2 228
EGCR Experimental Loops 230
Design Status 230
Process Analysis 233
Mechanical Joint Service Testing 246
Special Gas Compressors and Electric Motors 250
Grease-Lubricated Centrifugal Compressors 250
Regenerative Compressors 250
Compressors with Gas-Lubricated Bearings 252
Compressor for High-Temperature Electric-Motor Test System 252
Compressors for ORR In-Pile Loop No. 2 253
Compressors for EGCR Experimental Loops 253
Study of Back Diffusion Through Labyrinth Seals 254

GAS-COOLED REACTOR PROJECT QUARTERLY PROGRESS REPORT

SUMMARY

Part 1. Design Investigations

1. Reactor Physics

In EGCR design studies, the energy deposition in the core graphite has been calculated for the initial reactor loading with the experimental tubes empty. Heating from both gamma-ray absorption and neutron moderation were included. Calculations of the shutdown worth of the EGCR control rod bank were made both for empty experimental tubes and for a typical experimental assembly in each tube. An investigation was also made of the neutron-flux and power-density perturbations produced by a half-empty fuel channel in the EGCR. The maximum value of the ratio of power density in the perturbed condition to that in the unperturbed condition at a given position is 1.7, and, since part of the perturbation exists even when the fuel assembly is fully inserted, the perturbation attributable to partially removing the rod is only about 1.6.

In advanced design studies, the effect of Pa^{233} absorption on the conversion ratio in a BeO-moderated reactor was calculated. The one-region reactor considered uses Th^{232} as fertile material and U^{233} as fuel. Conversion ratios obtainable in a BeO-ThO_2 blanket were compared with those obtainable in a blanket composed of graphite and ThO_2. The core diameter, the blanket thickness, and the thorium concentration in the blanket were varied in the calculations. Beryllium oxide was found to give better conversion ratios than graphite for thin blankets by minimizing the leakage; BeO also gives better conversion ratios for thick blankets as long as the thorium concentration is very low.

In order to compare the nuclear characteristics of BeO- and graphite-moderated cores, multigroup calculations were made for a two-region reactor consisting of a cylindrical core containing a homogeneous mixture of U^{233}, Th^{232}, and moderator surrounded by a cylindrical blanket containing the same moderator mixed homogeneously with Th^{232}. Equivalent core leakage was obtained when the diameter of the graphite-moderated

core was about twice that of the BeO-moderated core. Equal fractions of core conversion divided by total conversion were also found for a graphite-moderated core about twice the diameter of a BeO-moderated core. Higher total conversion ratios were obtained with BeO-moderated cores because of the fast reactions in beryllium.

2. Reactor Design Studies

Several alternate designs for the EGCR fuel element spacers and the top and bottom spiders are being considered. The design of the web structure for both the top and bottom spiders appears to be the controlling factor in the magnitude of the gas and surface temperature asymmetries throughout the seven-rod cluster. The original "H" structure was found to cause serious maldistribution of the flow. Preliminary analyses of a new design have indicated considerable improvement in the flow distribution. An analytical model that describes the flow distribution in a rod cluster has been derived that agrees well with experimental results. The effects of fission-gas pressure buildup in fuel elements under various conditions have been studied in relation to the behavior of fuel element cladding. The two fuel loading schemes that have been considered for the EGCR were studied in terms of the effects on fuel element surface temperatures.

Preliminary design studies of the EGCR control rods have been completed. There will be either 21 or 25 rods located on a 2-ft lattice, and they will contain, as the poison material, annular rings of B_4C clad with 3 1/4-in.-o.d. type 304 stainless steel tubing. The rods will be flexible and each rod will consist of three segments supported internally on stainless steel cable. Thermal analyses have indicated that coolant flow of 100 lb/hr up through the center of a control rod will maintain the cladding temperatures below the allowable limit of 1600°F.

Studies of the deflections and stresses in the cladding of the EGCR fuel elements have been continued. Unrestrained and restrained thermal bowing curves were obtained which show that the maximum deflection is less when the element is unrestrained than when it is restrained.

Deflection curves obtained for rods having circumferential temperature distributions show that the maximum unrestrained deflection occurs between the center and the higher temperature end of the rod, and the restrained bowing curve is S-shaped. The maximum displacements in both cases are small compared with the 1/8-in. minimum clearance around an EGCR fuel rod.

The central restraining forces and the deflection profiles have also been obtained as functions of time for mean temperatures of 1200 to 1600°F and diametral temperature differences of 25 and 50°F. The initial force is directly proportional to the temperature difference, but, after a given time corresponding to the temperature, the force becomes independent of the temperature difference.

Equations have been developed for thermal stress analysis of anisotropic material subjected to an axisymmetrical temperature distribution. Since irradiation-induced dimensional changes in graphite are similar to thermal strains, the equations can be used for studying the stresses in the graphite of the EGCR.

A mathematical model was developed for a seismic analysis of the EGCR. The analysis, which was based on available data and realistic assumptions, showed that the combined stresses induced by seismic disturbances present no hazard to the EGCR.

Methods for decontaminating the EGCR charge and service machines are being studied. Experiments have shown that metal surfaces contaminated with UO_2 can be decontaminated with the use of several reagents aspirated into a steam jet apparatus. Methods for the removal of deposited fission products are also being studied.

Design criteria have been established for the EGCR helium purification system. A proposed system consists of an oxidizer and an adsorber, A separate system will be provided to purify the buffer gas from the compressor seals. Apparatus for testing oxidizers and adsorbers is being set up in order to obtain design information.

In further studies of the hazards involved in the operation of gas-cooled reactors, the existing data on the diffusion of fission products

from UO_2 have been evaluated. Also, an analysis is being made of the graphite oxidation hazard in the EGCR. A preliminary study has shown that a possibility of graphite combustion in the EGCR exists in the event of accidental admission of air to the main coolant system.

3. Experimental Investigations of Heat Transfer and Fluid Flow

The investigation of heat transfer in the septafoil geometry was continued for the situation of tubes restrained at the mid-plane to the design position and a modified inlet configuration. Circumferential temperature profiles were obtained for three of the peripheral tubes and the central tube at 12 axial positions; the remaining peripheral tubes were studied only near the mid-plane and the exit. The temperature patterns showed a consistent clockwise shift (as compared with earlier results), with the maxima occurring at the expected 180-deg location and the minima in the vicinity of 340 deg. Local heat transfer coefficients for the three peripheral tubes were comparable to within 1.7% but were about 8% below the values calculated for the central tube; agreement with previous results was excellent.

Preliminary determinations of mass-removal patterns in the vicinity of the mid-cluster spacer were attempted with the use of a modified profilometer. Interpretation of the data was complicated by sporadic calibration shifts. A measurement of the density of the naphthalene in the as-formed condition resulted in a 4 1/4% increase in previously reported mass-transfer factors.

Velocity profiles were redetermined in a septafoil for a $\gamma = 2$ tube spacing following corrective modification of the apparatus, and the velocity contour obtained appeared to be more symmetrical than those measured originally. No change in the essential details of the patterns was observed for an almost twofold change in the Reynolds modulus. The circumferential variation in the local heat transfer coefficient was predicted from the velocity data using the Prandtl-Taylor analogy. An extrapolation of this result to the conditions of the heated-tube experiment yielded a heat transfer coefficient which was considerably below the asymptotic value developed from the heat transfer data.

Part 2. Materials Research and Testing

4. Metallurgical Investigations

The fabrication of special UO_2 specimens for irradiation has been continued. Tests of stabilized CrO_2, which was proposed for use as a thermal insulator around UO_2 pellets, showed the material to be unsatisfactory. The ZrO_2-UO_2 couples tested showed reaction by diffusion and then by swelling and distortion.

Work continued on the development of a low-cost production process for the fabrication of UO_2 fuel bodies. A pilot plant is in operation, and a continuous process is being tested on production quantities of material. Three oxides are being compared from the standpoint of achieving higher densities or cheaper feed material. The three oxides are Hanford-denitrator UO_3 that is hydrogen reduced at 400°F to UO_2, ground UO_2 powder prepared by wet milling of previously fired UO_2 prepared by the continuous process, and calcined U_3O_8 prepared by air-calcining any available oxide at 2500°F and cooling in the absence of air.

An apparatus has been built for determining the thermal conductivity of UO_2. Calibration runs are being conducted.

The dimensional stability and mechanical behavior of 95%-dense hollow UO_2 pellets in stainless steel tubes are being studied in tests in which the pellets are heated internally to simulate the thermal gradients expected in operation in the EGCR. The axial expansion of the pellets has been observed to be proportional to the central temperature and to be unaffected by the temperature differential across the walls of the pellets. The expansion profile changes, however, with increases in the temperature differential, and the contact area between the pellets is reduced.

A series of measurements have been made of rates of release of Kr^{85} or Xe^{133} from small specimens of UO_2 at high temperatures after irradiation at low temperatures to a low burnup. Fission-gas-release rate parameter values, D', calculated from the measured release rates correlated, in general, with the D' values expected from surface area

measurements. The D′ values were below the value of 10^{-9} or less at 1400°C that is considered to be acceptable for an EGCR fuel element.

Techniques for fabricating high-density low-porosity graphite bodies are being developed that will be adaptable to the production of fueled graphite specimens. Tests of mixtures of graphite powder and thermosetting binder compounds have shown that the compacting pressure has little effect on the final density of such bodies. In general, the use of graphite powder of intermediate particle size and a low percentage of binder results in high densities that can be increased to some extent by impregnating the body with additional binding material.

In order to determine the limiting operating temperature of a fuel element consisting of UO_2 or other oxide fuel dispersed in graphite, the rate of reaction of UO_2 and graphite is being determined as a function of temperature, UO_2 particle size, and pressure. Since one of the reaction products is CO, the weight loss of the specimen is a direct function of the amount of UO_2 that has been reduced. In preliminary tests it was found that the major carbide phase present after the samples were quenched from test temperatures of 1320 and 1425°C was UC_2, but small amounts of UC were found.

The time-dependent mechanical properties of graphite at 750 and 1100°F are being investigated in order to determine whether graphite of the type specified for the EGCR will creep at these temperatures. If creep is observed, the applicable creep law will be determined. The time-dependence of the fracture ductility of graphite will also be determined.

Low-density pure BeO and high-density $BeO-UO_2$ and $BeO-UO_2-ThO_2$ bodies are being studied as materials for advanced gas-cooled reactors. Fueled bodies are being prepared for irradiation and fission-gas release studies, and beryllia tiles containing lithium are being heated for long periods of time to determine the extent of lithium evolution.

The creep of type 304 stainless steel in various environments is being studied at temperatures up to 1700°F. In air and nitrogen the creep rate is lowered because of the strengthening action of a nitride

precipitate. Data obtained at 1700°F indicate that a hydrogen atmosphere adversely affects the creep properties, but data obtained in hydrogen at 1500°F are inconclusive because of lack of reproducibility. Carburization occurs at both 1500 and 1700°F in CO and CO_2 and causes reductions of the rupture ductility. This effect is not considered to be serious, however, and is not cumulative.

Experimental studies of the reactions of type 304 stainless steel with CO and CO_2 have shown that, with CO at a pressure of 1 atm, carburization is inhibited by the formation of an adherent graphite surface film. It was also found the carburization in flowing CO_2 could be prevented by carefully removing all CO, but amounts as small as 0.1% led to extensive carbon pickup. The reaction rate data for type 304 stainless steel in CO_2 are contradictory because of the formation of oxide films which tend to spall during thermal cycling. Studies of the reactions with controlled CO-CO_2 mixtures are under way in a double thermal-convection loop.

Tube-burst tests of seamless, 0.020-in.-wall, type 304 stainless steel capsules in various environments have been continued, and annealed capsules are being tested in air to determine the effect of mid-plane spacer brazing. Excessive grain growth in certain areas of the wall of annealed tubes has resulted in premature failure. Thermal cycling of an annealed capsule produced wrinkling and axial expansion amounting to 0.84% in approximately 120 cycles.

Synthetic weld-heat-affected zones in type SA-212, grade-B, pressure vessel steel were prepared by cycling specimens to 1400 and 2400°F with an energy input of 50 to 100 kj/in. Structures having unsatisfactory notch toughness in the heat-affected zones were produced, but it was found that the impact properties could be improved by heat treatment. Welding procedures are being studied further in an attempt to produce microstructures having acceptable impact properties.

Fifty EGCR fuel elements were manufactured to confirm the fabricability of the design and obtain estimates of the assembly time. The inspection of components for these elements provided an evaluation of

the inspection techniques and the quality and dimensional requirements of the specifications. The rejection rate was very low for components and welds. Eddy-current inspection of the tubing and the graphite sleeves, on the other hand, resulted in extensive rejection. The tubing was later accepted on the basis of other inspections, but most of the graphite sleeves were found upon metallographic examination to have defects about twice as deep as those indicated by the eddy-current inspection. It appears that 80 to 90% of the sleeves produced by two vendors and about 40% of the sleeves produced by a third vendor will be rejected. The attachment of mid-plane spacers to the fuel capsules was accomplished by both furnace and induction brazing. Induction brazing was found to result in a minimum of distortion and grain growth in the tube wall and to produce sound joints.

Methods of joining the burst-slug-detection tubes and thermocouples to the reactor vessel nozzles were developed and are being tested by construction of mockups simulating the reactor design. Procedures for joining ferritic and austenitic steels by welding with INCO BP-85 and other filler metals were developed and will be used to fabricate specimens for thermal-cycling tests.

A study of the reaction of beryllium with CO_2 at low pressures and at temperatures up to 1000°C has shown the rate curve to be parabolic. The compatibility of stainless steel and beryllium in a NaK environment is being studied to assist in the design of capsules for studies of the effect of irradiation on beryllium tubing. At 600°C the transfer of beryllium to steel is slight, except in areas of contact or close proximity.

Beryllium tubing is being procured from several experienced manufacturers for evaluation and tesing. Of the tubing obtained thus far, the best quality tubing was that machined from hot-pressed blocks. An investigation of the variables in the extrusion process for producing beryllium tubing has been initiated.

The joining of beryllium tubing by fusion welding has been successful only with tubing machined from hot-pressed material. Brazing and

diffusion bonding are the more successful methods tried to date. Several alloys suitable for brazing are available, and leaktight brazed joints in capsules were prepared. Several diffusion-bonded joints prepared in helium or vacuum showed complete grain coalescence and were leaktight.

A number of thermal-cycling tests were run on beryllium specimens from various sources. Results indicate that cycling produces slight densification, especially in the case of hot-pressed material, but has no significant effect on the mechanical properties.

5. In-Pile Testing of Components and Materials

The second group of eight full-diameter prototype EGCR fuel capsules is being irradiated. New estimates of the total burnups for the first group of similar capsules were prepared. Irradiation of ten similar capsules has continued in the ETR. Four additional capsules have been prepared for insertion in the ETR.

New ceramic-insulated miniature capsules have been designed for use in fission-gas-release experiments, and three capsules of the new type are being irradiated. The insulating material being used is depleted UO_2. Data that have been obtained in the past and current fission-gas-release experiments have indicated that the thermal conductivity of UO_2 does not change with thermal neutron doses between 3×10^{16} and 4×10^{20} neutrons/cm^2·sec.

Irradiation of two graphite-clad UC_2-graphite matrix fuel elements in the MTR was completed. The test parameters have been estimated on the basis of the operating data. The estimated burnup of the U^{235} in the fueled graphite matrix is 101 000 Mwd/MT for the "A" element and 46 300 Mwd/MT for the "B" element.

Examinations were made of the first group of ORR-irradiated full-diameter prototype capsules. There were no evidences of significant distortion. Equipment is being assembled for postirradiation measurements at EGCR operating temperatures of the fission-gas pressure in four of the capsules. Data obtained recently on fission-gas release from LITR-irradiated miniature pellets are presented.

Postirradiation examinations of the GETR-irradiated capsules were completed, and ceramographic studies of the fuel are under way. When the capsules were slit open and the fuel had been removed, it was noted that the fractures in the UO_2 were imprinted on the interior of the cladding. Since the crack imprints have the same intensity as the imprints of the gaps between pellets, it appears that the cracks occurred suddenly and did not progress with time.

Data are being obtained in the instantaneous fission-gas-release experiment for an assembly that consists of two thin plates of high-density UO_2 with thermocouples sandwiched between them on the outer surfaces. Calculated diffusion constants based on the measurements for the various isotopes are reasonably consistent and support the thesis that xenon and krypton have diffusion constants of the same order of magnitude.

Preparations are being made for experimental investigations of the effects of radiation on structural metals, in particular, steel and beryllium. Analyses have been made of data obtained in in-pile tube-burst-type stress-rupture tests of Inconel, and an explanation for the shorter time to rupture under irradiation has been postulated. The hypothesis is that helium is being formed in the metal during irradiation by the neutron reaction $B^{10}(n,\alpha)Li^7$ and that the gas accumulates and creates voids in the grain boundaries which weaken the metal. A number of heats of Inconel are being made into tubing for further tests. The boron content and the B^{10} enrichment were varied in these heats.

6. Out-of-Pile Testing of Materials and Components

Analyses of the results of isothermal tests of graphite and structural materials in static helium have shown the effect of temperature on the reactions of the graphite and the metals with the impurities produced by the outgassing of the graphite. At 1400°F, reaction of the outgassed contaminants with the structural metals is extremely fast, and the gas mixtures approach equilibrium with the metals. Under these conditions, decarburization of some test specimens occurs. At 1100°F, the gaseous

impurities more closely approach concentrations in equilibrium with graphite. An over-all reduction of the impurities occurs but at a much slower rate than at 1400°F.

In a second thermal-convection loop test of graphite and structural materials in high-pressure helium, the weight gains of the metal specimens were found to be similar after test periods of 500, 1000, and 5000 hr. During the tests the hot leg of the loop was maintained at 1225°F and the system pressure was 325 psig. It appears therefore that most of the reaction of the metals with the impurities outgassed from the graphite occurred within the first 500 hr. This result is in agreement with the observed impurity concentrations of the helium. The cold leg of the loop showed no detectable carbon deposits.

The heavy, poorly adherent reaction films commonly found on low-alloy steels exposed at 1100 and 1200°F to helium containing impurities produced by the outgassing of graphite have been examined with the use of electron and x-ray diffraction techniques. The silver-colored outer layer has been identified as FeC and the black inner layer as Fe_3O_4.

Compatibility tests are also being conducted in low-pressure thermal-convection loops in which the impurity concentrations in the circulating helium can be controlled. After the first test, with a controlled CO concentration of 0.185 vol % and a graphite temperature of 1100°F, a type 304 stainless steel specimen that was individually heated to 1500°F and stainless steel coupons that were at the same temperature as the graphite showed thin protective oxide films. Low-alloy steels that were also exposed at the graphite temperature showed heavy, nonadherent oxide films. A second experiment is in progress with a controlled H_2O concentration in the helium of 0.122 vol %.

In experimental studies of the evolution of gases from graphite, two grades of graphite, R-1HLM and R-6HLM, obtained from the Great Lakes Corporation have been tested. It has been found that more consistent results can be obtained in these tests with the use of induction heating in place of external resistance heating. Specimens have been tested that were cut from different positions in a graphite bar, and no effect

of orientation has been found. The results obtained thus far do show a lower gas content for R-6LHM than for R-1LHM.

Silicon-silicon carbide coated graphite specimens obtained from the American Lava Corporation evolved surprisingly large volumes of gas when heated from room temperature to 1000°C. The data suggest that the coatings were imperfect.

Experimental studies of the interdiffusion coefficients of noble gases in graphite were continued. In determining the permeability of AGOT graphite, nonlinear curves were obtained that indicated turbulent flow regions. The experiments point up the fact that if back flow of helium through graphite fuel elements is to be employed as an aid in fission-product retention, the possibility of turbulent flow within the graphite must be considered. Interdiffusion coefficients of argon and helium have been obtained for AGOT graphite, and it has been found that the diffusion rates for the two gases are not the same. Models for correlating the data are being studied.

The expected state of combination at equilibrium for all products of fission of UO_2 with yields above 0.1 atom per 100 fissions has been predicted from available thermodynamic data. Estimates of properites such as vapor pressure, diffusion rates, and chemical reactivity of the fission products which depend on the state of chemical combination can be based on these predictions.

In the study of the measurement of high temperatures, a procedure has been developed for using the Oracle to make the calculations required to predict the variations of cooling corrections with the cooling conditions surrounding thermocouples. Cooling corrections are being obtained experimentally under the conditions used in the calculations in order to evaluate the results.

Further tests of Chromel-Alumel thermocouples in the presence of chromium, Inconel, and quartz in a flowing helium atmosphere have shown no fast emf drifts when there is limited access of the helium to the wires in the thermal-gradient range. Abnormal drifts may occur, however, under similar conditions in stagnant atmospheres.

The effect of helium carrier gas pressure on the dynamic adsorption of krypton by charcoal at 25°C has been studied experimentally, and preliminary tests have been made of a number of samples of commercially available activated carbons with respect to fission-gas retention. The activated charcoal traps designed for use with GCR-ORR loop No. 1 were studied and judged to be adequate.

A dual-column gas chromatograph is being tested on the low-pressure thermal-convection loop in order to evaluate its capabilities as a process instrument for the determination of impurities in helium. The maintenance required by the unit has been negligible, and the reproducibility of the results is somewhat better than it was thought to be initially. The moisture monitors being tested on the loop are not, as yet, satisfactory.

7. Development of Test Loops and Components

Installation work on GCR-ORR loop No. 1 has been started, and the design of loop No. 2 is approximately 70% complete. Data required for and analog simulator study of loop No. 2 operation have been assembled, and design conditions were determined for tests of graphite-clad fuel elements.

Design criteria have been developed for the helium- and CO_2-cooled experimental loops in the EGCR. A process flowsheet has been prepared, and design studies of the main loop components are under way, with prime consideration being given to those features that affect the reactor design.

Five 2 1/2-in. and two 10-in. standard Conoseal mechanical joints of the type to be used in the EGCR experimental loops were received, and tests of the 2 1/2-in. joints were started. Apparatus for testing the 10-in. joints is being fabricated. Initial tests of the double-gasketed, gas-buffered, mechanical joints that are being evaluated for use in experimental loops which will operate with gases containing fission products have indicated excessive leakage. Major improvements will be required to make these joints satisfactory for service with helium.

A grease-lubricated centrifugal compressor has satisfactorily completed a 3000-hr endurance test while operating at 12 000 rpm with

helium at suction conditions of 590°F and 400 psig. Performance data were obtained during 150 hr of continuous operation of a prototype regenerative compressor at 9000 rpm with helium at 385 psig and 600°F. A loop for testing the gas-lubricated compressor ordered from Bristol-Siddeley is being fabricated. The compressor is undergoing final tests at the factory. Additional studies of compressors for experimental loops are under way. Also, tests have been initiated in an apparatus designed for studying back diffusion of oil or water vapor against the flow of helium through labyrinth-type seals.

Part 1. Design Investigations

1. REACTOR PHYSICS

Energy Deposition in Graphite of EGCR

The heat deposition rate in each graphite column and fuel element sleeve in the EGCR core has been calculated for the initial reactor loading with the experimental tubes empty. Heating from both gamma-ray absorption and neutron moderation were included. The gamma-ray source was taken to have an energy of 15 Mev/fission, with 4.99 Mev/fission escaping the fuel rods.[1] The energy deposition from the moderation of neutrons was taken to be 4.95 Mev/fission. The calculated total heat generation rates were 2.09 Mw for gamma rays and 2.07 Mw for neutrons.

The distribution of the heat deposition over the core was determined by summing, at a point, the contributions from each fuel element inside a 32-in. square, with the summing point at the center of the square. Contributions from fuel elements outside the square were found to be negligible. The results of the calculations are summarized in Fig. 1.1.

Worth of EGCR Control Rod Bank

The shutdown worth of the EGCR control rod bank has been calculated by using methods described previously.[2] The calculations, both for empty experimental tubes and for a typical experimental assembly in each tube, were four-group two-dimensional calculations in which each rod in the bank was explicitly represented as a separate region. A square geometrical representation of the rods was used, since this had been shown to give excellent agreement with experimental measurements of the control rod worth.[2] The previous calculations were used to determine the extrapolation lengths in each group, and the boundary condition at

---

[1]E. A. Nephew, "Gamma-Ray Heating in the EGCR Experimental Loop Tube," ORNL CF-59-6-24 (June 1, 1959).

[2]"GCR Quar. Prog. Rep. Dec. 31, 1959," ORNL-2888, pp. 9–11.

UNCLASSIFIED
ORNL-LR-DWG. 47073

47.8	65.1	60.4	47.5	3.4	0.5
65.1	62.2	52.5	39.1	2.7	0.5
60.4	52.5	29.7	14.6	1.1	0.5
47.5	39.1	14.6	0.5	0.5	
3.4	2.7	1.1	0.5		
0.5	0.5	0.5			

(*a*) Total Heat Deposition (kw) in Each Graphite Column in Southeast Quadrant of Core.

7.57	7.45	7.68	7.79	7.51	6.90	6.01	5.40
7.45	–	7.49	7.62	7.29	6.65	5.75	5.14
7.68	7.49	7.51	7.38	6.89	6.16	5.27	4.66
7.79	7.62	7.38	6.93	6.22	5.38	4.50	3.95
7.51	7.29	6.89	6.22	5.30	4.32	3.59	3.24
6.90	6.65	6.16	5.38	4.32			
6.01	5.75	5.27	4.50	3.59			
5.40	5.14	4.66	3.95	3.24			

(*b*) Total Heat Deposition (kw) in Each Fuel Element Sleeve in Southeast Quadrant of Core.

Fig. 1.1. Heat Deposition in Graphite Columns and Fuel Element Sleeves of EGCR Core.

the rod surface was obtained from the extrapolation lengths. The results of the calculations are summarized in Table 1.1.

Table 1.1. Worth of EGCR Control Rod Bank in the Initial Core Loading (2.2% Enriched) at Room Temperature

Experimental Loop Condition	Number of Rods Inserted	Δk_{eff}
Tubes empty	21*	0.201
Tubes empty	25	0.269
Experimental assembly in each tube (C/U = 200)	25	0.240

*Four rods on core diagonal not inserted.

Perturbations Produced in the EGCR by a Half-Empty Fuel Channel

An investigation has been made of the neutron-flux and power-density perturbations produced by a half-empty fuel channel in the EGCR. The geometrical configuration used in making a two-dimensional flux calculation of this effect included a half-empty fuel channel and its associated moderator surrounded by a homogeneized medium whose thickness was such that the entire assembly involved a nine-by-nine fuel cell array.

Axial plots of the calculated perturbed thermal flux at various radial positions are presented in Fig. 1.2. Curves 1 and 2 are, respectively, flux plots at the center and outer edge of the half-empty fuel channel. Curves 3 and 5 are flux plots at the inner and outer edges, respectively, of the homogeneized region. Curve 4 is a flux plot along what would have been the axis of the fuel channel adjacent to the half-empty channel had this region not been homogeneized.

The maximum value of the ratio of power density in the perturbed condition to that in the unperturbed condition at a given position is approximately 1.7. This occurs in the very end of the partially removed

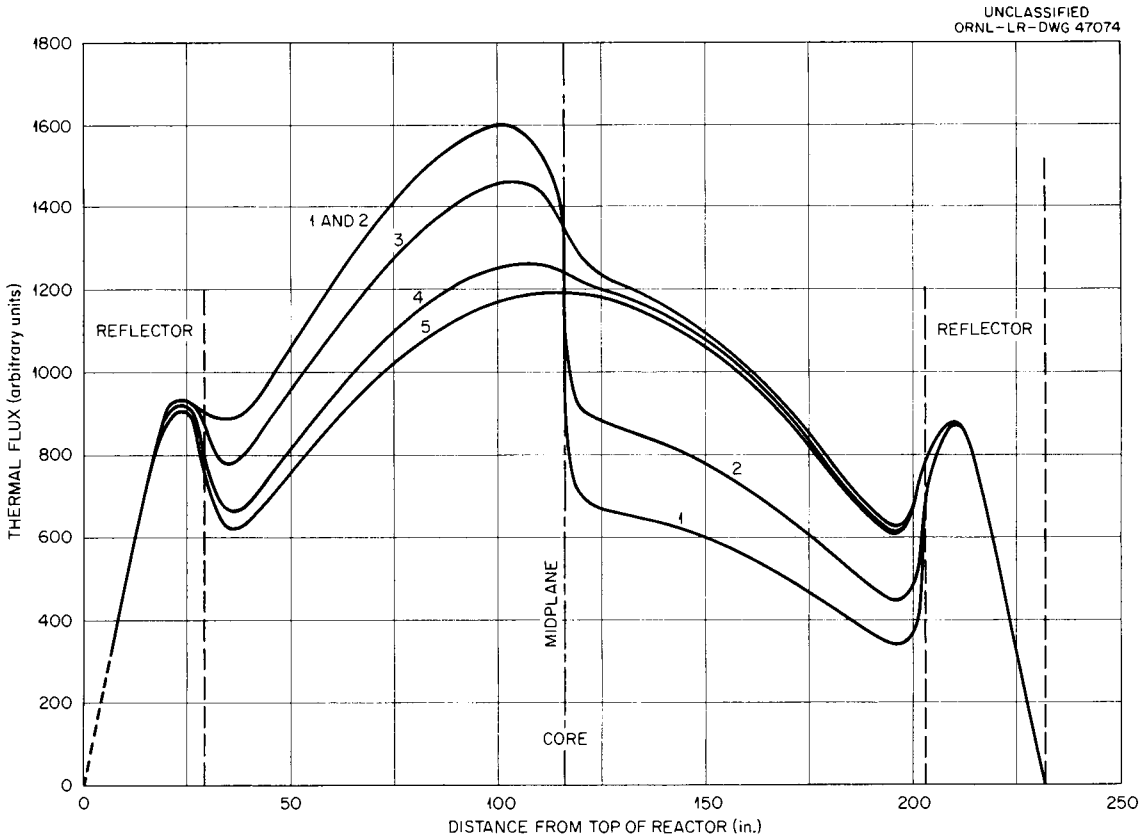

Fig. 1.2. EGCR Axial Thermal Flux Distribution with One Fuel Channel Half Empty.

fuel assembly, and it drops quite rapidly to 1.1 within about 1.5 in. The ratio of the total power generated in the perturbed condition to that generated in the unperturbed condition in the end fuel pellet of the partially removed fuel assembly is about 1.14. With reference to the power density ratio of 1.7 given above, it should be pointed out that a fraction of this perturbation exists at the ends of the fuel assembly even when the fuel assembly is fully inserted, and therefore the perturbation attributable to partially removing the rod is only about 1.6.

Protactinium Losses in a BeO-Moderated Reactor

In a one-region reactor which uses Th^{232} as fertile material and U^{233} as fuel, the intermediate nuclide Pa^{233} is subject to competition

between neutron capture and beta decay to U^{233}. The effect on the conversion ratio can be computed from the relationship:

$$R_c = R_{c_0}\left(\frac{1-\Delta}{1+\Delta}\right) ,$$

where R_{c_0} is the conversion ratio at zero specific power, that is, in the absence of Pa^{233} absorption, and

$$\Delta = \frac{\overline{\sigma_a^{13}\phi}}{\overline{\sigma_a^{13}\phi} + \lambda^{13}} .$$

In a reactor operating at a fixed power level, the fission rate is given by

$$\overline{\sigma_f^{23}\phi} = (1.207 \times 10^{-11})(\text{specific power}) ,$$

so

$$\Delta = \frac{\dfrac{\overline{\sigma_a^{13}\phi}}{\overline{\sigma_f^{23}\phi}}(1.207 \times 10^{-11})(\text{specific power})}{\dfrac{\overline{\sigma_a^{13}\phi}}{\overline{\sigma_f^{23}\phi}}(1.207 \times 10^{-11})(\text{specific power}) + 2.93 \times 10^{-7}} .$$

Recent measurements, as reviewed by Stoughton and Halperin,[3] indicate a value of 1200 barns for the resonance integral of Pa^{233}, which is a considerably higher value than has generally been assumed for the

[3]R. W. Stoughton and J. Halperin, "Heavy Nuclide Cross Sections of Particular Interest to Thermal Reactor Operation: Conventions, Measurements and Preferred Values," Nuclear Sci. and Eng. 6, 100–18 (1959).

resonance integral, and a value of 70 barns for the thermal cross section. These cross sections lead to particularly serious losses of Pa^{233} in reactors with decidedly intermediate spectra, for example, reactors that use BeO moderation.

The ratio $\overline{\sigma_a^{13}\phi}/\overline{\sigma_f^{23}\phi}$ varies with changes in neutron spectrum and thus is affected by changes in core composition. Values of the ratio were calculated by taking the fluxes obtained in infinite, homogeneous, multigroup (GNU) calculations of different compositions and computing

$$\overline{\sigma_a^{13}\phi} = \sum_g \sigma_a^{13g}\ \phi(u)^g\ \Delta u^g \quad ,$$

and

$$\overline{\sigma_f^{23}\phi} = \sum_g \sigma_f^{23g}\ \phi(u)^g\ \Delta u^g \quad ,$$

where the summation is performed over energy groups g. Since the energy dependence of the Pa^{233} cross section has not yet been measured, the method suggested by Perry, Preskitt, and Halbert[4] was used in deducing group cross sections appropriate to a 1200-barn resonance integral.

The effect of the Pa^{233} absorption is shown in Fig. 1.3, which is based on the values of $\overline{\sigma_a^{13}\phi}/\overline{\sigma_f^{23}\phi}$ obtained as outlined above. It was assumed that the introduction of heavy nuclides and leakage would not change the neutron spectrum significantly.

Comparison of Conversion Ratios of Blanket Materials

The conversion ratios obtainable in a BeO-ThO_2 blanket have been compared with the conversion ratios obtainable in a blanket composed of graphite and ThO_2. To make the comparison, multigroup calculations were performed in which each case consisted of a long $U^{233}O_2$-BeO-ThO_2

[4]A. M. Perry, C. A. Preskitt, and E. C. Halbert, "A Study of Graphite-Moderated Th-U^{233} Breeder Systems," ORNL-2666 (Jan. 18, 1960).

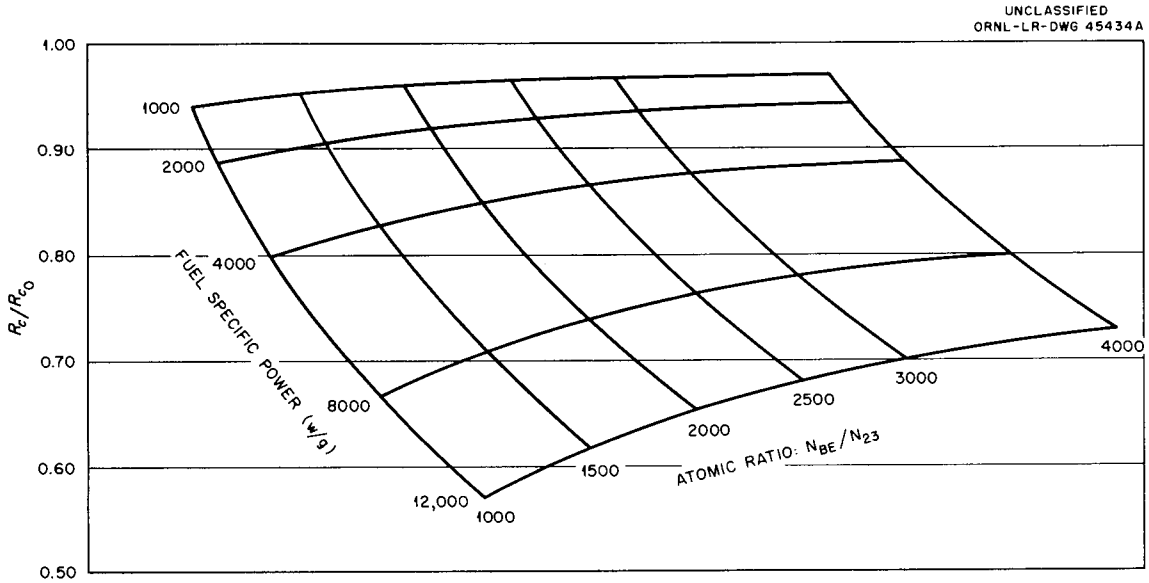

Fig. 1.3. Conversion Ratio of $U^{233}O_2$-BeO-ThO_2 Systems Compared with Conversion Ratio at Zero Fuel Specific Power.

cylindrical core surrounded by a cylindrical blanket. The beryllium cross sections were chosen to given an $\epsilon_{BeO} = 1.036$, which is within the range recommended by Häfele and Tsagaris.[5] The thorium concentration in the core was adjusted to maintain criticality.

In Fig. 1.4a the conversion ratios are plotted for 8-ft-diam cores with 2-ft-thick blankets as functions of the thorium concentrations in the blanket. The conversion ratio is always higher at a given thorium concentration for the BeO blanket than for the graphite blanket. The difference becomes less, however, as the thorium concentration increases, and both curves rise steeply enough so that equal conversions can be obtained, in most cases, by using a slightly higher thorium concentration in the graphite blanket. As the blanket is made thicker, the advantageous properties of the graphite become more apparent. The limiting case of an "infinitely thick" blanket is shown in Fig. 1.4b. Here, the graphite

[5]W. Häfele and M. E. Tsagaris, "The Fast Multiplication Effect of Beryllium Oxide in Reactors," ORNL-2849 (Nov. 30, 1959).

blanket gives slightly better conversion ratios except at very low thorium concentrations. At still higher thorium concentrations than those shown on the graph, the two lines will converge again as each blanket becomes essentially all thorium.

The effect of varying the core diameter is shown in Fig. 1.5. The differences mentioned above are emphasized in small cores, since a large fraction of the conversion takes place in the blanket, and are decreased in large cores. The situation can perhaps be visualized as the result of two contrasting properties of graphite and BeO. On the one hand, the effective absorption cross section of the graphite is lower than that of the BeO, except at points immediately adjacent to the core, even when the additional neutron production by the beryllium fast reactions is included. On the other hand, the reflecting properties of the BeO are superior to those of the graphite. Thus, the BeO gives better conversion ratios for thin blankets by minimizing the leakage; BeO also gives better conversion ratios for thick blankets as long as the thorium concentration is very low.

Comparison of Nuclear Characteristics of BeO-Moderated Cores and Graphite-Moderated Cores

In considering the possibility of using BeO for moderation in a gas-cooled reactor, it is also of interest to compare the nuclear characteristics with those of similar graphite-moderated reactors. A series of multigroup calculations was made using the IBM-704 GNU II code. For each case, a two-region reactor was specified that consisted of a cylindrical core containing a homogeneous mixture of U^{233}, Th^{232}, and moderator surrounded by a cylindrical blanket containing the same moderator mixed homogeneously with Th^{232}. The blanket thickness was 2 ft if the blanket was graphite and 1.4 ft if it was BeO, since previous calculations with no thorium in the blanket had indicated that these thicknesses were equivalent in neutron economy. The thorium concentration in the blanket was fixed at 6.21×10^{20} and 8.28×10^{20} atoms/cm^3 for BeO and graphite, respectively, since previous calculations

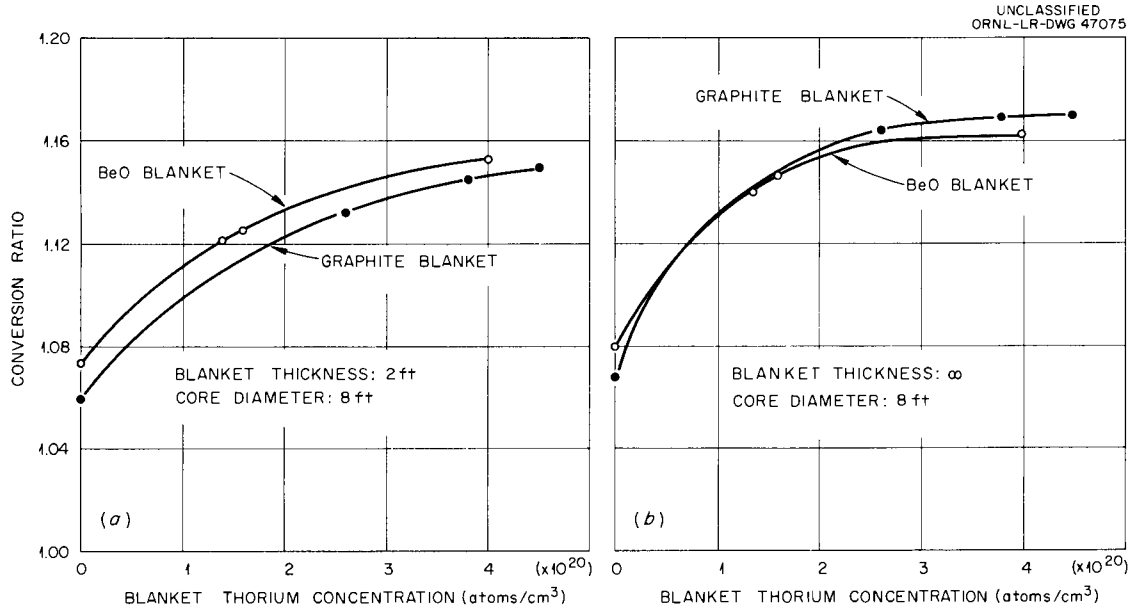

Fig. 1.4. Conversion Ratios for BeO and Graphite Blankets as Functions of Blanket Thorium Concentration.

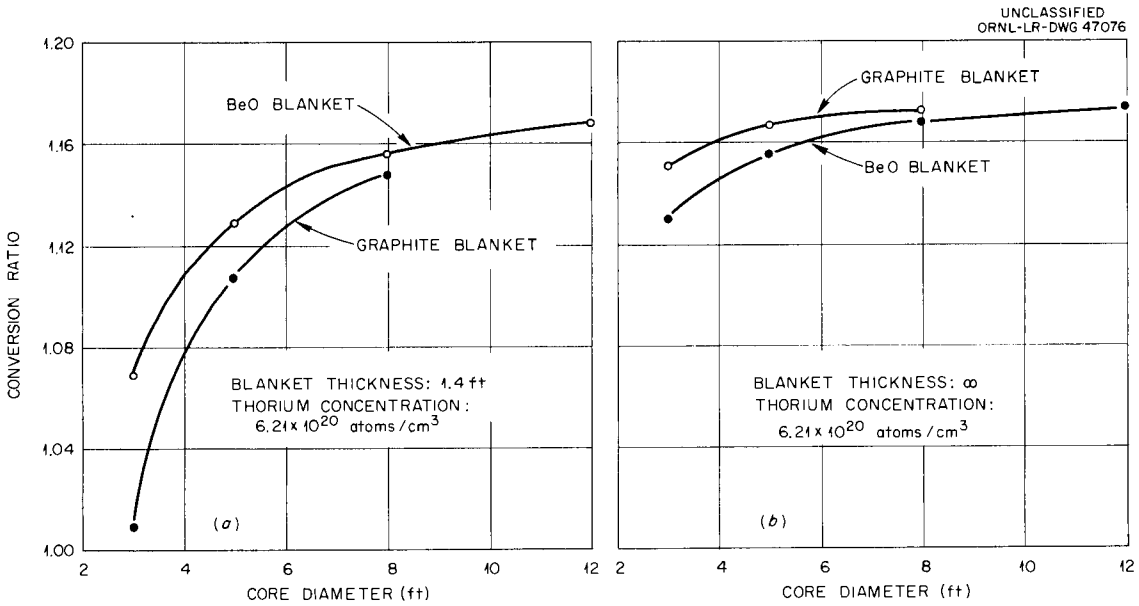

Fig. 1.5. Conversion Ratios for BeO and Graphite Blankets as Functions of Core Diameter.

had indicated that these concentrations would give equal leakage from the blanket.

The axial buckling was computed by using a core length of 10 ft plus a reflector savings due to a thick graphite reflector in the case of graphite-moderated cores or a thick BeO reflector in the case of BeO-moderated cores. The ratio of moderator atoms to fuel atoms in the core was fixed at 4000 with BeO and 8000 with graphite. In general it has been found in other multigroup calculations that approximately equal values of ηf are obtained when the moderator-to-fuel atomic ratio is twice as high with graphite as with BeO. The thorium concentrations in the core were adjusted to give an effective multiplication of 1.1. This value was chosen, rather than 1.0, in order to approximate the conditions which would prevail with the inclusion of appropriate fission-product poisons.

The quantities of particular interest in the calculations were the leakages from the core, the over-all conversion ratios, and the distributions of the conversion ratios between core and blanket. The net leakage from the core is shown in Fig. 1.6. The leakage increases with decreasing core diameter and with increasing void fraction. In comparing the graphite-moderated core with a BeO-moderator core of the same void fraction, the same core leakage is obtained when the graphite-moderated core is about twice the diameter of the BeO-moderated core. It should be kept in mind, however, that the exact shapes of these curves depend strongly on the composition of the blanket and to some extent on the thickness of the blanket.

The conversion ratios are shown in Figs. 1.7 through 1.10. The total conversion ratios in each case seem to decrease with decreasing core diameter and with increasing void fraction. Analyses of the results show, however, that the former effect is substantially due to an increase in radial leakage from the blanket, whereas the latter effect is due to an increase in axial leakage from the core. Hence the total conversion ratio would be nearly independent of void fraction and core diameter if the core were made longer and the blanket thicker. Decreasing

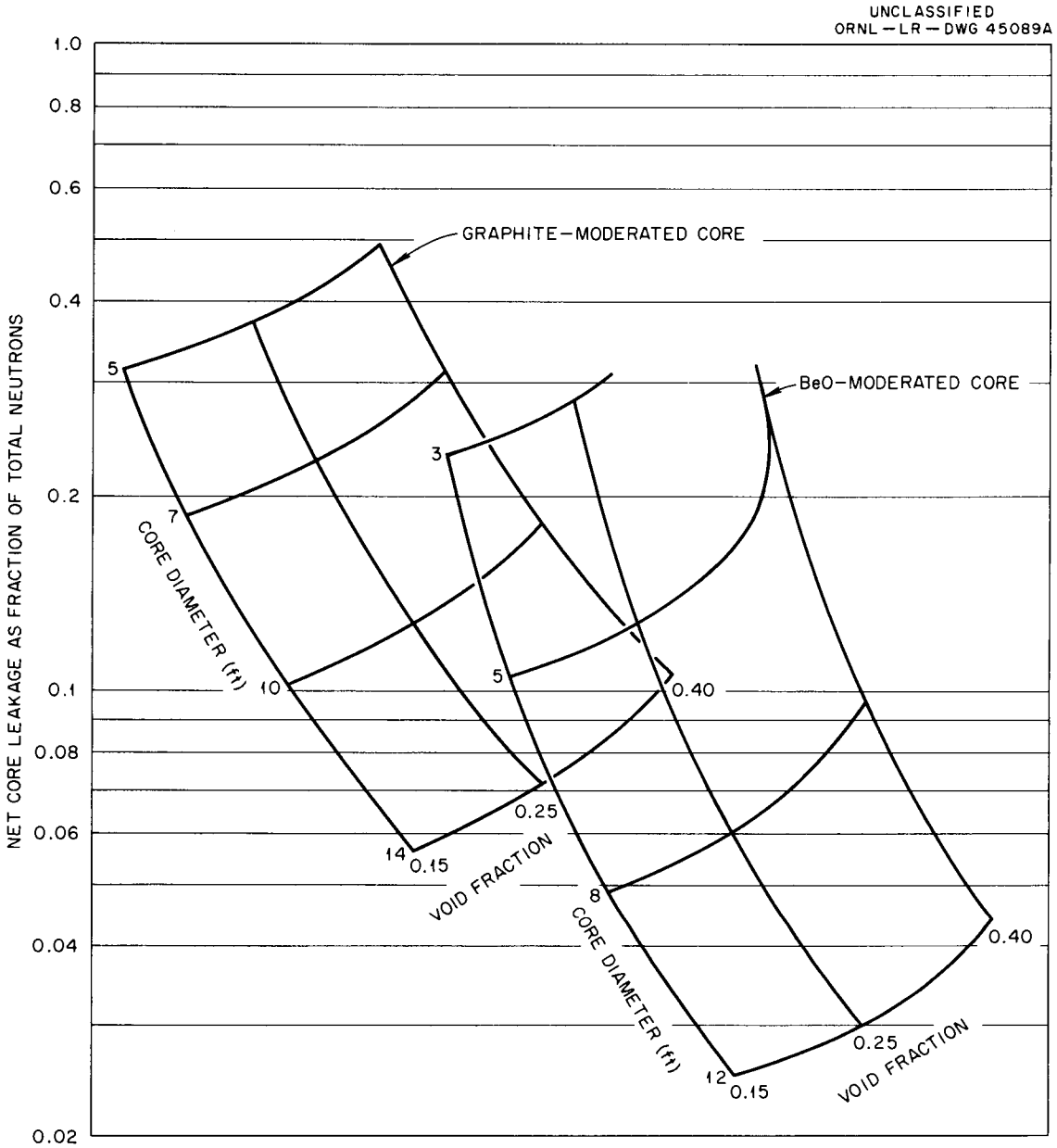

Fig. 1.6. Net Core Leakage from Graphite- and BeO-Moderated Cores.

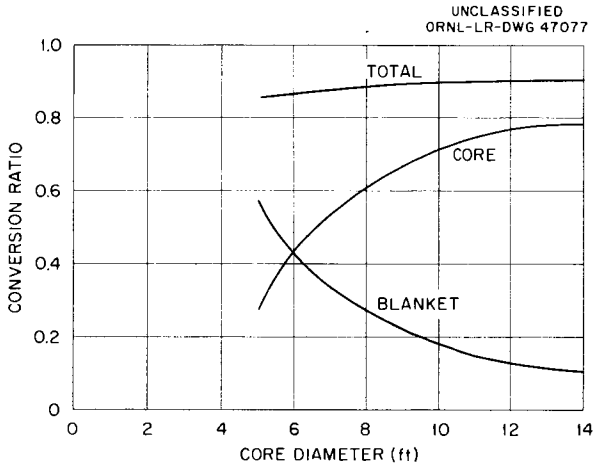

Fig. 1.7. Conversion Ratios for Graphite-Moderated Cores with 0.15 Void Fraction.

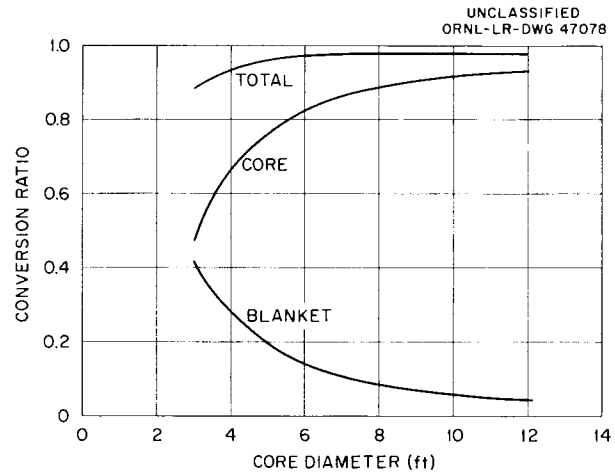

Fig. 1.8. Conversion Ratios for BeO-Moderated Cores with 0.15 Void Fraction.

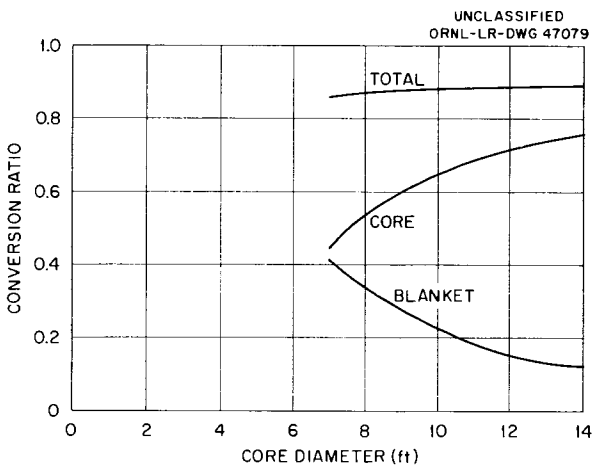

Fig. 1.9. Conversion Ratios for Graphite-Moderated Cores with 0.25 Void Fraction.

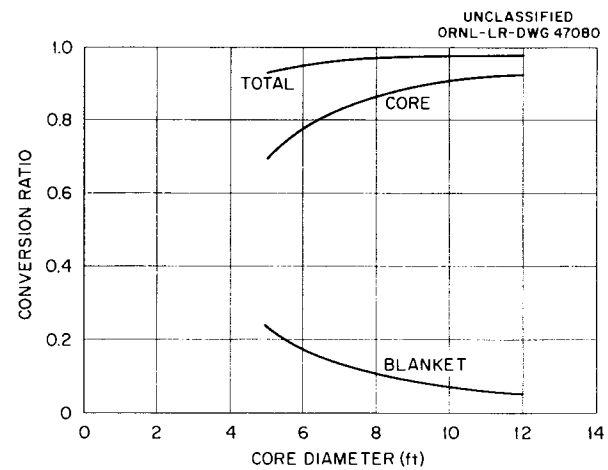

Fig. 1.10. Conversion Ratios for BeO-Moderated Cores with 0.25 Void Fraction.

the core diameter also had very minor effects on the total conversion ratio because it increased the fraction of the conversion in the blanket, since the amount of "parasitic" capture is not, in general, the same in the core as in the blanket. This effect was not shown accurately, since the fission products were not explicitly included in the calculation. Changing the core diameter did not have any perceptible effect on the total conversion ratio that could be attributed to changes in the neutron energy spectrum. These calculations did not include the effect of neutron absorption in Pa^{233}, which would be mostly in the core, and which could substantially decrease the conversion ratios of the large-diameter cores in comparison with the small-diameter cores.

The amount of conversion which takes place in the core naturally increases with increasing core size, whereas the amount of conversion in the blanket decreases. Again, the shapes of the curves obtained with BeO moderation are similar to the shapes of those obtained with graphite, and equal fractions of core conversion divided by total conversion are found with a graphite-moderated core of about twice the diameter of a BeO-moderated core. The higher total conversion ratios obtained with the BeO-moderated cores are primarily due to the fast reactions in beryllium, that is, the net result of the (n,2n) reaction and the (n,α) reaction.

2. REACTOR DESIGN STUDIES

EGCR Fuel Assemblies

Mechanical Design

Several alternate designs are still being considered for the EGCR fuel element spacers and top and bottom spiders. One concept of the design is shown in Fig. 2.1. The feature that was thought to be objectionable when used in an earlier design is the requirement that the bottom spider be welded to three of the outer elements after the cluster is inserted into the sleeve. Assembly of a number of elements has shown, however, that there is no difficulty or problem in attaching the bottom spider in this manner.

The design shown in Fig. 2.1 incorporates a "breakaway" feature in that the stainless steel and fuel parts of the assembly may be removed from the sleeve in case the sleeve becomes "jammed" in a channel. The radial centering tabs on the bottom spider are thin so that, if it is necessary to remove the cluster from the sleeve, the tabs will bend and pull through the sleeve; the tensile load applied to the three tubes welded to the bottom spider is small.

Both the shear pins and the tabs will be tested at room temperature and at 1100°F. Estimates of the strengths of the pins and tabs are given in Tables 2.1 and 2.2. Table 2.1 gives the estimated loads required to shear pins of various sizes at room temperature and at 1100°F. The reaction loads per tab, given in Table 2.2, are the maximum side loads that the tabs can withstand at 1100°F for a 0.2% offset. The approximate tensile loads necessary to bend the tabs and pull the lower spider through the sleeve at room temperature are given in Table 2.3.

Flow Distribution

The design of the web structure for both the top and bottom spiders appears to be the controlling factor in the magnitude of both the gas and surface temperature asymmetries throughout the seven-element cluster.

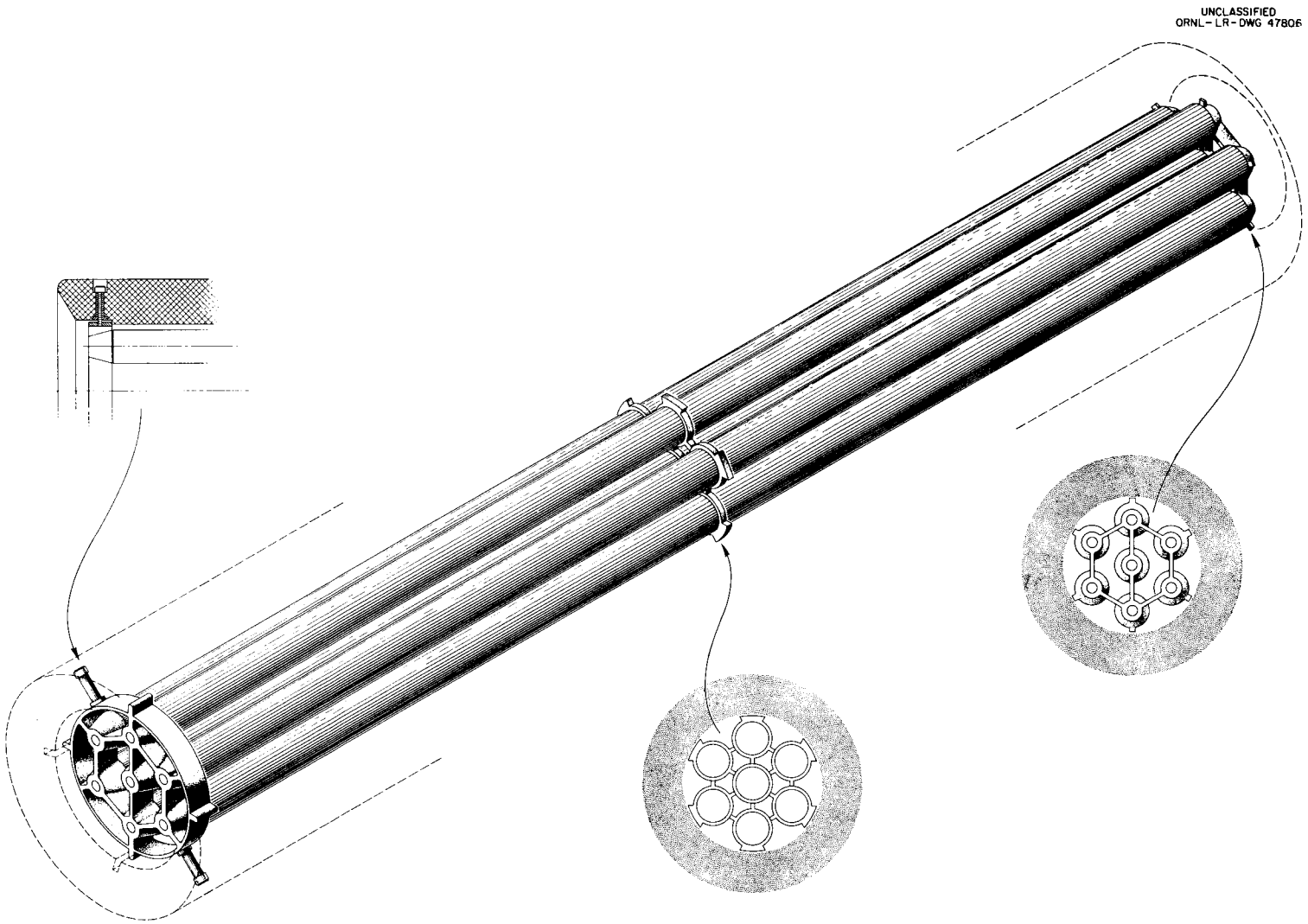

Fig. 2.1. Modified EGCR Fuel Assembly.

Table 2.1. Shearing Load As a Function of Pin Diameter

Pin Diameter (in.)	Lifting Force (lb)	
	At 1100°F	At Room Temperature
0.051	100	174
0.072	200	347
0.088	300	520
0.102	400	694
0.114	500	867

Table 2.2. Reaction Load Per Tab for Various Tab Thicknesses

Tab Thickness (in.)	Reaction Load per Tab (lb)
0.011	5
0.022	10
0.033	15
0.044	20
0.055	25

Table 2.3. Lifting Force Required to Bend Tabs and Pull Spider Through Sleeve

Tab Thickness (in.)	Lifting Force at Room Temperature (lb)
0.028	25
0.040	50
0.057	100
0.069	150
0.080	200

An analytical investigation of the flow distribution at the inlet of an assembly has indicated that the original "H" structure[1] for the web in the hangers will cause serious maldistribution of the flow through the assembly. Since the assemblies are to be randomly stacked in the channels, there would be several angular rotations of the top spider relative to the bottom spider that would reduce the inlet velocity around the central tube to about one-half the average velocity for the cluster. This would lead to large local surface temperatures and large temperature differences across the outer elements. The flow distribution analysis of the newer web design for the spider (shown in Fig. 2.1) has not been completed, but preliminary results indicate a considerable improvement over the flow distribution of the "H"-type structure. An experimental check is being made of the validity of the analytical method used in these calculations.

An analytical model describing the flow distribution in a rod cluster has been derived that agrees well with experimental results. In this model the static pressure at any axial location in a channel containing a rod cluster is assumed to be constant across the channel. To determine the flow distribution in the channel, it is necessary to divide the channel into several parallel passages, as shown in Fig. 2.2. For a seven-rod cluster there are 12 passages, six outer and six inner. As shown in Fig. 2.1 the equivalent diameter of the inner passages is greater than that of the outer passages, so the equilibrium velocity will be greater in the inner passages. Also, since all the passages communicate with each other, the static pressure in each passage will be approximately the same.

The velocity in one of the inner passages is compared in Fig. 2.3 with the average velocity for the whole channel. The abscissa for this case is the ratio of the channel length to the channel equivalent diameter. The relative location of the length-to-diameter scale is arbitrary, and the point at which the curve is intercepted to determine

---

[1]"GCR Quar. Prog. Rep. Dec. 31, 1959," ORNL-2888, p. 28, Fig. 2.1.

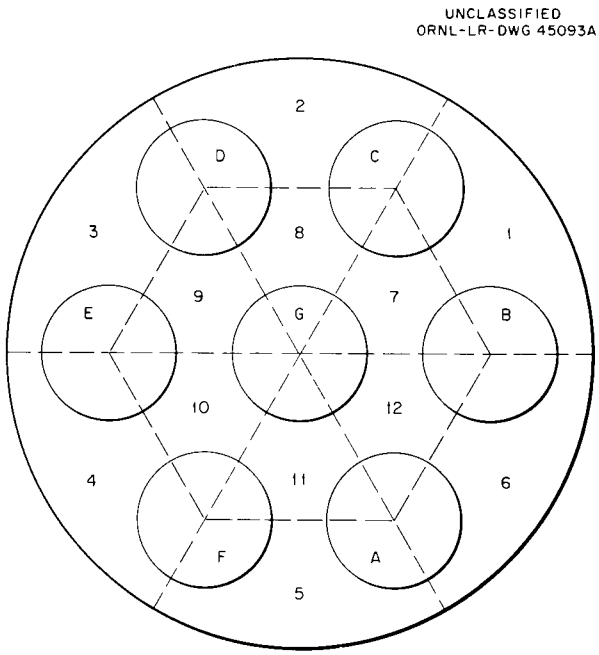

Fig. 2.2. Section of Seven-Element Cluster Showing Flow Passages for Flow Distribution Calculations.

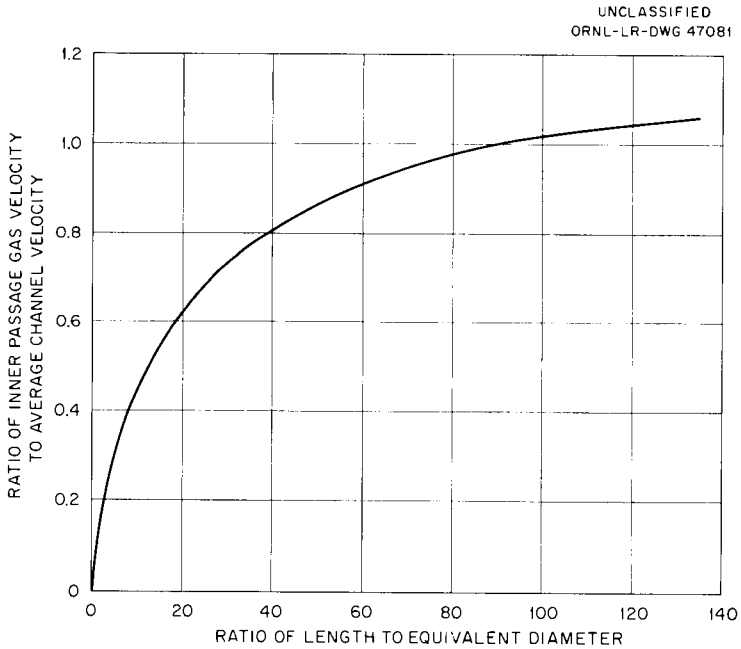

Fig. 2.3. Typical Velocity Distribution in a Rod Cluster as a Function of the Length-to-Diameter Ratio.

the velocity as a function of axial position in the cluster depends on the inlet velocity ratio. One interesting point shown by Fig. 2.3 is the large length-to-diameter ratio required to approach the equilibrium velocity which for this case was about 1.1. It should be noted that, if the inlet velocity ratio was greater than 1.1, the curve would be reversed; it would be decreasing with length and approaching the equilibrium velocity from above rather than below.

Fission-Gas Pressure Buildup in EGCR Fuel Elements

In the design of the fuel elements for the EGCR, the UO_2 pellets are cored so that the central region of the fuel element serves as a gas reservoir. Although this is a poor location for gas storage because of its high temperature, it will accommodate a fission-gas release equivalent to about 40% of the stable xenon and krypton formed during a lifetime of 10 000 Mwd/MT. Figures 2.4, 2.5, and 2.6 show the results of calculations of the effects of fission-gas pressure buildup on the EGCR fuel elements. In all cases the value of the apparent diffusion coefficient was assumed to be 10^{-9}/sec at 1400°C, with an activation energy of 65 kcal; the heat transfer rate was taken to be 31 500 Btu/hr·ft; the outside diameter of the UO_2 was assumed to be 0.705 in. and the inside diameter 0.323 in.; the stainless steel cladding thickness was taken to be 0.020 in.; and the initial gap in all cases was considered to be 0.0005 in. The exact magnitude of the gap is not known, of course, but, at the temperatures shown on Figs. 2.4, 2.5, and 2.6, the cladding will collapse onto the UO_2 during the early part of the irradiation and the gap will be very small. The element will be filled initially with helium at 1 atm.

The results presented in Fig. 2.4 are based on the assumption that the pellet diameter remains constant so that, as the internal pressure builds up and exceeds the external pressure, the cladding will creep and increase the clearance. Actually, as the clearance increases the temperature of the UO_2 will increase, and the UO_2 will expand and to some extent decrease the clearance. The results presented in Fig. 2.5

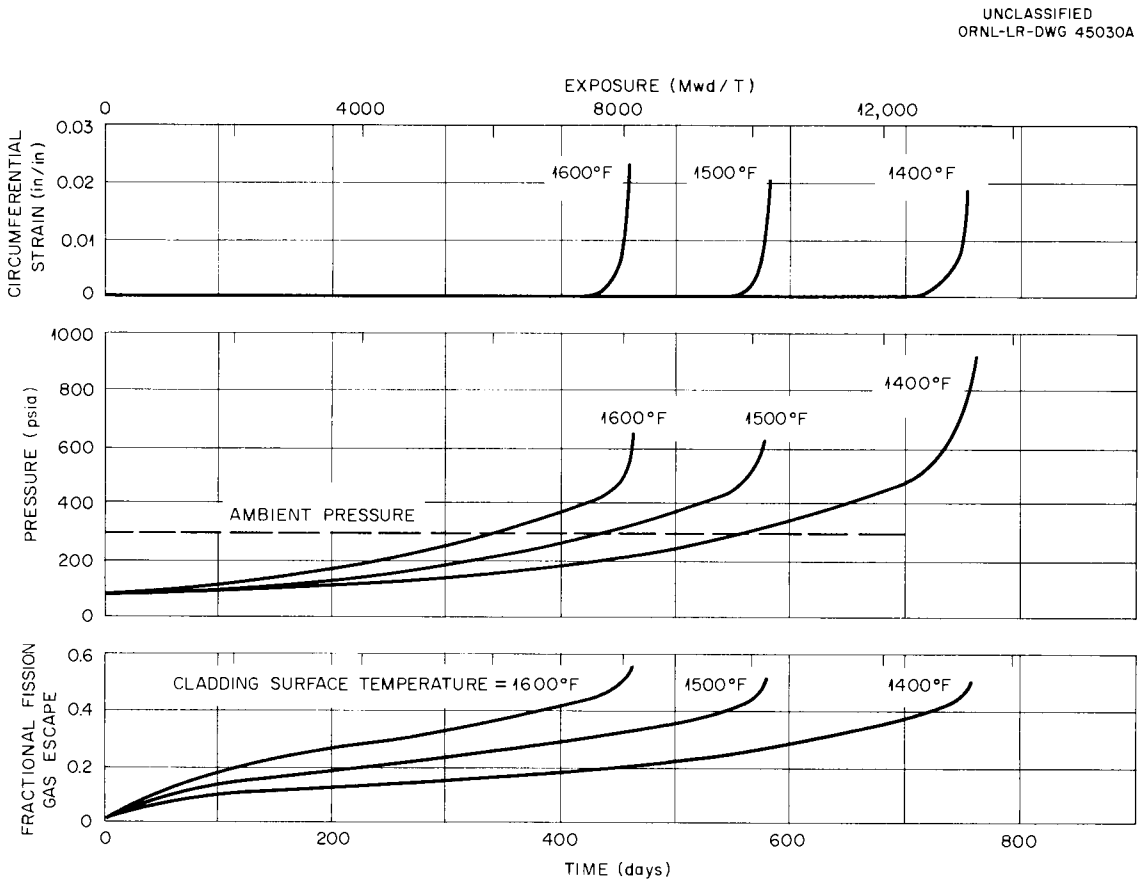

Fig. 2.4. Behavior of EGCR Fuel Element at Various Constant Surface Temperatures Based on Assumption that Gap Between Cladding and Fuel Increases as the Cladding Expands.

show the case where the clearance remains constant at 0.0005 in. over the entire lifetime of the element. In Fig. 2.6 the mean temperature of the cladding is assumed to be 1400°F, and the local cladding temperature is treated as a variable. Again the gap is assumed to remain constant at 0.0005 in.

Thermal Analysis

Two different fuel loading schemes have been considered for the EGCR. The surface temperature profiles through the maximum power channel for the two loading schemes are shown in Figs. 2.7 and 2.8. The surface

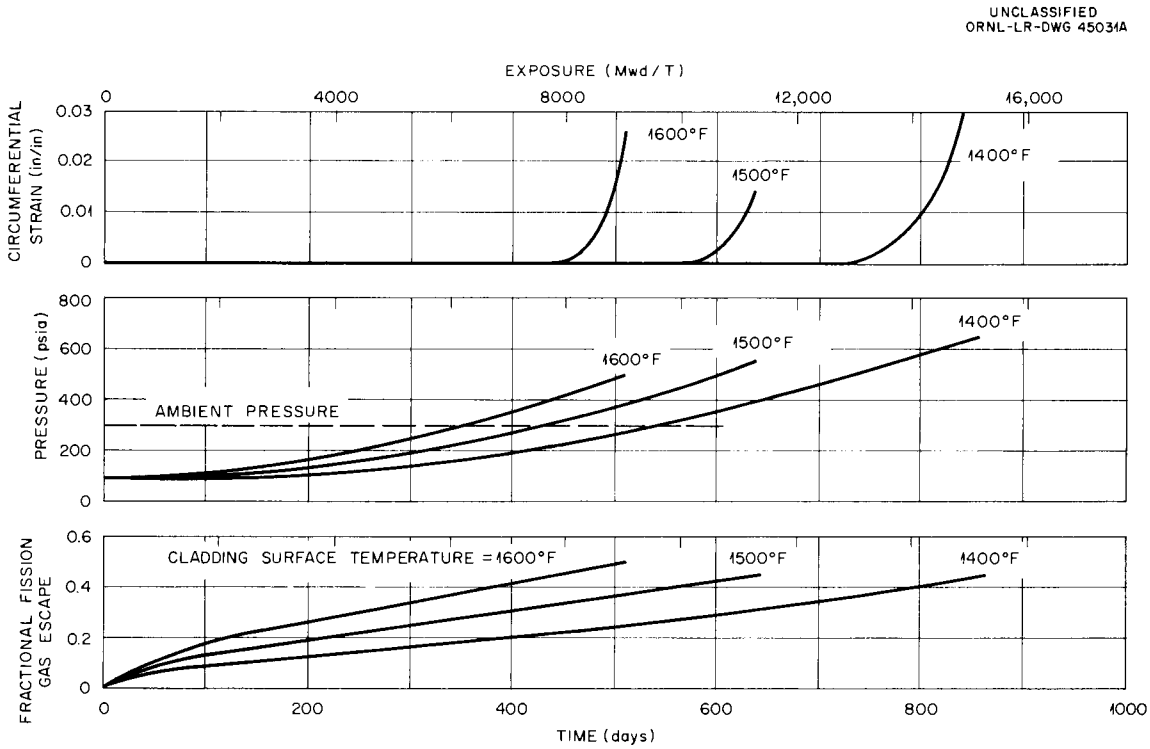

Fig. 2.5. Behavior of EGCR Fuel Element at Various Constant Surface Temperatures Based on Assumption that Gap Between Cladding and Fuel Remains Constant as Cladding Expands.

temperatures given are mean values and do not include the effects of flow maldistribution or hot-channel factors. The coolant enters the bottom of the core at 510°F and exits at 1050°F. The effects of the loading scheme in which three new assemblies are inserted at the top and the three lower assemblies are removed are shown in Fig. 2.7, and the effects of reversing the positions of the upper and lower three assemblies at one-half their lifetime are shown in Fig. 2.8. The latter scheme results in a considerable reduction in the surface temperature. The advantage in using the first scheme would be that by moving the fuel which had received the highest exposure to the bottom of the reactor where it would be at a lower power density and temperature, the pressure of the fission products would be lower. Each channel contains six fuel assemblies, and the very sharp breaks in the surface temperature result

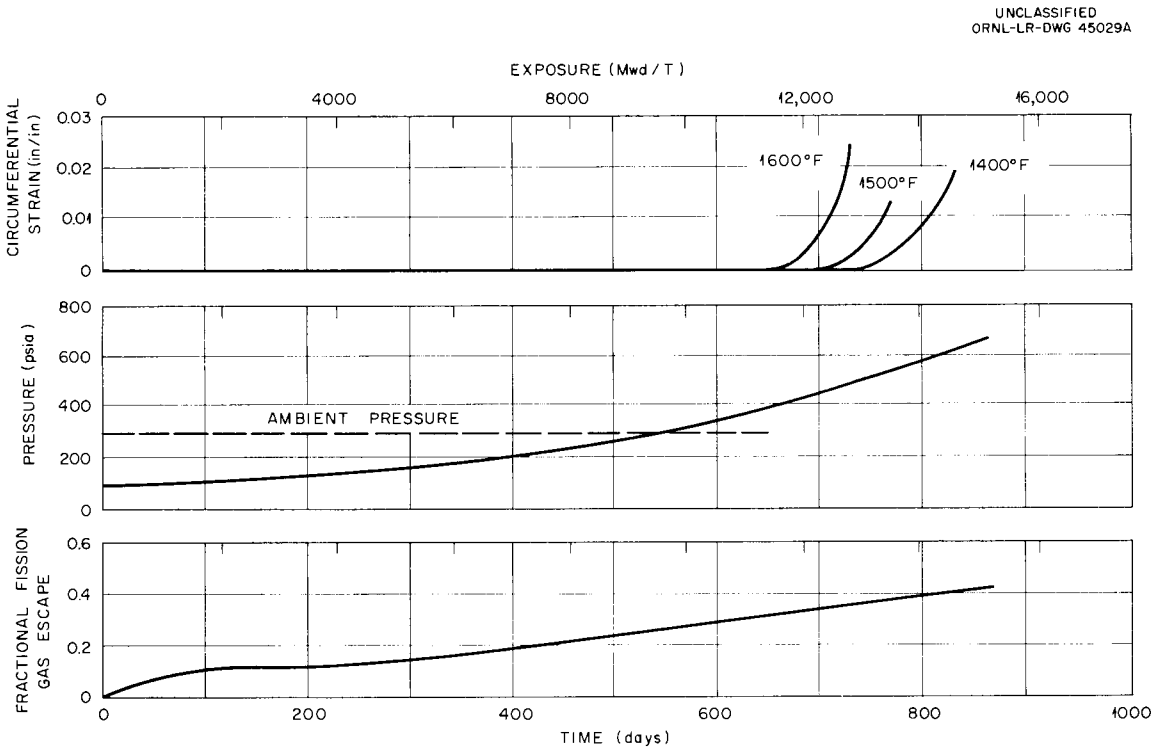

Fig. 2.6. Behavior of EGCR Fuel Element at an Average Surface Temperature of 1400°F and Various Local Cladding Temperatures Based on Assumption that Gap Between Cladding and Fuel Remains Constant as Cladding Expands.

from flow disturbances at the entrance to an assembly or at the mid-point spacers, which cause very high local heat transfer coefficients that decrease rapidly.

EGCR Control Rod Design

Preliminary design studies and thermal analyses of the EGCR control rods have been completed. There will be either 21 or 25 rods located on a 2-ft lattice, and they will contain, as the poison material, annular rings of B_4C clad with 3 1/4-in.-o.d. type 304 stainless steel tubing. The primary mechanical design consideration is that the rod must operate in a 4-in.-diam hole which develops a 1-in. bow as a result of graphite shrinkage due to the radial fast flux gradient across the core. Since

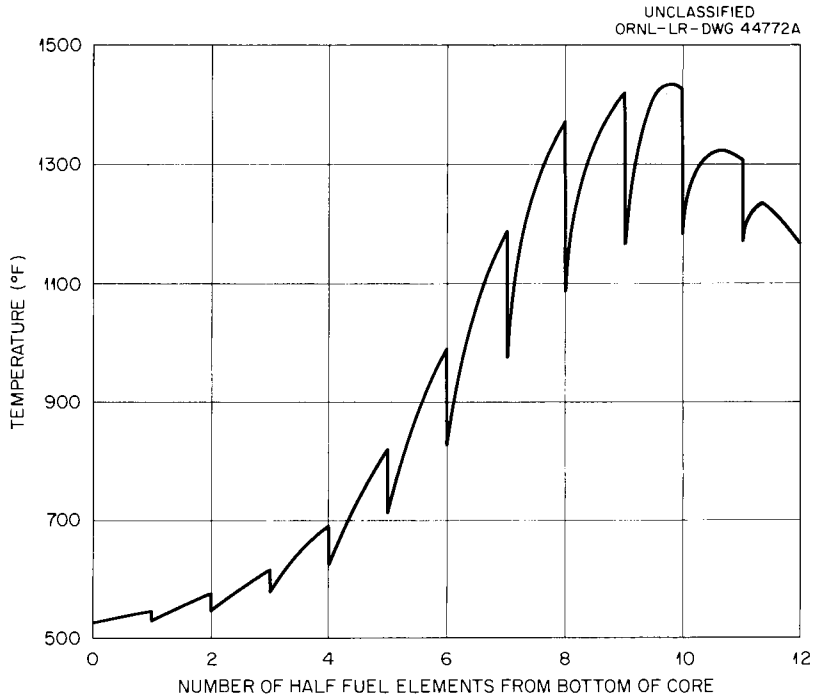

Fig. 2.7. Cladding Surface Temperatures of Elements in Channel with Maximum Power Generation Based on Top Loading Scheme.

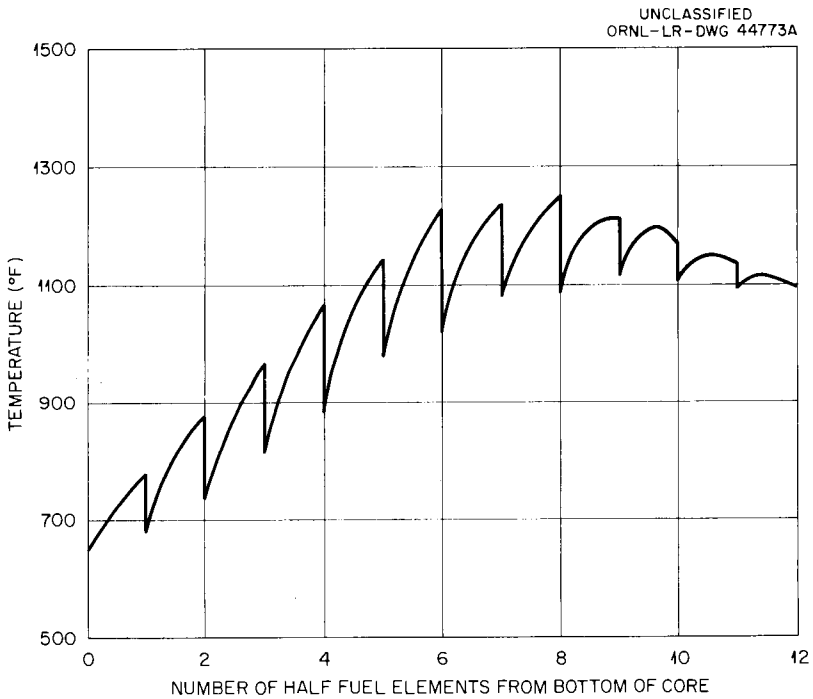

Fig. 2.8. Cladding Surface Temperature of Elements in Channel with Maximum Power Generation Based on Inverted Core Loading Scheme.

it was not practical to decrease the control rod diameter or to increase the hole size, a segmented flexible rod was designed. The preliminary design shows three segments, each approximately 6 ft long, supported internally on a stainless steel cable. Porous stainless steel filters are incorporated in each section to permit venting of the helium generated within the B_4C.

Since all but four of the control rod holes are located at intersections of graphite blocks (four holes are in the center of blocks), the coolant flow is dependent on other leakage paths through the core. In order to minimize this leakage and to aid in providing a more positive coolant flow for the control rods, the primary helium coolant will be directed through the inside of the rod. This method of cooling also allows the main structural components to be located inside the rod and thus minimizes the thickness of the outside cladding, which, in turn, reduces the amount of neutron scattering by the stainless steel. A flow restriction 6 in. long with a 3/16-in. radial clearance between the rod and the hole at the top of the core has been provided to achieve this method of cooling. The current core design provides for a flow of 100 lb/hr up through the center of a control rod and, depending on the rod position in the core, 25 to 75 lb/hr flow in the annulus between the rod and the walls of the hole. Heat transfer calculations for the case of a control rod fully inserted in the center of the core give an average heat generation rate of 8570 Btu/hr·ft, with a peak generation of 12 800 Btu/hr·ft. Allowances were made for heat transfer by radiation to the graphite and for the changes with temperature level in the clearances between the B_4C and the cladding. (Heat generation rates over the length of the rod were based on the axial flux gradient in a core with the inverted fuel loading scheme and with control rods inserted 9 in.) The results of these calculations, shown in Fig. 2.9, indicate that, for 100 lb/hr flow, the cladding temperatures are below the allowable limit of 1600°F. Also, since no credit was taken for convective cooling in the annulus, the cladding temperatures are somewhat high. An increase in the emissivity of the outside stainless steel cladding from 0.3 to

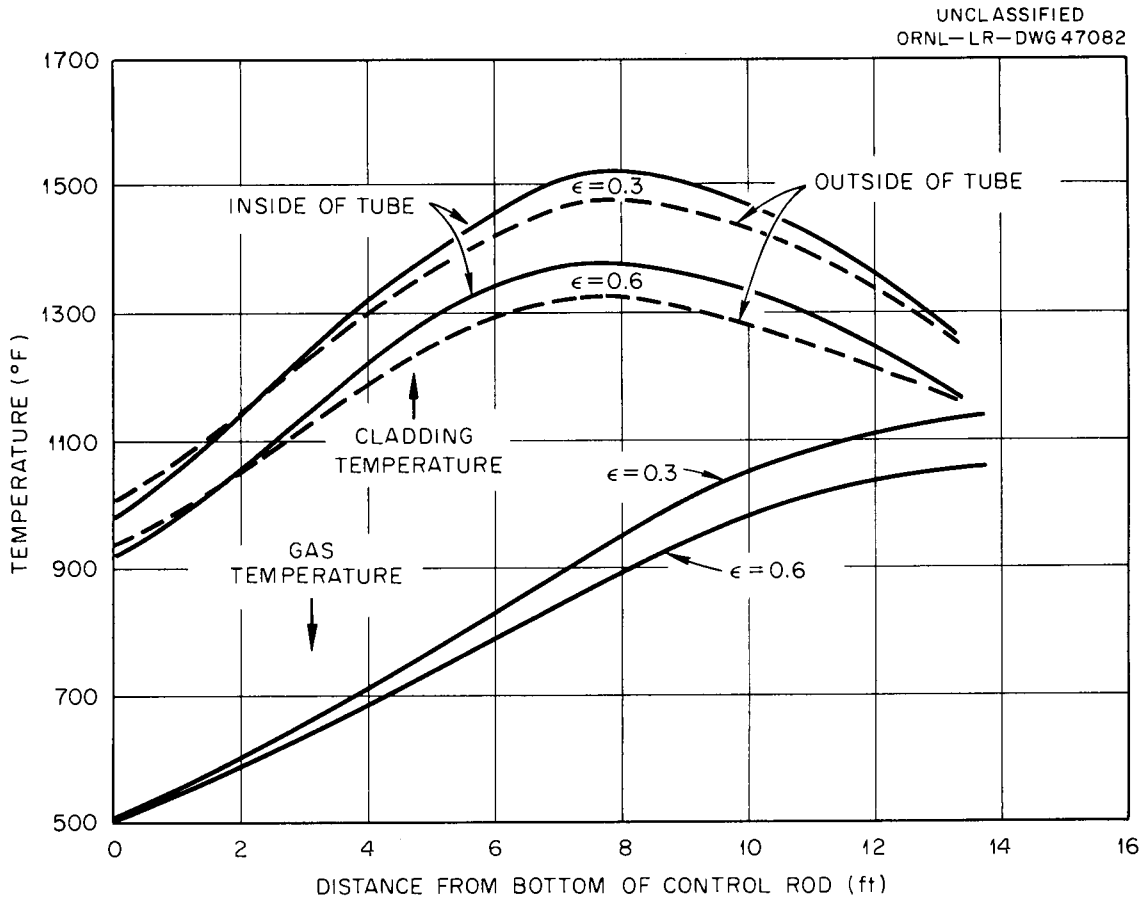

Fig. 2.9. Control Rod Temperature Profile for Coolant Flow of 100 lb/hr Inside the Rod and No Flow Outside the Rod for Two Values of the Emissivity, ϵ, of Stainless Steel.

0.6 was found to decrease the maximum cladding temperature by about 150°F. The average amount of heat transferred by radiation is 45% for the case of an emissivity of 0.6 and is 37% for the lower value of 0.3.

Structural Investigations

Study of Fuel Element Cladding Behavior Under Arbitrary Temperature Distributions

Data obtained in resistance-heated-tube heat-transfer experiments have shown that central spacers on the fuel rods in a seven-rod cluster cause reductions in both the temperature difference across a rod and in

the mean rod temperature. These changes are mainly confined to the spacer region. Using the methods of analysis described earlier,[2,3] the significance of such changes in terms of deflection and stresses for an EGCR rod have been evaluated by comparing the results from the following cases. In the first case there was a 50°F diametral temperature difference that was constant along the length and was a linear function of the diameter. In the second case the same temperature distribution was assumed, except for the central one-fourth of the tube, where the distribution, simulating spacer-induced variations, was that shown in Figs. 2.10 and 2.11. The maximum and minimum temperatures were located 180 deg apart. The mean temperature in both cases was 800°F.

Since the spacers prevent deflection at the midpoints of the rods, each deflection curve was obtained in the following manner. It was assumed that the displacements were determined by the cladding alone, that is, that the UO_2 pellets had no effect upon the deformation, and the deflection profile was calculated for a given temperature distribution. The member was then treated as a simply supported beam with a concentrated load at the center large enough to yield zero deflection at the center, and a second curve was obtained. Finally, the two curves were superposed to give the "restrained" deflection curve desired.

The unrestrained and the restrained thermal bowing curves are shown in Fig. 2.12. It may be seen from this figure that, when the changes in the temperature distribution produced by a spacer are taken into account, the maximum deflection is decreased when the element is unrestrained but is increased when it is restrained. This result is due to the difference in the general shapes of curves A and B when unrestrained. The difference may be visualized by assuming that curve A is partially restrained so that its center deflection coincides with the center deflection of curve B; that is, the maximum deflection point of curve A is "pushed down" to coincide with the maximum deflection

---

[2] "GCR Semiann. Prog. Rep. June 30, 1959," ORNL-2767, p. 26.

[3] "GCR Quar. Prog. Rep. Sept. 30, 1959," ORNL-2835, p. 24.

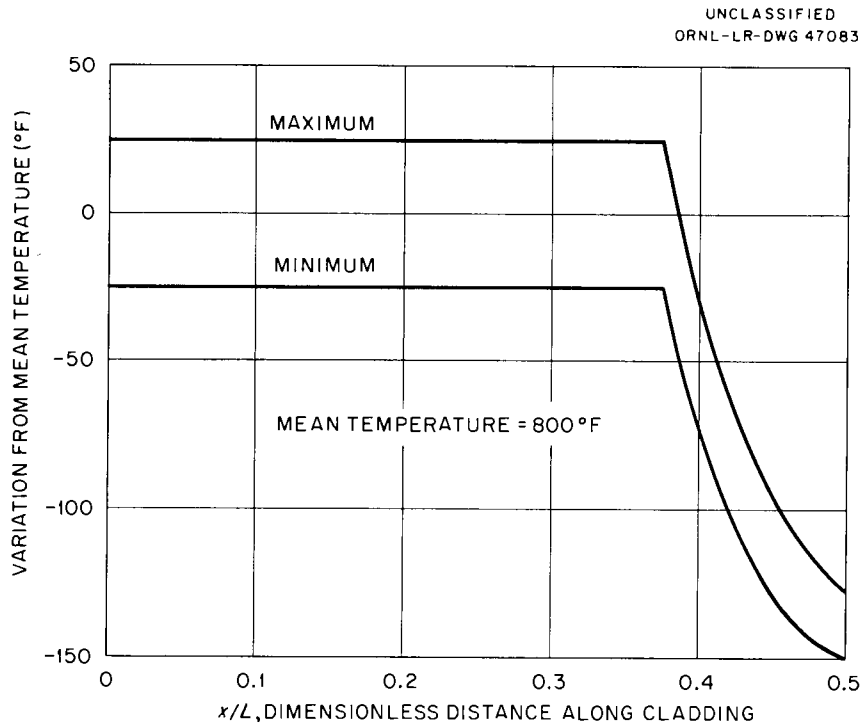

Fig. 2.10. Temperature Along Length of Fuel Element Cladding Including Spacer-Induced Variation.

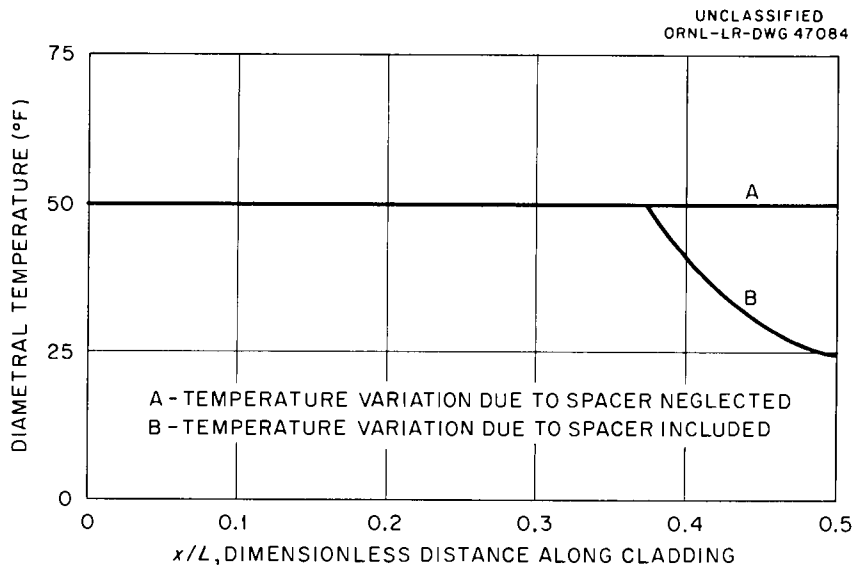

Fig. 2.11. Maximum Diametral Temperature Difference Along Length of Fuel Element Cladding With and Without Effect of Spacer Included.

point of curve B. Then all points (except the end points) along the resulting deflection curve (curve A partially restrained) are below the points on unrestrained curve B. Alternately, the maximum stress is greater for case A than case B, as shown in Fig. 2.13, because this value is directly proportional to the unrestrained deflection at the center. Except near the ends of the rods, both curves in Fig. 2.13 are characteristic of those for a simply supported beam with a concentrated load at the center. The nonlinear portions of the curves can be attributed to the use of zero radial and tangential displacements at the ends as boundary conditions in the analytical model.

Studies were also made for EGCR fuel rods having circumferential temperature distributions given by

$$t = t_0 \, (0.0632 \cos\theta - 0.4969 \sin\theta + 0.1629 \sin 2\theta) \qquad (1)$$

and

$$t = t_0 y \, (0.0632 \cos\theta - 0.4969 \sin\theta + 0.1629 \sin 2\theta) \quad , \qquad (2)$$

where

t_0 = one-half the maximum diametral temperature difference,

y = axial coordinate divided by the length of the shell, x/L,

θ = angular coordinate.[4]

The maximum diametral temperature difference, for both distributions, is along the 97.25–277.25 degree diameter. In the first case this difference was 50°F along the entire length, while, in the second, it varied linearly from 0°F at one end ($x/L = 0$) to 100°F at the other. The deflection curves, both restrained and unrestrained, for the first case are the same as those for A in Fig. 2.12. The deflection profiles for case 2 are plotted in Fig. 2.14, where it may be seen that the maximum unrestrained deflection occurs between the center and the higher

[4]A plot of this distribution is given in Fig. 2.2 of "GCR Quar. Prog. Rep. Sept. 30, 1959," ORNL-2835, p. 28.

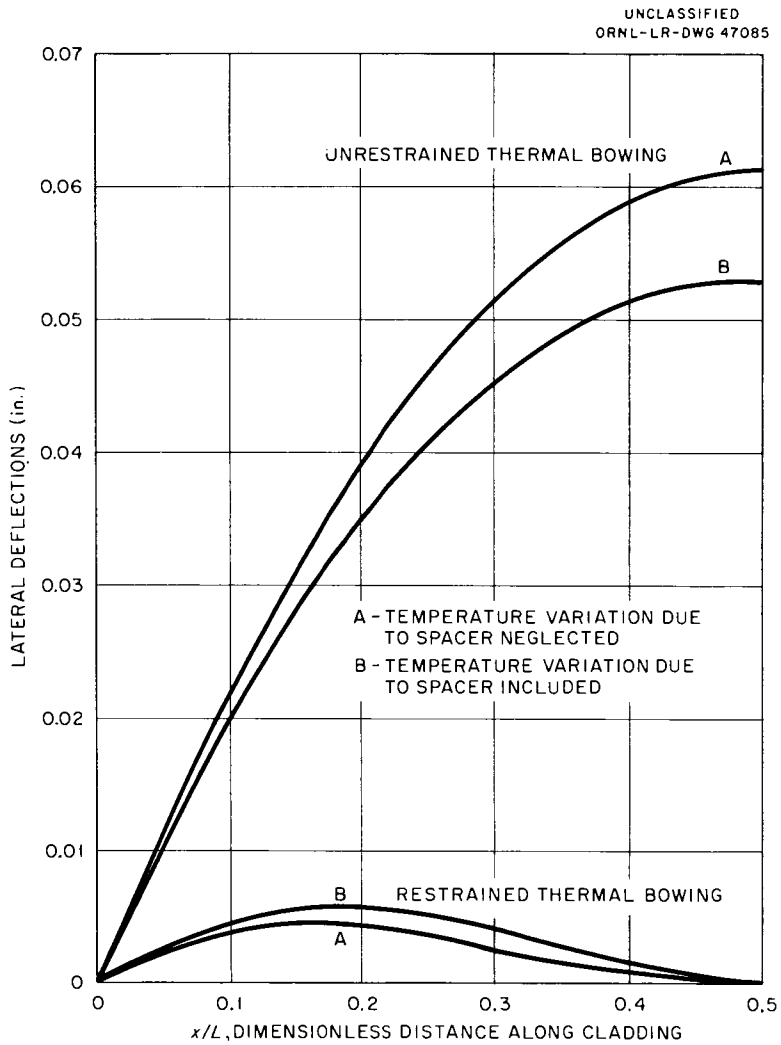

Fig. 2.12. Thermal Bowing of Fuel Element Cladding With Linear Diametral Temperature Variation.

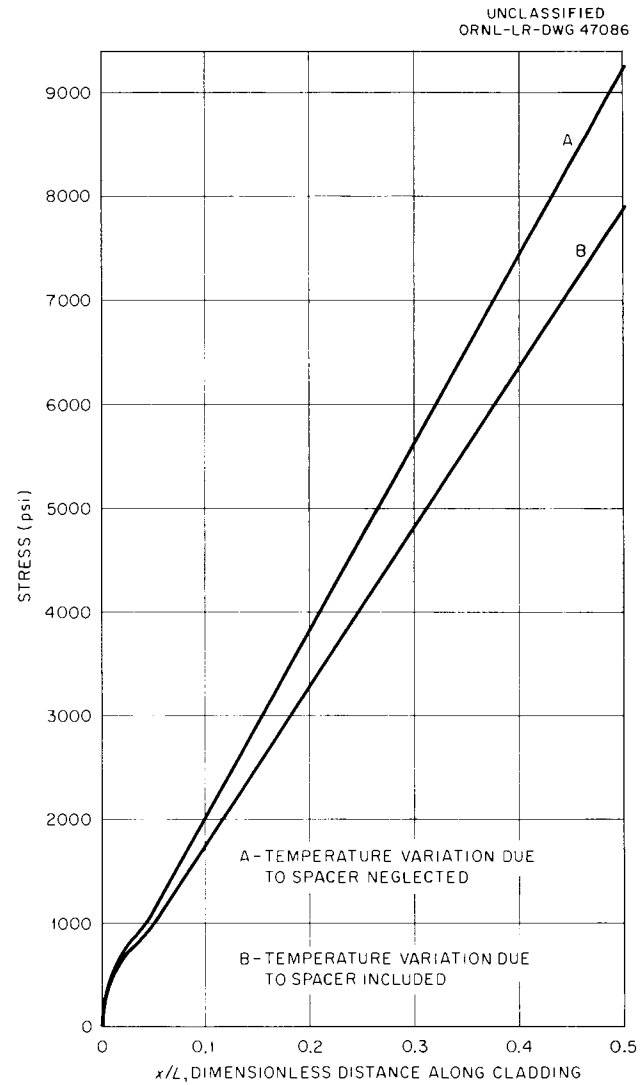

Fig. 2.13. Maximum Axial Stresses in Fuel Element Cladding When Element is Restrained at Center.

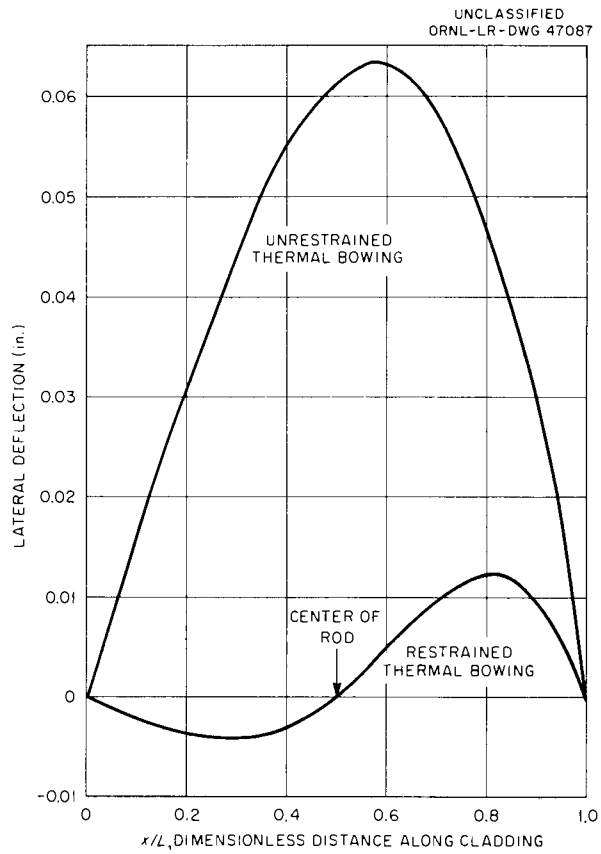

Fig. 2.14. Lateral Deflection of Fuel Element Cladding in the Plane Containing the 97.25–277.25-deg Diameter.

temperature end of the rod. Hence the restrained bowing curve is S-shaped. The maximum displacements in both cases are small compared with the 1/8-in. minimum clearance around an EGCR fuel rod.

The circumferential distribution of the total normal stress at the midplane is the same in both cases (see Fig. 2.15). The maximum normal stresses along the generatrices of the tubes are given in Fig. 2.16. A comparison of Figs. 2.13 and 2.16 shows slightly larger maximum stresses for cases 1 and 2 than for A, but the difference is not significant.

As discussed previously,[5] the cladding in the higher temperature regions of the reactor will creep under thermal loadings. If it is

[5]"GCR Quar. Prog. Rep. Sept. 30, 1959," ORNL-2835, p. 30.

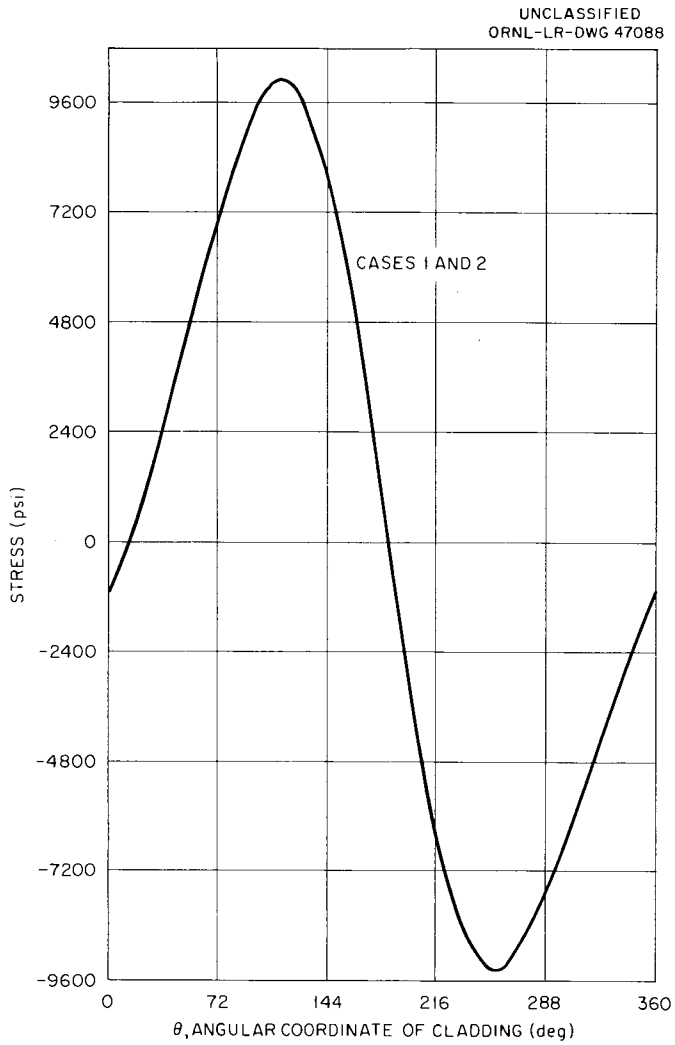

Fig. 2.15. Total Normal Stress Around Circumference of Fuel Element Cladding at x/L = 0.5 When Element is Restrained at Center.

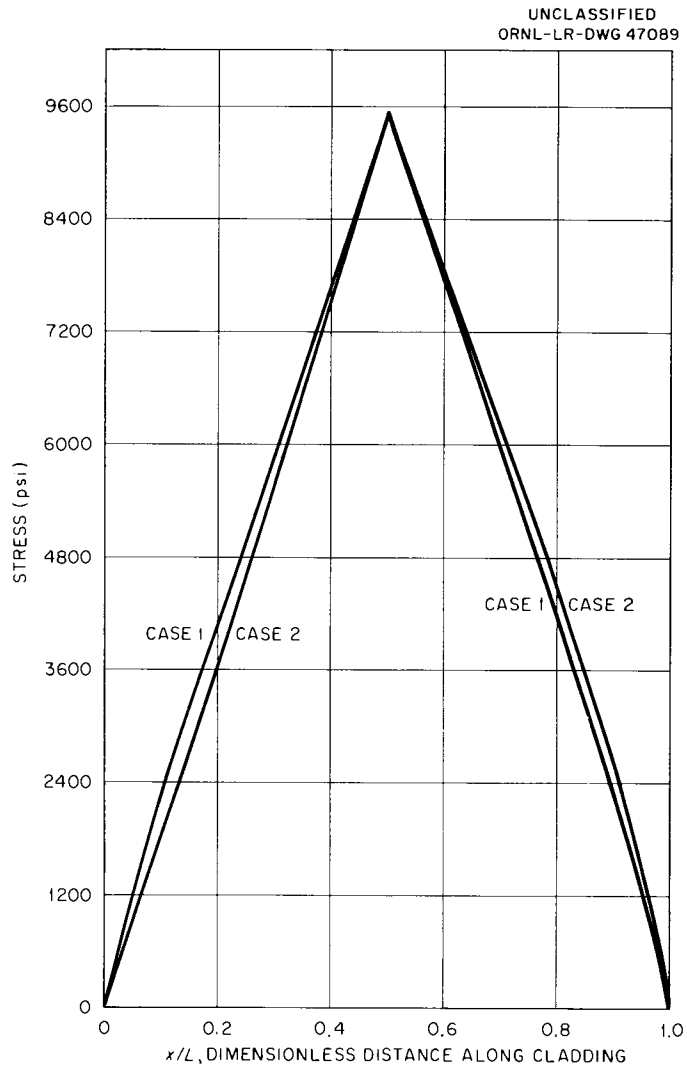

Fig. 2.16. Total Normal Stress Along Length of Fuel Element Cladding at θ = 97.25 deg When Element is Restrained at Center.

assumed that the temperature difference is applied suddenly, the element will deflect according to the elastic properties of the material, but ensuing creep strains will change the curvature of the element and cause increased displacements. Thus, both the deflection profile and the force imposed by the central spacer will be time dependent.

In accounting for fuel element behavior under creep conditions, a creep law for a variable-stress state is needed, but no satisfactory one has been formulated. Therefore, it is necessary to use a constant-stress relationship[5] and to choose the time increments so that negligible stress variations, relative to the total stress, occur over any increment. Equations describing the displacement of the neutral axis are then derived from the resulting stress-strain relationships. (The neutral axis is assumed to pass through the centroid of the cross section; therefore, the displacement is also that of the centerline.) Since the stress is constant over a given interval, the midpoint of the element moves, and the zero deflection condition at the midpoint is violated. This is corrected by "adjusting" the geometry with the use of elastic theory. Through the use of iteration techniques, the central force vs time and deflection vs time histories can be computed.

The central restraining force and deflection profiles of an EGCR rod have been obtained as functions of time for mean temperatures of 1200, 1300, 1400, 1500, and 1600°F. The diametral temperature differences used were 25 and 50°F, and in each case the temperature was a linear function of the diameter.

The force imposed by a central spacer, as a function of time, is shown in Fig. 2.17 for mean temperatures of 1300 and 1600°F. For either mean temperature, the initial force is directly proportional to the temperature difference; however, after a given time corresponding to the temperature, the force becomes independent of the temperature difference.

The results described above differ from those already presented[6] because a testing program has made available more accurate values for

[6] "GCR Quar. Prog. Rep. Sept. 30, 1959," ORNL-2835, p. 25.

the constants in the creep law (see chap. 4, this report). In addition, the dimensions of the analytical model have been changed.

The displacement profiles are shown in Figs. 2.18 and 2.19. Mean temperatures of 1300 and 1600°F are again considered, and, in both cases, the curves are for a temperature difference of 50°F. The curves labeled "initial elastic curve at zero time" show the position of the neutral axis immediately after the element is deflected elastically but before any creep has taken place. (It was assumed that the temperature difference was applied suddenly.) The remaining curves give the position of the element at the ends of the designated time intervals. The curves labeled "∞ time" give the limiting positions, and the stresses are decayed completely when this profile is reached.

In order to compare the deflection rates, the maximum deflection at any time, τ, was divided by the maximum at $\tau = \infty$, and the dimensionless quantity was plotted as a function of time (see Fig. 2.20). At $\tau = 0$ the quantity has a constant value of ~0.38, regardless of the mean temperature or temperature difference, and, as τ approaches infinity, the value approaches 1 by definition. Therefore the limiting deflection appears to be a constant multiple of the maximum initial displacement.

When $\tau = 0$, the maximum deflection is given by

$$w_{max} = \frac{e}{13.5} \quad , \tag{3}$$

where e is the maximum deflection which would be achieved by unrestrained thermal bowing and is given by

$$e = \frac{\alpha \, \Delta T L^2}{8 d_0} \quad . \tag{4}$$

In this expression, α is the coefficient of thermal expansion at the mean temperature, ΔT is the temperature difference across the element, L is the length, and d_0 is the outside diameter. These relations show that the limiting maximum deflection of a restrained element is e/5.14.

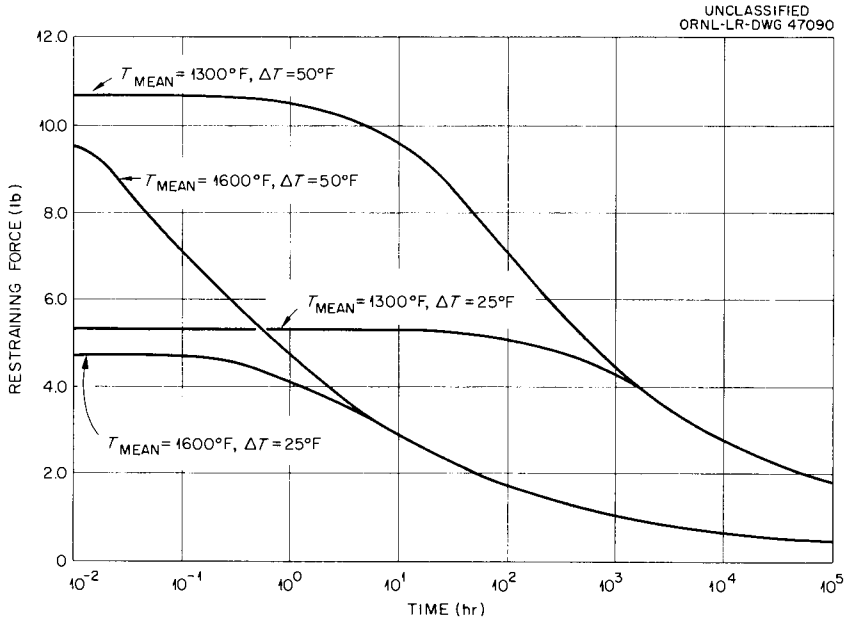

Fig. 2.17. Restraining Force of Central Spacer Versus Time at Mean Temperatures of 1300 and 1600°F and Diametral Temperature Differences of 25 and 50°F.

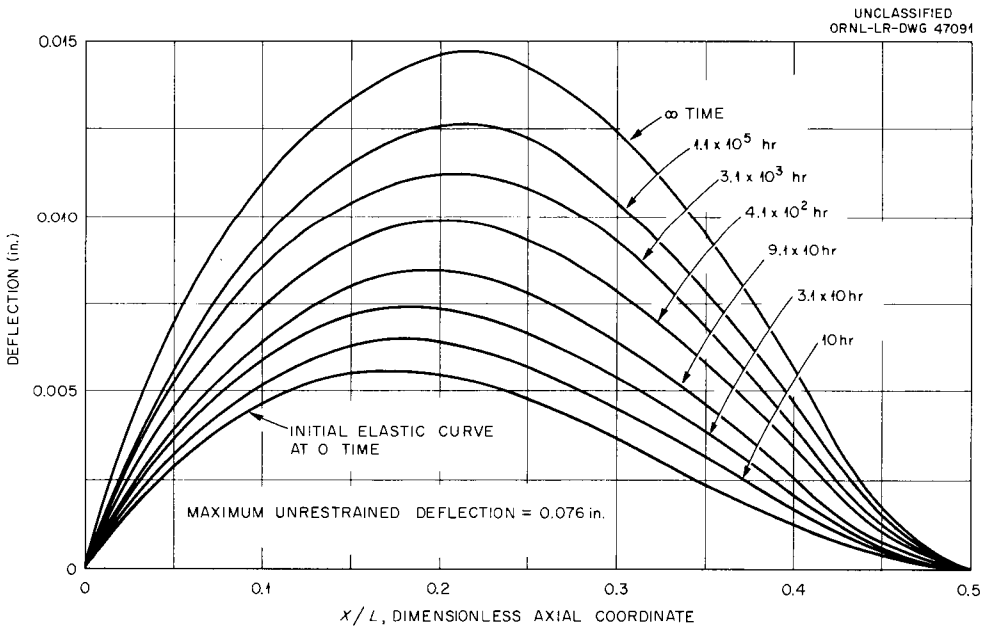

Fig. 2.18. Rod Deflection Versus Distance Along Cladding at a Mean Temperature of 1300°F and a Diametral Temperature Difference of 50°F.

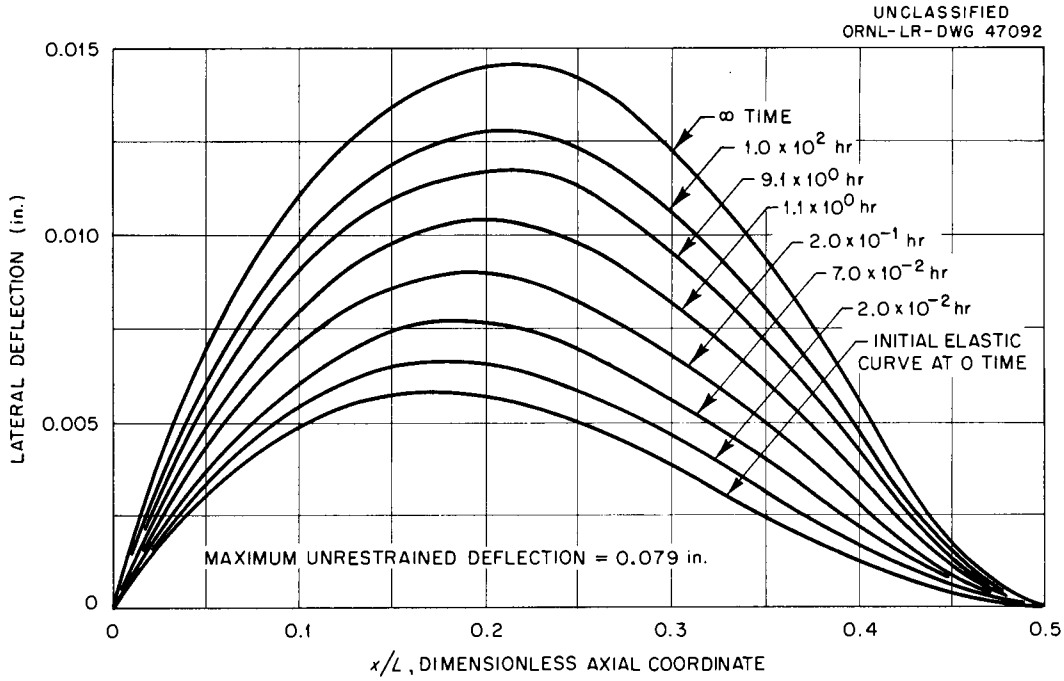

Fig. 2.19. Rod Deflection Versus Distance Along Cladding at a Mean Temperature of 1600°F and a Diametral Temperature Difference of 50°F.

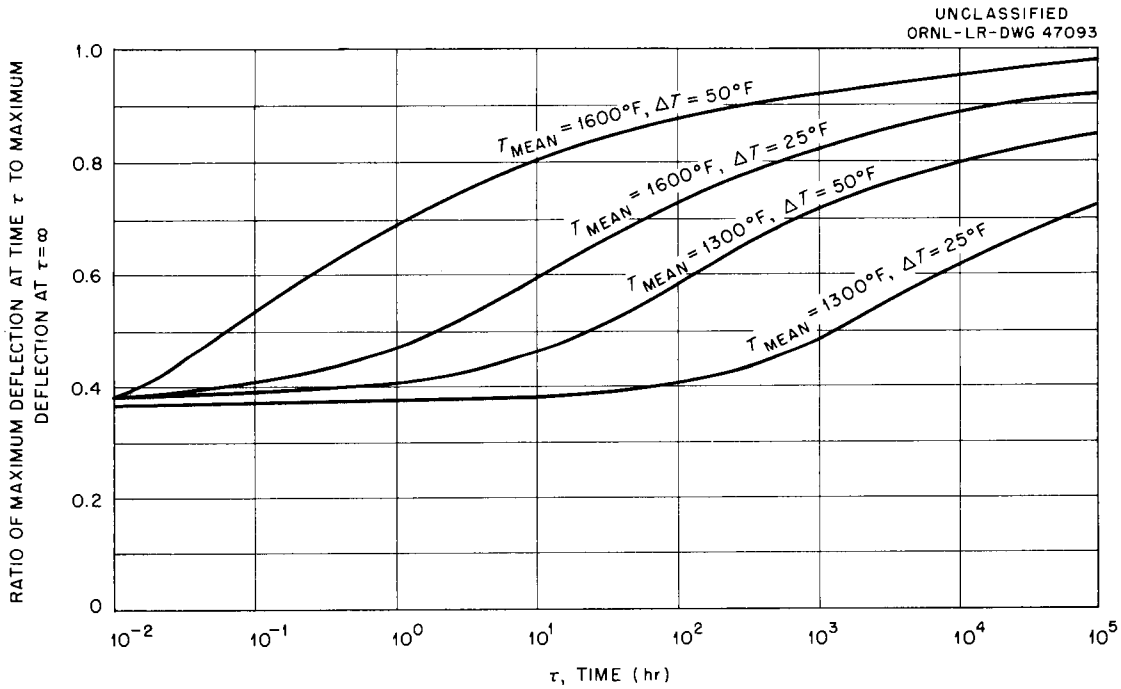

Fig. 2.20. Ratio of Maximum Rod Deflection at Time τ to Maximum Deflection at $\tau = \infty$ at Mean Temperatures of 1300 and 1600°F and Diametral Temperature Differences of 25 and 50°F.

(The maximum elastic deflection of a tube whose length is one-half the total is $e/4$. Hence, the limiting deflection under creep conditions approaches that which would occur if the element were hinged at the center.) This result is very significant because, although an infinite time is required for an element to reach its maximum deflection, in many cases this deflection will be closely approached during the fuel element residence time in the higher temperature regions of the reactor.

The temperature profile shown in Fig. 2.21 is given by

$$t = t_0(0.5 \cos\theta + 2.0 \sin 2\theta) \quad . \tag{5}$$

This profile was considered primarily to establish the plane of bowing. In all the cases considered previously, the bowing was in the diametral plane, which not only contained the maximum temperature difference but also passed through, or in close proximity to, the maximum and minimum temperature locations.

The maximum diametral temperature difference for the profile in Fig. 2.21 is t_0, and it occurs along the 0–180-deg diameter, while the maximum temperature of 2.36 t_0 is at $\theta = 42.57$ deg and the minimum temperature of -2.36 t_0 is at $\theta = 137.26$ deg. The results for this case established conclusively that the plane of bowing is indeed in the diametral plane containing the maximum temperature difference. The deflections for the cases with length-to-radius ratios of around 20 were approximately 2% greater than the deflections given by the elementary beam theory.[6] The deflections for cases with length-to-radium ratios of 50 or greater were identical with those obtained from the elementary theory.

Thermal Stress Equations for a Thick-Walled Cylinder of Anisotropic Material

The basic differential equations have been developed for the thermal stress analysis of a thick-walled circular cylinder of an anisotropic material which is subjected to an axisymmetrical temperature distribution.

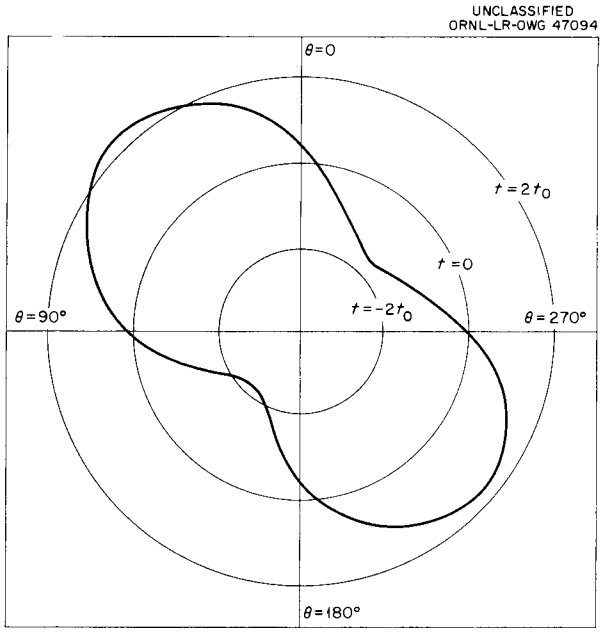

Fig. 2.21. Temperature Profile Given by the Expression $t = t_0 (0.5 \cos\theta + 2.0 \cos 2\theta)$.

The anisotropic material of particular interest is graphite, for which the elastic properties parallel to the axial direction are different from those in the radial and circumferential directions. The elastic properties in the radial and the circumferential directions are equal.

A completely general analysis requires the solution of two simultaneous linear partial-differential equations of second order with variable coefficients, or, alternately, the solution may be obtained from a single linear partial-differential equation of fourth order, also with variable coefficients. The variable coefficients depend only upon the radial coordinate; the angular coordinate does not appear in the equations because of the symmetry condition.

The two simultaneous equations are expressed in terms of the radial displacement, u, and the axial displacement, w, giving

$$C_1 L' u + C_2 u_{zz} + C_3 w_{rz} = C_4 t_r$$

and

$$C_3 L u_z + C_2 L w_r + C_5 w_{zz} = C_6 t_z \quad . \tag{6}$$

The subscripts designate partial differentiation with respect to the subscript used; t is the temperature function $t(r,z)$, where r and z are the radial and axial coordinates; the $C_n (n = 1, \ldots, 6)$ are constants that depend upon the elastic properties of the material; and L and L' are operators that operate with respect to r only, as illustrated below in an operation on u:

$$Lu = \frac{(ru)_r}{r} + \frac{u}{r}$$

and

$$L'u = (Lu)_r = u_{rr} + \frac{u_r}{r} - \frac{u}{r^2} \quad .$$

The single partial differential equation is obtained from (6) by expressing the two displacements in terms of a displacement function ϕ in the following manner:

$$u = L'\phi + b_1 \phi_{rzz}$$

and

$$w = b_2 L\phi_{rz} + b_3 \phi_{zzz} \quad . \tag{7}$$

The b_n's $(n = 1, 2, 3)$ are constants that depend upon the values of the c's in (1). The fourth-order equation then becomes

$$a_1 LL'\phi_r + a_2 L\phi_{rzz} + a_3 \phi_{zzzz} = t \quad . \tag{8}$$

Here, a_n (n = 1, 2, 3) is another set of numerical values corresponding to two sets in (6) and (7).

Unfortunately, a complete analytical solution for (8) [or (6)] that satisfies the necessary boundary conditions is not known. It may be possible, however, to develop an approximate solution that gives satisfactory results. For example, the problem may be simplified so that a differential equation with a known solution is obtained. One method of reducing the problem is to analyze a section located away from the ends of a long cylinder so that its behavior is not influenced by the end conditions. Provided the thermal loading is independent of the axial coordinate, a case of plane strain exists; that is, the deformation, w, in the axial direction is zero for the section under examination.

The differential equation for the case of plane strain is

$$\left[\frac{(ru)_r}{r}\right]_r = kt_r \quad , \tag{9}$$

where k is a numerical constant dependent upon the elastic properties of the material. The stresses and the radial displacement, u, are then represented by the following expressions:

$$\begin{aligned} \sigma^r &= \beta_1 \left[\frac{f(r)}{r^2} + A - \frac{B}{r^2}\right] , \\ \sigma^\theta &= \beta_1 \left[t - \frac{f(r)}{r^2} + A + \frac{B}{r^2}\right] , \\ \sigma^z &= \beta_2 t + \beta_3 A , \\ u &= k \left[\frac{f(r)}{r} + \beta_4 Ar - \frac{B}{r}\right] , \end{aligned} \tag{10}$$

where A and B are constants of integration, and

$$f(r) = \int tr\, dr \quad .$$

The constants β_n (n = 1, 2, 3, 4) and k in (9) and (10) contain the ratio of the two moduli of elasticity, $E = E^z/E^r$, the two values of Poisson's ratio, δ^{rz} and $\delta^{r\theta}$, and the two coefficients of thermal expansion α^z and α^r, as shown below:

$$k = \frac{E(\delta^{rz}\alpha^z + \alpha^r)(1 + \delta^{r\theta})}{E - (\delta^{rz})^2} \quad ,$$

$$\beta_1 = \frac{-(\delta^{rz}\alpha^z + \alpha^r)}{E - (\delta^{rz})^2} \quad ,$$

$$\beta_2 = \frac{E\alpha^z + \delta^{rz}\alpha^r}{E - (\delta^{rz})^2} \quad ,$$

$$\beta_3 = \frac{-2\delta^{rz}(\delta^{rz}\alpha^z + \alpha^r)}{E - (\delta^{rz})^2} \quad ,$$

$$\beta_4 = \frac{2(\delta^{rz})^2 - E(1 - \delta^r\theta)}{E(1 + \delta^{r\theta})} \quad .$$

The properties E and α in the radial and axial directions are designated with superscripts r and z, respectively. Poisson's ratio δ^{rz} is the ratio of the strain in the r direction to the strain in the z direction when the material is stressed in the z direction. A similar interpretation is to be given to the double superscript $r\theta$.

Since dimensional changes in graphite that are induced by irradiation are similar to thermal strains, the resulting stresses can be

evaluated using thermal stress analyses. In addition to providing a means for calculating these stresses, Eqs. (10) can also be used to study the influence of the anisotropic properties.

The influence of the material properties upon the radial and tangential stresses [the first two of Eqs. (10)] can be readily examined by merely studying the variation of the parameter β_1. However, the axial stress and the radial displacement are functions of the two radii of the cylinder, the radial coordinate, r, and the remaining β's. Therefore, the influence of anisotropy is more difficult to evaluate in these cases.

Seismic Analysis of the EGCR

The EGCR must be designed to withstand loadings caused by earthquakes which may occur in the East Tennessee area. The motion of the earth and the accompanying accelerations of the base of a structure during a quake impose both lateral and vertical forces upon the supported members. The initiating factor of an earthquake is a sudden shear failure at some dislocation in the earth's crust and subsequent readjustment of the shear stresses from the focal region outward; hence, a disturbance is a response to one or more impulses and is definitely not periodic. In predicting the behavior of a structure under seismic loadings, however, the maximum accelerations for the ground movement and the nature of the response for a body with periodic vibration characteristics to the nonperiodic ground motion must be known. Using accelograms from recorded quakes, Biot[7] determined the response of a single-degreee-of-freedom ideal oscillator with varying natural periods and found that the maximum acceleration occurred when the period of the oscillator was between 0.1 and 0.5 sec.

In the absence of adequate data, the U. S. Coast and Geodetic Survey was asked to set a value for the maximum horizontal acceleration to be used in designing the EGCR. The value given was 5% of that due

[7]M. A. Biot, "Analytical and Experimental Methods in Engineering Seismology," Trans. Am. Soc. Civil Engrs. 108, 365 (1943).

to gravity, and the vertical acceleration was taken as one-half this amount. With these facts, an analysis was made that considered only horizontal and angular displacements of the composite structure consisting of the core, pressure vessel, and supporting skirt.[8] The nozzles on the pressure vessel and the primary coolant piping were not taken into account, and all the graphite columns were treated as having identical geometries.

The mathematical model is described in Fig. 2.22. The absolute horizontal displacement of the top of the cylindrical supporting skirt is measured along the coordinate, x; the angular rotation of the centerline of the pressure vessel and the graphite supporting structure is θ (the core supporting structure was assumed to follow the movement of the pressure vessel); the displacement of an element of a graphite column relative to its undeflected position is designated as y; and the absolute horizontal displacement of the bottom of the supporting skirt (caused by the earth's movement) is S. The variables H_1 and H_2, which are the total lateral sheer forces at the top and bottom of the core, respectively respresent a summation of the forces acting on the individual columns. The latter are shown as H_1' and H_2' in the figure.

The columns will behave under lateral loadings as simply supported beams; therefore, the shape of the deflected centerline for each was approximated by the sine function

$$y = A(t) \sin \frac{\pi z}{L} \quad , \tag{11}$$

[8] "Experimental Gas-Cooled Reactor Preliminary Hazards Summary Report," ORO-196 (May 1959). In this report each graphite column consisted of five blocks of equal length which were fastened together by threaded graphite pins. However, monolithic columns will actually be used, and therefore the analysis described here was made using the monolithic column concept.

UNCLASSIFIED
ORNL-LR-DWG 47095

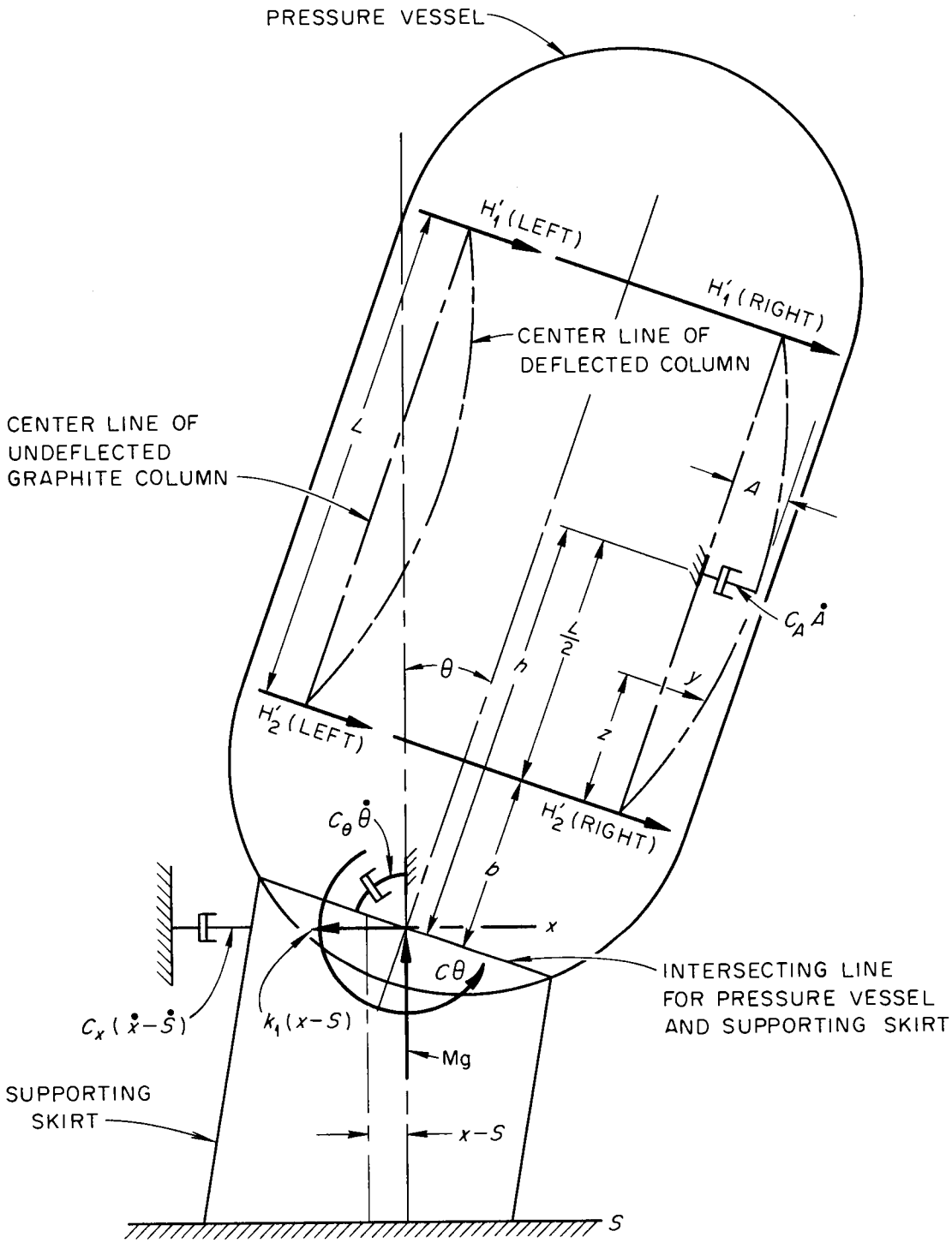

Fig. 2.22. Mathematical Model Used in the Seismic Analysis of the EGCR.

where

$A(t)$ = time-dependent deflection amplitude at the center of the column,

z = variable distance along the column, measured from its base,

L = column length,

t = time.

The center of gravity of the entire structure was assumed to coincide with that for the pressure vessel. Hence, the following equations which describe the system were derived by summing the forces on a graphite column and the forces and moments for the composite system, including damping forces corresponding to the displacements A, x, and θ:

$$M\ddot{x} + C_x\dot{x} + k_1 x + Mh\ddot{\theta} + \frac{2m_2}{\pi}\ddot{A} = k_1 S + C_x\dot{S} \quad , \tag{12}$$

$$\frac{m_2}{n\pi}\ddot{A} + C_A\dot{A} + \frac{EI_c\pi^3}{L^3}A + \frac{m_2}{2n}\ddot{x} + \frac{m_2}{2n}h\ddot{\theta} = 0 \quad , \tag{13}$$

and

$$I\ddot{\theta} + C_\theta\dot{\theta} + C\theta - k_1 hx = -k_1 hS \quad , \tag{14}$$

where

C = bending stiffness of the supporting skirt (that is, the moment required to give the top rim one radian of angular displacement with respect to the bottom rim),

C_A, C_x, C_θ = damping factor associated with the A, x, and θ displacements, respectively,

E = modulus of elasticity for graphite,

h = distance from the upper edge of the skirt to the center of gravity of the reactor (see Fig. 2.22),

I = mass moment of inertia for the core and pressure vessel taken about a horizontal axis through the center of gravity,

I_c = area moment of inertia for a graphite column,

k_1 = shear stiffness of the supporting skirt (that is, the amount of force required to produce one unit of relative displacement between the top and bottom of the supported skirt),

m_2 = mass of core,

M = total mass of core and pressure vessel,

n = number of graphite columns.

The classical method of solution was employed[9] in the analysis. The homogeneous solutions were obtained by taking $S = S = 0$, and they are given by

$$A_H = \sum_{j=1}^{3} e^{\tau_j t} (A_j \cos\sigma_j t - B_j \sin\sigma_j t) \quad ,$$

$$x_H = \sum_{j=1}^{3} e^{\tau_j t} (C_j \cos\sigma_j t - D_j \sin\sigma_j t) \quad ,$$

$$\theta_H = \sum_{j=1}^{3} e^{\tau_j t} (E_j \cos\sigma_j t - F_j \sin\sigma_j t) \quad ,$$

where $\tau_j \pm i\sigma_j$ $(j = 1, 2, 3)$ are the roots of the characteristic equation. The quantities τ_j depend upon the damping factors and the σ_j's correspond to the three fundamental frequencies of the system.

If the function for describing the displacement of the base of the supporting skirt (the forcing function in the first set of equations) is taken as

---

[9]T. VonKarman and M. A. Biot, "Mathematical Methods in Engineering," pp. 37–42, McGraw-Hill, New York, 1940.

$$S = \sum_{k=1}^{n} S_k \cos(w_k t + \phi_k) \quad ,$$

where S_k and w_k are numerical coefficients and ϕ_k is a phase angle, the particular solutions become

$$A_p = \sum_{k=1}^{n} (G_k \cos w_k t + H_k \sin w_k t) \quad ,$$

$$x_p = \sum_{k=1}^{n} (I_k \cos w_k t + J_k \sin w_k t) \quad ,$$

$$\theta_p = \sum_{k=1}^{n} (L_k \cos w_k t + M_k \sin w_k t) \quad .$$

The homogeneous solutions give the transient part of the response, the particular solutions give the steady-state portions, and combined they yield the general solutions:

$$A = A_H + A_p \quad ,$$

$$x = x_H + x_p \quad ,$$

$$\theta = \theta_H + \theta_p \quad .$$

The initial conditions used were

$$A = x = \theta = \dot{A} = \dot{x} = \dot{\theta} = 0 \quad ,$$

and the damping factors corresponding to the A, x, and θ displacements were 15, 5, and 5%, respectively, of those required to produce aperiodic motion (critical damping). Under these conditions, the fundamental frequencies of vibration were found to be 9.3, 16.0, and 72.0 cps, respectively. The lowest frequency falls within the range of periods corresponding to maximum acceleration from seismic disturbances, as discussed earlier, and therefore a forcing function with simple harmonic motion and a frequency of 9.3 cps was used in completing the analysis.

The first term of the function for S was used, with the maximum acceleration equal to 0.05 times that due to gravity and $\phi_k = 0$. This gave

$$S = -(4.67 \times 10^{-4}) \cos 58.71\ t\ .$$

In all cases, the transient response died out in a short period of time and left only the steady-state behavior. The displacement as a function of time is plotted for each of the coordinates A, x, and θ in Figs. 2.23, 2.24, and 2.25. The first part of each plot is the sum of the homogeneous and steady-state solutions, designated as transient in the figures, and the second part is the steady-state solution alone. Since A is the maximum displacement at the mid-plane of a graphite column ($z = L/2$), it is proportional to the maximum bending stress, as indicated by the right-hand ordinate of Fig. 2.23. The maximum bending stress in a column at any time is 100 psi. It is to be noted from this figure that the transient part of the curve builds up to the steady-state portion, thus indicating that 9.3 cps is the fundamental frequency associated with the motion of the graphite columns in the system as a whole. Figures 2.26 and 2.27 show the total shear forces at the top and bottom of the core, as given by the equations

$$H_1 = m_2 \left[\frac{\ddot{x}}{2} + \left(\frac{b}{2} + \frac{L}{3} \right) \ddot{\theta} + \frac{\ddot{A}}{\pi} - \frac{gA}{2L} \right] \tag{15}$$

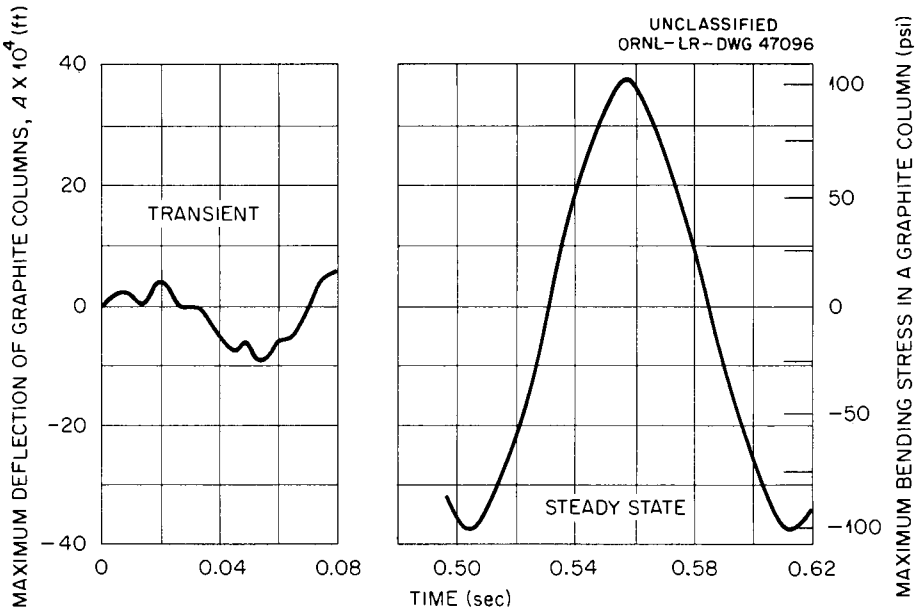

Fig. 2.23. Time-Dependent Maximum Deflection and Bending Stress in Graphite Columns.

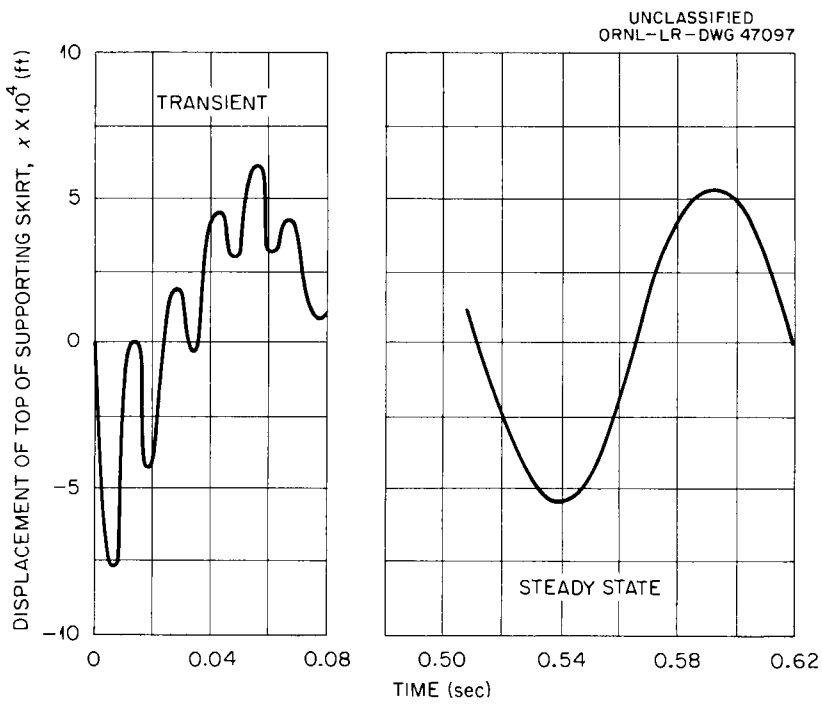

Fig. 2.24. Time-Dependent Displacement of the Top of the Supporting Skirt.

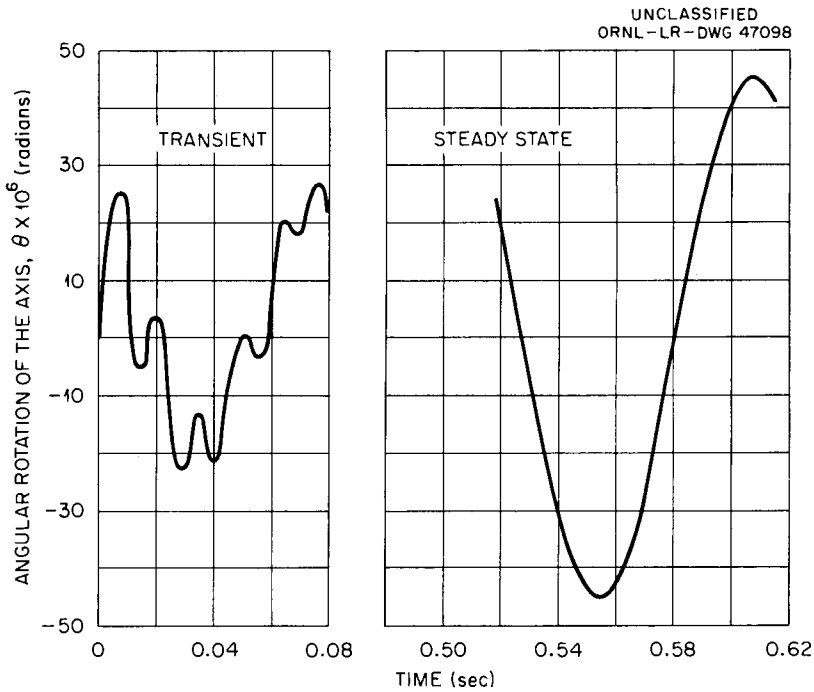

Fig. 2.25. Time-Dependent Angular Rotation of the Axis of the Pressure Vessel.

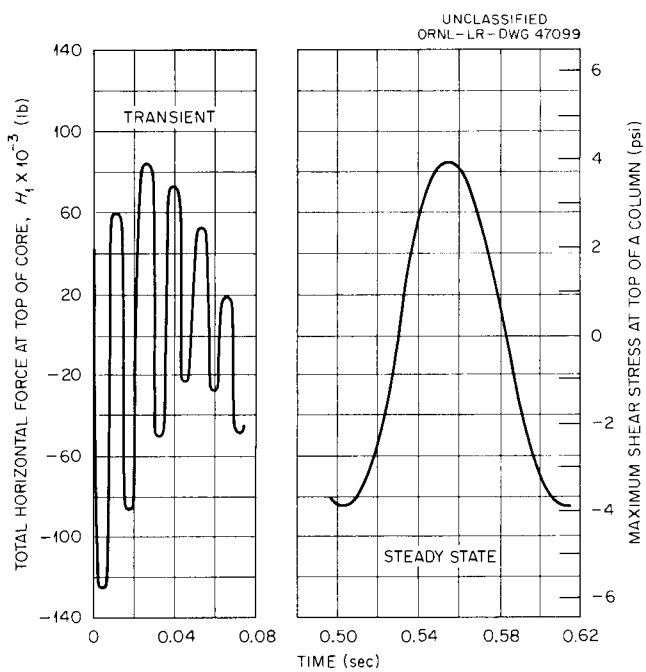

Fig. 2.26. Time-Dependent Total Horizontal Force at Top of Core and Maximum Shear Stress at Top of a Column.

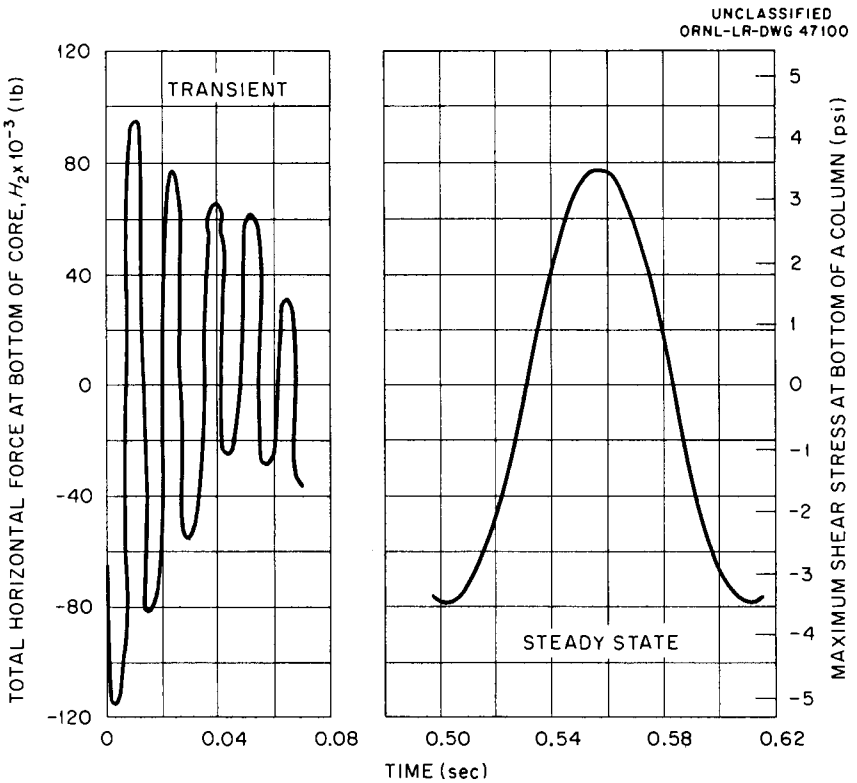

Fig. 2.27. Time-Dependent Total Horizontal Force at Bottom of Core and Maximum Shear Stress at Bottom of a Column.

and

$$H_2 = m_2 \left[\frac{\ddot{x}}{2} + \left(\frac{b}{2} + \frac{L}{6} \right) \ddot{\theta} + \frac{\ddot{A}}{\pi} + \frac{gA}{2L} \right] , \qquad (16)$$

where b is the distance from the base of the core to the intersection of the supporting skirt and pressure vessel (see Fig. 2.22), and g is the acceleration due to gravity. The right-hand ordinates of Figs. 2.26 and 2.27 indicate the resulting shear stresses. Thus, the maximum shear stress in a column reaches 5.6 psi. Consistent with the data and assumptions given herein, the combined stresses induced by seismic disturbances alone present no hazard to the EGCR, either structurally or operationwise.

Decontamination of EGCR Charge and Service Machines

Volatile fission products and UO_2 dust from ruptured fuel elements are expected to deposit on interior surfaces of the EGCR charge and service machines. Decontamination facilities must therefore provide both for the washing away or dissolving of the UO_2 and its contained fission products and for the removal of solid fission products and condensed volatile fission products. The decontamination reagent should be noncorrosive to mild steel, which will be the most-used material of construction in the service machines.

It has been reported[10] that a mixture of 0.25 M Na_2CO_3, 0.25 M $NaHCO_3$, and 1.0 M H_2O_2 will dissolve UO_2, and, in experiments at ORNL, powdered UO_2 was dissolved in a few minutes at 70°C. The corrosion rate on the mild-steel container was less than 0.001 mil/hr. It was also found that fission-product tellurium deposited from the solutions onto the steel.

In other experiments at ORNL the contamination of metal surfaces with particulate UO_2 was simulated by contaminating threaded mild-steel bolts with ultrafine UO_2 which had been irradiated in the ORR. The oxide was so tightly held to the metal that steam and detergent jets removed less than one-half of it, as determined by gamma-ray counting. On the other hand, decontamination by several reagents aspirated into a steam jet apparatus was successful. A 3-min impingement with a peroxide-carbonate reagent dissolved UO_2 from the bolts with a decontamination factor of about 100. After a steam-water rinse, a treatment with Turco 4518 in 10% solution and steam gave a further decontamination factor of about 3. Citric acid (10%) mixed with a detergent gave a decontamination factor of about 7 when used in place of the Turco 4518. Successive treatments with carbonate, Turco 4518, and citric acid, or with the two latter reagents used in reverse order, gave a total decontamination factor of about 800.

---

[10] J. E. Mendel, "Interim Report on the Laboratory Investigation of Carbon Steel Decontamination," HW-56875 (July 22, 1958).

The principal volatile fission products expected in the coolant are xenon, krypton, iodine, tellurium, cerium, and ruthenium, with traces of strontium, barium, and zirconium. In experiments for determining the extent of fission-product deposition to expect, a sheet of carbon steel was exposed to a stream of helium which had been passed over previously irradiated UO_2 heated to 1000 to 1400°C. The irradiated UO_2 had decayed for several days, and the steel sheet was located about 3 in. from the UO_2 sample. Only Te^{132}, I^{132}, and I^{131} could be identified on the steel with a gamma-ray spectrometer. In another experiment in which the helium stream was passed over UO_2 under irradiation in the ORR, through a long copper line at room temperature, and over the metal test specimens, much less activity, probably due to the rubidium daughters of Kr^{87} and Kr^{88}, was found on the metal specimens.

Decontamination tests were also made on mild-steel specimens on which the fission products tellurium, iodine, cesium, ruthenium, and zirconium-niobium had been deposited from aqueous solutions. Hot water removed iodine and cesium with decontamination factors of 10^2 to 10^3. Boiling Turco 4518, which contains inhibited oxalic acid, in 10% solution removed the remaining fission products with decontamination factors of 15 to 5000 in less than 1 hr; Turco 4501-A was less effective. The corrosion rate of boiling Turco 4518 in 10% solution on mild steel was 0.003 ± 0.002 mil/hr (95% confidence level) in an 18-hr test. Encouraging results were also obtained with citric acid solutions, but a method of reducing the corrosion by this reagent must be found before it can be used.

Helium Purification System for EGCR

When the original proposal for the EGCR purification system was presented by Anderson,[11] the available data were limited, and therefore

[11] F. A. Anderson, "Proposed Helium Purification System for the EGCR," ORNL-2819 (October 1959).

a re-evaluation of the requirements has been made.[12] The system described by Anderson was selected to control the concentrations of reactive impurities by treating a bypass stream of the coolant system. Since oil seals are presently being considered as an alternate to the water seals considered by Anderson, a separate system for treatment of the buffer helium for the seals will be needed.

A primary purification system test facility is being installed that consists of a once-through flow system that can accommodate a nonradioactive, helium stream at the pressures and temperatures of proposed systems and the various items of purification equipment that are to be tested. The first components to be tested will be oxidizers (for oxidizing all contaminants to H_2O and CO_2) and adsorbers (for adsorbing H_2O and CO_2).

The test facility provides metering systems for seven different gases which enter a common header and flow to a gas preheater, two parallel oxidation vessels, a gas cooler, and two parallel adsorbers (Fig. 2.28). A sampling system that consists of an electrolytic hydrometer and a gas chromatograph is included to permit gas analyses at any point in the system.

GCR Hazards Study

The existing data on the diffusion of fission products from UO_2 have been critically evaluated in order to arrive at a reasonable description for the mechanisms of release of fission products from the EGCR fuel elements. The detailed results of this investigation, together with an evaluation of the current knowledge of the escape of fission products from UO_2 fuels, are presented in a separate report,[13] which is summarized here. The complementary problem on the ultimate

---

[12] P. A. Haas and C. D. Scott, "EGCR Coolant Purification — Treatment of Buffer Helium from Water or Oil Seals," ORNL CF-60-1-46 (January 1960).

[13] W. B. Cottrell et al., "Fission-Product Release from UO_2," ORNL-2935, to be issued.

UNCLASSIFIED
ORNL-LR-DWG. 45353

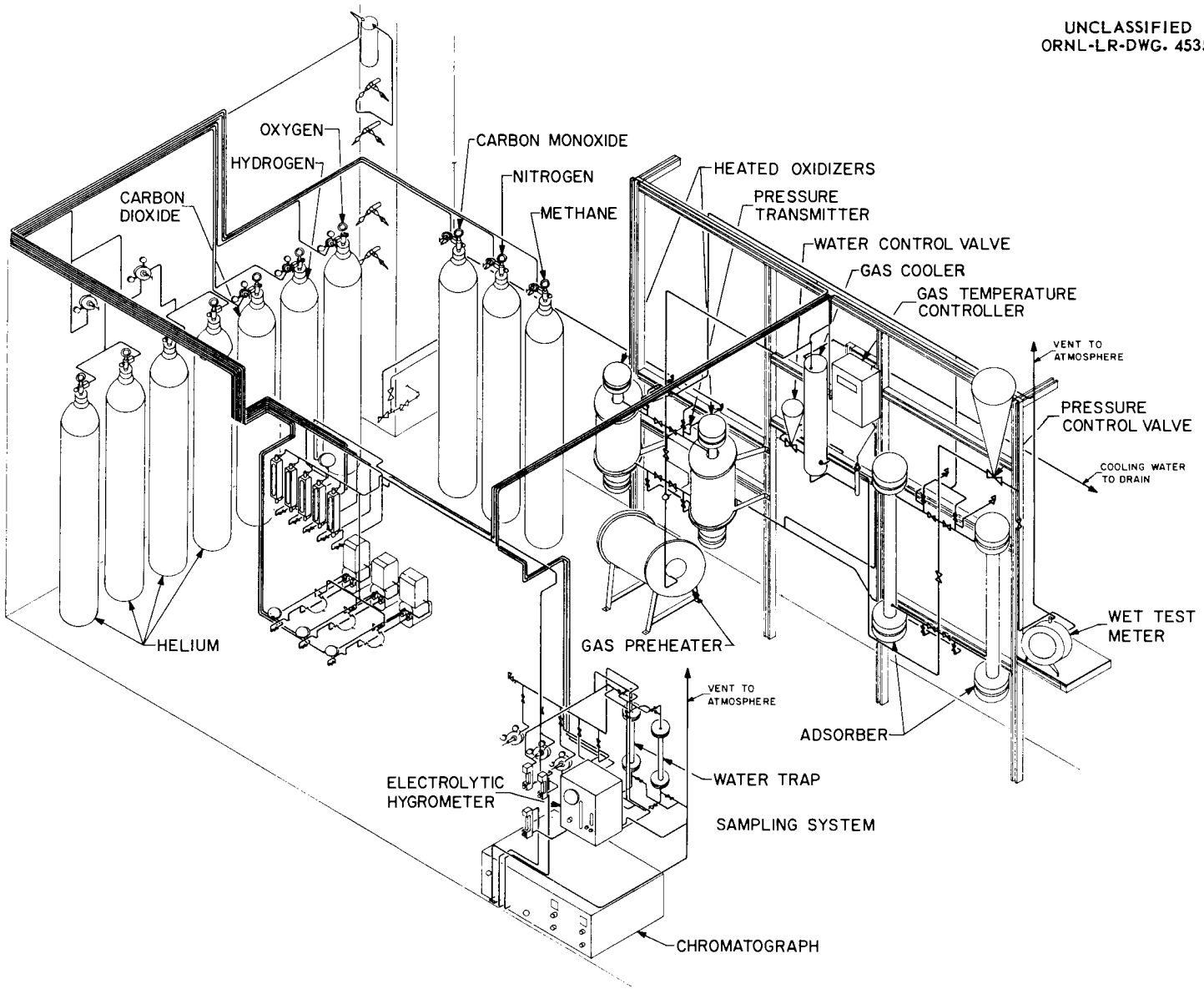

Fig. 2.28. EGCR Helium Purification System Test Facility.

disposition of fission products in large gas-cooled reactor systems is currently being studied. While the results of this analysis will be applicable to any gas-cooled system, regardless of the contamination level, the study is specifically directed to the problems of activity control in systems with high activity release rates, such as gas-cooled reactors operating with unclad fuel elements.

Fission-Product Release from UO_2

The buildup of pressure within the cladding of a fuel element because of the release of volatile fission products from the fuel is one of the most important factors governing the design of stainless-steel-clad high-density UO_2 fuel elements for use in gas-cooled power reactors. A study has therefore been made to establish the most suitable model for predicting fission-product release, to evaluate the applicability of existing data on UO_2 to the problem, and to determine what research and development work will be required to obtain an accurate method of predicting rates of release of fission products from UO_2.

A study of existing literature and discussions at Battelle Memorial Institute, the Westinghouse Bettis Plant, and Chalk River have indicated that the fission products may be released by recoil and a two-step diffusion process. It is apparent that the diffusion of fission products from the UO_2 crystal lattice is the controlling escape process. However, it has also been shown that, at moderate temperatures, recoil escape may be controlling and that, under conditions which create a change in the crystal structure of the UO_2 (that is, grain growth, sublimation, melting), a significant increase in the rate of release of fission products occurs. At the present time it may be concluded with certainty only that the diffusion process described above is both applicable and controlling in the relatively narrow temperature region between the temperature at which recoil escape is dominant and the temperature at which grain growth occurs.

The available experimental data and techniques permit the conclusion that a reasonably consistent picture of fission-gas release

exists despite the fact that much detail is missing and many gaps remain. The activation energy undoubtedly lies within the range 34 to 81 kcal/mole and is probably reasonably close to 65 kcal/mole, which is the average of all measurements and which is the value that has been employed in calculating the performance of the EGCR fuel elements.

The determination of an absolute value of the diffusion coefficient for general use in the diffusion equation is extremely difficult, not only because of the many parameters involved in such an evaluation, but also because of significant differences from one fuel material to another. At the present state of understanding, any particular fuel material must be characterized by a measurement of the diffusion rate constant, D', and preferably, the measurement is made under conditions as closely approximating those of the anticipated service as possible. Measurements of D' for materials of the same density manufactured by different processes have been found to differ by several orders of magnitude. While the reasons for such discrepancies are being investigated at several installations, much additional work will have to be done before the processes are understood and the various contributing factors can be controlled.

The wide scatter of the available release rate data precludes the optimization of the design of a reactor with stainless-steel-clad UO_2 fuel elements at this time. The scatter is a result of a lack of understanding of the effects of many of the important parameters that affect release, such as thermal conductivity, density, distribution of open and closed pores, grain growth, oxygen-to-uranium ratio, material discontinuities, and temperature structure. Nevertheless, the accumulated experience permits a number of conclusions to be drawn with regard to the effect of these parameters on gas release.

The presence of gaps either within the fuel material or between the cladding and the fuel material imposes temperature discontinuities on the fuel element temperature structure. In the case of gas-cooled reactors operating at high gas temperature with high gas-film temperature drops, the cladding temperature is within the creep range of the material, and collapse of the cladding material onto the UO_2 occurs.

This is in contrast to water-cooled reactors in which the cladding temperature remains close to the primary coolant temperature and collapse of the cladding material does not occur.

The existence of a gap between the cladding and the fuel material may markedly increase the temperature within the fuel region. This occurs as a result of dilution of the gas initially in the gap with fission-product xenon and krypton gases that have low thermal conductivities. A large initial gap may also result in a nonuniform collapse of the cladding material onto the fuel and consequent wrinkling of the cladding material.

Since UO_2 fuel material thermally cracks early in its operating life, the effect of an initial gap cannot be accurately predicted. In contradiction of the expected behavior, experimental data from the ORNL fuel irradiation program have not shown any effect of xenon and krypton in the gap on the UO_2 fuel temperature, although calculations have indicated the presence of a gap.

The calculation of a temperature profile within the fuel material requires knowledge of the effect of the variables mentioned above and requires an accurate reference temperature measurement. The determination and verification of the correct temperature structure of the fuel material while under irradiation is therefore probably the most important and most difficult task remaining in the accurate determination of fission-gas release from fuel material.

An increase of fuel temperature promotes grain growth within the fuel material, and, in regions where grain growth occurs, fission-gas release is very high. Although the time-temperature relationship for in-pile grain growth of UO_2 has not been established, grain growth has been observed at temperatures thought to be approximately 1500°C. The diffusion model is not believed to be applicable, as mentioned above, in regions where grain growth occurs, and the controlling mechanism for gas release in these regions is not understood. However, present practice is to use the diffusion model even in areas where grain growth has occurred.

Density, porosity, and surface area are interrelated and all have an important, though not necessarily independent, effect on gas release; in general, the higher the density, the lower the porosity and surface area and the lower the fission-product release. For a specific material, definite relationships have been established between density and surface area and between density and open and closed porosity. The relationship between density and surface area has been employed to determine the radius of the hypothetical fuel particle and thence the diffusion coefficient. This relationship, as well as that between density and porosity, is believed, however, to be valid only for the fuel material for which the measurement was made, and use of these relationships for materials other than the material for which they were determined is questionable. The effect of closed pores has not been considered in the models describing the release process, although it has been shown to reduce the calculated gas release, particularly for fuel materials in which the total surface area, including open pores, approaches that of the geometric surface area.

Since the rates of release of fission products could not be determined accurately from existing data, calculations were made to determine what value of the release rate parameter, D', at 1400°C would be acceptable in the EGCR. For these calculations it was assumed that xenon and krypton diffuse at the same rate with an activation energy of 65 kcal/mole and that other fission products could be neglected. In lieu of more definitive information, the calculations were carried out as a function of a number of parameters, the most significant of which were fuel-to-capsule gap, initial helium pressure in capsule, and D'. Analytical studies have indicated that, if the $D'_{1400°C}$ value for the EGCR fuel material is as high as 10^{-9}, the initial capsule pressure is 1 atm, and the operating gap is 0.5 mil, excessive pressures will not be generated within any EGCR capsule (see Fig. 2.29). Recent experiments have indicated that the capsule wall will collapse onto the surface of the UO_2 under EGCR operating conditions. Obviously smaller gaps and a lower D' will further improve an acceptable situation (see Fig. 2.30). On

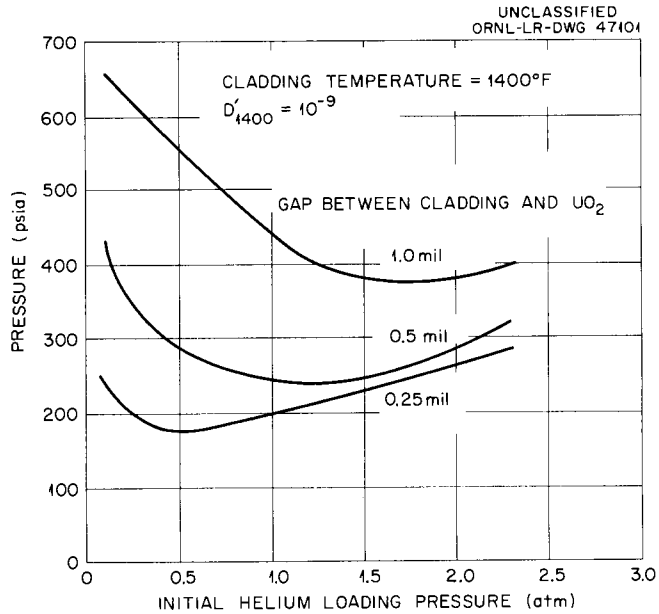

Fig. 2.29. Pressure in Rods of EGCR Fuel Element No. 2 After 485 Days of Reactor Exposure as a Function of Initial Pressure and Operating Gap Between Cladding and UO_2.

the basis of measured diffusion rate constants, there is no doubt that a fuel which has an acceptable D′ value may be specified.

Parametric Study of Fission-Product Contamination

When ceramic fuels are irradiated, a number of the fission products that are solids at nominal temperatures diffuse from the fuel body, in addition to the gaseous and volatile fission products, such as xenon, krypton, iodine, and bromine. If the ceramic fuel is clad with metal, fission products such as cesium and rubidium may contribute an appreciable fraction of the total pressure in the element. If the fuel is used in the unclad condition in gas-cooled reactors, fission-product metals or oxides will diffuse into the coolant. These fission products, if not removed as a result of adsorption, chemical reaction, or leakage, will increase in concentration until their respective partial pressures in the gas are equal to their vapor pressures at the lowest temperature in the coolant circuit. After a particular fission-product element has

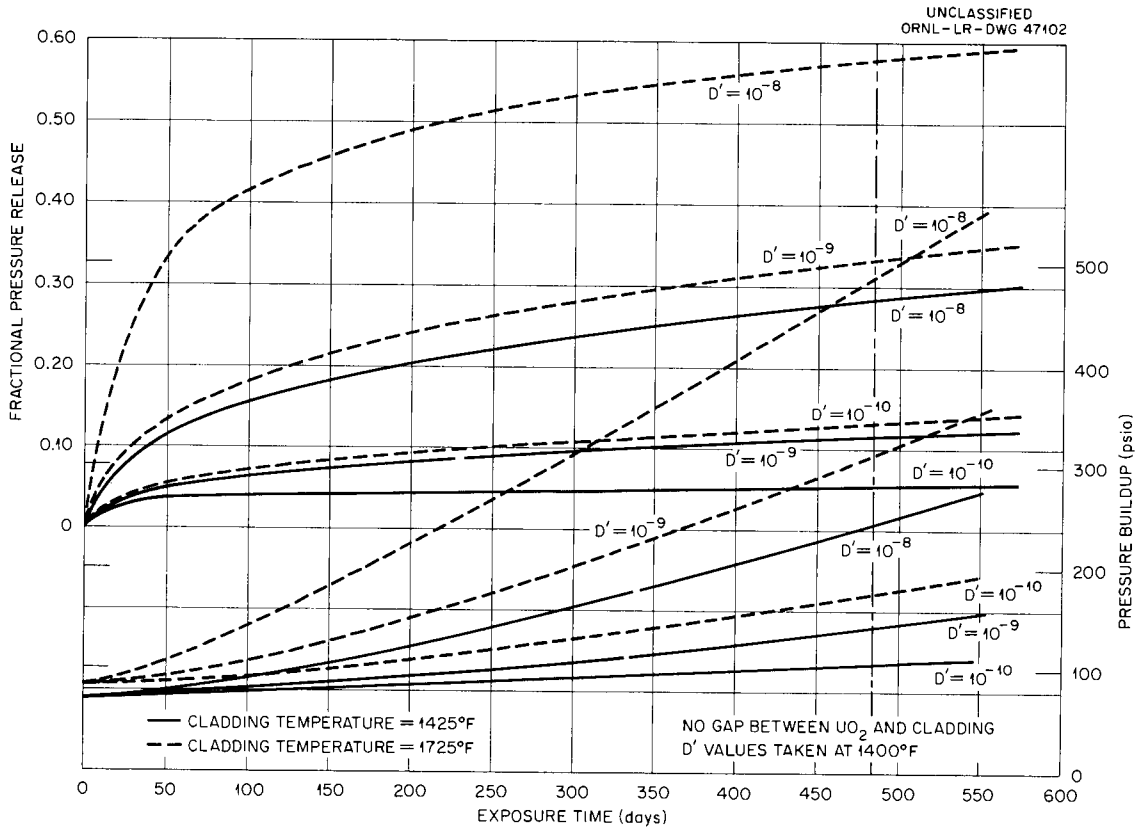

Fig. 2.30. Fractional Release and Pressure Buildup in Rods of EGCR Fuel Element No. 2 as a Function of Reactor Exposure Time.

reached saturation in the gas, additional release of that element from the fuel or its formation from a radioactive parent already in the gas will result in desublimation of a corresponding amount of that element. Solid matter formed in this manner may deposit on particulate matter in the gas or on surfaces in the gas circuit, in particular, the steam generator. Deposition may be reduced or eliminated by removing part or all of the fission products in a purification system.

A parametric study based on vapor-pressure data is being conducted to determine the buildup of "solid" fission products in the fuel and the gas and the rate of deposition of the solids. The mechanism of deposition by surface adsorption is being studied independently, and the results will be factored into the analysis if they are sufficiently conclusive.

The parameters and the ranges being covered in the study are:

Diffusion rate constant, D'	10^{-12} to 10^{-7} sec^{-1}
Purification rate constant, r	0 to 10^{-6} sec^{-1}
Time	10^{5} to 10^{8} sec

Personnel of the Central Data Processing Facility at K-25 are working out solutions to the differential equations covering buildup rates in fuel and gas and are preparing the code for the desired computations on the IBM-704 machine.

Graphite Oxidation in the EGCR

An analytical study has been initiated for determining the graphite combustion hazard in the EGCR in case of accidental admission of air to the main coolant system. A preliminary study[14] has shown that the possibility of burning does exist, and a more precise analysis made with the use of the IBM-704 computer should yield a more definitive result.

The analysis will consider transient thermal effects due to nuclear coastdown and afterheat generation and the effects of blower coastdown. The following model has been developed to describe the oxidation. The graphite reacts with oxygen at the surface to form CO, which is transferred across the boundary layer to the bulk gas stream, where the reaction of CO with oxygen takes place to form CO_2. As CO_2 accumulates in the gas phase, it is transferred to the containing wall, where it is reduced to CO at temperatures above 1300°F. The reaction is temperature-controlled at the lower temperature and is controlled by diffusion across the boundary layer at the higher temperatures. The heat generated by chemical reaction will be added to the nuclear heat and any heat generated by Wigner energy release, and a heat balance will be obtained by machine computations that will take into account the thermal absorption and conduction of the graphite. The calculations will also include the effects of the variations in composition and physical properties of the

[14] J. W. Prados, "Graphite Combustion Hazard," ORNL CF-59-11-134 (November 11, 1959).

gas as it progresses through the core and the variations in the inlet gas as a result of changes in composition of the gas in the containment shell, which is assumed to remain intact. The effects of coincident loss of power to one or both blowers will be considered.

Data on the reaction of graphite and air have been compiled, the equations for heat transfer to the coolant as a function of varying composition of the gas as it progresses through the core have been formulated, the basic heat balance equations for various increments in the core graphite adjacent to the coolant channels have been set up, and an approximate method has been developed for determining the extent of gamma energy absorption in the graphite from an evenly distributed source in a seven-rod fuel element cluster. Expressions for describing thermal radiation from the fuel to the graphite are being studied, and coding for machine computation is under way. It is expected that the results of this study will outline the requirements of an oxidation suppression system if it is found to be needed.

3. EXPERIMENTAL INVESTIGATIONS OF HEAT TRANSFER AND FLUID FLOW

Resistance-Heated-Tube Heat Transfer Experiment

The series 2 heat transfer studies with the tubes of the resistance-heated-tube heat transfer apparatus restrained at the mid-plane to the design position and a modified inlet configuration were continued.[1] Circumferential temperature profiles were measured for peripheral tubes 4 and 6 and central tube 7 at 12 axial positions; profiles for peripheral tubes 1, 3, and 5 were determined at the $L/d_e = 17.9$ and 35 positions only. The mean inner surface temperatures are given in Table 3.1. In this series of experiments, the over-all mean heat flux was 6700 Btu/hr·ft^2, and the average Reynolds modulus was 77 000. All the data have been adjusted[2] to a common inlet air temperature of 63°F. The agreement between

[1] "GCR Quar. Prog. Rep. Dec. 31, 1959," ORNL-2888, pp. 48–51.

[2] "GCR Quar. Prog. Rep. Sept. 30, 1959," ORNL-2835, pp. 54–59.

Table 3.1. Axial Variation in Mean Inner Surface Temperature (Series 2)

L/d_e	Mean Inner Surface Temperature (°F)						
	Peripheral Tube No.						Central Tube, No. 7
	1	2	3	4	5	6	
3.7		262		278		276	255
5		272		288		287	267
7.5		290					
10		301		313		317	295
15		319		324		335	317
17.9	328	325	325	329	334	340	327
20		237		235		245	222
22.5		278		278		289	267
25		317		316		329	311
30		356		355		369	349
35	384	386	380	376	384	390	372
38		389		376		383	377

tubes is reasonable despite some uncorrectable errors introduced by fluctuations in the inlet air temperature and in the power supply.

The circumferential surface temperature distributions at the two locations for all seven tubes are summarized in Tables 3.2 and 3.3. The

Table 3.2. Circumferential Temperature Profiles at $L/d_e = 17.9$

Angular Position[a] (deg)	Temperature[b] (°F)						
	Peripheral Tube No.						Central Tube, No. 7
	1	2	3	4	5	6	
0	4.8	1.6	4.8	0.2	2.5	0.3	0.2
20	9.4	5.2	7.3	4.0	7.6	5.3	0
40	12.7	11.5	15.6	7.3	13.5	11.4	0.3
60	14.3	14.5	20.3	15.1	16.1	16.2	0.7
80	12.8	16.5	21.0	16.0	17.6	17.6	1.0
100	12.9	16.7	22.3	16.9	19.7	19.8	1.8
120	12.3	19.6	24.6	17.3	22.9	20.3	2.0
140	14.2	22.9	27.5	20.2	27.6	22.7	2.6
160	17.7	23.2	29.8	23.2	30.5	24.4	3.2
180	20.1	22.6	27.1	22.4	32.0	24.1	2.9
200	22.1	21.4	28.9	22.5	31.3	24.2	2.8
220	22.5	19.6	25.5	21.4	29.2	23.0	3.1
240	20.3	17.7	21.4	20.1	26.3	19.9	2.3
260	16.7	14.7	16.4	16.6	21.4	17.2	2.3
280	10.7	12.9	10.6	12.0	15.3	13.3	2.6
300	4.0	5.1	3.8	6.8	8.7	7.9	1.8
320	0.1	1.4	0.6	1.5	2.7	3.1	1.4
340	0	0	0	0	0	0	0.8
$t_{surf,\ min}$	315.7	311.5	308.2	315.7	316.3	325.4	325.4
$t_{surf,\ mean}$	328.4	325.3	325.1	329.3	337.3	340.4	327.2

[a]The angular position on the tube surface was chosen such that the 0-deg point on a peripheral tube was on the side adjacent to the central tube (corresponding to the points of closest approach of the tubes to each other) and was measured in a clockwise direction facing downstream, that is, in the direction of flow. The 0-deg location on the central tube was matched to the 0-deg position for tube 5.

[b]Listed in °F above the minimum surface temperature for the tube.

data of Table 3.2 are for the $L/d_e = 17.9$ position immediately upstream of the mid-cluster spacer. A comparison with the series 1 data[2] shows a slight shift in the primary minimum from 320 to 340 deg. The primary maximum, however, now occurs close to the expected 180-deg position.

Table 3.3. Circumferential Temperature Profiles at $L/d_e = 35$

Angular Position[a] (deg)	Temperature[b] (°F)						
	Peripheral Tube No.						Central Tube, No. 7
	1	2	3	4	5	6	
0	1.5	0	3.6	0	5.3	0	0
20	3.9	0.9	5.0	1.0	10.1	1.8	1.0
40	4.8	2.3	5.8	2.2	16.2	4.5	2.3
60	4.6	3.2	5.4	4.1	19.0	7.8	4.0
80	4.3	3.8	6.2	5.8	23.1	8.8	4.1
100	5.3	3.4	8.0	7.2	27.0	10.2	4.4
120	7.4	5.9	11.2	8.6	31.1	10.2	5.7
140	10.4	7.5	14.8	10.2	32.9	11.5	7.2
160	14.2	11.0	16.9	10.3	32.2	13.4	8.8
180	16.7	12.8	17.4	13.9	26.8	15.3	9.0
200	17.3	14.4	16.8	15.9	21.0	15.0	8.7
220	16.7	15.4	14.2	16.8	16.0	14.8	7.8
240	14.0	13.0	11.4	16.5	11.9	12.9	7.6
260	10.2	11.2	7.6	14.5	7.9	11.3	7.8
280	6.8	9.1	5.0	11.9	5.1	9.4	7.0
300	2.7	6.6	1.6	8.3	2.3	6.4	5.9
320	1.0	4.4	0.3	6.0	0.3	2.8	4.1
340	0	1.9	0	2.4	0	0.7	2.5
$t_{surf,\ min}$	376.0	378.8	371.9	367.2	367.4	380.9	366.0
$t_{surf,\ mean}$	383.8	385.9	380.3	375.9	383.5	389.5	371.5

[a]The angular position on the tube surface was chosen such that the 0-deg point on a peripheral tube was on the side adjacent to the central tube (corresponding to the points of closest approach of the tubes to each other) and was measured in a clockwise direction facing downstream, that is, in the direction of flow. The 0-deg location on the central tube was matched to the 0-deg position for tube 5.

[b]Listed in °F above the minimum surface temperature for the tube.

Although a small counterclockwise displacement of the profiles is still noted (corresponding perhaps to a clockwise rotation of the flow), the series 2 profiles are more nearly symmetrical about the 0—180-deg radial axis joining the centers of the peripheral and central tubes. This is apparent from the graphical comparison presented in Fig. 3.1. The temperature distribution around tube 1, while retaining the same general profile features as observed for the other outer tubes, exhibits a stronger minimum in the 80- to 120-deg zone. This persists even at the $L/d_e = 35$ level. The reason for this deviation is not obvious, and it is planned to re-examine this tube at a future date. The depression of the profiles at the 180-deg location for tubes 2, 3, 4, and 6 results from the averaging procedure used in adjusting the surface temperatures measured at the beginning and end of a single circumferential traverse and is not to be taken as an indication of a real phenomenon. The secondary maxima, noted at approximately 60 deg on either side of the minimum temperature location, probably reflect the effect of adjacent peripheral tubes. The temperature pattern for the central tube is nearly uniform (an average fluctuation around the mean of only 0.55% as compared with 4.1 to 6.2% for the peripheral tubes); again, however, a 20-deg counterclockwise displacement of the profile is observed. Further, the central tube surface temperature averages 9°F above the temperatures of the adjacent tubes (at the 0-deg positions).

The data of Table 3.3 list the angular variations in temperature differences at the $L/d_e = 35$ level. The same general profile characteristics are present. For tube 5, however, the primary maximum occurs at 140 deg, and the maximum-to-minimum temperature difference is about 33°F (approximately twice that measured on the other peripheral tubes). Repeat runs gave essentially the same results. The peripheral profiles at this level exhibit less variability than at the $L/d_e = 17.9$ position. The average fluctuation for the outer tubes, except tube 5, has been reduced to 2.1% (4.2% for tube 5). The central tube, however, shows a threefold increase to 1.5%, and the surface temperature of tube 7 averages 4°F below the peripheral tube local temperatures in the regions of closest approach.

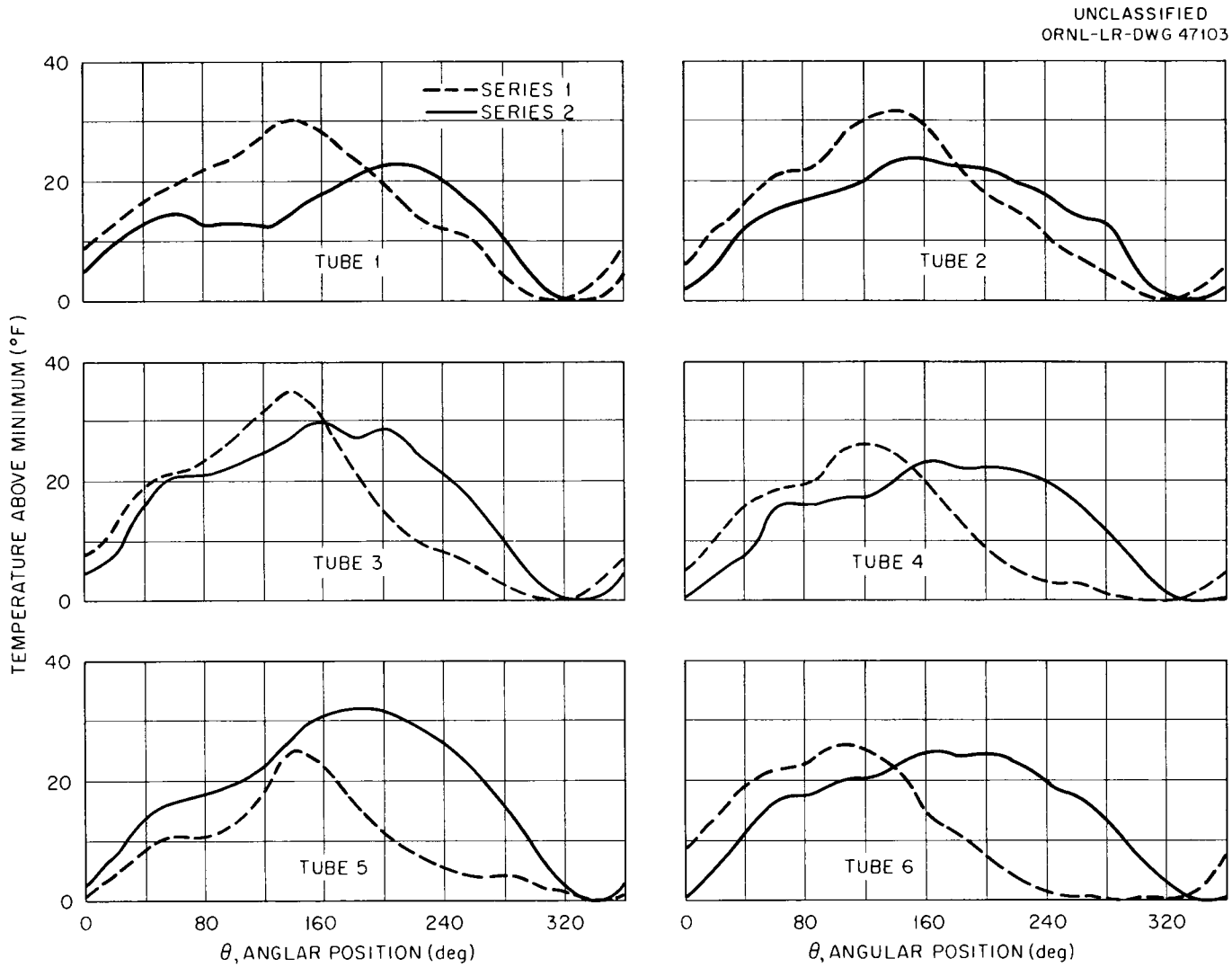

Fig. 3.1. Comparison of Circumferential Temperature Profiles of Peripheral Tubes at $L/d_e = 17.9$.

A comparison is made in Fig. 3.2 of the circumferential temperature profiles for tube 6 at six axial positions. The most prominent features of these distributions are the consistency of the patterns with respect to angular position, the flattening of the profiles in the lower region of the flow channel, and the marked effect of the mid-cluster spacer on the circumferential variation of tube temperature in the region just below the spacer. Essentially the same configurations are observed for tubes 2, 4, and 7. At $L/d_e = 20$, the profile shape results from the distortion of the flow by the mid-cluster spacer (located at $L/d_e = 19$). The minima at 120 and 240 deg show the effect (through boundary-layer interruption and increased turbulence) of small set-screws which contact the tube surface. A similar set-screw at the 0-deg position may in part account for the large maximum-to-minimum temperature difference at this level. It should be noted that, while the variation around the tube is large, the maximum tube temperature (270.3°F) is still below the minimum surface temperatures at the adjacent $L/d_e = 17.9$ (325.4°F) and 22.5 (279.9°F) positions.

The axial variation in the mean heat transfer coefficient is summarized in Table 3.4 for tubes 2, 4, 6, and 7. Air temperatures were assumed to be circumferentially uniform and to vary axially with the integral of the power generation between the inlet and any longitudinal position. This takes into account the axial variation in local heat production resulting from the change in tube resistivity with temperature; velocity contours for the 4:1 tube-spacing arrangement are needed in order to include in the analysis the circumferential change in heat generation. The asymptotic values at $L/d_e = 18$ and 36 are in good agreement with the previously reported results.[1,2]

Mass-Transfer Measurements

Preliminary measurements have been made of the mass removal from a naphthalene-coated rod located in the second (downstream) of two stacked

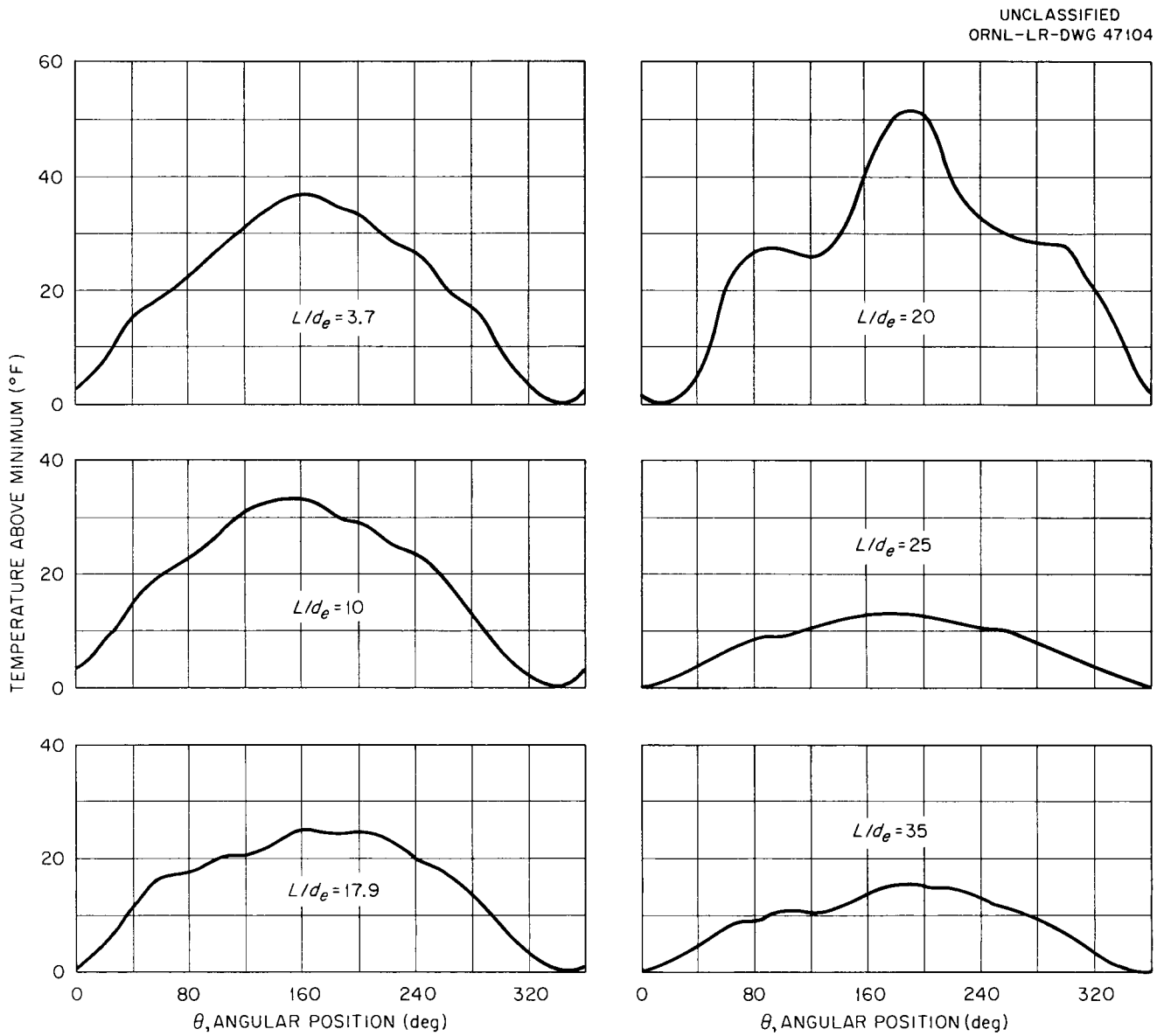

Fig. 3.2. Comparison of Circumferential Temperature Profiles for Tube 6 at Six Axial Positions. Mid-cluster spacer at $L/d_e = 19$.

Table 3.4. Axial Variation in Mean Heat Transfer Coefficient (Series 2)

L/d_e	Mean Heat Transfer Coefficient ($Btu/hr \cdot ft^2 \cdot °F$)			
	Peripheral Tube No.			Central Tube, No. 7
	2	4	6	
0	51.3	46.0	46.6	58.4
4	33.4	30.9	32.4	35.5
8	30.6	28.8	29.6	32.4
12	29.3	28.2	28.3	30.7
16	28.8	28.4	28.0	29.7
18	28.8	28.2	28.1	29.4
20	45.3	46.0	44.7	52.4
24	32.9	32.9	31.2	35.4
28	29.1	28.9	28.4	30.5
32	27.2	27.0	27.1	28.8
36	26.0	25.9	26.7	28.3
38	26.4	27.4	27.8	28.3

EGCR fuel element clusters. The test unit, described previously[3] and shown in Fig. 3.3, consists of a dummy and an active cluster. For the initial series of runs, the bundles were without mid-cluster spacers; and the adjacent hanger-spider combination was in line. The effect of the relative orientation of the two bundles will be studied in succeeding experiments. Details of the profilometer[3] are shown in Fig. 3.4; the angular position marker produces comparison pips on the recorder at 2.5-deg intervals. Typical traces are given in Fig. 3.5 for a number of successive scans of a rod at a single position; the high degree of reproducibility is apparent. It has been found that, with care, the radius of the naphthalene section can be measured to within ±0.0002 in. Since an average run results in a change in radius of the order of 0.010 in., it should be possible to determine the volume of naphthalene removed to within ±2%.

[3]"GCR Quar. Prog. Rep. Dec. 31, 1959," ORNL-2888, pp. 51–60.

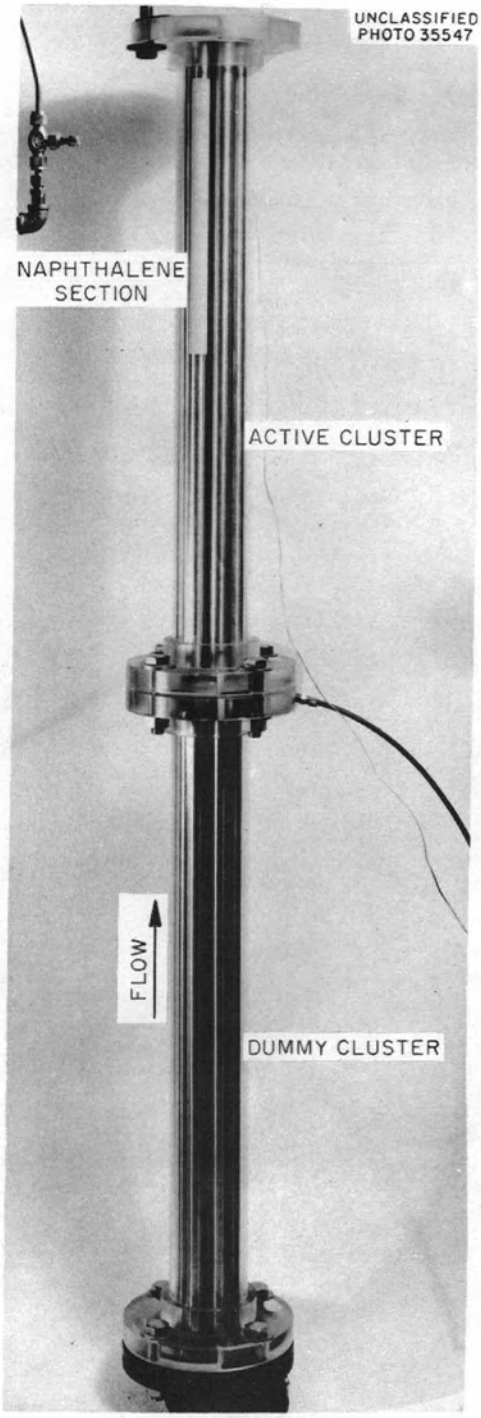

Fig. 3.3. Apparatus for the Study of Mass Transfer in the Vicinity of the Mid-Cluster Spacer.

UNCLASSIFIED
PHOTO 35543

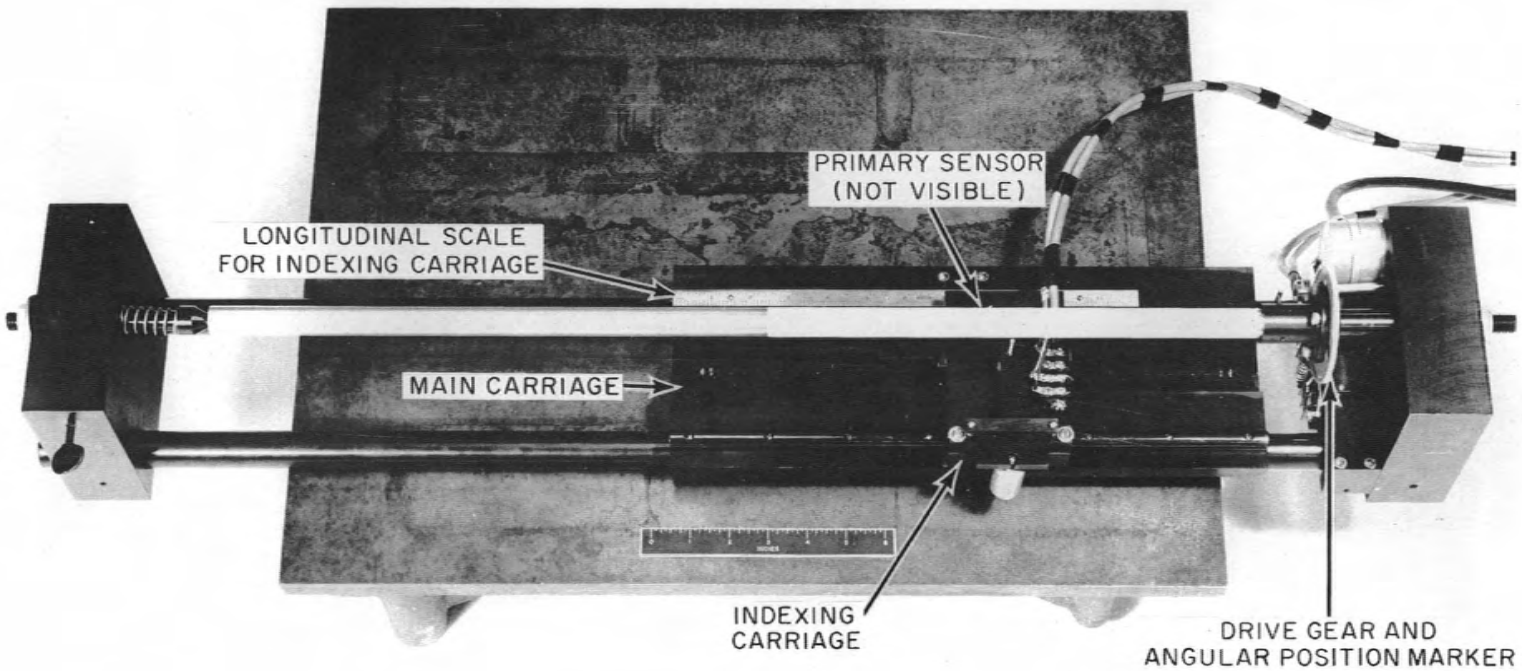

Fig. 3.4. Model 3 Mass-Transfer Profilometer.

UNCLASSIFIED
ORNL-LR-DWG 47105

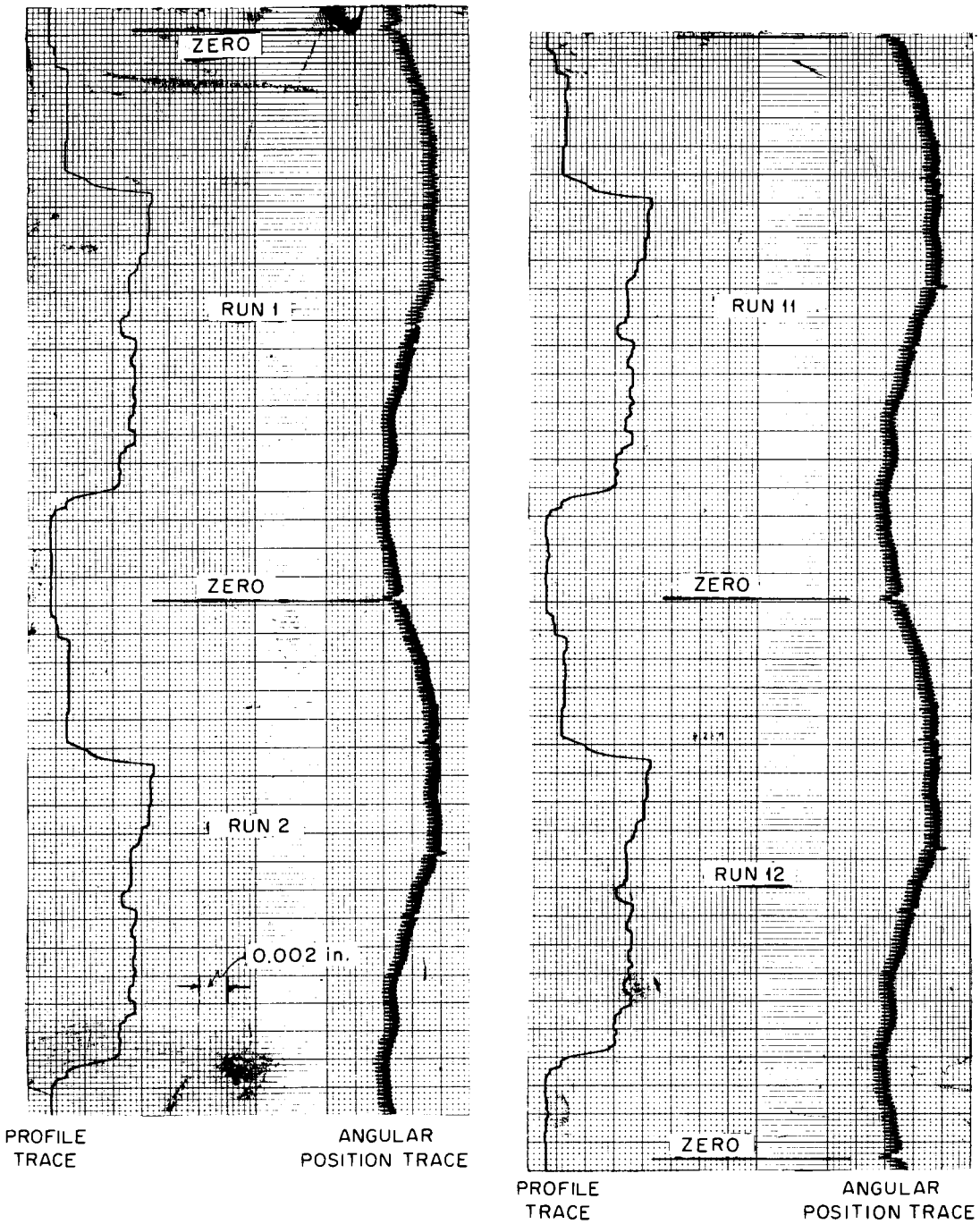

Fig. 3.5. Typical Profilometer Traces.

Interpretation of the data has been complicated by the unexpected appearance of a sporadic 30% shift in the profilometer calibration. This is believed to result from a change in sensitivity of the differential transformer sensing element induced by intermittent contact between the iron core and a brass adjusting screw. A slow 5% drift in calibration appears to be related to interference between the channels of the Sanborn recorder. Following appropriate modifications, the preliminary experiments will be repeated.

In the previous mass-transfer studies,[4] the naphthalene density was assumed to be 1.078 g/cm^3, as determined by Sherwood and Trass.[5] The theoretical density of naphthalene is 1.145 g/cm^3. Since the forming procedures utilized in the current investigation are somewhat different from those followed by Sherwood and Trass, a separate determination of the naphthalene density was made.

The samples studied were prepared in the same manner as the coated rods used for the mass-transfer experiments.[4] A solid aluminum rod (6 in. long and 0.875 in. in diameter) was undercut to a depth of 0.034 in. along a 3.005-in. length at the mid-section and coated with naphthalene. The weight and diameter of the specimen were then determined; the tare weight of the aluminum rod was found after removal of the naphthalene. Densities calculated from three measurements were 1.138, 1.107, and 1.126 g/cm^3; the precision of the determination was calculated to be ±1.5%. Since all three values fall within the ±1.5% band around the mean, a density of 1.124 ± 0.017 g/cm^3 will be used in subsequent data analyses. The previously reported[3,6-8] mass-transfer factors should accordingly be corrected (multiply by 1.0425).

---

[4]J. L. Wantland and R. L. Miller, "Heat Transfer in Septafoil Geometries by Mass-Transfer Measurements," ORNL CF-59-6-9 (June 30, 1959).

[5]T. K. Sherwood and O. Trass, "Sublimation Mass Transfer through Compressible Boundary Layers on a Flat Plate," AFOSR-TR-58-131 (Sept. 1, 1958).

[6]"GCR Semiann. Prog. Rep. June 30, 1959," ORNL-2767, pp. 80–91.

[7]"GCR Semiann. Prog. Rep. Dec. 31, 1958," ORNL-2676, pp. 47–54.

[8]"GCR Semiann. Prog. Rep. Sept. 30, 1959," ORNL-2835, pp. 59–63.

Velocity Distribution in Septafoil Channels

The determination of velocity profiles in septafoil channels has been continued with the use of the apparatus previously described.[9] A new set of top and bottom spiders was installed to assure more accurate spacing of the tube in the cluster. Velocity contours were then redetermined[10] at the $L/d_e = 39.7$ level with the $\gamma = 2$ tube spacing for $N_{Re} = 33\ 000$ and 57 000. The results are given in Figs. 3.6 and 3.7. In contrast to the previous data,[11] the profiles are very nearly symmetrical with respect to a channel radius drawn through the center of the peripheral tube; a counterclockwise rotation of as much as 5-deg had been observed in the earlier measurements. The slight deviation (about 4%) between the maximum velocities in the outer flow regions adjacent to the tube is again evident. It is now suspected that this discrepancy arises from a partial obstruction and/or deflection of the fluid either by a thermocouple or a channel-wall joint in the region upstream of the tube cluster.

The velocity profiles of Figs. 3.6 and 3.7 can be used not only to measure the relative flows in arbitrarily defined flow regions of the over-all channel, but also to estimate the circumferential variation in the heat transfer coefficient around any tube. To accomplish this, use is made of the analogy equations relating the transfer of momentum and heat. The earliest and simplest of these is the Reynolds analogy[12] which states that

$$N_{St} = \frac{f}{2} \quad . \tag{1}$$

---

[9] Ibid., pp. 63–69.

[10] J. A. Bast, M. L. Minges, and B. V. Makler, "Velocity Profiles in GCR Channels," MIT Eng. Practice School Report KT-517 (Jan. 20, 1960).

[11] "GCR Quar. Prog. Rep. Dec. 31, 1959," ORNL-2888, pp. 60–62.

[12] See J. G. Knudsen and D. L. Katz, "Fluid Dynamics and Heat Transfer," p. 417, McGraw-Hill, New York, 1958.

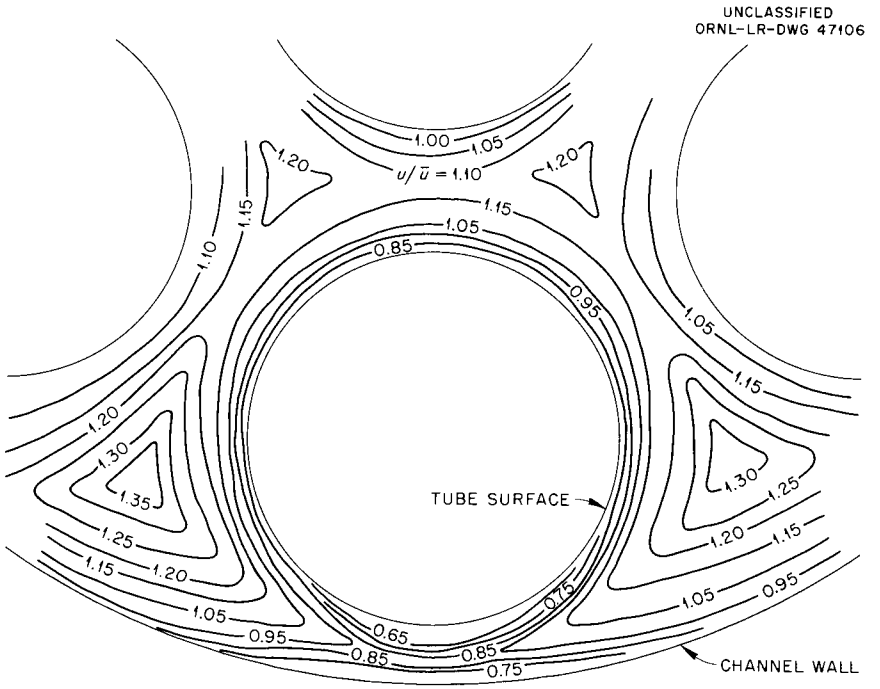

Fig. 3.6. Experimental Velocity Contours; N_{Re} = 33 000, L/d_e = 39.7, γ = 2.

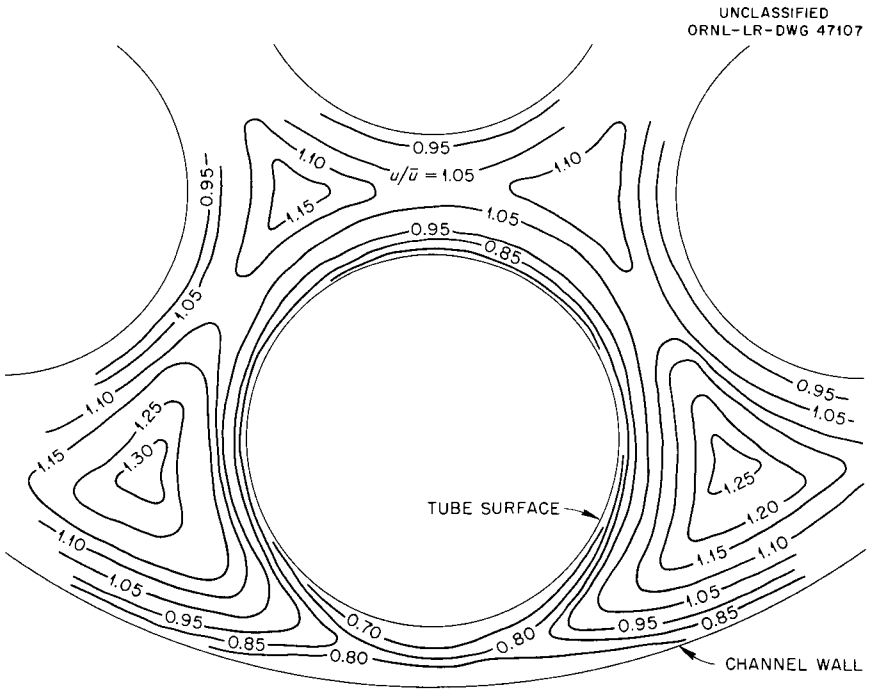

Fig. 3.7. Experimental Velocity Contours; N_{Re} = 57 000, L/d_e = 39.7, γ = 2.

In Eq. (1), the Stanton modulus is

$$N_{St} = \frac{h}{c_p \rho \bar{u}} , \tag{2}$$

where h is the heat transfer coefficient (Btu/hr·ft^2·°F), c_p is the heat capacity of the fluid (Btu/lb·°F), ρ is the fluid density (lb/ft^3), and $\bar{u}$ is the average fluid velocity (ft/hr); f in Eq. (1) is the Fanning friction factor.[13] The Reynolds analogy is somewhat unrealistic, however, in that it does not take into account the velocity distribution normal to the surface. An extension of this analogy by Prandtl and Taylor[14] incorporated the velocity distribution in the laminar sublayer; the resulting relation, which involves the ratio of the velocity at the edge of the laminar sublayer (u_F) to the average fluid velocity, is given by

$$N_{St} = \frac{f}{2}\left[\frac{1}{1 + \frac{u_F}{\bar{u}}(N_{Pr} - 1)}\right] . \tag{3}$$

This reduces to Eq. (1) for $N_{Pr} = 1$.

For the septafoil geometry, in which the velocity varies around the perimeter of the tube, the average fluid velocity was determined as a mean value ($\bar{u}_s$) over small regions adjacent to the tube. These regions were defined by dividing the tube perimeter into 10-deg sectors; the average velocity was then evaluated by graphical integration of the velocity profiles in the area bounded by the tube surface, the two radii defining the 10-deg sector, and the line of maximum fluid velocity (Fig. 3.8). The velocity contours were first "idealized" by averaging values of $u/\bar{u}$ (the ratio of local velocity to bulk average velocity in the channel) for symmetrical positions about the tube. The calculated

---

[13]W. H. McAdams, "Heat Transmission," 3d ed., p. 145, McGraw-Hill, New York, 1954.

[14]Knudsen and Katz, op. cit., p. 420.

average velocity, normalized with respect to the maximum of the sector velocities, is given in Table 3.5 for six of the sectors between 0 and 180 deg. The velocity, u_F, at the outer edge of the laminar sublayer was obtained from the universal velocity profile[15] for turbulent flow in circular tubes.

The heat transfer coefficient in each sector was then calculated from the Prandtl-Taylor analogy relation using a friction factor based on the bulk flow.[16] The circumferential variation in h, for N_{Re} = 33 000 and 57 000, is shown in Fig. 3.9. A similar calculation based on the Reynolds analogy gives values of h which are 6 to 8% lower than those shown in

[15]E. R. G. Eckert and R. M. Drake, Jr., "Heat and Mass Transfer," 2d ed., p. 157, McGraw-Hill, New York, 1959.

[16]While convenient, the assumption of a constant friction factor (see ref. 9) is not necessary. A simple analysis shows that the friction factor for each flow sector is inversely proportional to $(\bar{u})^{0.5}$; f then varies about 37% around the tube circumference. Re-evaluation of the data is in progress.

Table 3.5. Average Sector Velocities

Angular Position[a] (deg)	Velocity $(\bar{u}/\bar{u}_{max})_s$	
	N_{Re} = 33 000 u_{max} = 91.2 ft/sec	N_{Re} = 57 000 u_{max} = 126.3 ft/sec
0–10	0.580	0.535
30–40	0.765	
40–50		0.755
80–90	1.000	1.000
110–120	0.870	0.895
150–160	0.925	0.910
170–180	0.820	0.685

[a]The 0-deg position on the peripheral tube was chosen to correspond to the point of closest approach of the central and peripheral tubes (lies on the radius joining the centers of the inner and outer tubes).

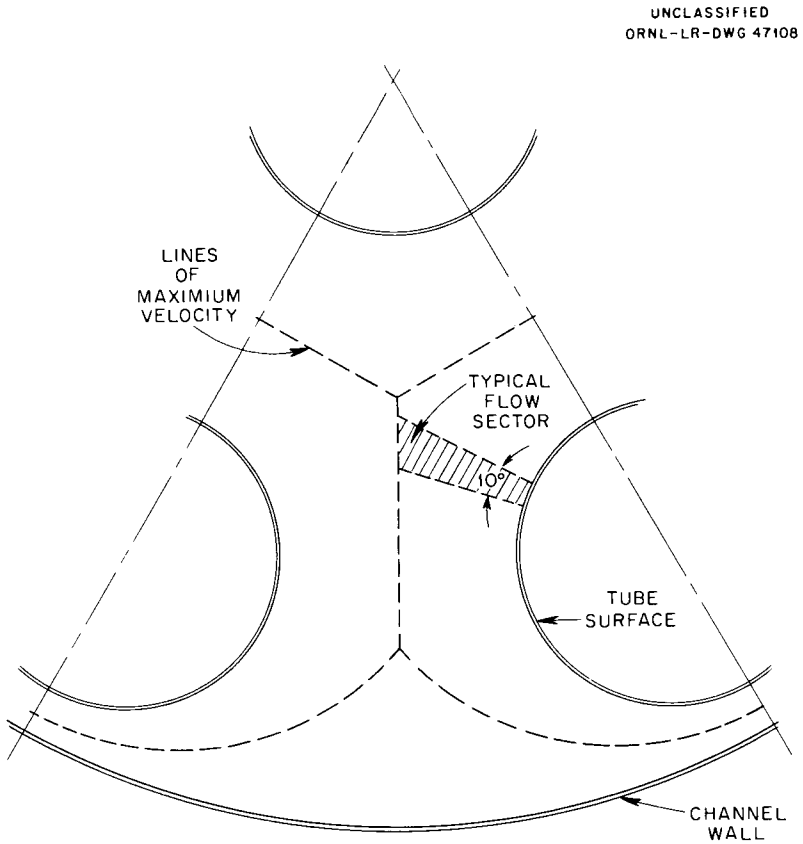

Fig. 3.8. Arbitrary Flow Sector as Defined in Analysis for Predicting the Circumferential Variation in the Local Heat-Transfer Coefficient.

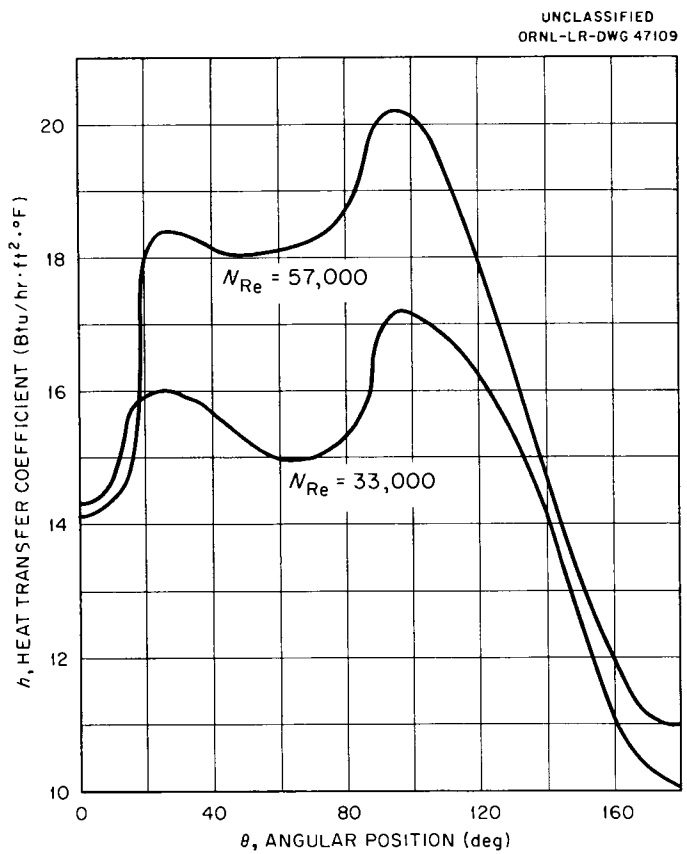

Fig. 3.9. Circumferential Variation in the Local Heat Transfer Coefficient as Predicted by the Prandtl-Taylor Analogy.

Fig. 3.9, while the Colburn analogy[17]

$$j_H = N_{St} \cdot N_{Pr}^{2/3} = \frac{f}{2} \qquad (4)$$

yields h values 12 to 15% above those found by the Prandtl-Taylor relation.

The mean heat transfer coefficients at the $L/d_e = 39.7$ level (as estimated by planimeter from the curves of Fig. 3.9) are 14.8 Btu/hr·ft^2·°F for $N_{Re} = 33\ 000$ and 16.7 Btu/hr·ft^2·°F for $N_{Re} = 67\ 000$. An extrapolation of these results to $N_{Re} = 77\ 000$ (assuming h to vary as $N_{Re}^{0.8}$) yields the value 18.4 Btu/hr·ft^2·°F. This is considerably below the asymptotic value of 27 Btu/hr·ft^2·°F developed from the heat transfer data.

---

[17]Knudsen and Katz, op. cit., p. 424.

Part 2. Materials Research and Testing

4. METALLURGICAL INVESTIGATIONS

Fuel and Moderator Materials Development

Fabrication of UO_2

A large portion of the effort on UO_2 fabrication continued to be devoted to the preparation of specimens and accessory pieces for irradiation tests. The close diametral tolerances (±0.001 in.) and the variety of sizes and enrichments specified require special handling of each batch.

Two experimental induction furnaces have been constructed and put into operation. One, a molybdenum susceptor furnace, is used for rapid sintering of UO_2 in a pure hydrogen atmosphere. The other furnace, which has a large, 5 1/2-in.-i.d., graphite susceptor, is used to sinter the large disks needed for the study of the thermal conductivity of UO_2. This furnace will also be used in studying the problems involved in fabricating large, experimental, UO_2 fuel bodies.

Stabilized ZrO_2 has been proposed for use as a thermal insulator around miniature UO_2 pellets in irradiation tests. In these tests, the stabilized ZrO_2 would also be in contact with BeO spacers. Compatibility tests were therefore conducted on ZrO_2-UO_2 and ZrO_2-BeO couples by firing test specimens in hydrogen through four cycles consisting of heating slowly to 1750°C in 27 hr, holding for 3 hr at 1750°C, and slowly cooling to room temperature. The ZrO_2-UO_2 test specimens exhibited reaction by diffusion after the first cycle, and swelling and distortion occurred during the fourth cycle. Reactions evidenced by cracking and distortion also occurred in the ZrO_2 specimens that were in contact with BeO. In this case, much of the CaO constituent used to stabilize the ZrO_2 seemed to diffuse into the BeO, and the cracking was typical of the thermal fractures that occur as unstabilized ZrO_2 is cooled through the transformation temperature range. Because of these results, work on ZrO_2 insulators has been discontinued.

UO_2 Process Development

With the constantly increasing use of UO_2 as a fuel material, the incentive for developing a low-cost production process for the fabrication

of UO_2 fuel bodies has become more apparent. The relative cost advantages of a continuous process for the conversion of UF_6 to UO_2 and a simplified process for the fabrication of fuel bodies were described previously.[1]

A pilot plant has been assembled, and the continuous process is being tested on production quantities of material. The pellets produced initially were of moderately good quality but did not conform to the dimensional requirements for sintered pellets. Slight modifications were therefore made to the equipment and techniques, and high-quality fuel bodies are now being produced consistently.[2] Additional studies[3] are under way on the pressing and sintering characteristics of various oxides in order to determine the requirements for attaining densities greater than 95%. The control required to insure maximum density and uniform shrinkage has been difficult to maintain because considerable variations in the properties of the oxide can occur during each step of the process.

Exploratory tests to determine the effects of thermal and chemical reoxidation, metal and organic additives, various oxygen-to-uranium ratios, particle size and shape, and wet milling on the pressing pressures and sintering temperature have been completed. As a result of these tests, three oxides are being evaluated further from the standpoint of achieving higher densities or cheaper feed material.[4] The three oxides are Hanford-denitrator UO_3, hydrogen reduced at 400°F to UO_2; ground UO_2 powder prepared by wet milling of previously fired UO_2, as prepared by the continuous process; and calcined U_3O_8 prepared by air-calcining any available oxide at 2500°F and cooling in the absence of air. The previously fired material is characterized by high green and fired densities throughout the firing range. The denitrator-derived

---

[1]"GCR Semiann. Prog. Rep. Dec. 31, 1958," ORNL-2676, pp. 67–77.

[2]"Y-12 Tech. Prog. Rep., Second Quarter, FY 1960," Y-1268, pp. A36–A40 (Classified).

[3]Ibid., pp. A54–A58.

[4]"Y-12 Tech. Prog. Rep., Third Quarter, FY 1960," Y-1269 (in publication, Classified).

material was better than the product from the continuous process at lower temperatures, but it was not so good when fired at 1900°C.

Thermal Conductivity of UO_2

An apparatus has been built for determining the thermal conductivity of UO_2 as a function of temperature that is based on the method of radial heat flow developed by Powell[5] and modified by Hedge and Fieldhouse.[6] The specimen used is a 3-in.-diam disk with a central hole in which a heater is positioned. Auxiliary heaters are used at the top and bottom of a stack of specimens to insure radial heat flow. A muffle furnace around the outside of the stack is used to heat the specimens to a predetermined temperature in a hydrogen atmosphere. The temperature is measured at two accurately spaced radial positions. The apparatus will operate at temperatures up to 1350°C. Calibration runs are currently being conducted using Armco iron as a standard.

Mechanical Behavior of Encapsulated UO_2

The dimensional stability and mechanical behavior of 95%-dense UO_2 pellets are being observed in an experimental device described previously.[7] The pellets are encapsulated in a type 304 stainless steel tube and subjected to thermal gradients comparable to those predicted for the EGCR.

An effort has been made to increase the temperature differential between the center of the UO_2 pellet and the stainless steel wall in a helium environment to values higher than previously reported.[7] Data showing the average temperature gradients at steady-state conditions for several runs are given in Table 4.1.

Axial-expansion measurements are being made at elevated temperatures through the use of low-voltage radiography. The radiographic technique being utilized permits an accuracy of ±0.003 in. in measuring the total

---

[5]R. W. Powell, Proc. Phys. Soc. 50, 407 (1938).

[6]J. C. Hedge and I. B. Fieldhouse, "Measurement of the Thermal Conductivity of Uranium Dioxide," AECU-3381 (Sept. 20, 1956).

[7]"GCR Quar. Prog. Rep. Dec. 31, 1959," ORNL-2888, p. 67.

Table 4.1. Average Steady-State Temperature Gradients Achieved in Experimental Studies of the Mechanical Behavior of Clad UO_2

Maximum Pellet Inner Surface Temperature (°F)	Average Cladding Wall Temperature (°F)	Average Temperature Gradient (°F)
1000	785	215
1500	1160	340
2000	1385	615
2500	1520	980
3000	1705	1295

height of the UO_2 pellet at temperature. Radiographs showing the relative expansion of UO_2 at various temperatures are presented in Fig. 4.1

Two different loadings of UO_2 pellets have been tested to date. Axial-expansion data obtained in several tests are plotted in Fig. 4.2, along with values of expansion calculated from dilatometer test results. The data from runs 2 through 5 fall on a single curve, within the experimental errors of the technique. The data obtained in run 6 are low, but subsequent runs show a trend toward agreement with the data obtained in the earlier runs. This behavior indicates that a mechanical restraint may have been imposed on the pellets during run 6 that was relieved in successive tests.

The expansion appears to be a function of the pellet inner surface temperature rather than the mean temperature. Radiographs taken at an inner surface temperature of 1256°F show no decrease in the column height of the UO_2 when the capsule wall temperature is lowered 100°F, but the expansion profile of the pellets is changed. The gaps that are formed between pellets as the thermal gradient is increased at high temperatures are shown in Fig. 4.3. In effect these gaps reduce the area of contact between pellets to a fraction of the normal value.

Examinations of the UO_2 pellets tested in the first loading have been made. Most of the cracks found in the UO_2 pellets were radial, as

UNCLASSIFIED
ORNL-LR-DWG 44950R

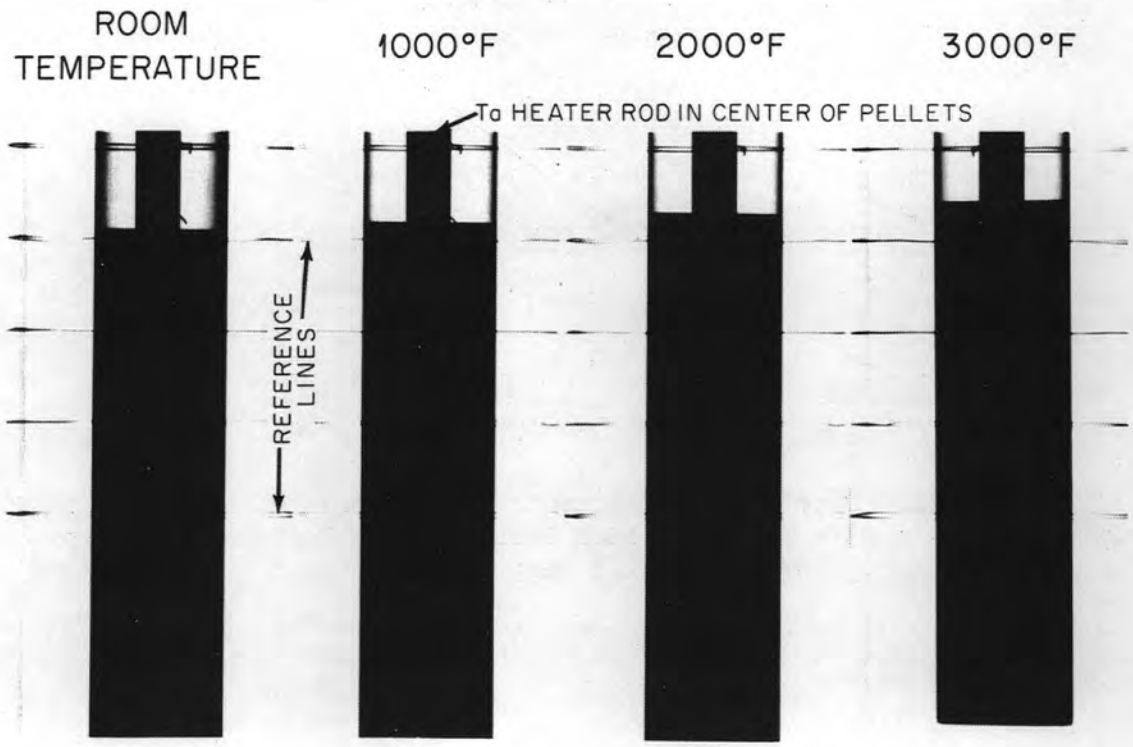

Fig. 4.1. Radiographic Measurements of Axial Growth of UO_2 Pellets in Simulated EGCR Fuel Capsules. 1 X (Reduced to 91% of original)

shown in Fig. 4.4. Dimensional measurements showed an average decrease in pellet length of 0.20%. The original diametral gap between the pellets and the capsule was 0.010 in., and it was found that the gap had not changed more than 0.001 in., which is the accuracy limit of the radiographic technique.

The radiographic measuring technique now being used accommodates a maximum stack height of 14 in. The accuracy of measurements is independent of the original stack height, and therefore, to reduce the error in predicting the axial growth of UO_2 pellets in the EGCR fuel capsules, a new experimental rig is being built which will accommodate a fuel capsule of the design dimensions.

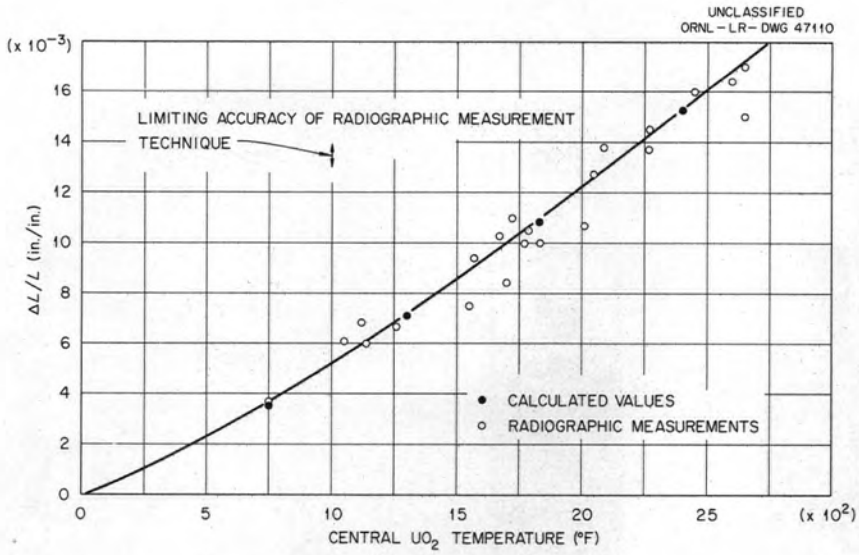

Fig. 4.2. Data from Radiographic Measurements of Expansion of 95% Dense UO_2 Pellets in Simulated EGCR Fuel Capsules Compared with Expansion Values Calculated from Dilatometer Test Data.

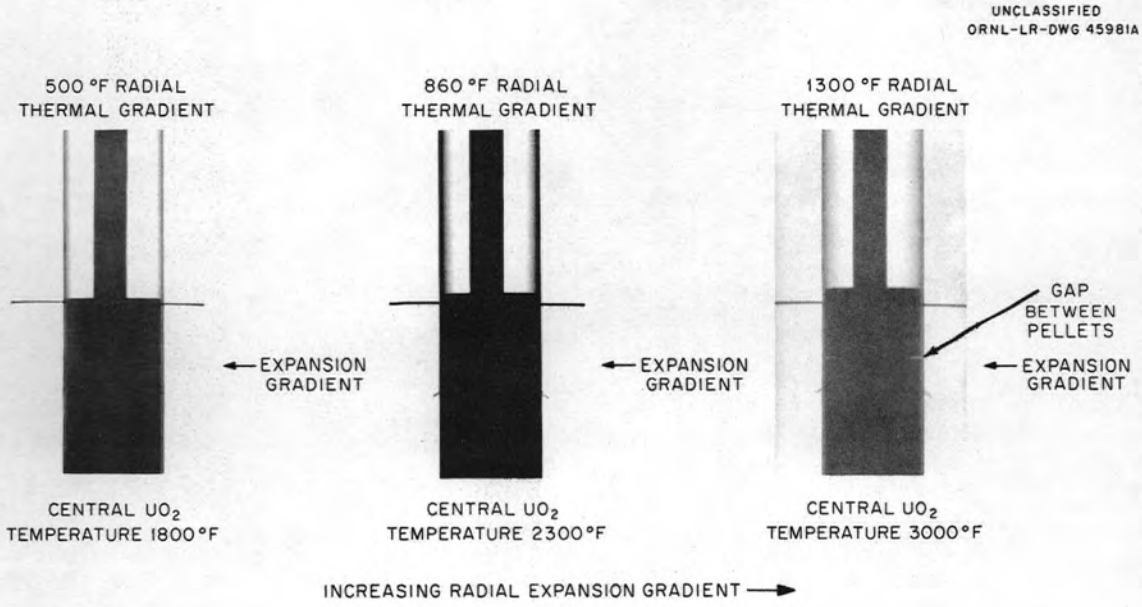

Fig. 4.3. Effect of Radial Thermal Gradient on Expansion of UO_2 Pellets in Simulated EGCR Fuel Capsules. 1 X

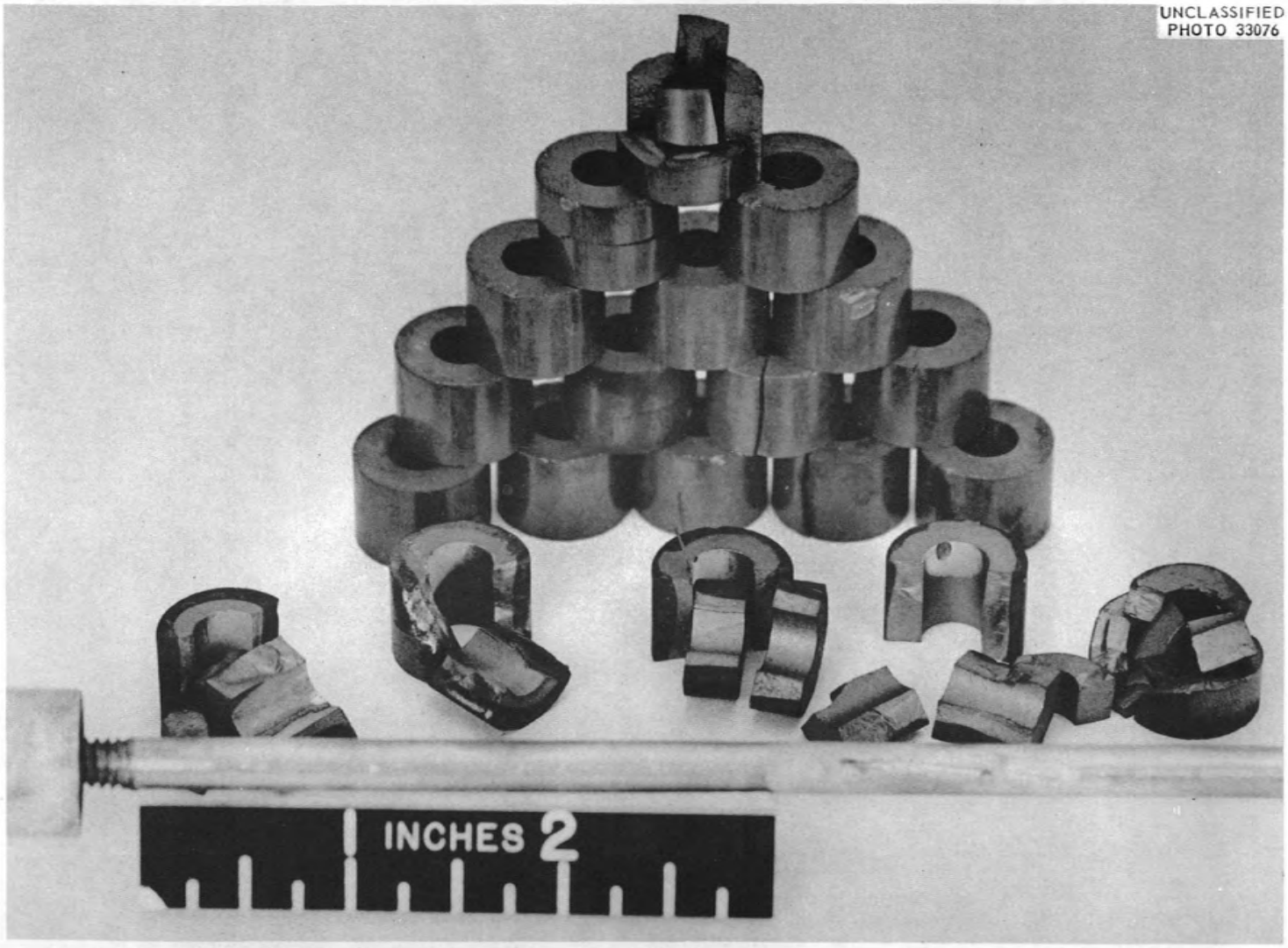

Fig. 4.4. Appearance of UO_2 Pellets After Test in Simulated EGCR Fuel Capsule.

Fission-Product Release Studies

A series of measurements have been made of rates of release of Kr^{85} or Xe^{133} from small specimens of UO_2 at high temperatures after irradiation at low temperatures and to a low burnup. The specimens were fragments or sections of prototype EGCR fuel pellets. The apparatus and procedures were described previously.[8]

The results obtained to date are presented in Table 4.2. The first specimens of UO_2 studied, samples designated 2-1 and GE-H-4, had decayed for long periods, and it was necessary to count the Kr^{85}. Since the counting of Kr^{85} is not efficient and the rates of release of fission products from these pellets were low, the counting errors were high, and the amounts of gas collected in individual tests were barely above the limits of detection. In order to eliminate these problems, tests on the samples designated 1173 were conducted shortly after irradiation (1 to 2 weeks), and the Xe^{133} was counted. The decay rates of the gas samples collected in these tests were several orders of magnitude greater than in the early tests, so more confidence is placed in the results. The release rate parameter values, D', in Table 4.2 were computed from the data with the use of the relation

$$D' = \frac{\pi f^2}{36t} ,$$

where f is the fractional release in time t. This equation was derived from the Lustman model for fission-gas release from UO_2.[9] If this model is applicable, the D' values should characterize the performance of UO_2 samples as fuel materials. It has been shown (see chap. 2, this report) that a D' value of 10^{-9} or less at 1400°C is acceptable for an EGCR fuel element if the activation energy for release is 65 kcal/mole. This value may be used to evaluate qualitatively the different batches of UO_2 pellets.

---

[8]Ibid., p. 68.

[9]See J. D. Eichenberg et al., "Effect of Irradiation on Bulk UO_2," WAPD-183 (October 1957).

Table 4.2. Results of Fission-Gas Release-Rate Measurements on UO_2 Pellets

Run No.	Sample Designation	Manufacturer	Pellet Density (% of theoretical)	BET Surface Area (cm^2/g)	Test Temperature (°C)	Test Time (sec)	Isotope Counted	Incremental Fraction Released	Release-Rate Parameter, D' (sec^{-1})
2	2-1	ORNL	94.8	11.2	1400	7 200	Kr^{85}	1.0×10^{-3}	1.5×10^{-11}
						9 000	Kr^{85}	1.1×10^{-3}	6.5×10^{-12}
3	2-1	ORNL	94.8	11.2	1400	3 600	Kr^{85}	1.1×10^{-4}	3.0×10^{-13}
						10 800	Kr^{85}	2.3×10^{-4}	7.0×10^{-13}
						18 000	Kr^{85}	1.9×10^{-4}	7.6×10^{-13}
						25 200	Kr^{85}	1.8×10^{-4}	7.6×10^{-13}
4	2-1	ORNL	94.8	11.2	1600	10 800	Kr^{85}	5×10^{-4}	2.0×10^{-12}
5	GE-H-4	GE	93.6	8.11	1600	10 800	Kr^{85}	2.7×10^{-4}	8.4×10^{-13}
6	GE-H-4	GE	93.6	8.11	1700	10 800	Xe^{133}	3.4×10^{-4}	9.7×10^{-13}
7	GE-H-4	GE	93.6	8.11	1700	10 800	Xe^{133}	2.5×10^{-4}	5.0×10^{-13}
8	1173	ORNL	95	89.3	1600	7 200	Xe^{133}	2.04×10^{-2}	5.0×10^{-9}
9	1173	ORNL	95	89.3	1400	10 800	Xe^{133}	1.39×10^{-2}	1.56×10^{-9}
10	1173	ORNL	95	89.3	1400	3 600	Xe^{133}	1.83×10^{-2}	8.14×10^{-9}
						10 800	Xe^{133}	5.9×10^{-3}	3.73×10^{-9}
						18 000	Xe^{133}	2.4×10^{-3}	1.99×10^{-9}
						25 200	Xe^{133}	2.1×10^{-3}	1.33×10^{-9}
11	1173	ORNL	95	89.3	1200	10 800	Xe^{133}	8.6×10^{-3}	5.97×10^{-10}
12	1173	ORNL	95	89.3	1000	10 800	Xe^{133}	1.28×10^{-4}	1.32×10^{-13}

Some caution must be applied in making comparisons, however, because the calculations of Chapter 2 are based on an average D' over the lifetime of the fuel, whereas the data presented here were obtained from specimens irradiated to low burnups.

It may be seen in Table 4.2 that D' values for samples designated 2-1 and GE-H-4 are orders of magnitude lower than those for samples from lot 1173 at the same temperature. It should also be pointed out that the BET surface areas of the pellets from batch 1173 are approximately an order of magnitude greater than the surface areas of the other pellets. According to the Lustman model the fraction of fission-gas released, f, is proportional to the total surface area. Since D' is proportional to f^2, an order of magnitude increase in the surface area would be expected to produce two orders of magnitude of increase in D'.

Two special runs were made to determine the relationship between time and percentage release. The percentage release of Kr^{85} from pellet 2-1 at 1400°C is shown in Fig. 4.5 as a function of the square root of time. The deviation from linearity in the 1-hr test is attributed to

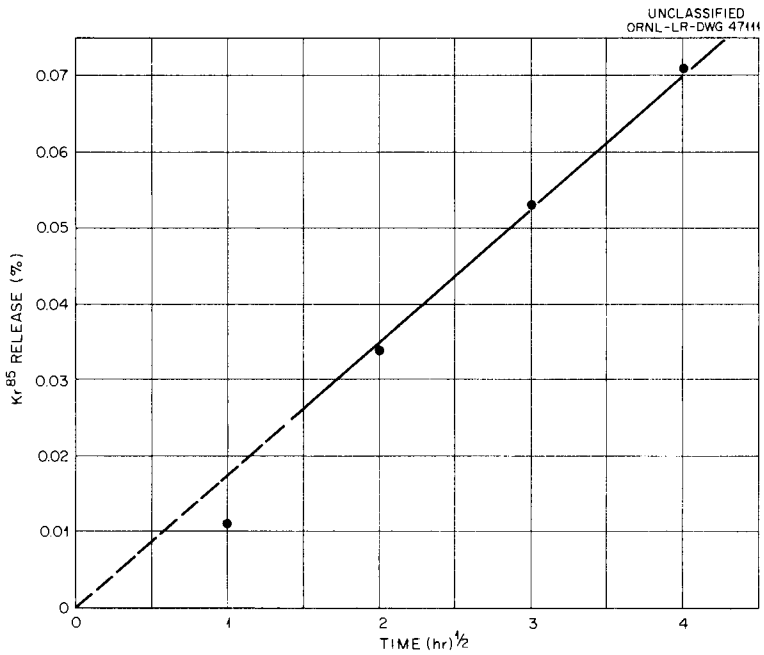

Fig. 4.5. Total Release of Kr^{85} from Pellet 2-1 as a Function of Time at 1400°C.

counting errors. These data are in agreement with the Lustman model. The percentage release of Xe^{133} from a pellet of batch 1173 is shown in Fig. 4.6. These results show an initial rapid rate of release followed by a period in which the square root dependence seems to apply. As a result of the initial rapid release, D' values computed on the basis of the Lustman model are strongly time dependent and decrease with increasing time. Perhaps a better measure of D' for this sample is the final slope of the curve relating percentage release and the square root of time. A value of D' was computed for the pellet of batch 1173 from the final slope of the curve in Fig. 4.6 and was found to be 1.3×10^{-10} sec^{-1} at 1400°C.

In order to obtain a qualitative measure of the other isotopes being released from UO_2 during these tests, samples were taken from the charcoal hot trap and from the tantalum radiation shield. The temperature of the shield at the point where the samples were taken was 500 to 700°C. Isotopes found in the trap were Sb^{125}, Ru^{103}, and Te^{129}. The major activity

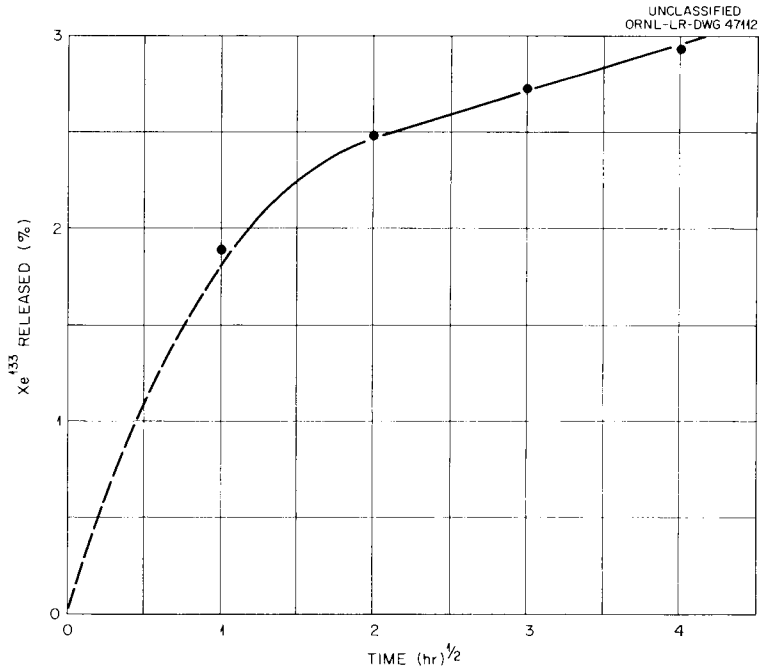

Fig. 4.6. Total Release of Xe^{133} from Pellet 1173 as a Function of Time at 1400°C.

detected on the shield was from Ce^{141}, Ce^{144}, and Cs^{137}, but traces of I^{131}, Ru^{103}, La^{140}, and Ba^{140} were also found. The two UO_2 specimens tested in the apparatus prior to the sampling had 14 months and 9 weeks of decay, respectively, so no short-lived isotopes were present. Similar tests are being run on samples with short decay times.

Graphite Fabrication

The fabrication of high-density low-porosity graphite bodies is being studied, and the fabrication techniques developed will be adapted to the preparation of fueled graphite specimens. Various grades of artificial and natural graphite powder from several sources are being tested with commercial binders and impregnating solutions. The variables being studied include the particle size of the graphite, the ratio of amount of binder to amount of graphite, and the fabrication procedure.

Samples of thermosetting compounds that leave a high carbon residue have been received from three manufacturers for use as binders, and a

number of experiments have been performed on various mixtures of these compounds with graphite powder. The materials were compacted and fired to 1000°C on firing schedules that ranged from 30 to 100 hr. The Durite binder (Borden Company) was mixed with the graphite as a dry powder, but the other binders were added as liquids. The results of these preliminary experiments are presented in Table 4.3.

Table 4.3. Fired Densities of Various Graphite Mixtures Prepared with Natural Graphite Obtained from the Superior Graphite Co. and Designated Superflake 198

Specimen No.	Compacting Pressure (tsi)	Particle Size (mesh)	Average Fired Density (g/cm^3)	Body No. and Composition
5S1	36	-100 +200	1.40	Body 58A containing 500 g of natural graphite and 500 g of Bakelite binder
5S2	36	-200 +325	1.41	
5S3	36	-325	1.46	
5S4	45	-100 +200	1.42	
5S5	45	-200 +325	1.43	
5S6	45	-325	1.46	
5S7	54	-100 +200	1.41	
5S8	54	-200 +325	1.43	
5S9	54	-325	1.48	
5S10	36	-100 +200	1.62	Body 5SB containing 500 g of natural graphite and 400 g of Bakelite binder
5S11	36	-200 +325	1.65	
5S12	36	-325	1.61	
5S13	45	-100 +200	1.61	
5S14	45	-200 +325	1.66	
5S15	45	-325	1.61	
5S16	54	-100 +200	1.64	
5S17	54	-200 +325	1.66	
5S18	54	-100	1.63	
5S19	36	-100 +200	1.87	Body 5SC containing 500 g of natural graphite and 100 g of Bakelite binder
5S20	36	-200 +325	1.90	
5S21	36	-325	1.88	
5S22	45	-100 +200	1.87	
5S23	45	-200 +325	1.90	
5S24	45	-325	1.89	
5S25	54	-100 +200	1.89	
5S26	54	-200 +325	1.90	
5S27	54	-325	1.90	

Table 4.3 (continued)

Specimen No.	Compacting Pressure (tsi)	Particle Size (mesh)	Average Fired Density (g/cm^3)	Body No. and Composition
6S1	26	-100 +200	1.92	Body 6SA containing 500 g of natural graphite and 200 ml of Furacarb P-3 binder
6S2	36	-200 +325	1.96	
6S3	32	-100 +200	1.92	
6S4	45	-200 +325	1.97	
6S5	45	-200 +325	1.96	Body 6SB containing 500 g of natural graphite and 350 ml of Furacarb P-3 binder
6S6	54	-200 +325	1.96	
6S7	45	-325	1.93	
6S8	54	-325	1.93	
8S1	45	-325	1.46	Body 8SA-1 containing 50 g of natural graphite and 50 g of Durite SD-5143 binder
8S2	54	-325	1.48	
8S2a	45	-325	1.61	Body 8SA-2 containing 50 g of natural graphite and 50 g of Durite SD-5143 binder
8S3	36	-325	1.60	
8S5	27	-325	1.64	Body 8SB containing 50 g of natural graphite and 30 g of Durite SD-5143 binder
8S6	36	-325	1.66	
8S7	45	-325	1.67	
8S8	54	-325	1.67	
8S9	27	-325	1.83	Body 8SC containing 50 g of natural graphite and 10 g of Durite SD-5143 binder
8S10	36	-325	1.83	
8S11	45	-325	1.84	
8S12	54	-325	1.84	

The relatively low densities obtained in bodies 5SA, 5SB, and 8SA-1 were the result of heating too rapidly during firing; this was confirmed when body 8SA-2, with the same compositon as 8SA-1, was fired slowly at a rate of ~10°C/hr to a higher density. To eliminate the effects

of rapid firing a standard heating schedule of 10°C/hr has been adopted for future experiments.

This preliminary work indicates (1) that the compacting pressure has little effect on the fired density; (2) that, with the exception of body 5SA, the highest densities are obtained with the intermediate (-200 +325 mesh) particle size; (3) that, with Furacarb P-3 as the binder, changes in the ratio of binder to graphite do not result in changes in density, and (4) that, with other binders, higher densities were obtained with lower percentages of binder. Bodies prepared with Furacarb P-3, a product of the Quaker Oats Co., as the binder have had the highest densities. Experiments with this binder will be continued. Durite SD-5143 showed little promise as a binder when used as a dry powder, so attempts will be made to use it in liquid form. No further work is planned with the Bakelite binder.

As noted in Table 4.3, all the specimens tested thus far have contained Superflake 198 graphite, which is a natural graphite obtained from Superior Graphite Co. The graphite samples obtained thus far from other manufacturers have been found to have ash content far in excess of the specified amounts. Additional samples are being obtained.

The impregnation of graphite bodies with solutions of thermosetting compounds that leave a high carbon residue is also an effective means of increasing the bulk density. A number of experiments were conducted with Furacarb P-3 as the impregnating compound, and the results are presented in Table 4.4.

Reactions of UO_2 with Graphite

The rate of reaction of UO_2 and graphite is being determined as a function of temperature, UO_2 particle size, and pressure. The purpose of this study is to determine the limiting operating temperature of a fuel element consisting of UO_2 or other oxide fuel dispersed in graphite. Tests have been completed at temperatures of 1320 and 1425°C with -325 mesh UO_2 in vacuum.

Table 4.4. Increase in Density of Graphite by Impregnation

Specimen No.	Density Prior to Impregnation (g/cm^3)	Fired Density After Impregnation (g/cm^3)	Number of Times Tested	Increase in Density (%)
3S15	1.51	1.60	2	5.63
3S19	1.50	1.57	2	4.67
3S24	1.57	1.66	2	5.42
4S11	2.04	2.10	2	2.86
4S14	2.05	2.11	2	2.84
4S15	2.03	2.10	2	3.33
6S1	1.92	1.95	1	1.54
6S2	1.96	2.02	2	3.06
6S3	1.92	1.96	1	2.04
6S4	1.97	2.03	2	3.05
6S5	1.96	1.99	1	1.53
6S6	1.96	2.00	1	2.04
6S7	1.93	1.97	1	2.07
6S8	1.93	1.97	1	2.07

The samples used for this study were made by mixing -325 mesh UO_2 particles of greater than 95% theoretical density with graphite flour and phenolic resin; the mixture was then cold pressed and fired to 1000°C under argon. The resulting pellets contained 35 wt % UO_2 and had a graphite density of 1.4 g/cm^3.

For the reaction-rate observations, the samples were heated to the test temperatures in an induction furnace under a vacuum ranging from 5×10^{-4} to 5×10^{-5} mm Hg. The specimen was hung from a sensitive steel spring, and the weight loss was measured continuously. Since one of the reaction products is CO, the weight loss is a direct function of the amount of UO_2 that has been reduced. The major carbide phase present after the samples were quenched from the test temperatures was UC_2, although small amounts of UC were detected. The data obtained thus far can best be fitted by the equation

$$x = kt^{1/2} ,$$

where x is the fraction of UO_2 reduced, k is the reaction rate constant, and t is time. The reaction rate constant, k, has been calculated to be 0.30 ± 0.05 per $hr^{1/2}$ at 1425°C and 0.12 ± 0.03 per $hr^{1/2}$ at 1320°C.

Mechanical Properties of Graphite

Current data from irradiation studies on graphite have demonstrated a contraction rate which is proportional to the dose. Such contraction will produce an accumulation of tensile stresses in the graphite moderator blocks of the EGCR. Therefore the time-dependent mechanical properties of graphite at 750 and 1100°F are being investigated. The test program is directed toward determining whether graphite of the type specified for the EGCR will creep at these temperatures, and, if creep is observed, to determine which creep law is applicable. The time-dependence of the fracture ductility of graphite will also be determined.

Fabrication Development of BeO and BeO-UO_2 Bodies

The materials investigation program for advanced gas-cooled reactors includes studies of low-density (~80% of theoretical), pure BeO as moderator material and high-density (~95% of theoretical) BeO-UO_2 and BeO-UO_2-ThO_2 bodies as fuel element materials. Techniques are being developed for fabricating these materials and for providing specimens complete with physical property data and fabrication history for use in irradiation tests.

The first group of specimens being prepared are small high-density BeO-UO_2 bushings for the determination of fission-gas release upon irradiation in LITR capsules. These specimens are to consist of 54.8 wt % (~25 vol %) UO_2 as a fine-particle dispersion in BeO, and they will be fired to as high a density as possible.

In preliminary fabrication experiments, extruded rods of BeO-UO_2 bowed slightly during isostatic pressing, probably because of nonuniformity in the as-extruded piece. No further deformation occurred during sintering. A bulk density of 95% of theoretical was obtained, although microscopic examination showed a number of small holes in the piece. The holes can

be attributed to air pockets in the extruded piece or to volatilization of agglomerates of binder material. Extruded $BeO-U_3O_8$ rods have been isostatically pressed and are ready for sintering.

Cold-pressed and sintered specimens of $BeO-UO_2$ were low in density (~83% of theoretical). During microscopic examination, a number of large, apparently dense grains of UO_2 were observed that were separated from the matrix by a pocket-like area. The large grains are attributed to UO_2 agglomerates that were not broken during mixing operations and subsequently sintered to a single dense particle.

Specimens of $BeO-U_3O_8$ were cold pressed without a lubricant and sintered but were also of low density (~83% of theoretical). The density was increased to 91% of theoretical, however, by the addition of 2% Carbowax as a lubricant.

Evolution of Lithium From BeO

With the increased interest in BeO as a moderator material, more information is needed concerning the equilibrium concentration of Li^6 produced by the (n,α) reaction. In order to determine the rate of release of lithium from BeO at high temperatures, an experiment is in progress in which beryllia tiles containing approximately 300 ppm lithium are being heated for extended periods of time (1 to 6 months) in a CO_2 atmosphere at temperatures of 850 ± 5°C. The tiles, 4 × 4 × 1 in., were cold pressed and sintered at 850°C. Spectrochemical analyses indicated no change in lithium content during the initial heat treatment. Measurements of the neutron adsorption properties of the tiles will be made in the ORNL Critical Experiments Facility before and after the long-term heat treatment. The results of these measurements will indicate the extent to which lithium is evolved.

As a means of control of the experiment and to obtain additional information, samples are being removed from the heat-treatment equipment at regular intervals for lithium analysis. Changes found in samples heated one, two, and four weeks were within the error of the analyses.

Structural Materials Evaluation

Creep Tests in Various Environments

Creep-rupture tests of type 304 stainless steel in argon, CO, CO_2, hydrogen, air, helium, and nitrogen have been continued. The tests in the various atmospheres are being run at 1500 and 1700°F and at stresses from 1200 to 3500 psi. The results obtained thus far are summarized in Figs. 4.7, 4.8, and 4.9 for test series that have provided sufficient data to warrant comparison. The variations of the data presented in Figs. 4.7 and 4.8 emphasize the preliminary nature of the curves; no conclusive trends in the data can be seen at this time. In most cases the curves are based on data obtained in at least two tests. The creep behavior in argon is used as the reference for comparison of the behavior in other environments.

Environments of both air and pure nitrogen lower the creep rate at 1500 and 1700°F. It is felt that this strengthening is due to the

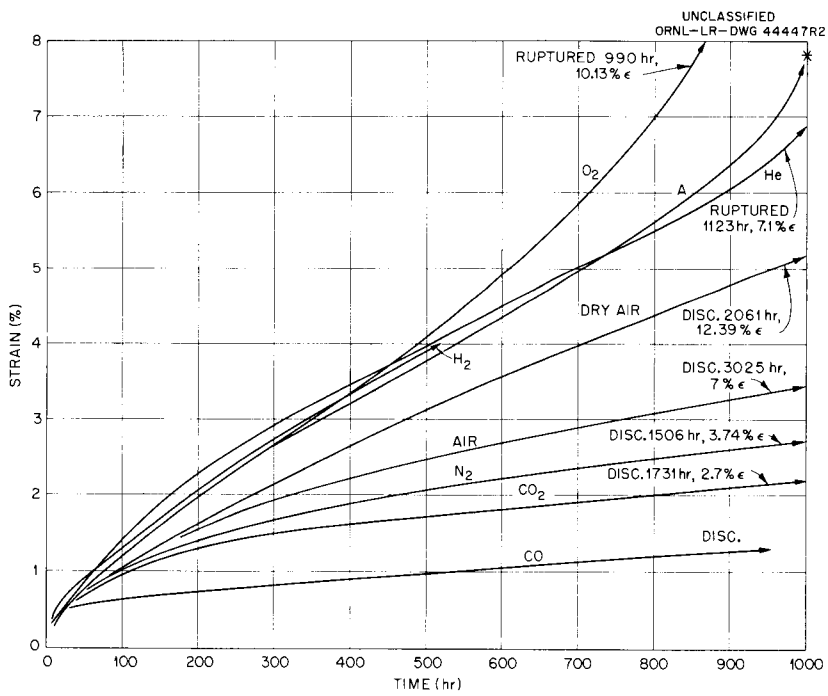

Fig. 4.7. Effect of Environment on the Creep Properties of Type 304 Stainless Steel at 1500°F and 3400 psi.

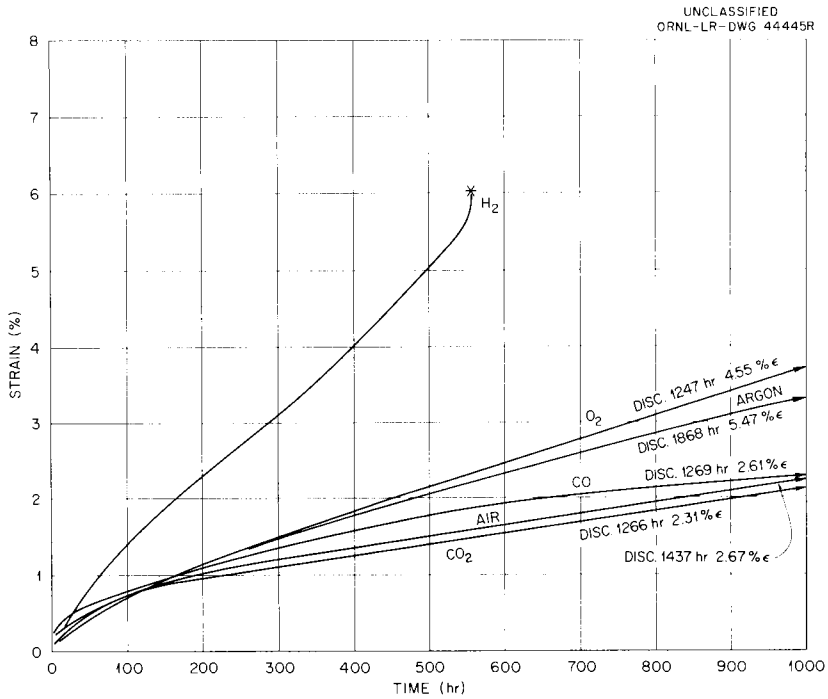

Fig. 4.8. Effect of Environment on the Creep Properties of Type 304 Stainless Steel at 1500°F and 3000 psi.

increased nitrogen content of the material, since an environment of pure oxygen increased the creep rate. A microstructure typical of specimens tested in air and in nitrogen at 1500 and 1700°F is shown in Fig. 4.10. The precipitate has been identified as CrN and Cr_2N. The amount of the precipitate was found to depend on the stress level, the test temperature, and the time of exposure to the test environment. A test run at 1500°F in dried air has indicated that water vapor increases the strengthening effect of an air environment.

As previously reported,[10] specimens tested in CO and CO_2 are carburized and the creep rate decreases. This is illustrated by the analytical data presented in Table 4.5. As discussed in detail in the following section, the CO_2 used in the tests contained approximately 0.1% CO. Removal of this CO by passing the gas over hot copper oxide

[10]"GCR Semiann. Prog. Rep. June 30, 1959," ORNL-2767, p. 109.

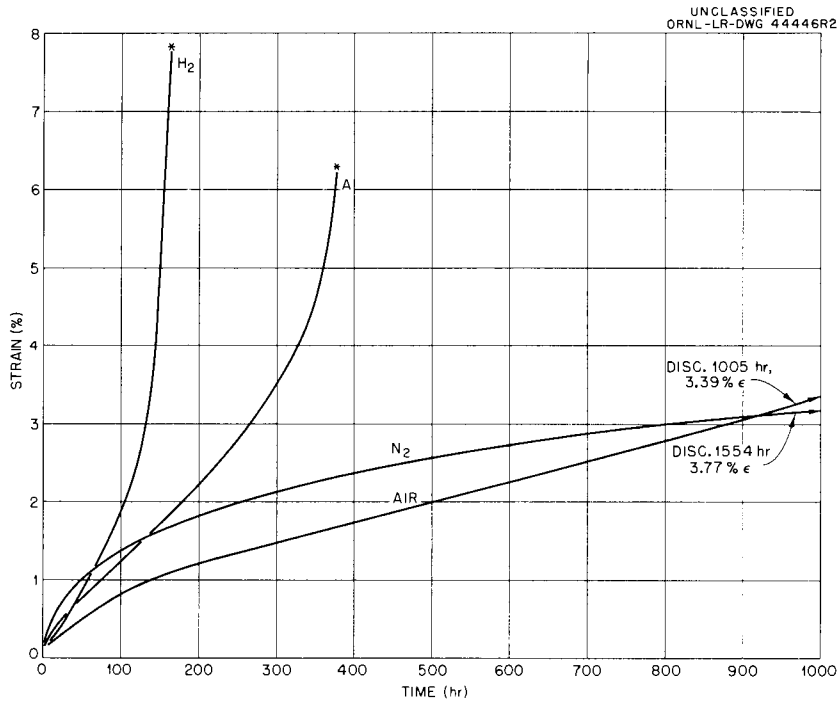

Fig. 4.9. Effect of Environment on the Creep Properties of Type 304 Stainless Steel at 1700°F and 1200 psi.

Table 4.5. Carbon Content of Type 304 Stainless Steel Specimens Creep Tested Under Various Conditions in Flowing CO_2

Specimen History	Carbon Content of Stressed Portion of Sample (wt %)	Carbon Content of Unstressed Portion of Specimen (wt %)
As annealed	0.048	0.048
Tested for 1266 hr at 1500°F and 3000 psi	0.18	0.16
Tested for 1005 hr at 1500°F and 3400 psi	0.18	0.17
Tested for 929 hr at 1500°F and 3400 psi	0.20	0.17
Tested for 1731 hr at 1500°F and 3700 psi	0.21	0.12

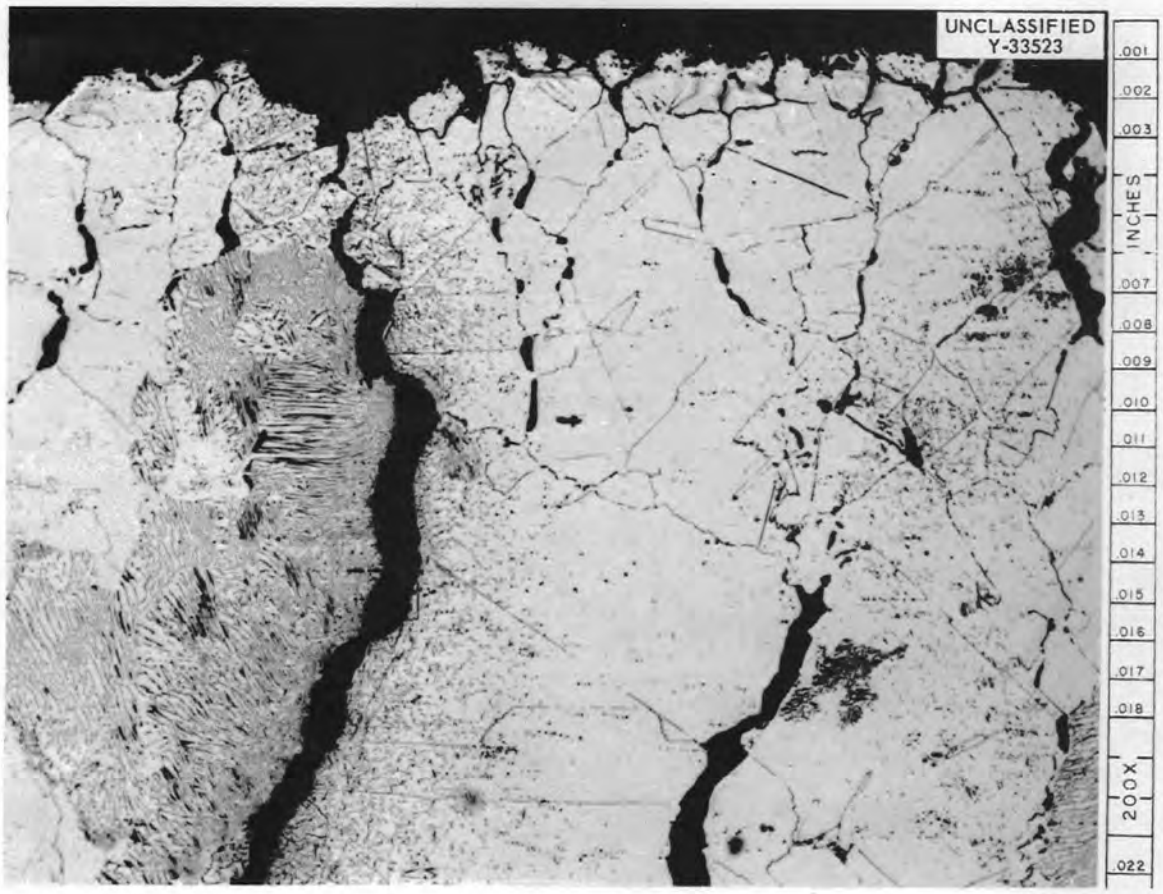

Fig. 4.10. Stressed Portion of Type 304 Stainless Steel Specimen Tested in Air at 1700°F and 2500 psi. Etchant: 10% oxalic acid.

eliminated carburization of unstressed tabs under similar conditions. A creep test currently under way on specimens in a CO_2 environment purified by this procedure indicates a higher creep rate, as shown in Fig. 4.7, and thus carburization is probably not occurring.

The detailed effects of hydrogen on the creep properties of type 304 stainless steel at 1500°F have not been clearly established because of the lack of reproducibility of the test data obtained under these conditions. Hydrogen does, however, adversely affect the creep properties of the material at 1700°F.

The surface characteristics of a series of specimens tested in various environments are described in Table 4.6, based on macroscopic

Table 4.6. Surface Characteristics of Type 304 Stainless Steel Specimens After Creep Tests in Various Environments

Creep Test Environment	Test Temperature (°F)	Microscopic Observations
Hydrogen	1300–1700	Bright, nonmagnetic
CO	1300–1500	Sooty, dark, adherent oxide; slightly magnetic
CO_2	1500	Dark, scaly oxide; magnetic
Air	1300	Dark, adherent oxide; slightly magnetic
	1500–1700	Dark, scaly oxide; strongly magnetic
Oxygen	1500	Dark, scaly oxide; strongly magnetic
Argon (or helium)	1300–1700	Bright, nonmagnetic

examinations. Because of the significant increase in carbon content of specimens tested in CO and CO_2, a limited number of tensile specimens were also tested to investigate the effect of carbon on the ductility of type 304 stainless steel. The specimens tested were 0.060-in.-thick sheet that had been carburized by a variety of treatments. The test results are summarized in Table 4.7.

Although the addition of carbon reduced the strain at rupture, a specimen containing approximately 0.3 wt % carbon still had a ductility of 19% at 1500°F, and the yield strength was increased by a factor of 1.7. Addition of a similar amount of carbon reduced the rupture ductility at room temperature from 83 to 11%.

The tensile properties of a similar series of specimens of 0.020-in.-thick sheet carburized by annealing in CO at 1900°F are summarized in Table 4.8. The first 0.2 wt % carbon added to the specimen reduced

Table 4.7. Tensile Data Showing the Effect of Carbon on the Tensile Properties of Type 304 Stainless Steel Sheet Specimens

Sheet thickness: 0.060 in.
Annealing time: 1 hr
Annealing temperature: 1900°F
Annealing atmosphere: hydrogen

Specimen History	Test Temperature (°F)	Yield Strength (psi)	Tensile Strength (psi)	Elongation (%)	Carbon Concentrate (wt %)
As annealed	Room	26 500	87 100	83	0.048
As annealed	1500	10 500	19 500	35	0.048
Carburized 233 hr in CO at 1500°F	1500	16 800	25 600	37	0.23
Carburized 500 hr in CO at 1500°F	1500	18 400	25 800	25	0.28
Homogeneized 1 hr at 1900°F in argon	1500	17 600	25 100	19	~0.3
Tested in CO_2 for 1727 hr at 3400 psi	Room	25 000	79 900	60	0.093
Tested in CO for 1731 hr at 3700 psi	Room	30 200	81 000	23	0.21
Carburized 233 hr in CO at 1500°F	Room	32 600	76 300	11	~0.2
Carburized 500 hr in CO at 1500°F	Room	34 300	83 900	11	~0.3

the room-temperature rupture ductility from 56.5 to 28.5%. Additional carbon did not cause further reductions of the ductility.

As shown in these tests, the addition of carbon reduces the ductility, but the amount of reduction is not serious. Additional tests are being run to evaluate the effect of carbon on the ductility of type 304 stainless steel when the carbon is added under stress and is more heavily concentrated along the grain boundaries of the material. Failure in these tests will be detected by the propagation of a crack through the material rather than by a fracture.

Table 4.8. Tensile Data Showing the Effect of Carbon on the Room-Temperature Tensile Properties of Type 304 Stainless Steel Specimens Annealed and Carburized by Exposure to CO

Sheet thickness: 0.020 in.
Annealing time: 1 hr
Annealing temperature: 1900°F
Annealing atmosphere: hydrogen
Carburization temperature: 1900°F

Carburization Period (hr)	Yield Strength (psi)	Tensile Strength (psi)	Elongation (%)	Approximate Carbon Content (wt %)
0	26 700	87 200	56.5	0.05
2	36 100	92 600	28.5	0.25
4	36 600	96 600	29.5	0.29
4	34 700	97 300	32.0	0.29
6	36 100	97 900	35.0	0.32
6	34 700	98 600	35.0	0.32
24	35 500	99 200	32.0	0.70
24	36 100	99 100	38.0	0.70

Preliminary tests have been run to determine the effectiveness of a thin copper film in reducing the rate of carburization of type 304 stainless steel in CO and CO_2 environments, in case it is found to be desirable to avoid carburization. Tests in which no stress was applied look quite promising.[11] The effects of stress are indicated in Figs. 4.11, 4.12, and 4.13, which show a specimen with a 0.001-in.-thick copper film after more than 1000 hr in CO at 1300°F and a stress of 9500 psi. Although considerable carburization occurred at the point of rupture, only a small amount of carburization was detected along the rest of the gage length of the test specimen. The film on the unstressed portion of the specimen remained intact, and no carburization was found by metallographic examination. The effectiveness of the copper film is also demonstrated by the fact that the creep curve of this specimen was almost identical with that observed for

[11] "GCR Quar. Prog. Rep. Sept. 30, 1959," ORNL-2835, p. 85.

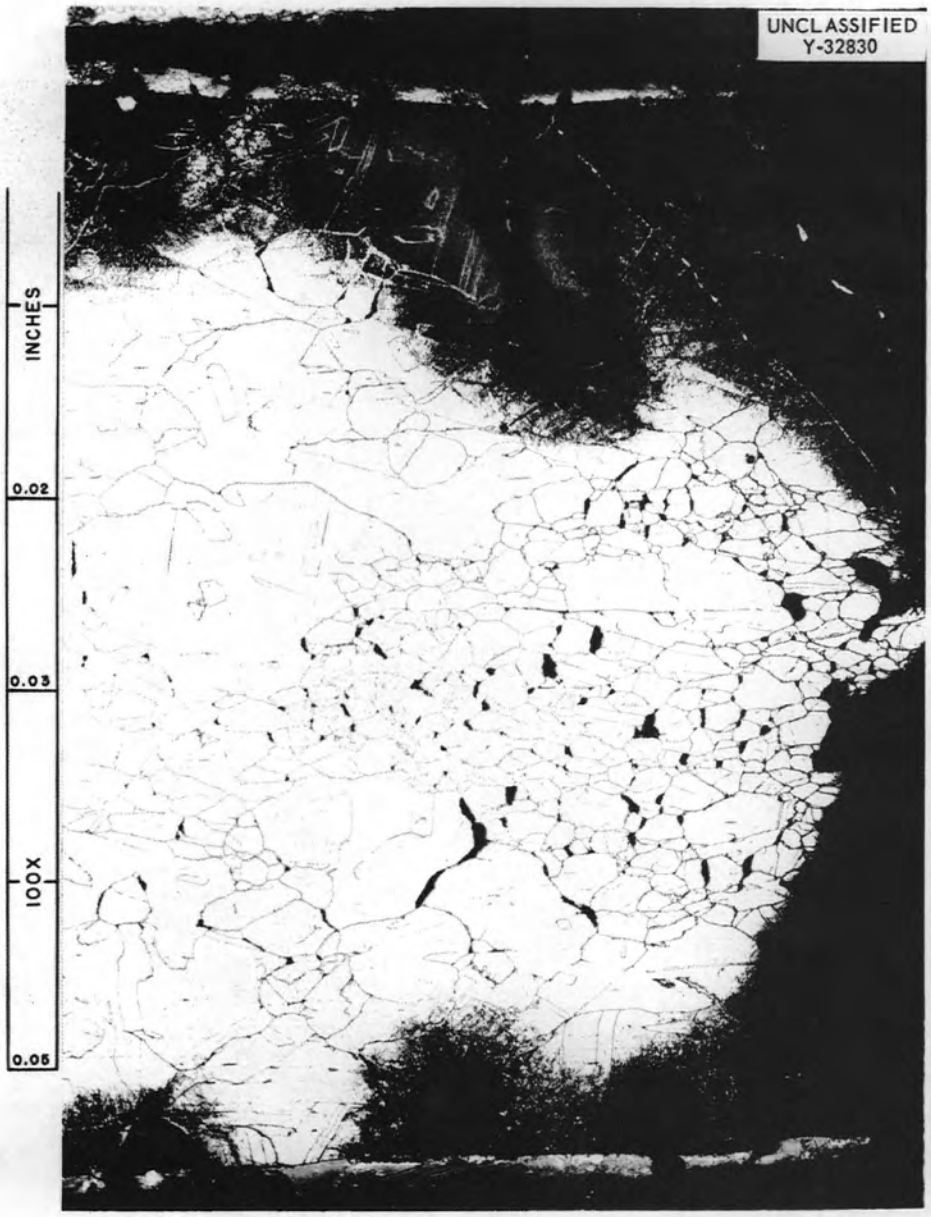

Fig. 4.11. Copper-Plated Type 304 Stainless Steel Specimen That Was Tested in CO at 1300°F for 1000 hr Showing Effect of Rupture of Plating. Etchant: 10% oxalic acid.

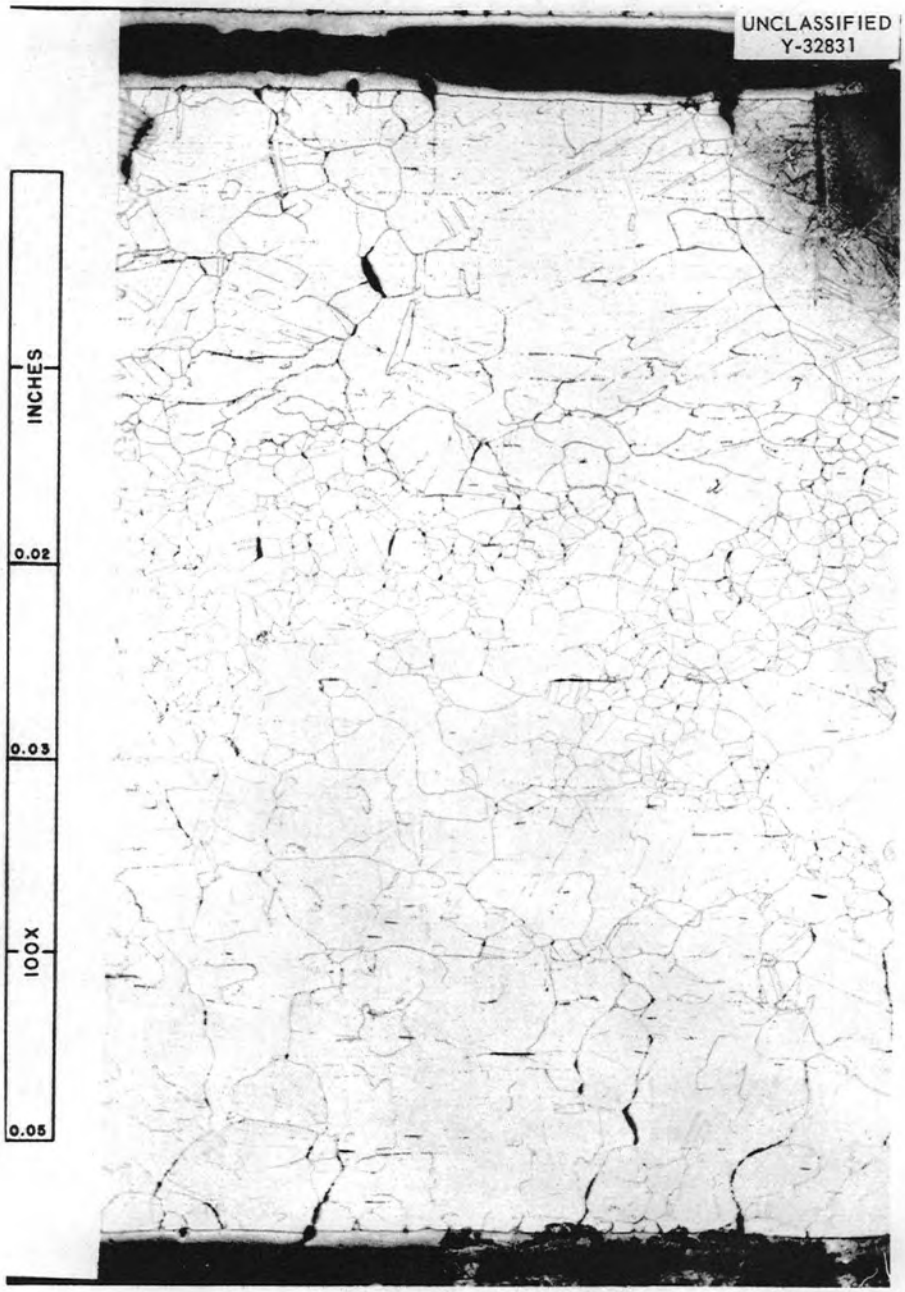

Fig. 4.12. Edge of Stressed Portion of Copper-Plated Type 304 Stainless Steel Specimen Tested in CO at 1300°F for 1000 hr at a Stress of 9500 psi. Etchant: 10% oxalic acid.

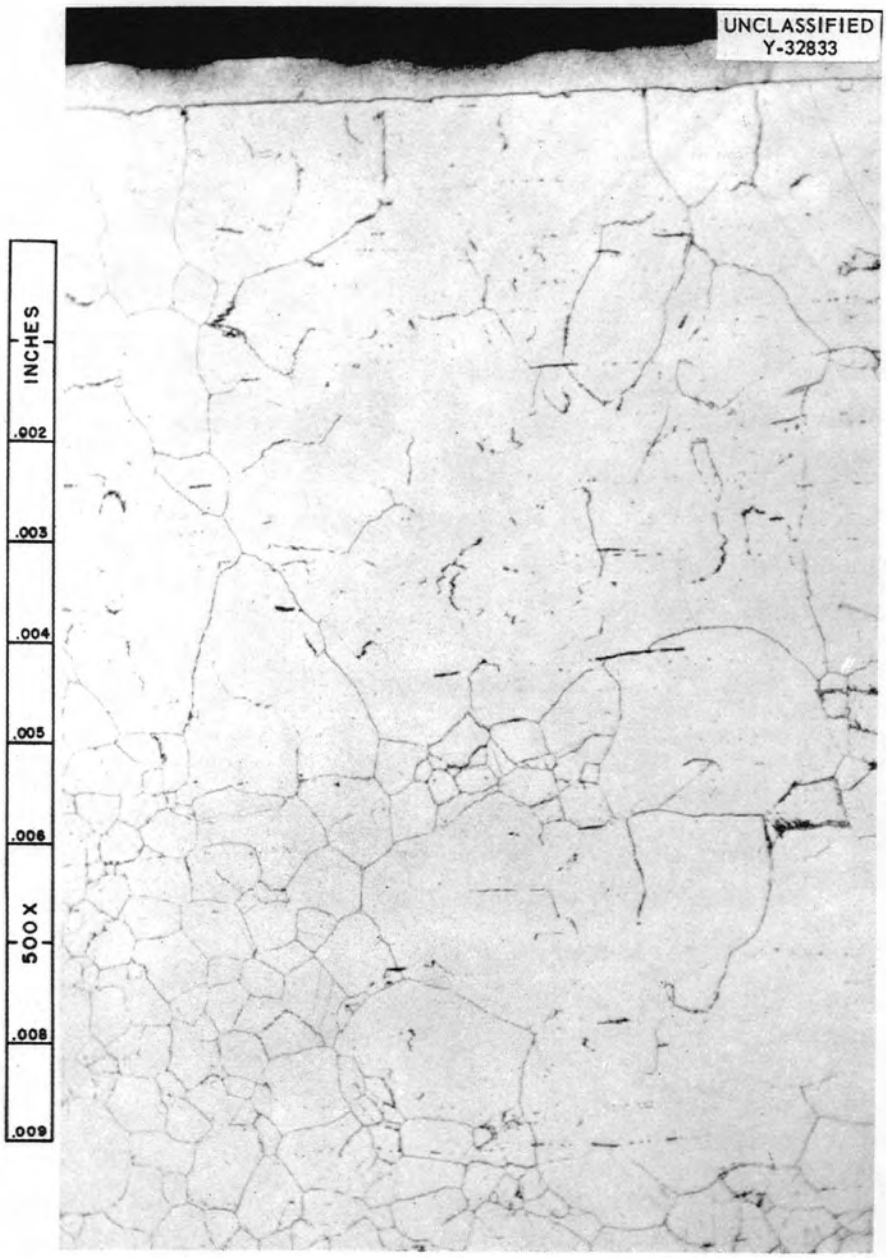

Fig. 4.13. Edge of Unstressed Portion of Copper-Plated Type 304 Stainless Steel Specimen Tested in CO at 1300°F for 1000 hr. Etchant: 10% oxalic acid.

an unplated specimen tested in argon at the same stress and temperature.

On the basis of these tests it is felt that the environments present in the EGCR will not adversely affect the creep properties of type 304 stainless steel. The environments will be carburizing and oxidizing and will reduce the creep rate of the material. Although these processes will also reduce the ductility, it is felt that the extent of this effect will not be serious.

Reactions of Type 304 Stainless Steel with CO and CO_2

Tests in Flowing CO_2. It was reported previously[12,13] that carburization occurred on type 304 stainless steel specimens exposed to flowing CO_2 at 1500°F. Analysis of the gas used in the tests indicated that it contained approximately 0.1 vol % CO. In subsequent tests, in which the CO was removed by passing the test gas over hot copper oxide, no detectable carbon pickup occurred during a 1500-hr exposure. The tests with a small amount of CO present more closely simulate reactor conditions, however, and the results illustrate the very low CO-to-CO_2 ratio at which carburization may occur.

Reactions in Flowing CO. Type 304 stainless steel specimens tested at 1500°F in flowing CO at a pressure of 1 atm showed high initial rates of weight gain and subsequent rapid losses in weight. The rate of weight loss decreased in a period of approximately 24 hr, and subsequent weight changes were very small. Carbon analyses indicated that the carbon concentration of the sample followed a pattern similar to the weight loss pattern. The losses in carbon content and total weight may have resulted from a reaction between the surface oxide and the carbon present in the sample to form free metal and CO. The adherent graphite layer formed on the specimen surface may have prevented free access of CO from the test environment to the specimen surface and thus made the conditions favorable for the reaction. The possibility of removal of the surface oxide film

[12]"GCR Semiann. Prog. Rep. June 30, 1959," ORNL-2767, p. 109.

[13]"GCR Quar. Prog. Rep. Sept. 30, 1959," ORNL-2835, p. 85.

during thermal cycling and therefore the recurrence of an initially high reaction rate upon reheating is being investigated.

Mechanism of Reactions with CO_2. The study of the reactions of type 304 stainless steel with CO_2 has continued. It was reported previously that CO_2 is oxidizing and possibly decarburizing to the metal at elevated temperatures.[14] The oxidizing reaction results in the formation of oxides with the compositions $3Cr_2O_3 \cdot Fe_2O_3$ and $FeO(NiO) \cdot Cr_2O_3$. Additional tests have confirmed the decarburizing tendencies of CO_2.

In the course of these studies it was found that the reaction rates were essentially independent of the CO_2 concentration in the pressure range from 10 to 6000 μ Hg (approximately 0.001 to 0.6 vol %). The reaction rate at 1400°F in CO_2 at a pressure of 10 μ can be described by the equation

$$\Delta X = 9.46 \times 10^{-3}\ t^{0.64} \quad ,$$

where ΔX is weight gain in mg/cm^2 and t is time in hours. A comparison of the data with those reported by other workers,[15,16] whose tests were conducted at pressures up to 100 psi CO_2, showed that the reaction rates at the higher pressures were an order of magnitude lower than reported here. In view of this apparent discrepancy, it was concluded that the intermittent weighing technique might be in error. This conclusion is based upon numerous tests in which the stainless steel samples showed weight increases greater than 0.3 mg/cm^2 when weighed at temperature and exhibited very slight weight gains or even weight losses by the "before-and-after" weighing technique. Spalling of the oxide was found to be responsible for the discrepancy.

---

[14]"GCR Semiann. Prog. Rep. Dec. 31, 1958," ORNL-2676, pp. 86–87.

[15]S. R. Billington, C. G. Stevens, and M. W. Davis, "The Oxidation of Four Austenitic Stainless Steels and the Nickel Alloy Inconel in Carbon Dioxide," GCM/UK/16 (January 1960).

[16]"Studies on the Compatibility of High Temperature Carbon Dioxide with Stainless Steels and Other Materials (Preliminary Report)," GNEC-121 (December 17, 1959).

Further evidence of the spalling of the oxide from stainless steel is shown in Fig. 4.14, which is a record of the weight changes that occurred when a test specimen was being cooled to room temperature. The apparent weight gain of the specimen in this test was 0.04 mg/cm^2. The uniform loss of oxide shown by the curve indicates that the spalling was due to stresses developed between the oxide and base metal, probably as a result of phase transformations in the oxide film.

Reactions with CO-CO_2 Mixtures. The double thermal-convection loop described previously[17] for use in studying the reactions has been modified to some extent and is being operated with mixtures of CO and CO_2. It was found in a test in which the type 304 stainless steel specimen were exposed to CO and CO_2 at a ratio of 10:1 that control of the concentration of impurity gases at low amounts is feasible for extended test periods. In the test the gas composition was originally determined by the temperatures of the generating chemicals, but it gradually approached the theoretical equilibrium concentrations in flowing gases. It is of interest

[17] "GCR Quar. Prog. Rep. Sept. 30, 1959," ORNL-2835, p. 82.

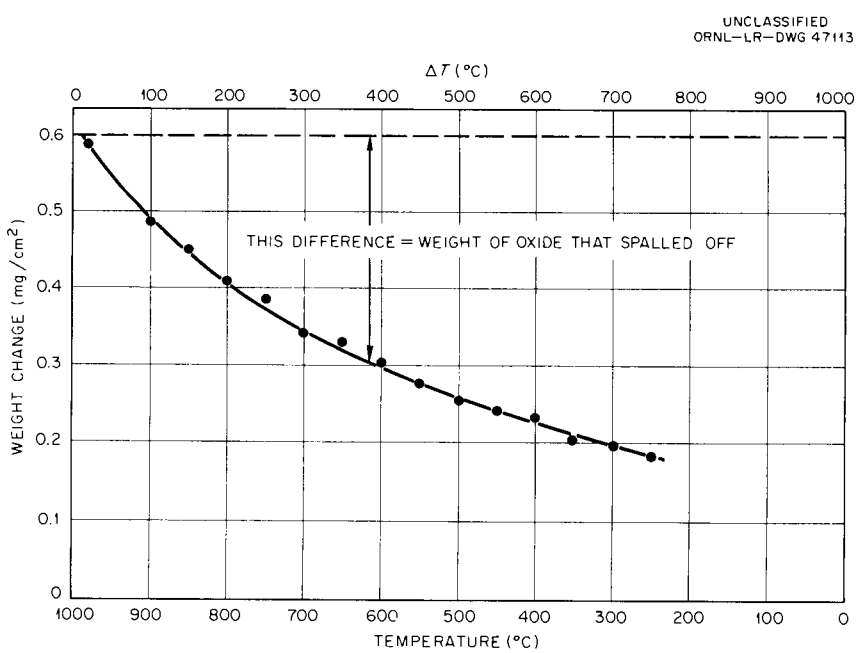

Fig. 4.14. Weight Change of Oxidized Type 304 Stainless Steel as a Result of Oxide Spalling During Cooling from 1000°C to Room Temperature.

to note that, at a temperature of 600°C, a 200-hr period was required for the reaction of CO_2 with graphite to reach equilibrium. Equilibrium was attained within 24 hr, however, when cast iron was used as the source of graphite. The observations indicate that contamination of graphite with iron may accelerate its reaction with CO_2.

Mechanical Property Studies of Structural Materials

Tube-Burst Tests. Studies are continuing on the effect of differential pressure, temperature, and environment on the time to rupture of seamless, 0.020-in.-wall, type 304 stainless steel capsules. The data obtained for as-received material tested in air were summarized previously.[18] Because of the metallurgical changes in the capsule material during brazing of the mid-plane spacer, portions of the tube-burst test program are being repeated to obtain realistic design data. The results obtained thus far for annealed material are presented in Table 4.9.

After tests were completed on material annealed at 2150°F for 2 hr, metallographic examinations revealed that the specimens contained several areas with very large grains, some of which extended completely across the wall of the tube. An example of this condition is shown in Fig. 4.15. The areas with large grains spiraled around the tube in the same manner as the marks left from the straightening operation, and thus it appears that the cold work remaining from the straightening operation causes abnormal grain growth when the material is annealed under the above conditions. It was also found that cracking occurred only in the areas containing the extremely large grains. The normal fine-grained microstructure of the tube wall is shown in Fig. 4.16.

The times to rupture being obtained in these out-of-pile tests give a scatter band that includes the results previously reported[18] for four in-pile tube-burst tests of type 304 stainless steel. It should be pointed out, however, that the in-pile specimens were fabricated from a different heat of material and were only 2 1/2 in. long, whereas the

[18]"GCR Quar. Prog. Rep. Dec. 31, 1959," ORNL-2888, p. 78.

Table 4.9. Results of Burst Tests of Type 304 Stainless Steel Seamless Tubes at 1500°F

Specimen Heat Treatment Prior to Testing	Test Environment	Tangential stress (psi)	Time to Rupture (hr)
Annealed at 2150°F for 2 hr in hydrogen	Argon	5500	66
Annealed at 2150°F for 2 hr in hydrogen	Argon	5500	95
Annealed at 2150°F for 2 hr in hydrogen	CO	5500	90
Annealed at 2150°F for 1/2 hr in hydrogen	Air	3378	933
Annealed at 2150°F for 1/2 hr in hydrogen	Air	5042	94
Annealed at 2150°F for 1/2 hr in hydrogen	Air	6750	10
Annealed at 2150°F for 1/2 hr in hydrogen	Argon	5066	474
Annealed at 1950°F for 1/2 hr in hydrogen	Argon	5500	210
Annealed at 1950°F for 1/2 hr in hydrogen	Argon	5500	264
Annealed at 1950°F for 1/2 hr in hydrogen	CO	5500	614
Annealed at 1950°F for 1/2 hr in hydrogen	CO	5500	505

out-of-pile specimens have all been 6 in. long. Two additional out-of-pile tests have been conducted at 1500°F with specimens from the same heat of material and with the same dimensions as the in-pile specimens. The results indicate that the out-of-pile time to rupture is about twice the in-pile time to rupture. Standard 6-in.-long specimens prepared from the in-pile test material are currently being tested to determine whether the differences in the time to rupture are due to the specimen geometry or to variations in heats of material.

Fig. 4.15. Microstructure of Cold-Worked Type 304 Stainless Steel Tube-Burst Specimen Annealed at 2150°F for 2 hr Prior to Testing. Note that fracture is in area with extremely large grains. Etchant: 10% oxalic acid.

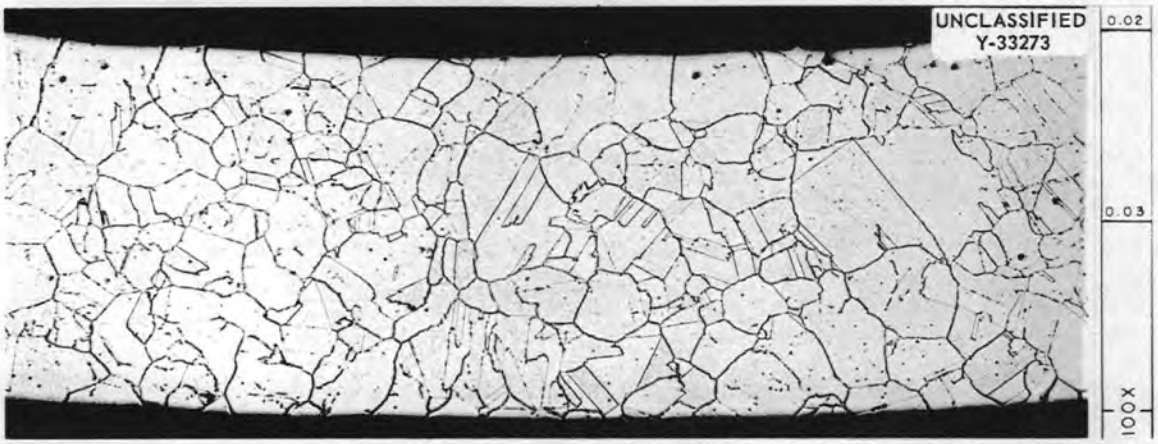

Fig. 4.16. Normal Microstructure of Unworked Type 304 Stainless Steel Tube-Burst Specimen Annealed at 2150°F for 2 hr. Etchant: 10% oxalic acid.

Thermal-Cycling Tests. The study of the effect of temperature transients on the behavior of capsule material has continued. Tubular specimens (3/4 in. o.d., 0.020 in. wall) without inserts were annealed at 2150°F for 2 hr and were cycled between 1000 and 1600°F with a 2-hr hold time at the higher temperature. After 117 cycles at a heating rate of 100°F/min, one specimen was bowed and wrinkled. The specimen length

increased by 0.84%. Another specimen subjected to 10 cycles at a cycling rate of 250°F/min increased in length by only 0.05%.

Pressure-Vessel Steel Investigations

Studies of Weld Zones. The impact behavior of synthetic weld-heat-affected zones on type SA-212, grade-B, steel plate is being studied as part of a subcontract at the Rensselaer Polytechnic Institute. The specimens being tested are subjected to the same thermal treatment as typical areas of welds. The impairment of the impact properties of Charpy V-notch specimens cycled to a peak temperature of 2400°F as compared with specimens cycled to 1400°F at an energy input of 50 kj/in. was reported recently.[19]

Additional studies have been conducted at RPI on specimens that were prepared by using an energy input of 50 kj/in. to simulate the weld heating and then stress relieved at 1150°F. The effects of various thermal cycles on the impact strength of type SA-212, grade-B, carbon steel in heat-affected zones are summarized in Fig. 4.17. The mid-energy-range transition temperatures for the impact-strength curves shown in Fig. 4.17 are listed in Table 4.10. Various specimens have been examined metallographically, and it has been found that the microstructures help to explain the changes in notch toughness resulting from the various heating and cooling cycles. Specimens cycled to 1400°F at 50 kj/in. (without stress relief) showed an improvement in the notch toughness as a result of refinement of the grain size. The pearlite grains transformed completely into small grains of austenite upon heating to 1400°F. Also, the ferrite grains became smaller as a result of partial solubility in the austenite at 1400°F. During cooling, the small grain size and the low austenitizing temperature effectively caused early transformation of the austenite to the soft and ductile transformation products (fine-grained ferrite and pearlite). The microstructures of the original

[19]Ibid., pp. 82–84.

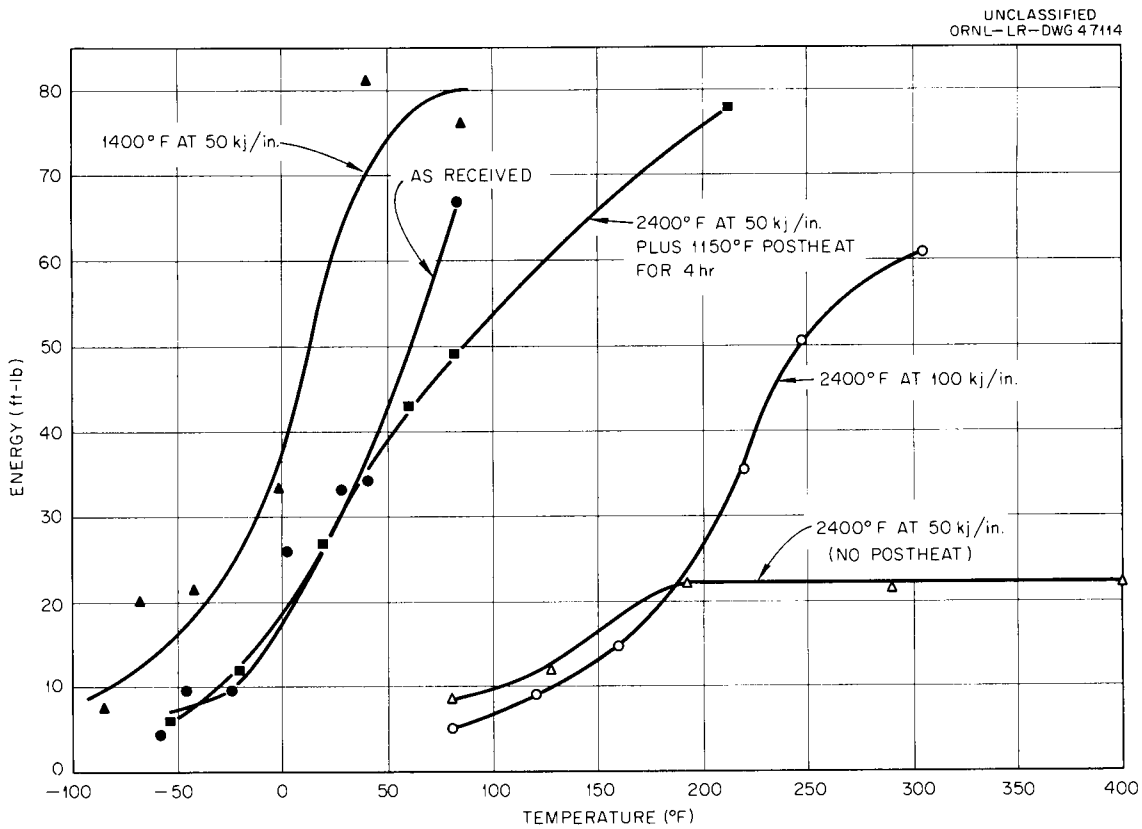

Fig. 4.17. Charpy V-Notch Impact Strength of ASTM Type SA-212, Grade-B, Carbon-Silicon Steel Cycled to 1400°F Using 50 kj/in. and 100 kj/in. Energy Inputs.

as-received material and of a specimen cycled to a peak temperature of 1400°F are shown in Fig. 4.18.

Specimens cycled synthetically to 2400°F with an energy input of 50 kj/in. developed a very coarse-grained mixed structure containing primarily martensite, with ferrite, pearlite, and possibly some bainite, as shown in Fig. 4.19a. The large grain size and the high austenitizing temperature apparently shifted the T-T-T diagram to the right, and thereby permitted sufficient time for martensite to form as a considerable portion of the transformation products. In addition, the low energy input of 50 kj/in. caused the cooling rate to be relatively rapid. Charpy V-notch specimens with this structure were comparatively brittle, having a maximum inpact strength of 22 ft-lb and a shear value of only

UNCLASSIFIED
PHOTO 49640

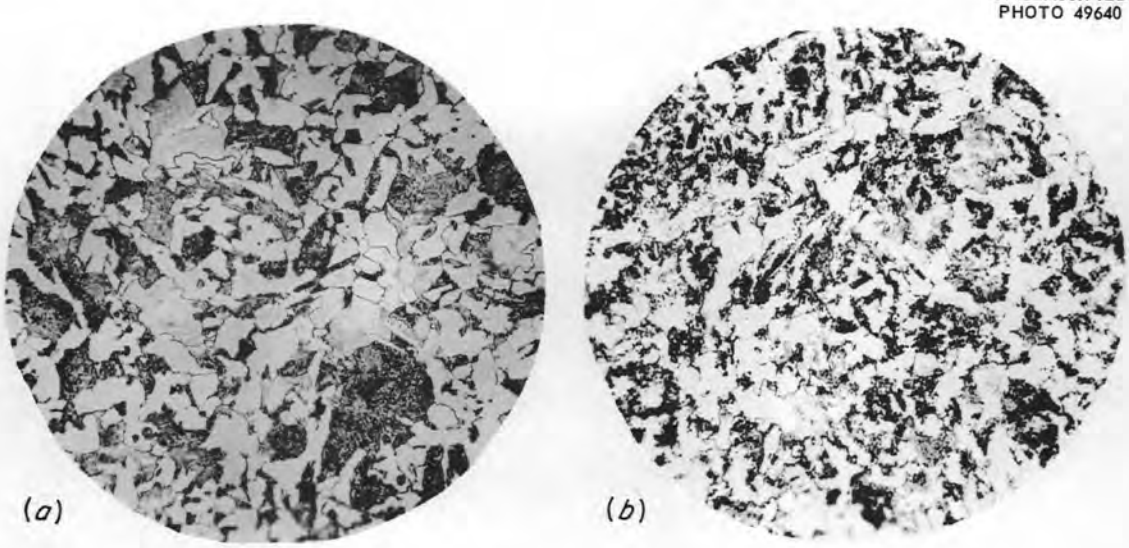

Fig. 4.18. Microstructure of Type SA-212, Grade-B, Carbon-Silicon Steel in (a) As-Received Condition and (b) After Being Thermally Cycled to 1400°F with an Energy Input of 50 kj/in. 500X. Etchant: nital.

UNCLASSIFIED
PHOTO 49641

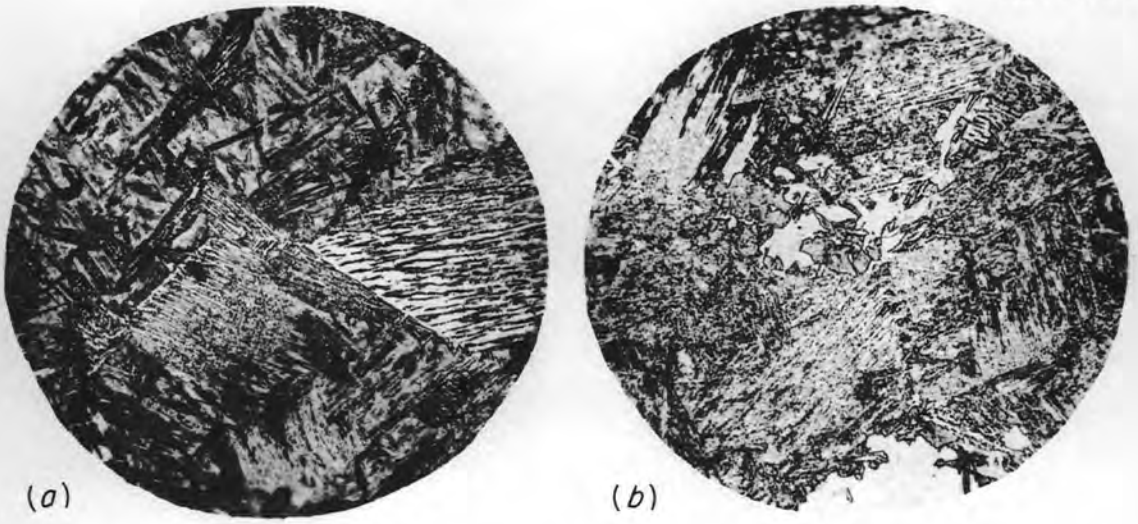

Fig. 4.19. Microstructure of Type SA-212, Grade-B, Carbon-Silicon Steel (a) Cycled to 2400°F Using an Energy Input of 50 kj/in. and (b) Cycled to 2400°F Using 50 kj/in. Energy Input Followed by Postheating at 1150°F for 4 hr. Structure in (a) shows ferrite, pearlite, and, primarily martensite material. Structure of (b) is similar to that of (a) except that the martensite material is tempered. 500X. Etchant: nital.

Table 4.10. Transition Temperatures of Type SA-212, Grade-B Steel Specimens with Synthetic Heat-Affected Zones

Thermal Cycle		Mid-Energy-Range Transition Temperature (°F)	Remarks
Peak Temperature (°F)	Energy Input (kj/in.)		
As-received		30	
1400	50	5	
2400	50	150	Ductile portion of impact curve occurred at only 22 ft-lb, with 25% shear
2400 (stress-relieved at 1150°F for 4 hr)	50	50	
2400	100	205	

25% in the ductile or high-temperature portion of the impact curve. However, when specimens having this structure were stress relieved at 1150°F for 4 hr, the martensite was tempered as shown in Fig. 4.19b, thereby reducing the hardness. The notch toughness of the resulting structure approached that of the as-received plate.

Cycling of specimens to 2400°F with an energy input of 100 kj/in. produced a very coarse-grained austenite and a slower cooling rate than obtained when using an energy input of 50 kj/in. The transformation products formed, as shown in Fig. 4.20, were essentially ferrite and pearlite, which are characteristic of slow cooling. The ductile portion of the impact curve was improved, but the transition temperature was still high. The effect of a stress-relief anneal on the transition temperature will be determined.

The tests conducted thus far show that structures having unsatisfactory notch toughness in the heat-affected zone are produced during welding. However, the impact properties of these structures can be improved by heat treatment after welding. Additional studies are being

Fig. 4.20. Microstructure of Type SA-212, Grade-B, Carbon-Silicon Steel Cycled to 2400°F Using an Energy Input of 100 kj/in. Structure shows very coarse-grained ferrite and pearlite material characteristic of slow cooling from just below the fusion temperature. 500X. Etchant: nital.

conducted to determine a welding procedure which will produce microstructures having acceptable impact properties.

Drop-Weight Tests on Parent Plate. The studies on drop-weight specimens prepared from the type SA-212, grade-B, steel plate are continuing. Twenty-eight longitudinal drop-weight plates from the surface, mid-section, and one-quarter thickness of a 4-in.-thick plate have been machined and welded with a crack-starter weld bead. The information obtained from the tests completed thus far indicates that the NDT (nil-ductility transition) temperature of specimens from the surface is approximately 15°F, as reported previously,[19] and that the NDT temperature of specimens from the mid-section is about 30°F. The tests indicate no significant differences between the NDT temperatures in the longitudinal and transverse directions.

Manufacturing and Inspection Methods

Fabrication of EGCR Fuel Elements

The assembly of 50 prototype fuel elements was undertaken, as mentioned previously,[20] in order to determine the fabricability of the design and to obtain a realistic estimate of the labor and component costs. The first 25 fuel elements were fabricated in the Welding and Brazing Laboratory of the Metallurgy Division. An end view of the fuel element is shown in Fig. 4.21, and Fig. 4.22 shows the arrangement of mid-plane spacers in a cutaway section of the graphite sleeve. The components of the fuel element, shown in Fig. 4.23, were inspected prior to assembly, and all closure welds were inspected by dye-penetrant, x-ray, and mass-spectrometer helium leak tests prior to final assembly.

The approximate time that would be required in a pilot plant production run for each step of the assembly, exclusive of intermediate setup and inspection time, is indicated below:

	Time per Element (min)
Cleaning tubes	7
Preplacing alloy for brazing	28
Brazing	28
Welding bottom end caps	27
Loading fuel	7
Dry-box assembly and welding	35
Element assembly	30
	162

It should be noted that excessive time is involved in the brazing alloy preplacement operation. This operation can be simplified greatly by preplacement of the alloy in the form of rings rather than as a powder slurry. Vendors are currently being contacted to determine the availability of rings of the GE No. 81 alloy selected for this use.

[20] "GCR Quar. Prog. Rep. Dec. 31, 1959," ORNL-2888, pp. 84–90.

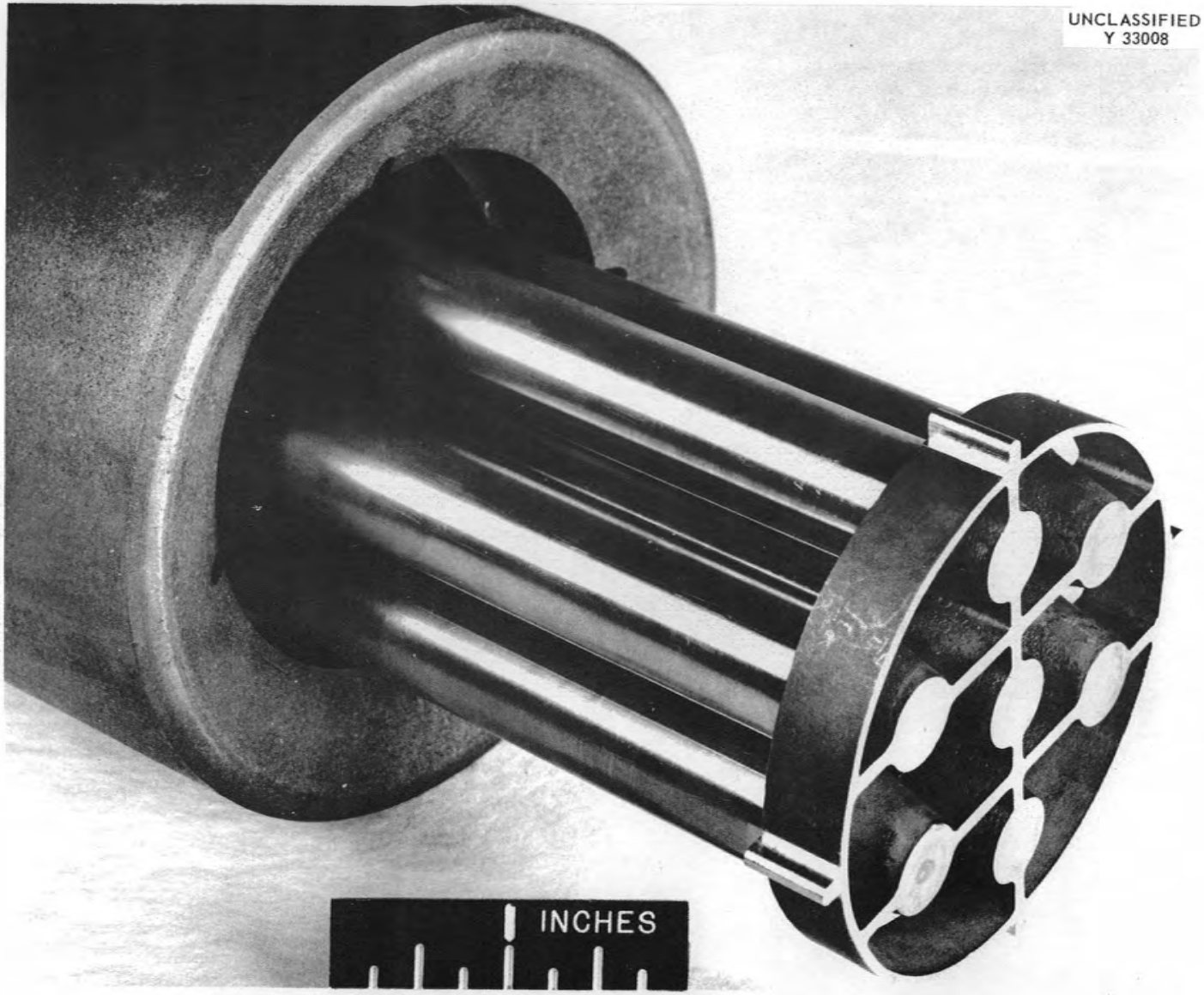

Fig. 4.21. EGCR Fuel Element.

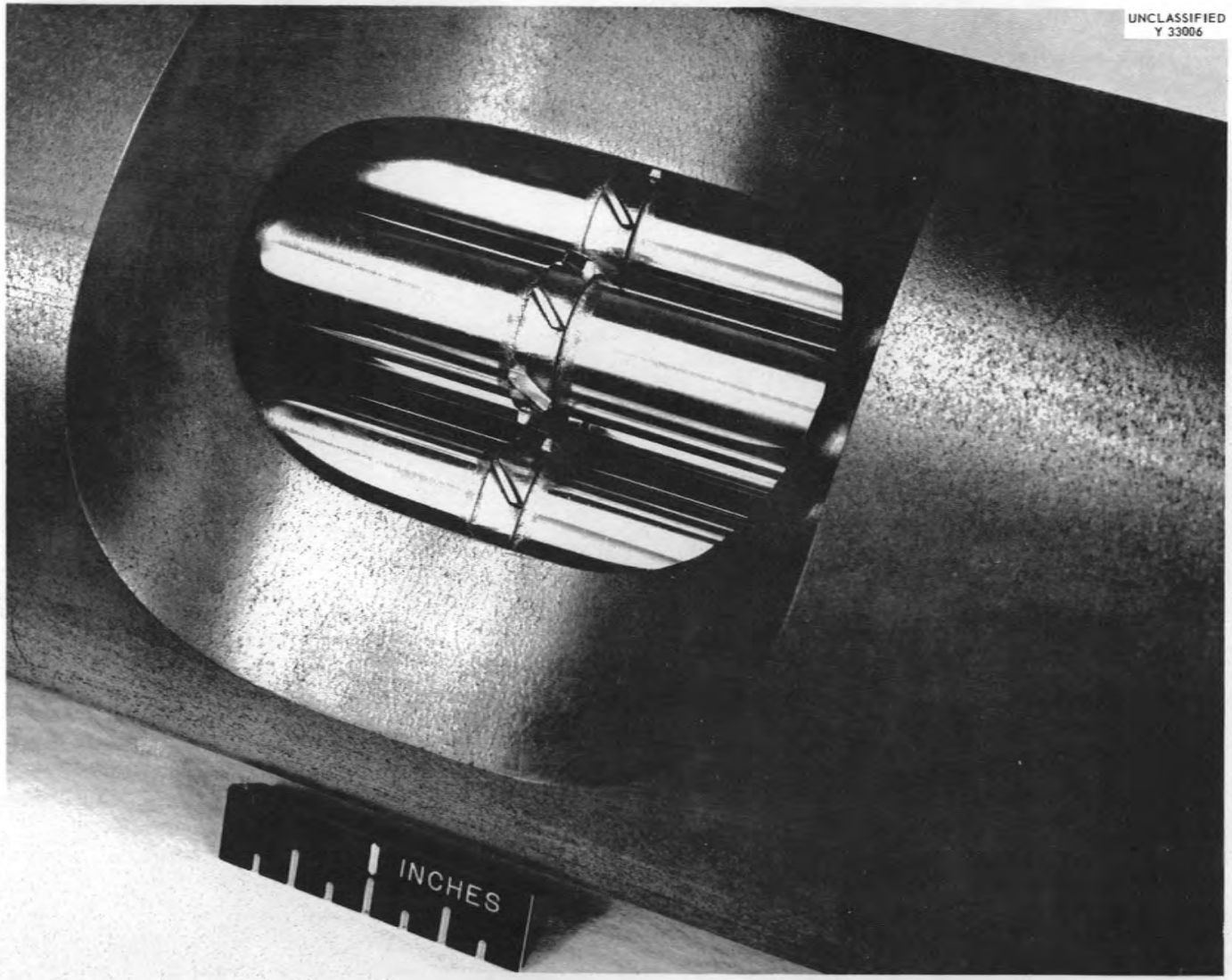

Fig. 4.22. Mid-Plane Spacer Arrangement on EGCR Fuel Element.

UNCLASSIFIED
Y 33141

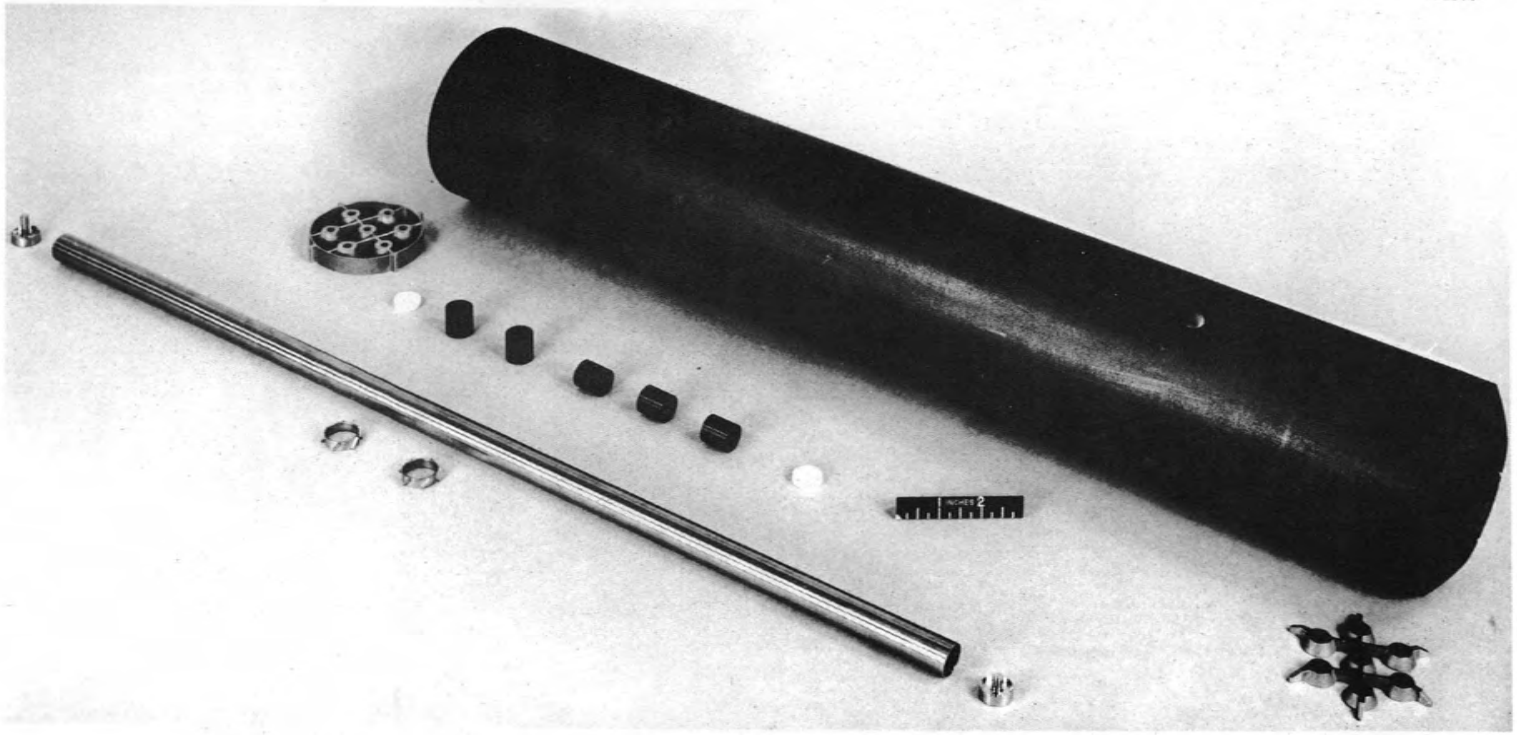

Fig. 4.23. Unassembled Parts of EGCR Fuel Element.

The first 100 mid-plane spacers were brazed in a Globar type of furnace in a dry hydrogen atmosphere. Subsequent experiments indicated, however, that a more satisfactory braze could be obtained by using induction heating in a helium atmosphere. The latter process, which could be carried out in the same amount of time, essentially eliminated distortion of the tube during the brazing cycle. The induction brazing also limited the grain growth in the tube to the immediate vicinity of the mid-plane spacer. The deleterious effect of abnormal grain size on the creep properties of capsule tubing was discussed above.

The fuel elements were welded in the inert-atmosphere chamber in order to provide the specified helium atmosphere inside the capsules. The positioning apparatus is shown in Fig. 4.24. It was found that the fuel capsules for three or four fuel elements could be conveniently handled in the chamber at one time. The welds made in the inert-atmosphere chamber were of high quality and integrity.

Fabrication of the first 25 units was carried out without difficulty on a routine basis. Assembly of the remaining 25 fuel elements is being

UNCLASSIFIED
Y 48816

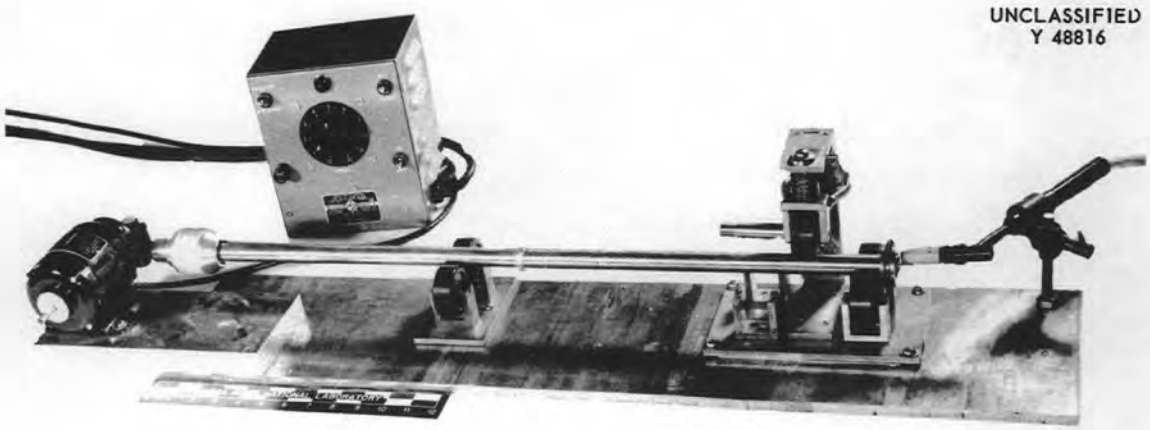

Fig. 4.24. Positioning Apparatus for Welding Fuel Elements in the Inert-Atmosphere Chamber.

done in the Welding and Brazing Specialty Shop of the Engineering and Mechanical Division in order to obtain a better evaluation of typical vendor techniques. A preliminary manufacturing procedure was prepared, and the jigs and fixtures, along with the components for the remaining 25 elements, were transferred to the shop. All tubes were supplied with the mid-plane spacers brazed in place, since induction brazing facilities are not available in the Specialty Shop and studies of the induction-brazing cycle are still under way.

Component Evaluation. Much of the developmental work on procedures for the nondestructive evaluation of EGCR fuel element components has been described previously.[20] The proposed inspection techniques have been used for evaluation of a number of components and closure welds, and a summary of the inspection results is presented here.

Fluorescent penetrant inspection was applied to 475 top caps, 574 bottom caps, and 598 helical spacers, and there were no rejections. Some flaw indications were noted, but further evaluation proved the items to be acceptable. Fluorescent penetrant inspection was also applied to 95 top spiders and 56 bottom spiders. Two top spiders were rejected because of the presence of crack-like indications. Further examinations of these flaw indications are in progress. Radiographic examination was applied to all the spiders, and small amounts of acceptable porosity were the only discontinuities detected.

Six hundred lengths of tubing were examined by eddy-current, penetrant, resonance- and pulse-echo-ultrasonic, visual, and air-gage techniques. Total rejection included 99% by eddy-current inspection (eventually waived), 2% by penetrant inspection because of outer-surface defects, 5% by resonance-ultrasonic inspection for excessive wall thickness, and 4% by air-gage inspection for inside-diameter variations in excess of tolerance.

Penetrant inspections were made on 178 bottom closure welds and 142 top closure welds. After all flaw indications had been evaluated, none of the welds were rejected. Radiographic inspections were also made on the 178 bottom closure welds and 142 top closure welds. After full

evaluation of all flaw indications, the only remaining discontinuities were small, high-density inclusions in two of the bottom closure welds. Helium leak tests were performed on 178 bottom closure welds and 113 of the top closure welds. One top closure weld was rejected because of helium leakage.

Graphite Sleeve Inspection. Eddy-current inspections of graphite sleeves for the assembly test of EGCR fuel elements were completed. These inspections were accomplished by spiral scanning along both the inner and outer surfaces of the sleeves with a small probe coil. The techniques previously discussed,[20] in which an encircling coil and a bobbin coil were to be used, proved inadequate to detect all naturally occurring defects. The reference standard for the inspection of the sleeves is a milled notch 0.100 in. deep (10% of the wall thickness). Any sleeve producing a signal as large as the signal produced by the reference standard was considered to be rejectable. Fifty sleeves from each of three vendors were examined. Although the analysis of the data is incomplete, it appears that the rejection rate will be 80 to 90% for sleeves produced by two vendors and about 40% for sleeves produced by the third.

Metallographic examination of the defective areas has indicated that most of the defects are about twice as deep as indicated by the eddy-current inspection. This is possibly due to most of the defects being cracks that are oriented so that the deepest portion is not in the field of the inspection coil when the coil is positioned over the crack at the surface. Since the metallographic examinations have indicated that the signal from a 0.100-in.-deep crack may be smaller than that produced by the 0.100-in.-deep milled notch, it is possible that some of the sleeves considered to be acceptable contain cracks deeper than 0.100 in.

Brazing of Mid-Plane Spacers. Several commerically available high-temperature brazing alloys were considered for use in brazing the mid-plane spacers to the fuel tubes. Since a high surface temperature is anticipated adjacent to the spacer, the GE No. 81 alloy (66% Ni–19% Cr–10% Si–4% Fe–1% Mn; mp, ~2050°F) was selected, as mentioned above. The fillet of a tube-to-spacer joint which was furnace brazed with GE

No. 81 alloy for 10 min at 1170°C in hydrogen is shown in Fig. 4.25. As may be seen, tube-wall dilution by the braze alloy did not occur to any measurable depth; however, these joints did occasionally crack, as shown in Fig. 4.26. Cracks in the braze material that extended up to 90 deg around the periphery of the tube were often observed. It was found that the incidence and severity of cracking increased with shorter brazing times and faster cooling rates.

As stated above, induction brazing was investigated as a means of attaching the mid-plane spacers. The tube and a spacer with the braze alloy preplaced were mounted in a quartz tube surrounded by a short

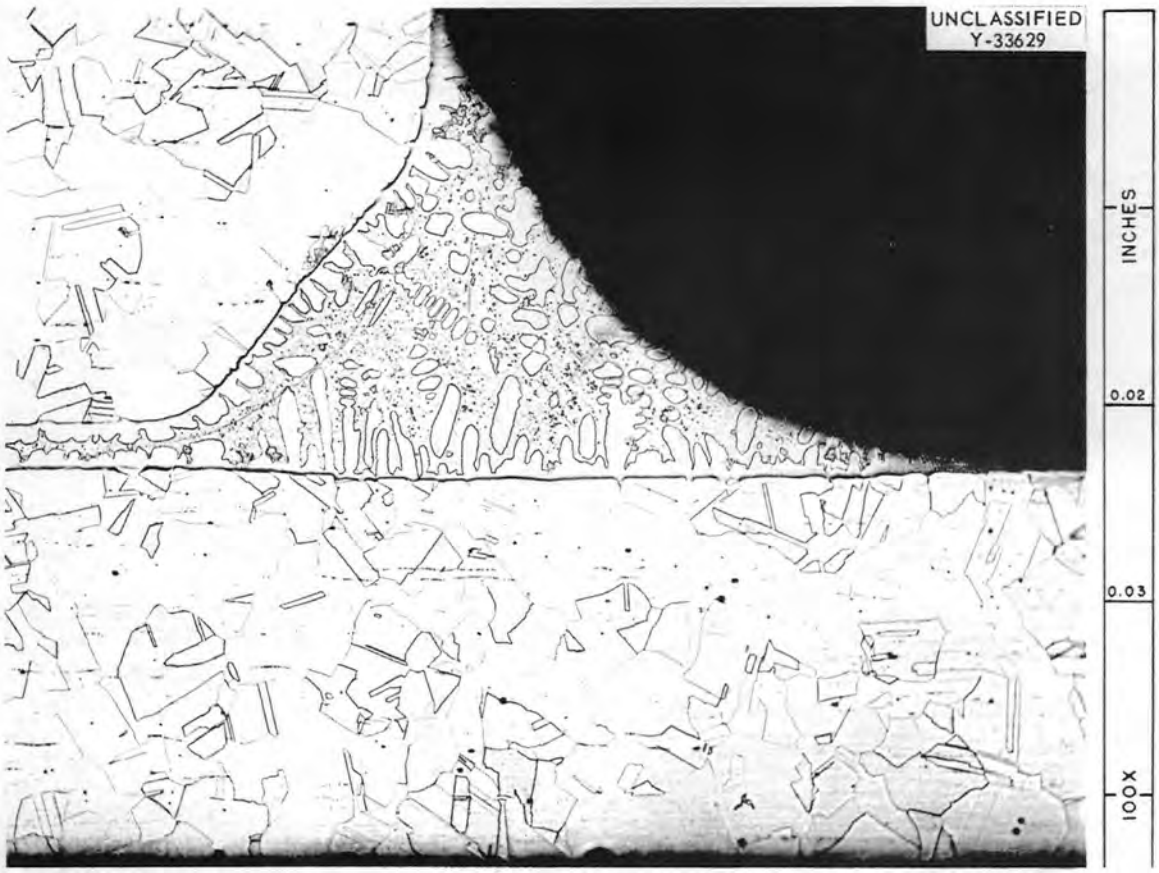

Fig. 4.25. Fillet of Tube-to-Spacer Brazed Joint Made by Furnace Brazing. Only minor tube wall dilution is evident. Etchant: modified aqua regia.

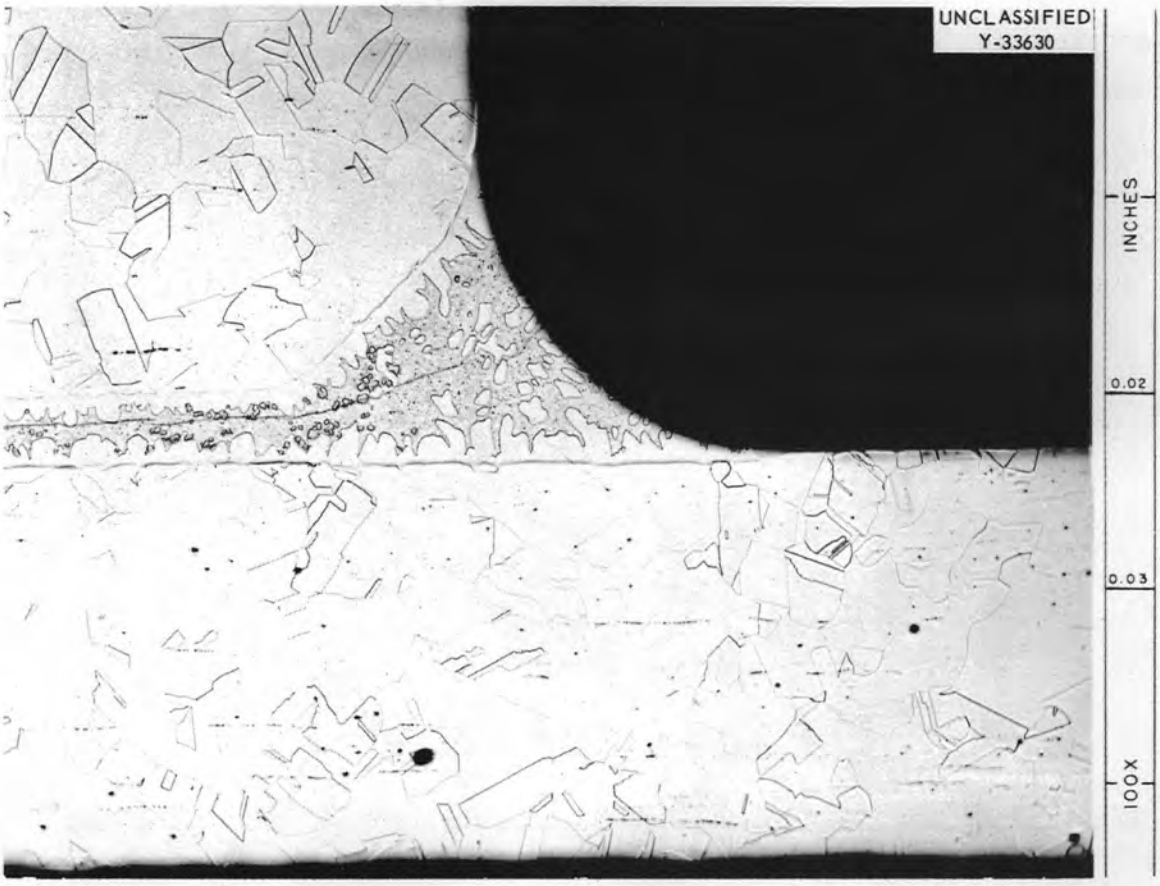

Fig. 4.26. Fillet of Tube-to-Spacer Brazed Joint Showing Cracks. Etchant: modified aqua regia.

induction coil. The brazing was carried out in helium, with the total brazing time being of the order of 3 to 4 min. Brazed joints of this type, as shown in Fig. 4.27, did not crack, but dilution of the tube wall by the braze alloy to a depth of 0.004 in. was observed. Since induction brazing localizes grain growth in the tube wall to the immediate braze area and minimizes distortion of the tube, studies will be continued to determine a satisfactory induction-brazing cycle.

UO_2 Fuel Pellet Inspection. Complete data on the source, physical properties, and chemical composition of fuel pellets used in the EGCR irradiation test program have been compiled,[21] and a detailed procedure

[21]R. L. Heestand and R. M. Evans, "GCR Irradiation Program Fuel Data Summary," ORNL CF-59-12-1 (April 7, 1960).

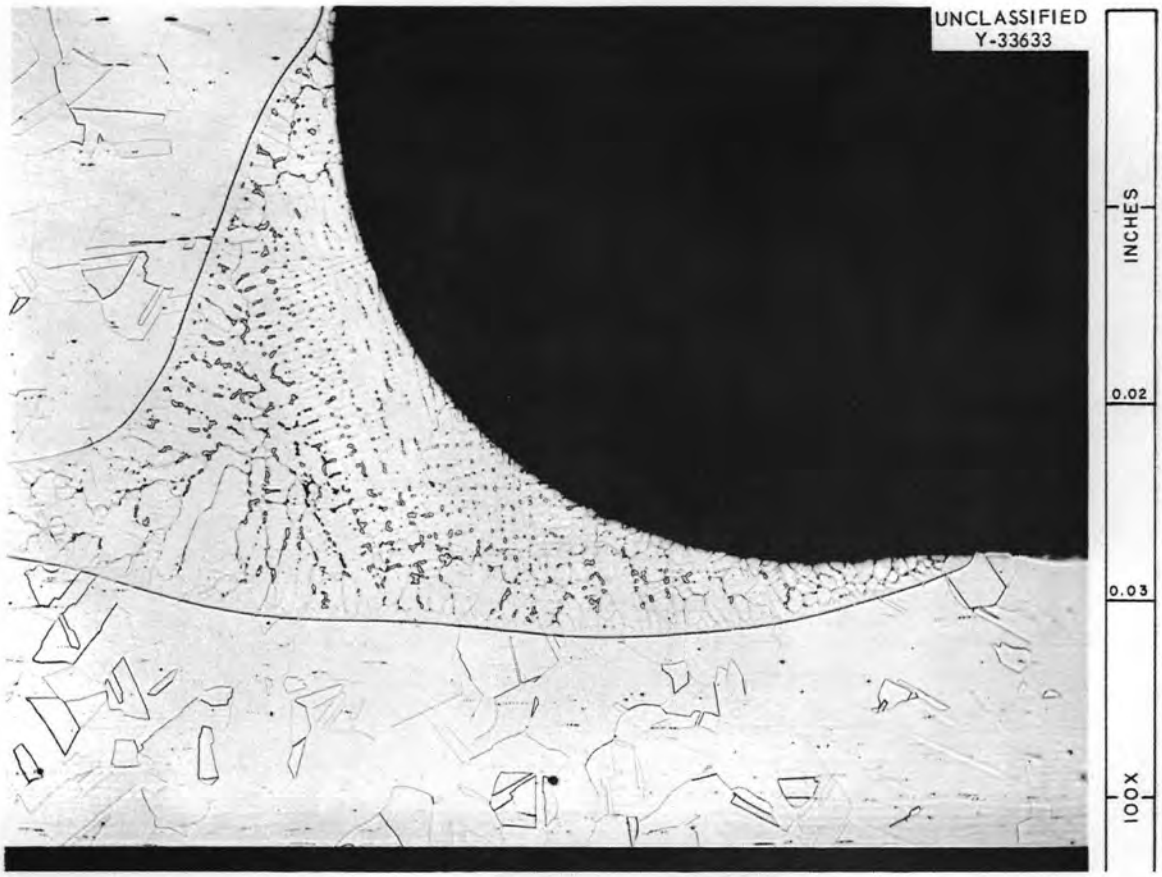

Fig. 4.27. Fillet of Induction-Brazed Tube-to-Spacer Joint. Tube wall dilution of approximately 0.004 in. is evident. Etchant: modified aqua regia.

for inspecting the pellets has been prepared. As mentioned above, this work is now being performed as a part of the UO_2 fabrication program.

Reactor Vessel Penetrations

Burst-Slug-Detection Tubes. A highly promising procedure has been developed for extending the EGCR burst-slug-detection tubes through the pressure shell. The feasibility of the procedure was determined by the satisfactory construction of the small mockup, BSD-2, shown in Fig. 4.28. The details of the composite joints are illustrated in Fig. 4.29.

During construction of the reactor vessel, the attachment of the machined transition adapters to the 1-in.-thick stainless steel plate

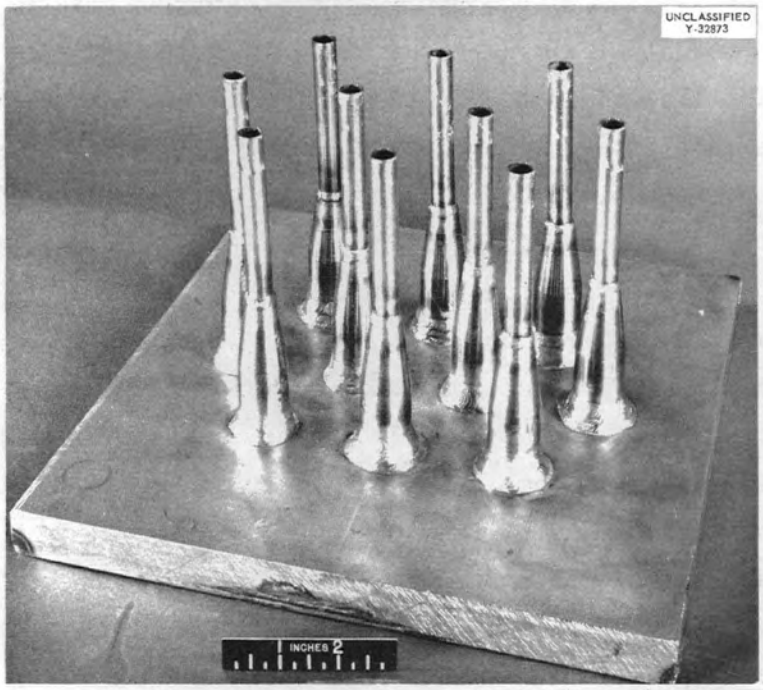

Fig. 4.28. Mockup of Burst-Slug-Detection Tube Penetrations of Pressure Shell.

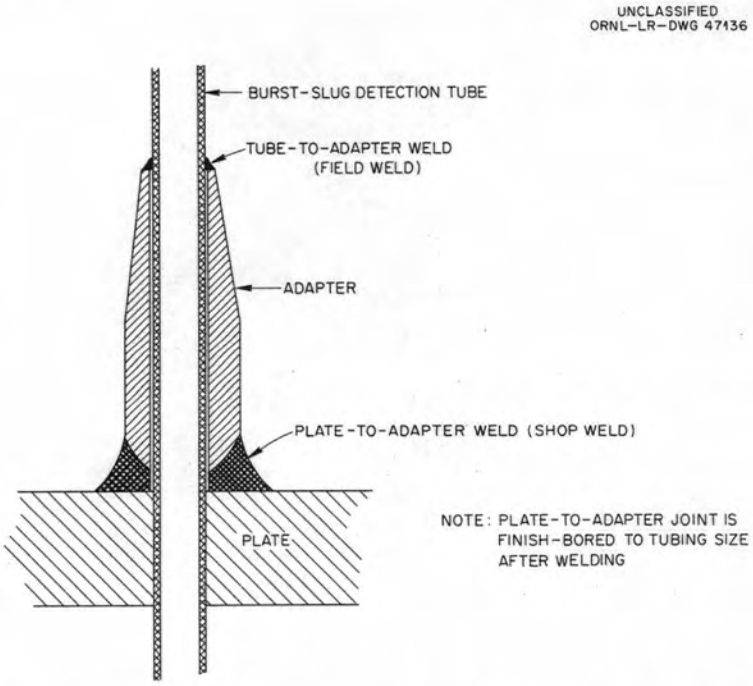

Fig. 4.29. Joint Design Utilized in Fabricating Burst-Slug-Detection Mockup No. 2.

would be performed under shop conditions. Although accessibility for welding is obviously limited by the close spacing specified in the design, the production of satisfactory welds is feasible. The tube-to-adapter fillet welds must necessarily be made in the field following welding of the stainless steel plate to the carbon steel pressure shell. Again, accessibility for welding is limited for the fillet weld, particularly since welding in all positions is required, but the feasibility was demonstrated in the BSD-2 mockup.

In order to confirm the specifications for fabrication and weld inspection, a full-size mockup (BSD-3) of one quadrant of an EGCR burst-slug-detection nozzle assembly is being fabricated. A 1-in.-thick stainless steel plate was rolled into a 2-ft-diam cylinder, and 30 tubes will penetrate through it. Every effort is being made to simulate conditions to be expected in the construction of the actual EGCR components.

Thermocouple Penetrations. A procedure is also being developed which appears to be applicable for extending the EGCR thermocouples through the pressure shell. Two possible joint designs are illustrated in Fig. 4.30.

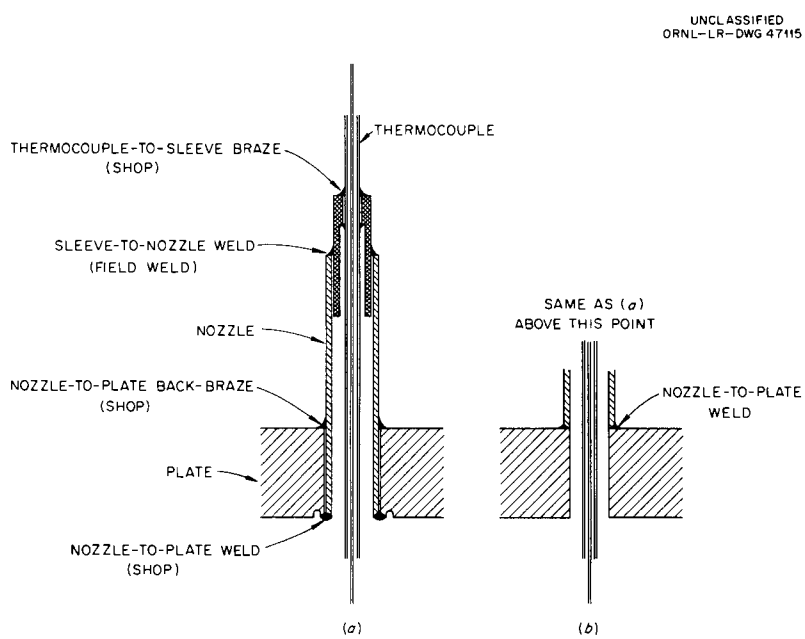

Fig. 4.30. Possible Joint Designs for EGCR Thermocouple Penetrations.

Adapter nozzles would be attached to the 1-in.-thick stainless steel plate, and the thermocouples would be brazed to the sleeves under shop conditions. The accessibility for welding the sleeve-to-nozzle fillet weld would be limited, but a preliminary experiment has indicated the feasibility of the 1 1/2-in. center-to-center spacing specified in the design.

Components for a full-size mockup are being machined to permit the specification of fabrication and inspection procedures. If accessibility for welding appears to pose a problem in the mockup, slight fanning of the nozzles will be recommended.

Welding of Austenitic to Stainless Steel

Quantities of type SA-212, grade-B, carbon steel and Croloy (2 1/4% Cr—1% Mo) plate are being obtained, and the welding procedure previously developed[22] for the joining of type 1020 carbon steel to stainless steel will be applied to the joining of these materials to stainless steel.

The following combinations of filler metal and weld position have been established for the metallic-arc process of joining type 1020 steel to type 304 stainless steel:

Filler Metal	Weld Position
INCO BP-85	2, 3, or 4 G
Type 347 stainless steel	1 G
Type 310 stainless steel	1 G
INCO "A" electrode	1 G

Welds made with these combinations have satisfactorily passed the ASME Boiler and Pressure Vessel Code requirements. The INCO BP-85 electrode appears to be especially promising because it can be deposited in all positions, it is free from porosity, and it has an intermediate coefficient of thermal expansion.

---

[22]"GCR Quar. Prog. Rep. Dec. 31, 1959," ORNL-2888, p. 90.

The fabrication of tubular weld specimens of dissimilar metals for thermal-cycling studies has been initiated. The first group of specimens will include carbon steel-to-stainless steel joints, which will be cycled between room temperature and 600 to 650°F. Subsequent groups of specimens will include stainless steel-to-Croloy joints for cycling from room temperature to 1050°F.

Beryllium Investigations

Reactions of Beryllium with CO_2

The manometric method of rate determination is not suited to the study of the reaction of CO_2 with beryllium because CO is a product of the reaction. Therefore a test system was prepared in which the change in weight of the specimen is determined by measuring the deflection of a calibrated spring from which the specimen is suspended. Ordinarily this method is not suitable for determining reaction rates of metals with gases under conditions where the reaction rates are slight. In order to overcome this difficulty, it was necessary to increase the surface area of the beryllium specimen without increasing its weight above approximately 1 g. This was done by using -200 mesh beryllium powder with a surface area of approximately 0.7 m^2/g as the specimen.

The first test was run at 700°C with a CO_2 pressure of 1 μ Hg. The rate curve obtained under these conditions was parabolic, and it flattened out after approximately 250 hr of exposure. After 500 hr of exposure at a CO_2 pressure of 1 μ the weight gain was of the order of 0.1 mg/cm^2 of beryllium. X-ray diffraction analysis of the specimen after the test showed the powder to consist of beryllium and BeO. Two additional tests are being conducted at 850 and 1000°C to determine the effect of temperature on the reaction. Preliminary results are similar to those of the test at 700°C.

Methods of investigating the reaction of beryllium with CO are being evaluated. A preliminary test at a pressure of 200 mm Hg has been initiated in which the manometric method is being used. In addition,

the effect of water vapor on the corrosion of beryllium in CO_2 is to be investigated. Methods of generating small partial pressures of water vapor by thermal decomposition of CaOH and other hydroxides are being studied.

Compatibility Tests of Beryllium-NaK-Type 304 Stainless Steel Systems

Since the capsules designed for irradiation in ORR pool positions incorporate NaK as a heat transfer medium, the compatibility of beryllium with stainless steel in a NaK environment is being investigated.

Experimental assemblies consisting of a beryllium cylinder step-machined to provide NaK annuli of 2, 5, 10, 15, 25, and 50 mils between the cylinder and the type 304 stainless steel containment capsule have been tested for 500 hr at 600, 700, and 800°C. A type 304 stainless steel coupon (1/2 × 1 × 1/8 in.) held in contact with a beryllium coupon (1/2 × 1 × 1/4 in.) was also included in each test.

The inner surface of the stainless steel container used for the test at 800°C is shown in Fig. 4.31, along with the beryllium content of drillings from the surface at positions corresponding to the various annuli. The transfer of beryllium through the NaK increased with decreased annulus thickness.

The weight changes that occurred in these tests are listed in Table 4.11. The weight loss of the beryllium cylinder was most severe at the highest test temperature. The data show that the weight loss

Table 4.11. Weight Changes of Components from Beryllium-Type 304 Stainless Steel-NaK (56-44 wt %) Compatibility Tests

Test Temperature (°C)	Weight Change (g/in.^{2})		
	Beryllium Cylinder	Beryllium Coupon	Type 304 Stainless Steel Coupon
600	-0.66	Nil	Nil
700	-1.7	-1.1	+1.1
800	-6.2	-7.1	+7.9

UNCLASSIFIED
Y-33807

NaK ANNULI (mils)	BERYLLIUM CONTENT ON CONTAINER SURFACE (mg/cm^2)
50	0.14
25	0.17
15	0.31
10	0.78
5	2.30
2	4.86

Fig. 4.31. Type 304 Stainless Steel Container After Exposure in Beryllium-NaK-Stainless Steel Compatibility Test at 800°C for 500 hr.

of the beryllium was nearly equal to the weight gain of the type 304 stainless steel.

Procurement of Beryllium Tubing

Tubing is being procured from several vendors experienced in fabricating beryllium in order to carry out a thorough investigation of beryllium as a capsule material. A total of 640 ft of seamless beryllium tubing is on order from the Pechiney Company of France. One lot consisting of 140 ft of 0.520-in.-i.d., 0.040-in.-wall tubing is ready for shipment. A second lot of 500 ft of 0.300-in.-i.d., 0.040-in.-wall tubing is being fabricated. One hundred twenty-five feet of 0.300-in.-i.d., 0.040-in.-wall seamless beryllium tubing prepared by each of four fabrication methods has been ordered from the Brush Beryllium Co. The four methods of preparation are machining from a hot-pressed block; warm extrusion of rod,

followed by boring; hot extrusion of rod, followed by boring; and hot extrusion over a mandrel. To date, 67 ft of machined tubing has been received.

An additional 500 ft of 0.300-in.-i.d., 0.040-in.-wall seamless beryllium tubing has been ordered from the Chesterfield Tube Company, Ltd., of Great Britain. None of this tubing has been received to date. Another purchase order was negotiated with Chesterfield whereby technical information on their latest and best methods for fabricating and testing beryllium tubing will be made available through the Superior Tube Co., the United States representative of the Chesterfield Tube Co. This information is being compiled into a technical report by personnel of the Superior Tube Company.

In addition to the extruded and machined tubing, ten tubes fabricated from powder by isostatic hot pressing were purchased from the Sylvania-Corning Nuclear Corporation for evaluation. These tubes were 0.400 in. in diameter, had 0.050-in.-thick walls, and were 6 in. long. Work has also been initiated on a development contract with Nuclear Metals, Incorporated, for a study of the effect of extrusion parameters, that is, speed, temperature, reduction ratio, and billet design, on the quality and properties of the resultant tubing. All tubing fabricated will be extruded directly to size within the range 0.300 to 0.750 in. in outside diameter and 0.030 to 0.100 in. in wall thickness. To assist in the evaluation, the Oak Ridge National Laboratory will receive samples of each lot of tubing prepared.

Beryllium-Tubing Evaluation

Inspection of 67 pieces of machined beryllium tubing received from the Brush Beryllium Company has begun. The pieces are each 1 ft long, 0.300 in. in inside diameter, and 0.040 in. in wall thickness. Radiographic examinations have indicated that the tubing is of high quality. The only defects noted were small amounts of high-density contamination near the end of a few tubes and a few small wall thickness variations. Fluorescent penetrant examination has revealed only a few tiny, shallow pinholes.

This is in contrast to the very many pit-like defects observed in extruded tubing.

Radiographic inspection of the ten isostatically pressed tubes showed a film or coating of high-density material on the inner surface. Further evaluation of this tubing has been deferred until the foreign material can be removed by pickling.

Joining of Beryllium

The studies of beryllium-joining techniques are continuing. The investigations include fusion welding, high-temperature brazing, diffusion bonding, and upset welding. Techniques are being developed for fabricating components for various tests and for determining the suitability of the techniques for joining beryllium tubing produced by the various fabrication methods.

Welding. Experiments were conducted to determine the suitability of electron-beam welding for the manufacture of beryllium tube-to-end cap joints. One sample was prepared that consisted of machined QMV tubing welded to a machined QMV end cap. Another sample consisted of an extruded tube (made by Nuclear Metals, Incorporated) welded to a machined QMV end cap.

The tube-to-end cap edge weld produced on the QMV-to-QMV joint had a good bead contour and was helium leaktight. Metallographic examination revealed only minor porosity, as shown in Fig. 4.32. The sample containing the extruded tube did not weld satisfactorily; the end plug and the tubing had different melting characteristics. Accelerated vaporization of impurities in the base metal was observed during welding. In addition, excessive porosity and cracking in the weld were noted upon metallographic examination.

Brazing. Preliminary melting point determinations have been made, and base-metal-wettability tests have been conducted on 15 experimental precious-metal-base brazing alloys by observing the behavior of samples of crushed alloy on small beryllium pads at various temperatures. Six alloys with melting points between 1000 and 1150°C showed good wetting properties.

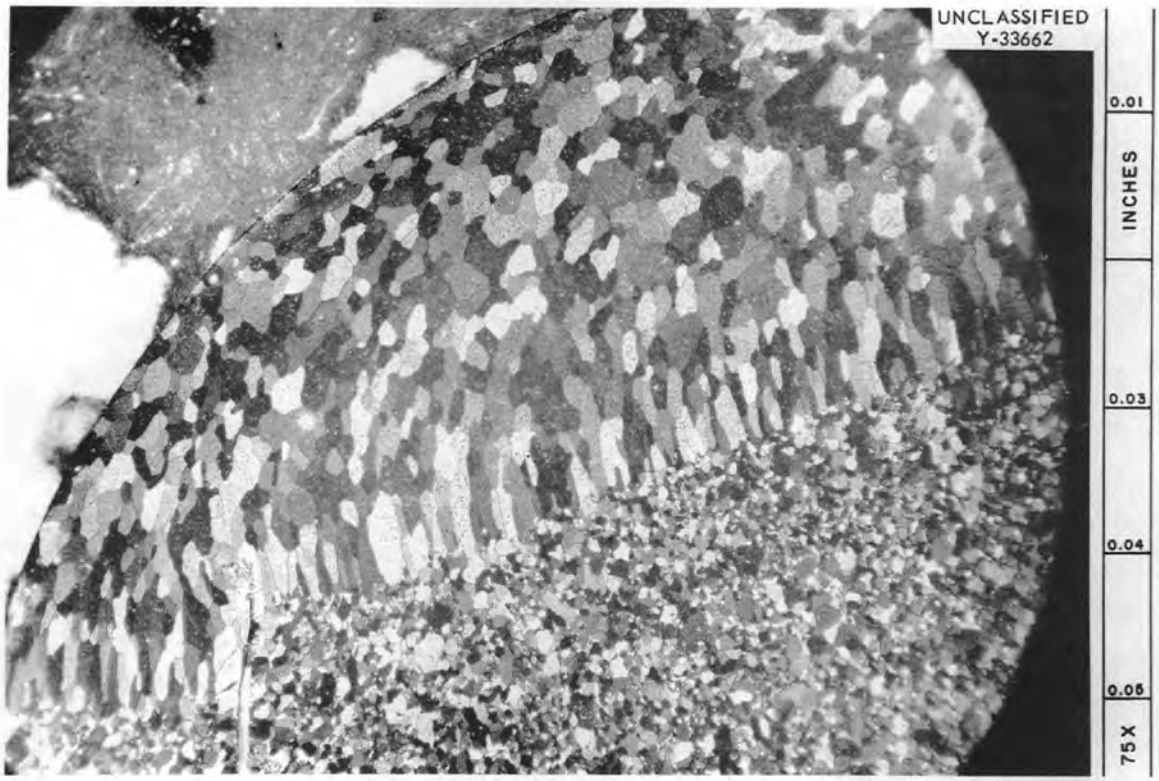

Fig. 4.32. Electron-Beam Welded Beryllium Tube-to-End Plug Joint. Material was machined from QMV beryllium. Polarized light. Unetched.

Flowability tests are being made on T-joints, and metallographic examinations of samples are presently under way. Tests designed to evaluate the relative feasibility of brazing beryllium in vacuum, argon, helium, and hydrogen are in progress. The brazing is conducted without the use of flux or fluxing agents.

Joints that are leaktight to helium have been produced by using two of the experimental brazing alloys on tube-to-end cap samples. The joints are presently being subjected to thermal-cycling tests and are to be examined metallographically. A leaktight tube-to-end cap joint is to be prepared for in-pile tests in NaK at approximately 1200 to 1300°F. Alloys that are known to be suitable for lithium service[23] at

[23]R. G. Gilliland, "Progress Report on Refractory Metal-Base Brazing Alloy Study," ORNL CF 58-12-112 (Dec. 29, 1958).

the desired temperature are being studied for this application. The alloys presently undergoing testing are 47% Ti–47% Zr–6% Be, 46% Ti–46% Zr–4% Be–4% V, 45% Ti–45% Zr–10% Fe, and 63% Ti–27% Fe–10% Mo. All these alloys flow well on beryllium, and brazed joints are being made for evaluation tests.

Diffusion Bonding. The diffusion-bonding studies are being conducted with the use of the molybdenum jig described in a previous report.[24] The joints are being made under various conditions of time, temperature, and environment. The results of the tests completed thus far are summarized in Table 4.12. As shown by the comments in the table, leaktight joints could be made in vacuum at 1100°C. When the temperature was raised to 1150°C, however, the joints were not leaktight. One joint which was made

[24]"GCR Quar. Prog. Rep. Sept. 30, 1957," ORNL-2835, p. 100.

Table 4.12. Results of Diffusion Bonding Studies

Test No.	Bonding Conditions			Comments
	Time (hr)	Temperature (°C)	Atmosphere	
1	16	1000	Vacuum	No grain coalescence, joint leaked
2	24	1000	Vacuum	No grain coalescence, joint leaked
3	16	1000	Vacuum	No grain coalescence, joint leaked
4	2	1100	Vacuum	Partial grain coalescence, joint leaktight
5	4	1100	Vacuum	Complete grain coalescence, joint leaktight
6	2	1150	Vacuum	Partial grain coalescence, joint leaked
7	4	1150	Vacuum	Complete grain coalescence, joint leaked
8	2	1150	Helium	Joint leaktight

by bonding at 1150°C for 2 hr in a helium atmosphere was leaktight. It appears that bonding in vacuum at temperatures greater than 1100°C results in a sufficient amount of vaporization or mass transfer of base metal and impurities to cause leakage through the joint. The leaktight joint obtained in test 8 is being examined metallographically. Metallographic examinations of leaktight bonds made at 1100°C in vacuum have shown partial grain coalescence after 2 hr at temperature (see Fig. 4.33) and complete grain coalescence after 4 hr (see Fig. 4.34).

A leaktight specimen was prepared for high-temperature tube-burst testing to obtain mechanical property data on beryllium tubing. The tubing used was machined from QMV beryllium, and the end plugs were diffusion bonded at 1100°C for 2 hr in a vacuum. A 1/8-in.-diam type 304 stainless steel pressurizing tube was then brazed through one end plug with the use of the experimental brazing alloy consisting of 49% Cu–49% Ti–2% Be. A preliminary discussion of this type of joint between

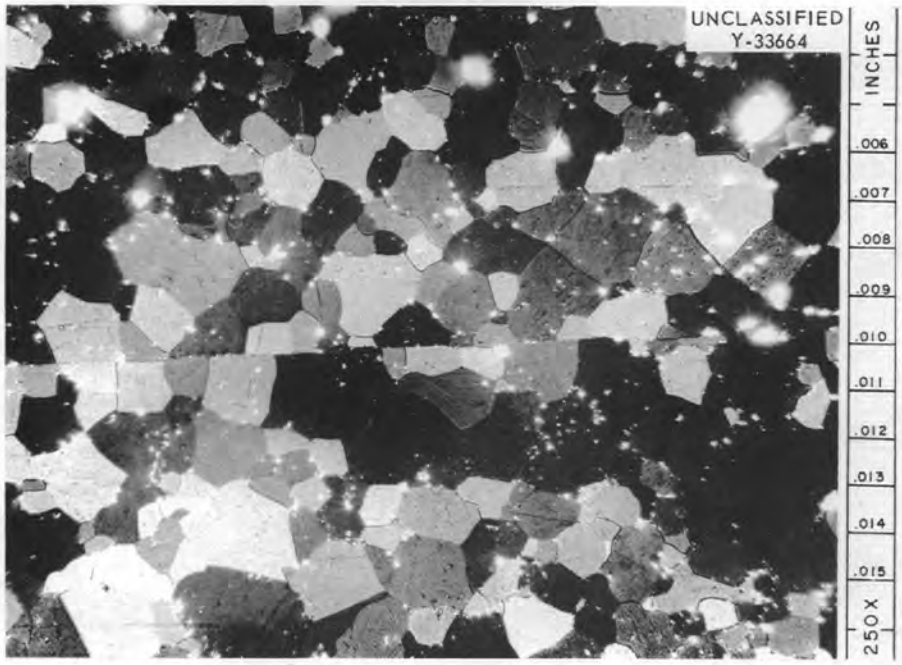

Fig. 4.33. Beryllium Diffusion Bond Held at 1100°C for 2 hr in Vacuum. Note partial grain coalescence. Polarized light. Unetched.

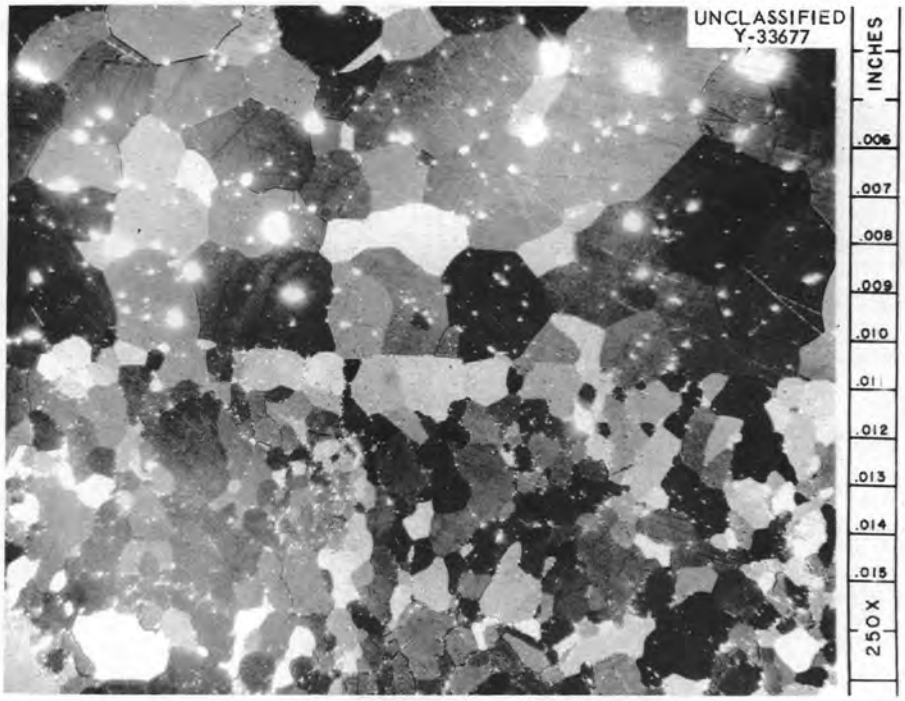

Fig. 4.34. Beryllium Diffusion Bond Held at 1100°C for 4 hr in Vacuum. Note complete grain coalescence. Polarized light. Unetched.

dissimilar materials was presented previously.[25] The specimen, which is shown in Fig. 4.35, is presently being tested.

Upset Welding. Suitable dies machined from INOR-8 were constructed, and experiments are being conducted in an attempt to produce end closures on beryllium tubing using the upset-welding method developed in Great Britain.[26] The method depends upon the ability of a malleable ring to deform the wall of the beryllium tube and the end plug sufficiently to produce a leaktight joint. This method is reported to produce as much as 50% deformation at the joint and to result in a fine-grained joint interface.

---

[25]"GCR Quar. Prog. Rep. Dec. 31, 1959," ORNL-2888, pp. 95–97.

[26]"Trip Report – Visit of US Gas-Cooled Reactor Team to UK – July 7–18, 1958," Part II, ORNL-2588 (Classified).

Fig. 4.35. Beryllium Elevated-Temperature Tube-Burst-Test Specimen.

Thermal-Cycling Tests on Beryllium

Thermal cycling of beryllium will occur during high-temperature irradiation as well as during postirradiation heat treatment of specimens irradiated at low temperatures. In order to determine whether thermal cycling will cause dimensional instability or mechanical damage of the beryllium, experiments were performed in which specimens annealed at 800°C for 2 hr were heated through 80 thermal cycles at approximately 150°C/min and subjected to bend tests. The results of these experiments are presented in Table 4.13. The dimensional data indicate that thermal cycling causes slight densification of beryllium, especially in the case of hot-pressed blocks, even though the data are not precise because of the inherent limitations of the measuring techniques.

The bend tests were performed by three-point, simple beam loading of the specimen with the ram opposite the notch. The stress, σ, was computed from the equation

$$\sigma = \frac{3fPL}{2wh^2} ,$$

Table 4.13. Dimensional Changes and Bend Test Data on Thermally Cycled Beryllium Specimens

Minimum and Maximum Thermal Cycling Temperatures (°C)	Origin of Specimen	Dimensional Changes (%)			Bend Test	
		Width*	Thickness**	Length*	Fracture Stress (psi)	Fracture Deflection (mils)
None	Rod				193 000	12
	Block				115 000	5
	Unidirectionally rolled sheet				143 000	2.5
	Cross rolled sheet				94 000	2
100–400	Rod	0.0	-1.0	-0.1	235 000	6.5
	Block	-0.1	+0.2	+0.3	124 000	5.5
	Unidirectionally rolled sheet	0.0	+1.0	-0.1	124 000	2.5
	Cross rolled sheet	0.0	-0.7	-0.1	98 000	2.5
400–700	Rod	-0.1	-0.5	-0.1	193 000	15
	Block	-0.1	-0.3	-0.2	114 000	5.5
	Unidirectionally rolled sheet	-0.1	+0.2	-0.1		2
	Cross rolled sheet	-0.3	+0.1	-0.2	103 000	2.5
100–700	Rod	0.0	-0.1	-0.1	197 000	17
	Block	-0.1	-0.5	0.0	109 000	5
	Unidirectionally rolled sheet	0.0	-1.0	0.0		3
	Cross rolled sheet	-0.1	-0.5	0.0	92 000	2
100–850	Rod	-0.1	-0.2	-0.1	198 000	15
	Block	-0.5	-1.2	-0.3	125 000	6.5
	Unidirectionally rolled sheet	0.0	+0.5	-0.1	149 000	4.5
	Cross rolled sheet	-0.1	0.0	0.0	83 000	2

*An error of ±0.1% is applicable to the width and length values.

**An error of ±1.0% is applicable to the thickness values.

where f is the stress concentration factor for the notch geometry (1.1), P is the load at fracture, L is the distance between supports, w is the width of the specimen, and h is the thickness of the specimen. The stress calculated in this manner has little relationship to the stress-strain characteristics of the material and is useful only for comparisons. It may be seen from the bend-test data that thermal cycling has had no

deleterious effect on the mechanical properties. The changes in the mechanical behavior with changes in fabrication history are interesting but unexplainable at present.

5. IN-PILE TESTING OF COMPONENTS AND MATERIALS

Fuel Element Irradiation Program

Full-Diameter Prototype EGCR Fuel Capsules

ORR Experiments. Irradiation of the eight full-diameter prototype group II capsules is progressing with the desired cladding temperatures having been obtained for all capsules by adjustment of the helium-nitrogen thermal-barrier gas mixtures. Various mixtures have been required in the 0.012-in. gas annuli to adjust for flux variations and to achieve uniform temperatures. For the capsules operating at 1300°F, the nitrogen content of the gas has been varied from 8 to 30%; for the capsules operating at 1600°F, the nitrogen content has been varied from 20 to 58%. Twenty controlled thermal cycles consisting of a temperature decrease of about 750°F were applied to capsules 03-2 through 08-2 to complete the controlled thermal cycles planned for this group of capsules until just before removal from the reactor, at which time 20 more thermal cycles will be applied.

Evidence that the thermal-barrier gas mixture undergoes thermal diffusive separation is more pronounced than it was for the group I capsules. Changes in the configuration of the spacers in the annulus or the increased spacing may be responsible for the greater separation of the constituents of the gas. With each operation that is capable of disturbing the gas mixture within the capsule, a predictable temperature shift occurs. It is postulated that the gas mixture separates into a vertical gradient along the capsule, with the helium enriching at the top. Since there is appreciable space at the bottom, the heat transfer annulus gas is also slightly enriched in helium. When a new gas mixture is admitted at the top, the first effect is to push the small amount of gas that is more highly enriched in helium past the capsule and thus to produce a slight temperature depression. Following this, the original, unseparated gas mixture in the line enters and causes the temperature to rise 100 to 150°F. When the new mixture arrives, the temperature shifts upward or downward

according to the change being made in the nitrogen content of the gas. When the flow of new gas is stopped, the temperature drifts down about 150°F, in approximately 30 min, as the separation gradient for the new mixture reaches equilibrium. Since these adjustments produce undesired thermal changes, it is planned to hold them to a minimum. Although the gas separation effect is greater than for the group I capsules, the new gas flow arrangement facilitates more rapid and orderly temperature adjustments, and the total number of unscheduled thermal cycles has been greatly reduced.

The operating temperatures recorded on March 3, 1960, and the estimated total burnup through February 21, 1960, are given in Table 5.1.

Estimated total burnups for the group I capsules, based on measurements of the thermocouple harness monitors, are presented in Table 5.2, along with new estimates calculated from the design perturbed flux for comparison. The values for total burnup of the group I capsules reported

Table 5.1. Temperature and Burnup Data for the Group II Capsules Being Irradiated in the ORR

Capsule No.	Nitrogen in Gas Mixture (%)	Capsule Temperature (°F)				Estimated Total Burnup[a] (Mwd/MT)
		Design	High	Low	Average	
01-2	17	1300 ± 50, average	1368	990[b]	1303	910
02-2	40	1600 (+0,-50), high	1580	1230[b]	1455	930
03-2	19.5	1300 ± 50, average	1340	930[b]	1286	960
04-2	8.5	1300 ± 50, average	1360	975[b]	1298	960
05-2	20	1600 (+0,-50), high	1600	1385	1476	980
06-2	44	1600 (+0,-50), high	1570	1400	1487	930
07-2	30	1300 ± 50, average	1400	1190	1258	630
08-2	58	1600 (+0,-50), high	1550	1373	1467	680

[a]Burnup is based on an accumulated reactor power generation of 30 817 Mwhr as of February 21, 1960.

[b]Specially placed thermocouples 1/4 in. from the ends of the pellet stacks in capsules 01-2 through 04-2 are indicating these low temperatures.

Table 5.2. Total Burnup Estimates for Group I Capsules

Capsule No.	Total Burnup Estimate* (Mwd/MT of UO_2)	
	Based on Thermocouple Harness Flux Monitors in Capsules	Based on Preirradiation Flux Measurements
01	1680	1880
02	1840	1900
03	1530	2130
04	2380	2430
05	3030	2370
06	1880	1960
07	980	1520
08	950	1310

*These estimates of total burnup are based on a nuclear reaction energy of 200 Mev/fission.

previously[1] were estimated on the basis of 176 Mev/fission as the nuclear reaction energy rate, and gamma heating from external sources was included. The new values presented in Table 5.2 are based on the 200 Mev/fission and do not include gamma heating from external sources except as it results from secondary reactions of the specimen fissions.

ETR Experiments. Irradiation of the ten full-diameter prototype fuel capsules in the ETR has continued satisfactorily, although the reactor operating schedule has been somewhat limited. As indicated in Table 5.3, the operating temperatures are generally satisfactory, but the heat generation rates have been lower than desired. Accordingly, reactor flux mapping is in progress as a step toward locating the capsules in more favorable irradiation positions. The goal is to achieve heat generation rates of approximately 35 000 Btu/hr·lin ft and to operate capsules E-3, E-8, and E-10 at 1600°F.

[1]"GCR Quar. Prog. Rep. Dec. 31, 1959," ORNL-2888, p. 99.

Table 5.3. Typical Operating Temperatures for the Full-Diameter Prototype EGCR Fuel Capsules Being Irradiated in the ETR

Capsule No.	Capsule Temperature (°F)				Estimated Total Burnup[a] (Mwd/MT)
	Design	Highest	Lowest	Average	
E-1[b]	1300	1293	1250	1273	1005
E-1A[b]	1300	1330	1215	1273	664
E-2[c]	1300	1327	1078	1246	34
E-3	1300–1600[d]	1320	1092	1270	33
E-4	1300	1353	1250	1304	664
E-5	1300	1100	1065	1080	734
E-6	1300	1160	1075	1125	765
E-7	1300	1310	1195	1258	777
E-8	1300–1600[d]	1340	1141	1265	56
E-9	1300	1292	1226	1267	961
E-10	1300–1600[d]	1332	1212	1275	57

[a]These estimates of total burnup are based on 200 Mev/fission as the nuclear reaction energy and were calculated as of January 10, 1960.

[b]Capsule withdrawn October 19, 1959; the temperature readings were taken on October 13, 1959, with the reactor operating at 175 Mw; the total burnup given is the final calculated value.

[c]The temperature readings for capsules E-2 through E-10 were taken on January 5, 1960 with the reactor operating at 175 Mw.

[d]The test specifications call for an increase in the maximum design temperature to 1600°F late in March 1960.

Miniature Capsule Fission-Gas-Release Experiments

Three new capsules with depleted UO_2 insulating bushings have been assembled and are being irradiated. The design of these new ceramic-insulated capsules is compared in Fig. 5.1 with the design of the gas-insulated capsules used previously. In the gas-insulated capsule a large temperature drop occurred through a small, 0.001 to 0.004 in., radial gap filled with argon gas, and the gap dimensions and gas content were subject to continuous change as the fuel specimens fractured and/or

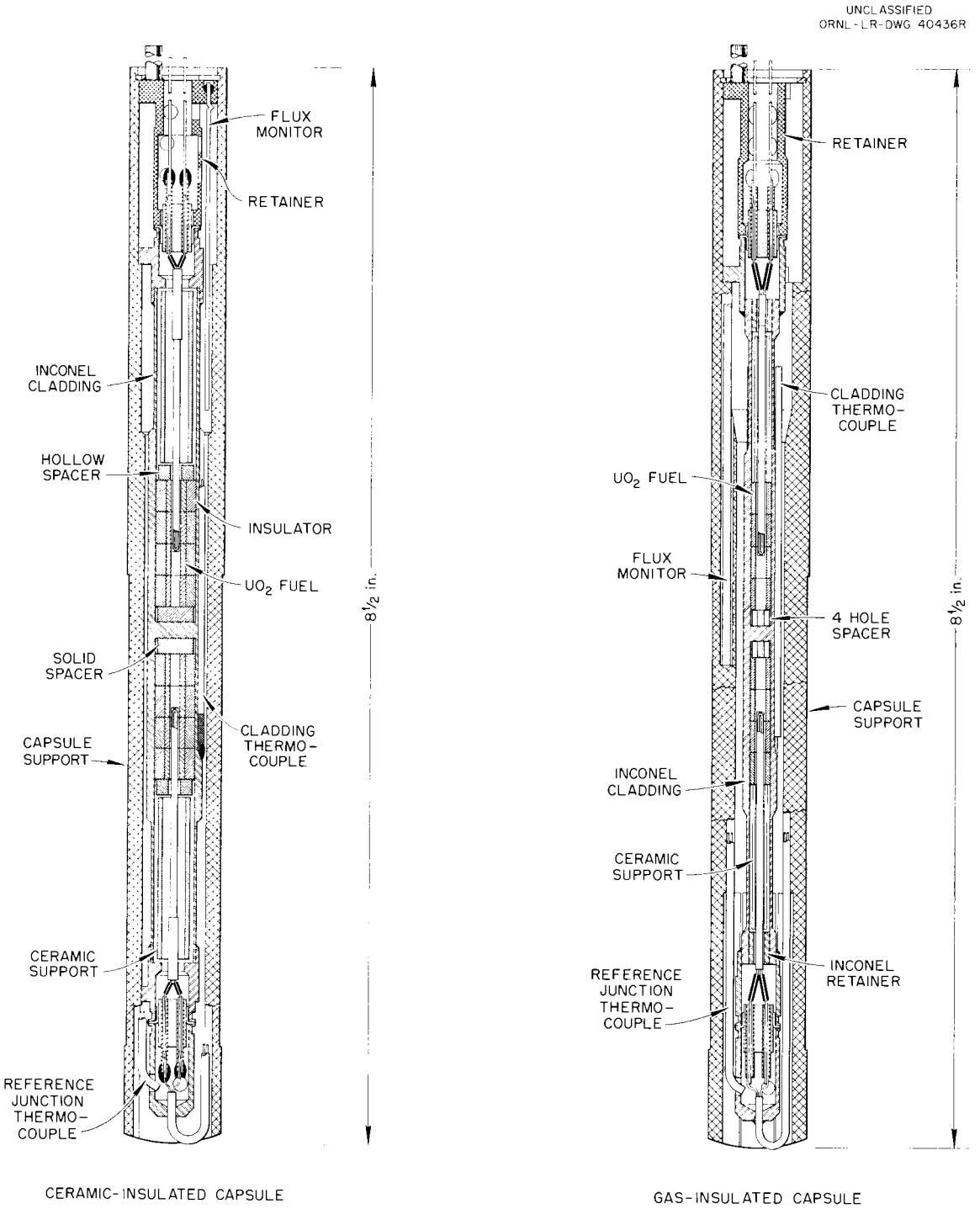

Fig. 5.1. Experimental Assemblies for Fission-Gas-Release Experiments.

fission gas was released. In the new capsules, a cylindrical depleted UO_2 bushing that has a low thermal conductivity provides a high thermal resistance between the fuel and the metal container. The ceramic cylinder is fabricated to close tolerances so that the radial gaps are small, and the capsule is filled with high-purity dry helium; thus, the contribution of gas gaps to the total temperature drop is minimized.

The central void temperatures in the capsules are measured with tungsten-rhenium thermocouples. The drifts of some of the thermocouples in the gas-insulated and ceramic-insulated capsules are compared in Figs. 5.2 and 5.3. The maximum scatter of the central void temperatures measured at random in the ceramic-insulated capsules was about ±2%. This is considered very good accuracy, since the readout instrument and lead wire have guaranteed accuracies of only ±1%.

Data on completed and currently operating fission-gas-release experiments are presented in Table 5.4. As indicated by the absence of changes in central fuel temperatures for conditions of constant heat rates, the thermal conductivity of UO_2 does not appear to change with thermal neutron doses between 3×10^{16} and 4×10^{20} neutrons/cm^2·sec.

Table 5.4. Data on Completed and Currently Operating Fission-Gas-Release Experiments

Experimental Assembly No.	UO_2 Density (% of theoretical)	UO_2 Enrichment (% U^{235})	Central UO_2 Temperature (°F)		Date Installed	Date Removed
			a Capsule	b Capsule		
L-7abx	95	20	*	2950	9-22-59	2-9-60
L-11ab	85	20	2460	2850	7-7-59	2-9-60
L-22ab	95	10	1400	1600	11-10-59	
L-23ab**	95	15	2750	2800	12-8-59	
L-24ab**	95	20	2625	3125	12-15-59	
L-25ab**	95	20	2150	2500	2-10-60	

*Thermocouple failed during initial heatup.

**Ceramic-insulated capsules.

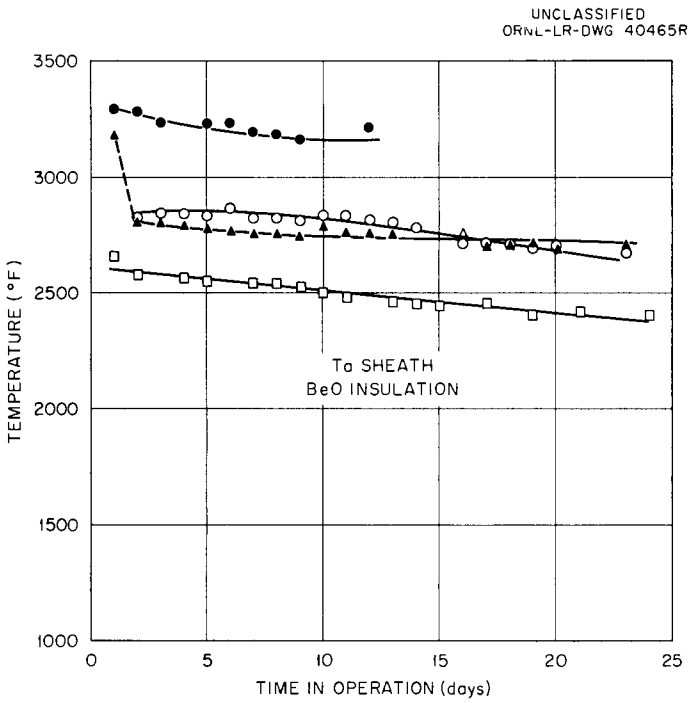

Fig. 5.2. Changes in Temperature Indications of Tungsten-Rhenium Thermocouples as a Function of Time in Gas-Insulated Capsules

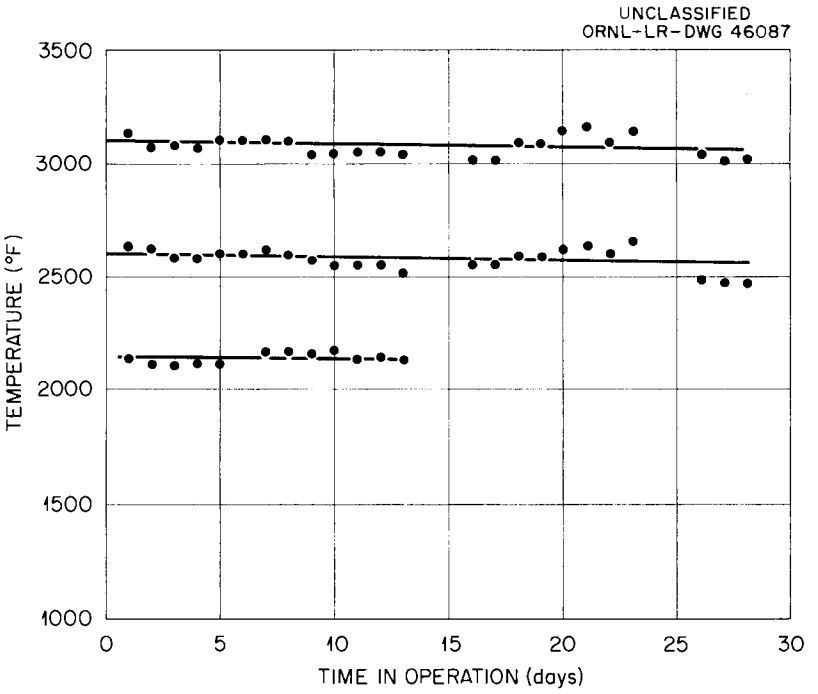

Fig. 5.3. Changes in Temperature Indications of Tungsten-Rhenium Thermocouples as a Function of Time in Ceramic-Insulated Capsules.

Advanced Fuel Element Testing

The ORNL-MTR-48-1 test of two graphite-clad UC_2-graphite matrix fuel elements was terminated on January 25, 1960. The capsule containing the elements was irradiated during MTR cycles 130 through 133 in the HB-3 beam hole. Except for a loss of one thermocouple, the equipment operated smoothly. The double containment vessel with the fuel elements inside was returned to ORNL for postirradiation examination.

Prior to irradiation, the two fuel elements were assembled in the double containment vessel with a 3 1/2-in. axial distance between the centers of each fuel element matrix. The "A" matrix, which was nearest to the reactor core, was manually adjustable between 5 1/8 and 12 1/2 in. axially from the inside surface of the end plate of the beam hole liner. The position of the fuel element was adjusted during irradiation as necessary to compensate for changes in the thermal neutron flux profile and in U^{235} concentration due to burnup. The position was determined to be correct when the hottest thermocouple in the wall of the graphite capsule read 1600 ± 50°F.

The capsule wall temperature for each element was taken to be the average at three thermocouple junctions located 120 deg apart, at the midpoint of the graphite wall, and in a plane perpendicular to each fueled graphite matrix axis at its center. The average temperature for each element and the position of the A element are shown in Fig. 5.4. These temperatures were unaffected by the temperature of the coolant water, which varied between 105 and 115°F.

Once during each of five different MTR core loadings, the capsule was pulled out of the reactor as far as possible and then reinserted in 1/2-in. steps until the normal operating position was reached. After each step the capsule wall temperature readings were recorded. The average wall temperatures computed from these data are plotted in Fig. 5.5.

Preirradiation data and design operating conditions for each element were presented previously,[2] and estimates of the test parameters based

[2] "GCR Quar. Prog. Rep. Dec. 31, 1959," ORNL-2888, p. 107.

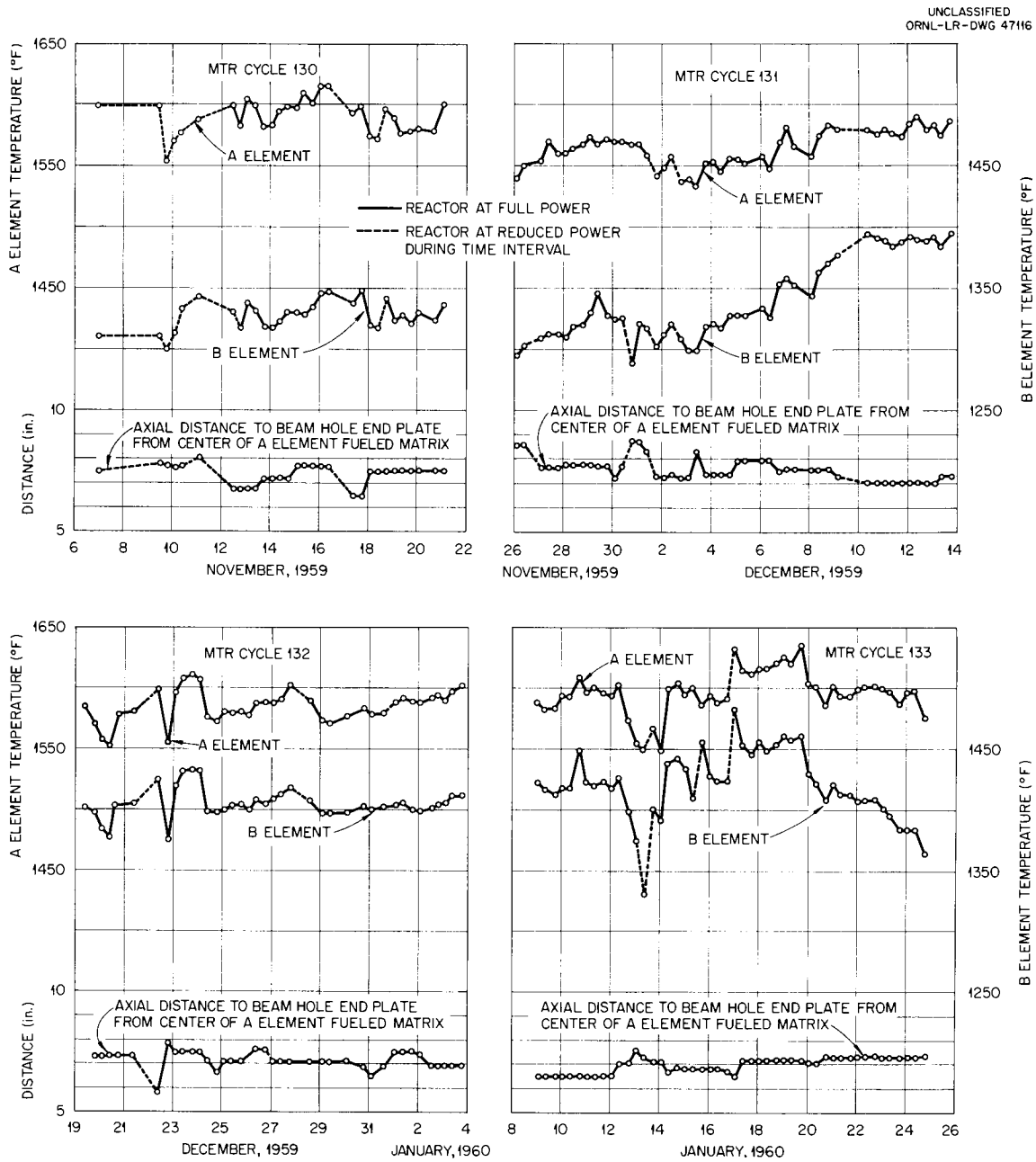

Fig. 5.4. Average Temperature of Encapsulating Graphite at Wall Midpoint Versus Day of Reactor Operation for MTR Irradiation of Graphite-Clad Fuel Elements Consisting of UC_2 in a Graphite Matrix (ORNL-MTR-48, Capsule Test 1).

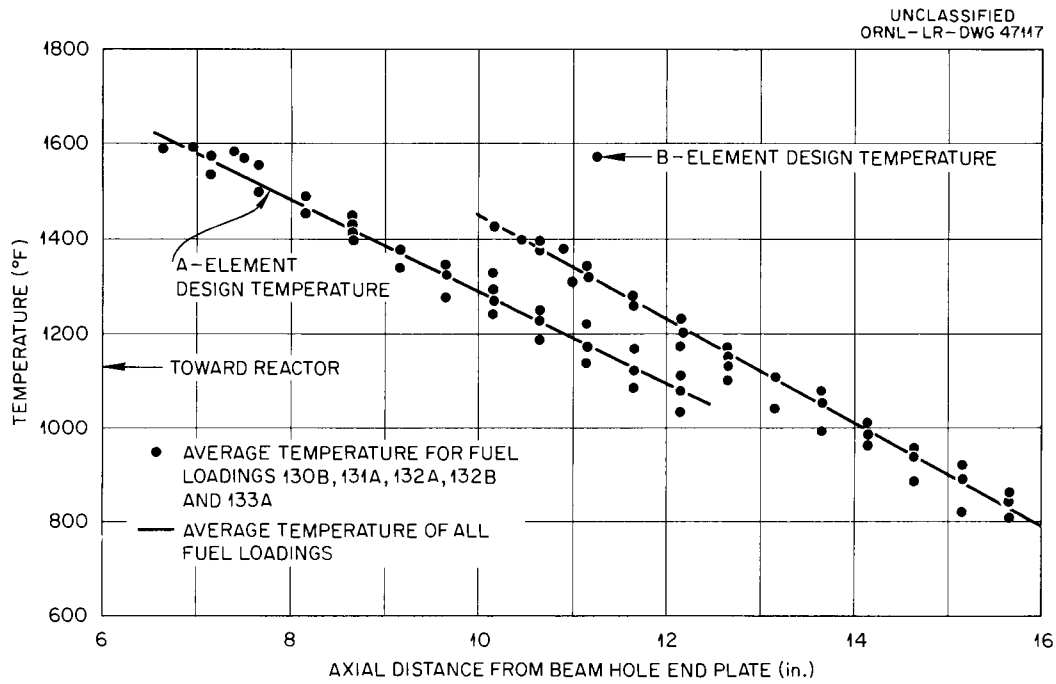

Fig. 5.5. Average Temperature of Encapsulating Graphite at Wall Midpoint Versus Axial Distance of Fueled Graphite Matrix Centers from HB-3 Beam Hole End Plate (ORNL-MTR-48, Capsule Test 1, MTR Cycles 130–133).

on the preirradiation data, the operating temperatures, and time at a reactor power level of 40 Mw are presented in Table 5.5.

The thermal neutron flux was computed from the heat flux based on the temperature differential between the thermocouples in the fuel cladding and in the cooling water and the thermal conductivities of the graphite, gas gap, and metal wall. An approximate correction was made for gamma heating based on a previous experiment in the HB-3 beam hole. The resulting values of flux as a function of position are shown in Fig. 5.6.

Examination of Irradiated Capsules

ORR- and ETR-Irradiated Full-Diameter Capsules

The first eight ORR-irradiated prototype capsules are shown in Fig. 5.7 after being removed from the NaK container and cleaned. There

Table 5.5. ORNL-MTR-48-1 Fuel Element Test Parameters Estimated from Operating Data

Test Parameters	Fuel Element A	Fuel Element B
Test duration (MTR at 40 Mw), hr	1446	1446
Graphite capsule wall temperature less coolant water temperature (110°F), °F		
Design	1392	1467
Value for B element when A element was at design point		1205
Average operating value	1450	1240
Thermal neutron flux, neutrons/cm^2·sec		
Design	4.6×10^{13}	2.6×10^{13}
Value for B element when A element was at design point		2.1×10^{13}
Average operating value	4.8×10^{13}	2.2×10^{13}
Weight of fueled graphite, g	35.41	37.84
Weight of UC_2, g	10.52	19.33
U^{235} content (93.12% enrichment), wt %	8.89	16.33
U^{235} concentration, g/cm^3	0.1677	0.3295
U^{235} concentration, atoms/cm^3	42.9×10^{19}	84.3×10^{19}
Fission power density, w/cm^2		
Design	270	300
Value for B element when A element was at design point		242
Average operating value	282	254
U^{235} atoms fissioned, atoms/cm^3	5.24×10^{19}	4.72×10^{19}
U^{235} atoms fissioned based on average power, %	12.2	5.6
Burnup of fueled graphite matrix, Mwd/MT	8970	7560
Burnup of U^{235}, Mwd/MT	101 000	46 300

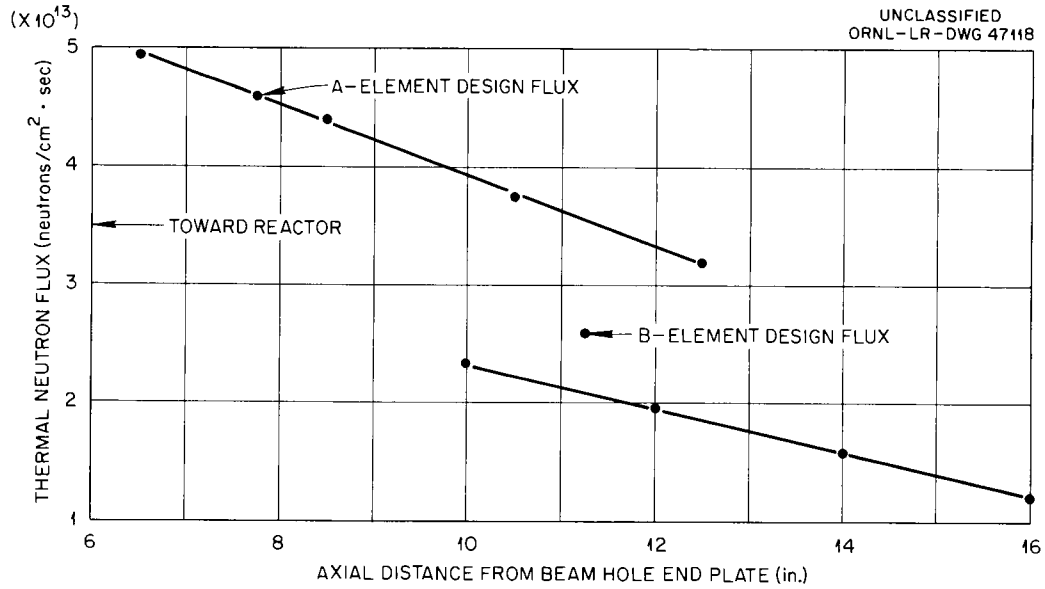

Fig. 5.6. Thermal Neutron Flux Versus Axial Distance of Fueled Matrix Centers from HB-3 Beam Hole End Plate (ORNL-MTR-48, Capsule Test 1, MTR Cycles 130–133).

was no visible evidence of significant distortion. Postirradiation diameter and profile measurements also showed little change. Typical dimensions are given in Fig. 5.8 for capsule O-1. Gamma radioactivity scans were taken by slowly raising the pellet can past a 1/16-in. slit in a lead shield containing a proportional counter. The counter consisted of an ion chamber connected to a DD-2 amplifier and the linear count-rate meter driving a recorder. The relative values of the radioactivity of the O-1 capsule thus obtained are also indicated in Fig. 5.8.

A summary of the data obtained in examinations of the eight ORR capsules and one ETR capsule is presented in Table 5.6. The fission-gas release values were calculated from pressure measurements on the four capsules containing hollow pellets. Uncertainties in the central pellet temperatures may account for the spread in the data.

Measurements of Fission-Gas Pressure at EGCR Operating Temperature

Since iodine and cesium and their compounds have boiling points that are near the temperature at which the cladding of the EGCR fuel elements

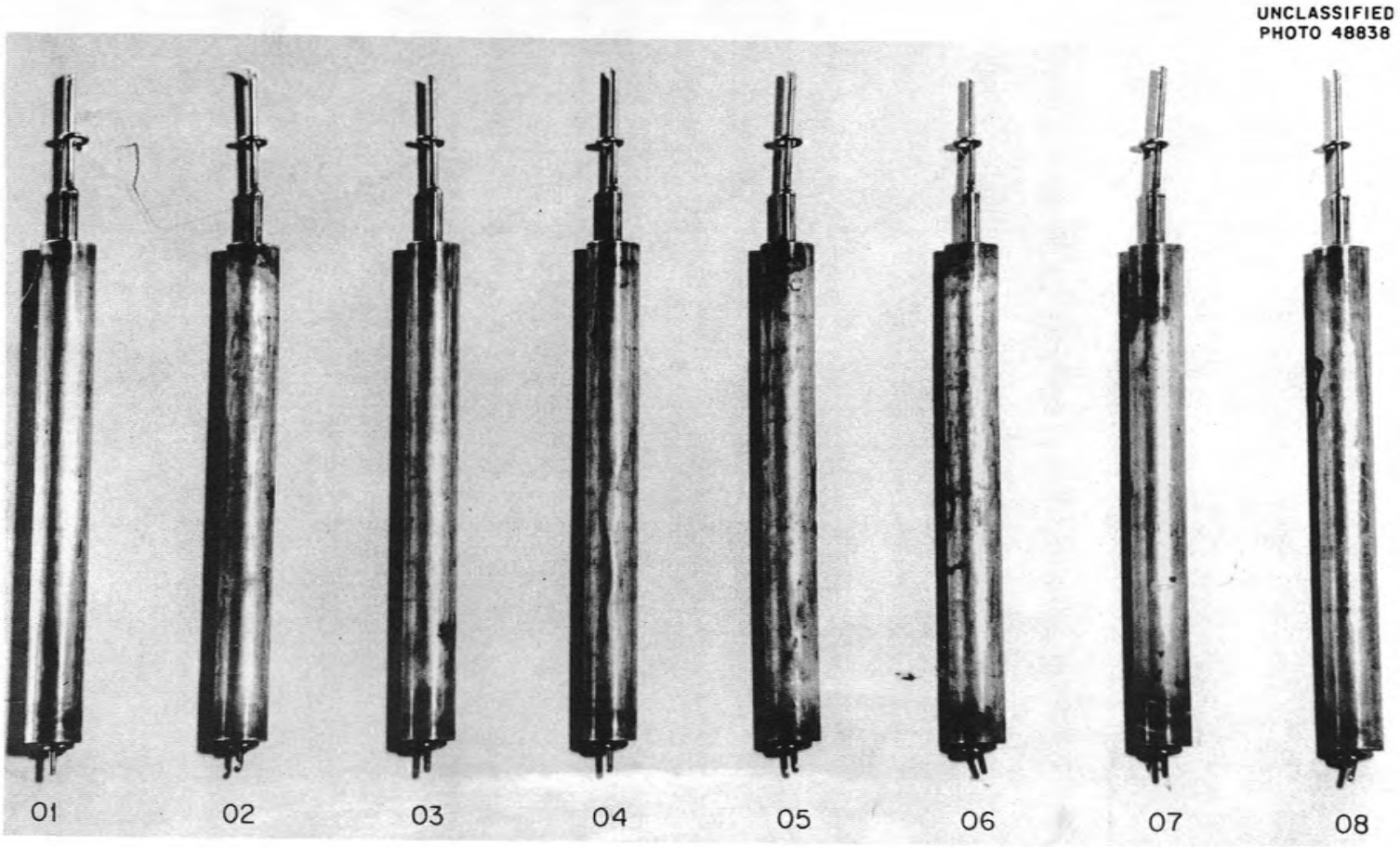

Fig. 5.7. Full-Diameter Prototype EGCR Fuel Capsules After Irradiation in ORR.

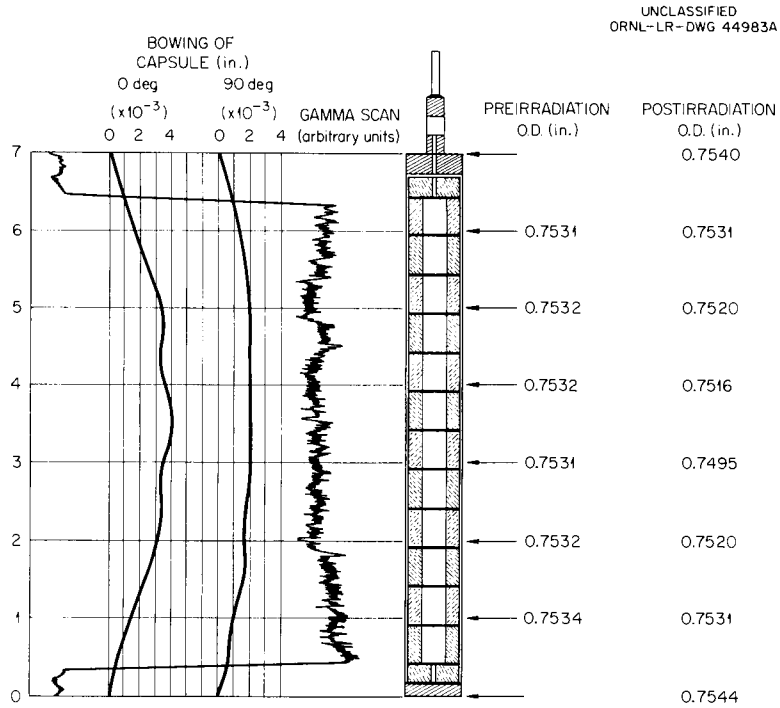

Fig. 5.8. Results of Dimensional Measurements and Gamma Activity Scan of ORR Capsule O-1.

will operate, it is necessary to find out whether these fission products will make a significant contribution to the over-all pressure buildup in the fuel elements. A postirradiation pressure measurement at the EGCR operating temperature is therefore planned for the remaining ORR capsules O-4, O-6, O-7, and O-8. The apparatus for making the pressure measurement is shown in Fig. 5.9. The capsule container is equipped with a piercing device and a pressure transducer, and the entire apparatus can be placed in the furnace.

One test assembly has been completed and tested; all parts functioned satisfactorily. The tapered plug had a leakage of less than 1×10^{-4} standard cubic centimeters of helium with a differential pressure of 1 atm at 1650°F after being previously tested at the same temperature, disassembled, and reassembled. The piercing needle pierced 1/32-in.-thick stainless steel four times after being brazed at 2000°F. The pressure transducer drifted less than 0.1 psi from room temperature to

1650°F. Four more pressure-measuring chambers are nearly completed and will be used for making the pressure measurements on the ORR capsules.

Table 5.6. Data Obtained in Postirradiation Examinations of Eight ORR-Irradiated Capsules and One ETR-Irradiated Capsule

Capsule No.	Cladding Temperature (°F)	Burnup[a] (Mwd/MT)	Type of Pellet	Average Capsule Diameter (in.)		Internal Capsule Pressure[b] at 86°F (mm Hg)	Fission-Gas Evolution (%)
				Before Irradiation	After Irradiation		
0-1	1300	1760	Hollow	0.7532	0.7525	790	9.3
0-2	1600	1910	Hollow	0.7528	0.7494	830	11.6
0-3	1300	1640	Hollow	0.7530	0.7539	790	10.2
0-4	1300	2510	Bushing	0.7520	0.7526	c	
0-5	1600	3260	Hollow	0.7522	0.7504	900	8.1
0-6	1600	1980	Bushing	0.7525	0.7501	c	
0-7	1300	1100	Solid	0.7526	0.7527	c	
0-8	1600	1050	Solid	0.7528	0.7525	c	
E-1	1300	1000	Solid	0.7530	0.7552		

[a]Calculated from neutron activation of thermocouple band.

[b]Preirradiation pressure assumed to be 690 mm Hg on the basis of measurements on dummy capsules.

[c]Capsule to be used later for temperature versus pressure experiments.

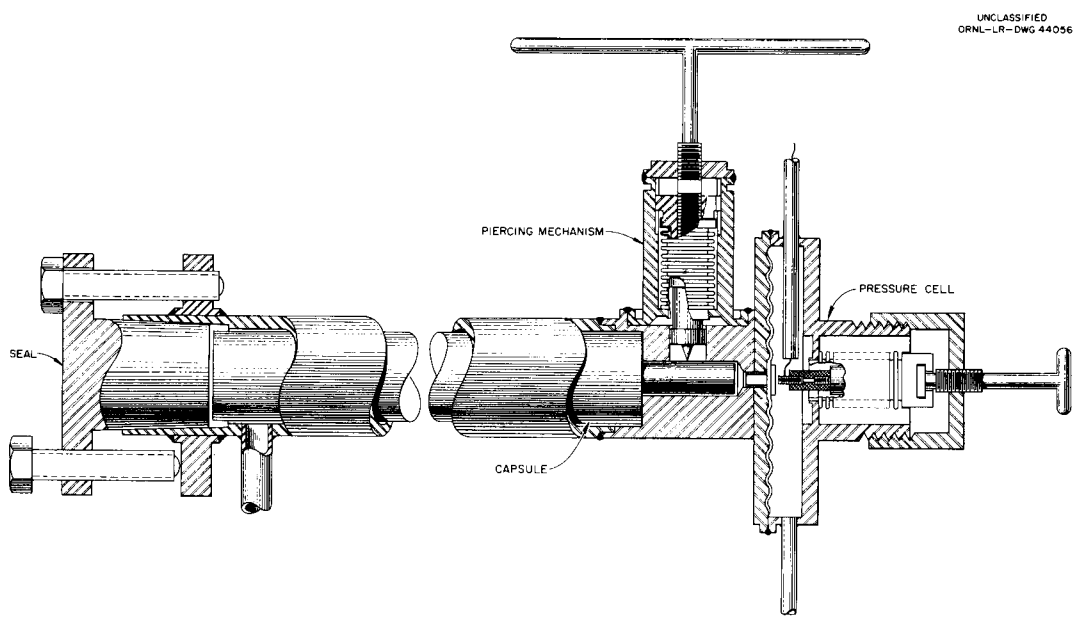

Fig. 5.9. Apparatus for High-Temperature Measurements of Fission-Gas Pressure in Irradiated Capsules.

LITR-Irradiated Miniature Capsules

Experimental assemblies L-7x and L-11 were withdrawn from the LITR on February 9 and disassembled in the ORR hot cell. The capsules were pierced for fission-gas sampling and then placed in temporary storage. The fission-gas sample is being analyzed, and measurements are to be made of the densities of the UO_2 pellets.

Measurements of postirradiation densities that were made during the quarter are compared in Table 5.7 with preirradiation values. Fission-gas evolution data obtained during the quarter from samples taken previously are summarized in Table 5.8.

It was mentioned previously that, when capsule L-8a was examined, extensive damage of the thermocouple was noted. Further examination has revealed that the tantalum sheath on the thermocouple had disintegrated, as shown in Fig. 5.10. Such bursting of the sheath and exposure of the rhenium-tungsten junction is typical of the experience with high-temperature irradiations.

Table 5.7. UO_2 Density Data

Capsule No.	Pellet Density Before Irradiation			Pellet Immersion Density After Irradiation (g/cm^3)
	Bulk Density (% of theoretical)	Bulk Density (g/cm^3)	Immersion Density (g/cm^3)	
L-3a	75.00	8.23	10.66	10.6
L-3b	74.87	8.21	10.66	10.4
L-8a	84.58	9.28	10.19	10.1
L-8b	85.01	9.33	10.18	10.3
L-13a	93.68	10.28	10.60	10.7
L-13b	92.07	10.19	10.60	10.7
L-17a	93.69	10.28	10.43	10.5
L-17b	93.80	10.29	10.38	10.5
L-18a	84.91	9.32	10.35	10.4
L-18b	85.19	9.35	10.40	10.5

Table 5.8. Fission-Gas Release from LITR-Irradiated Miniature Capsules

Capsule No.	UO_2 Density (% of theoretical)	Central UO_2 Temperature (°F)	Burnup (Mwd/MT)	Fission-Gas Evolution (%)				Oxygen-to-Uranium Ratio	Carbon Content of UO_2 (ppm)
				Kr^{85m}	Kr^{88}	Xe^{133}	Xe^{135}		
L-3a	75.00	~3000	5 000			0.42		2.1178	2400
L-3b	74.87	~3000	5 000			19		2.1178	2400
L-16a	94.35	1800	9 000			0.027	0.012	2.0052	70
L-16b	94.38	2050	9 000	<0.030		0.062	0.014	2.0052	70
L-17a	93.69	2450	11 000	0.04	0.04	0.20	0.050	2.0034	210
L-17b	93.80	2600	11 000	0.13	0.24	1.3	0.32	2.0022	97

UNCLASSIFIED
PHOTO 49932

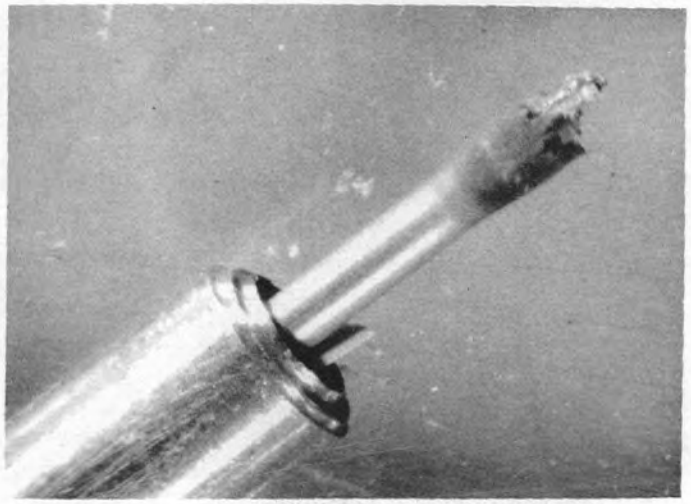

Fig. 5.10. Tantalum-Sheathed Thermocouple from Capsule L-8a Showing Typical Damage to Sheath.

GETR-Irradiated Capsules

Postirradiation examinations have been completed on the GETR-irradiated capsules, except for ceramographic studies of the fuel. The dimensional data taken included profile plotting (for evidence of warping) and diameter measurements. Since the distortion of the capsules was primarily due to the axial thrust from thermal expansion of the sheathed

thermocouples, no conclusions could be drawn from the profile measurements except that the capsules were all more or less warped. Diameter measurements were made on each capsule at 1/2-in. intervals along the length, and each measurement was repeated at a 45-deg rotation, that is, measurements were made at 0, 45, 90, and 135 deg. Thus there were 56 diameter measurements made on each capsule both before and after irradiation. Although the capsules were warped and the range of diameters changed during irradiation, it was expected that the average diameter remained unchanged. The range of diameters and the average of the 56 measurements are given in Table 5.9. The largest change is a 0.0037-in. decrease in the diameter of capsule 3 of stringer 1-4. The irradiation history of these stringers is summarized in Table 5.10, and a detailed history of the experiments has been published.[3]

Gamma-activity scans of the stringers were made by moving them past a slit in a lead shield and measuring the activity as a function of distance along the stringer. The activity along the stringer was expected to be proportional to the burnup, and the activity profiles of stringers 1-2, 1-3, 1-4, and 1-5 showed normal flux curves. Capsule 3 (bottom) of stringer 1-1, however, showed a possible redistribution of the fuel (see Fig. 5.11). This capsule and capsule 3 from stringer 1-3 were punctured for fission-gas release, and no significant pressure increases were measured. The fission gas was analyzed for Xe^{133} and Kr^{85}, and, on the basis of 0.06% release of Kr^{85}, the burnup was 0.1%. This burnup value agrees with that obtained from the flux monitor for this capsule, and, since the amount of gas release was insignificant, no other capsules were sampled for fission gas.

Capsule 3 of stringer 1-1 was impregnated with plastic and sectioned to ascertain the cause of the peak in the gamma-activity profile. Although the fuel did not appear to be fractured in an abnormal manner, some fuel was present in the form of large fragments in the central cavity of the element (see Fig. 5.12). For comparison, capsule 3 of

[3] "GCPR-Prototype Fuel Irradiation Program Progress Report No. 15, October 18, 1959 to November 18, 1959," GEAP-3350.

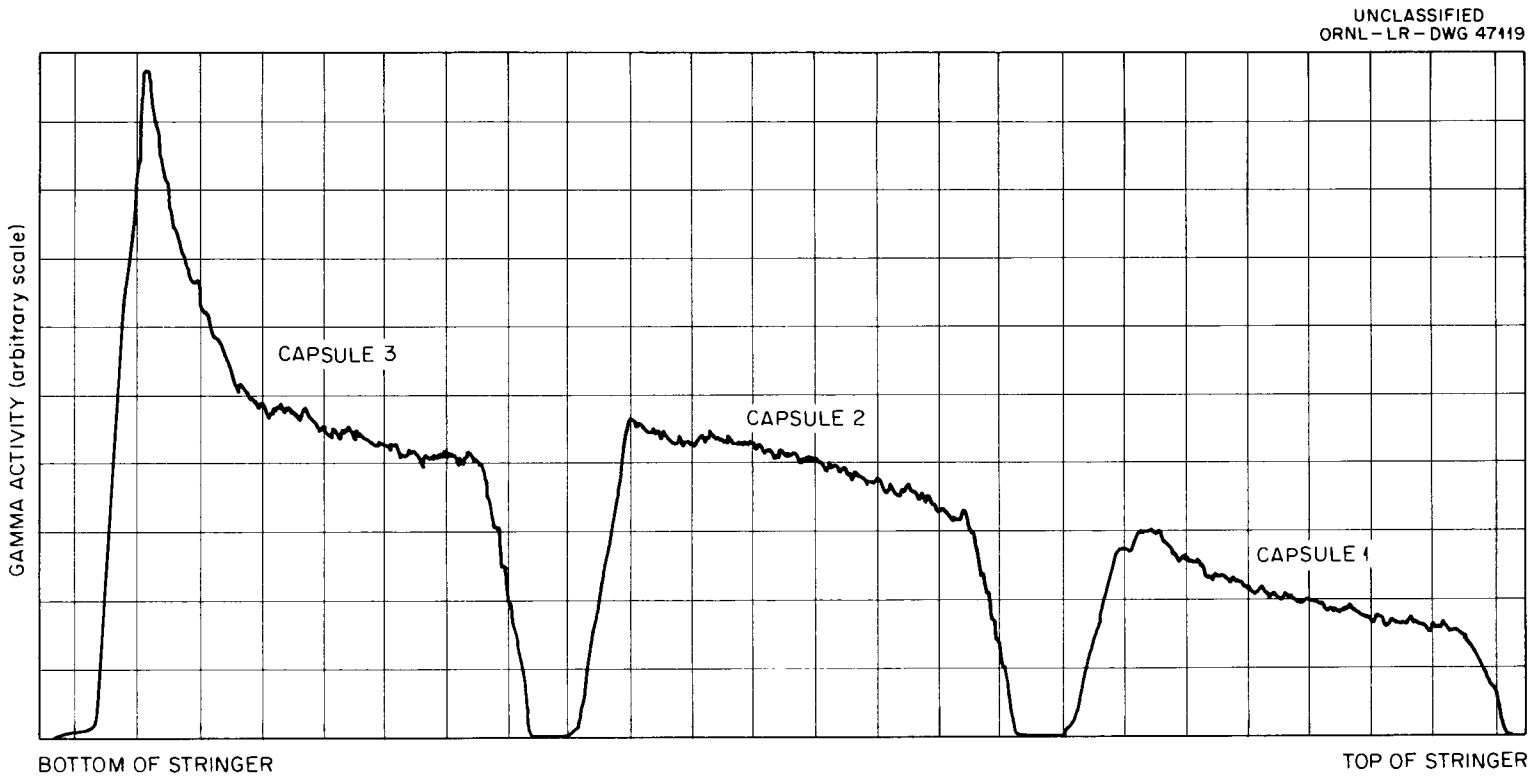

Fig. 5.11. Gamma Activity Profile of GETR-Irradiated Stringer 1-1.

Fig. 5.12. Section Through Bottom of Capsule 3 of Stringer 1-1.

Table 5.9. Comparison of Pre- and Postirradiation Dimensions of Capsules Irradiated in Stringers in the GETR

Capsule No.	Capsule Diameter (in.)					
	Before Irradiation			After Irradiation		
	Minimum	Maximum	Average	Minimum	Maximum	Average
			Stringer 1-1			
1 (top)	0.532	0.534	0.5328	0.5298	0.5348	0.5325
2 (middle)	0.532	0.533	0.5327	0.5290	0.5349	0.5319
3 (bottom)	0.532	0.533	0.5329	0.5270	0.5357	0.5320
			Stringer 1-2			
1	0.532	0.534	0.5327	0.5312	0.5356	0.5331
2	0.532	0.534	0.5327	0.5273	0.5527	0.5325
3	0.532	0.534	0.5329	0.5191	0.5671	0.5339
			Stringer 1-3			
1	0.532	0.535	0.5329	0.5292	0.5356	0.5332
2	0.532	0.534	0.5329	0.5200	0.5373	0.5304
3	0.532	0.534	0.5331	0.5276	0.5359	0.5306
			Stringer 1-4			
1	0.532	0.534	0.5328	0.5282	0.5338	0.5311
2	0.532	0.534	0.5330	0.5247	0.5359	0.5295
3	0.532	0.534	0.5328	0.5219	0.5355	0.5291
			Stringer 1-5			
1	0.532	0.534	0.5331	0.5315	0.5338	0.5328
2	0.533	0.535	0.5331	0.5283	0.5380	0.5314
3	0.532	0.534	0.5330	0.5274	0.5354	0.5306

stringer 1-4 was impregnated with plastic and sectioned (see Fig. 5.13). Radial cracks are clearly visible, but the fuel did not move.

All the capsules were slit open, and the fuel was removed. Typical pellets are shown in Figs. 5.14 and 5.15. Fractures in the UO_2 were imprinted on the interior of the cladding, as shown in Fig. 5.16. The reason for the appearance of the markings is not known. Since the crack imprints have the same intensity as the imprints of the gaps between

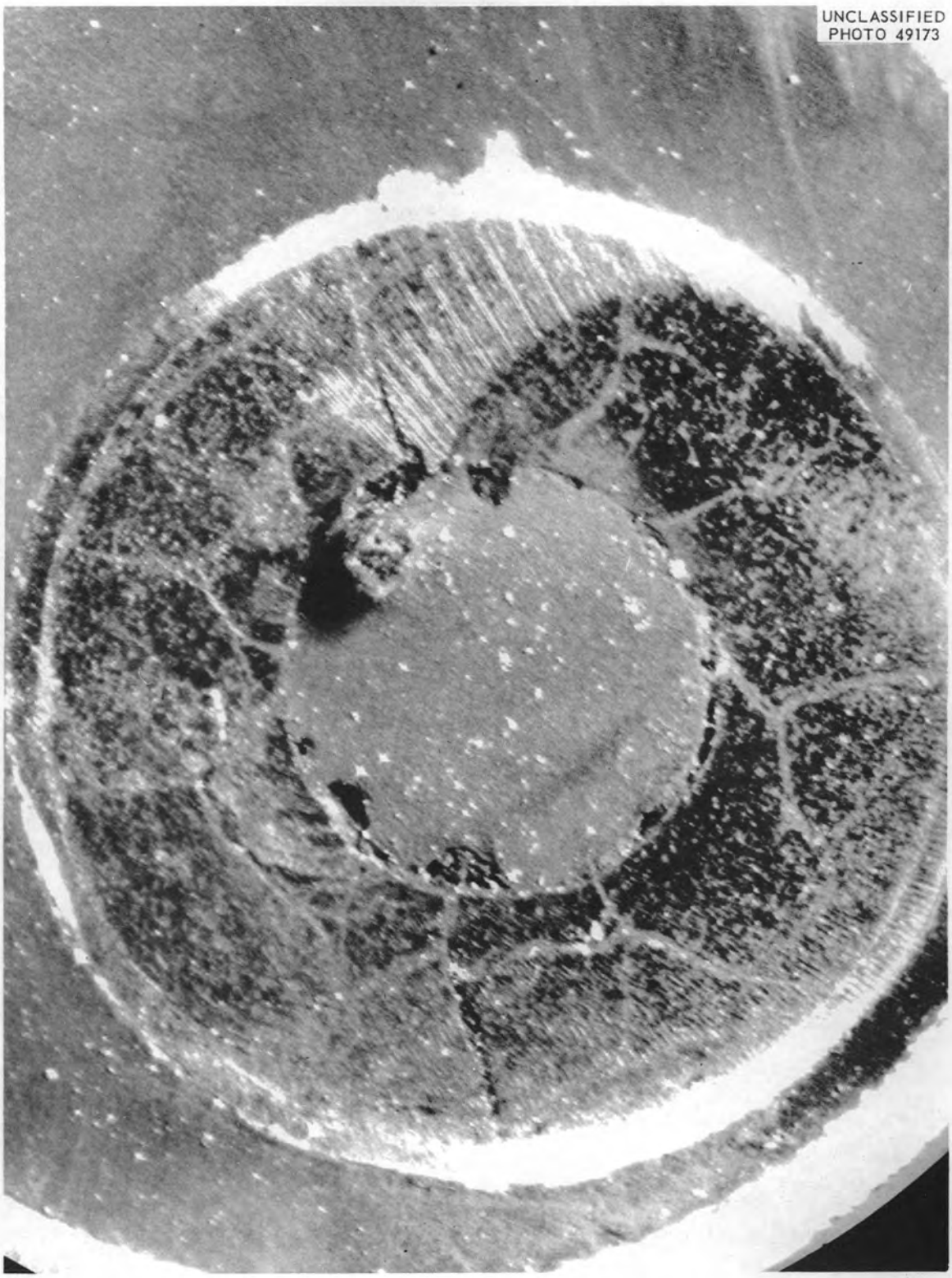

Fig. 5.13. Section Through Bottom of Capsule 3 of Stringer 1-4.

Fig. 5.14. Typical UO_2 Pellets from Capsules Irradiated in GETR.

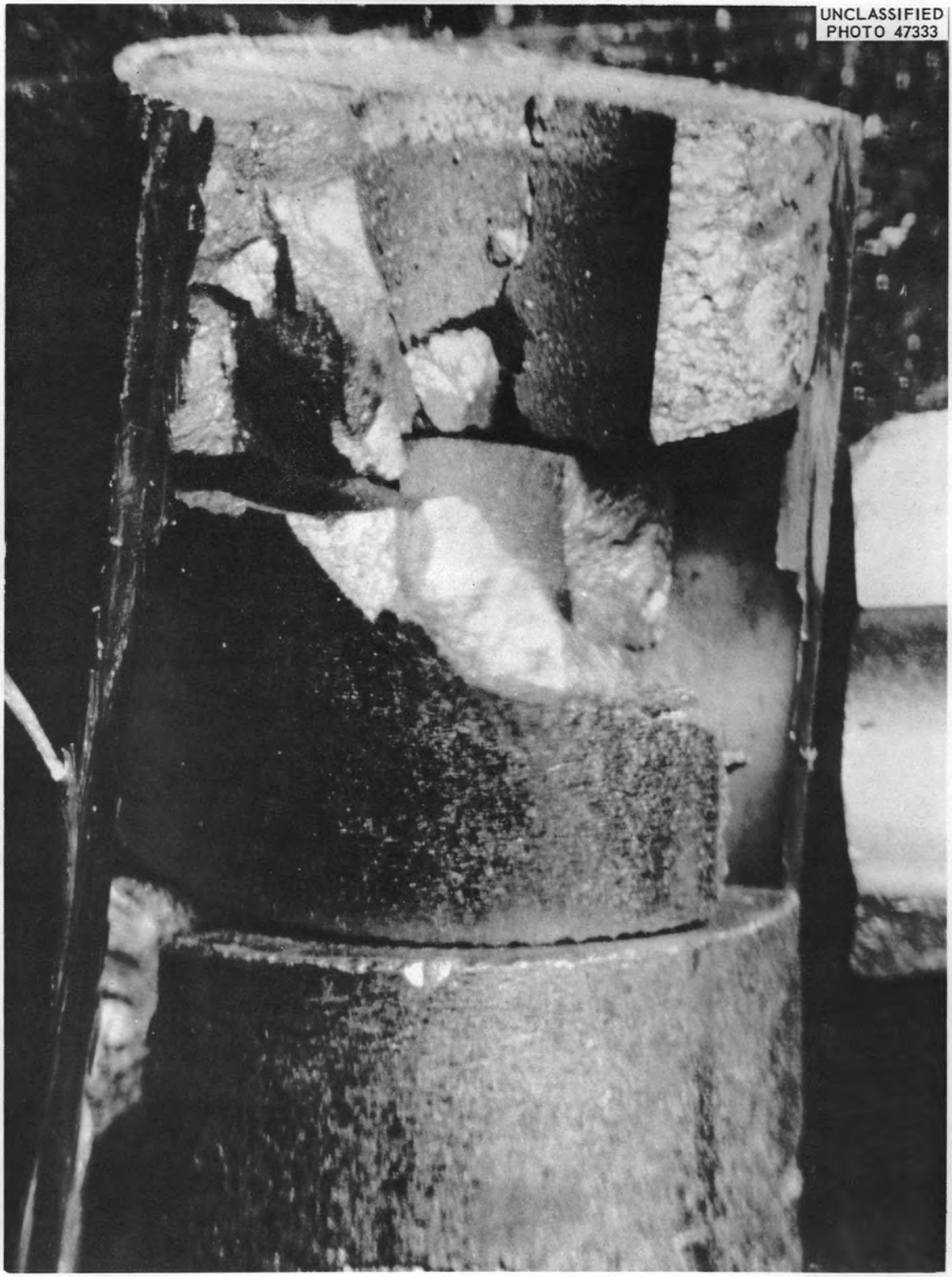

Fig. 5.15. UO_2 Pellets in Opened Capsule.

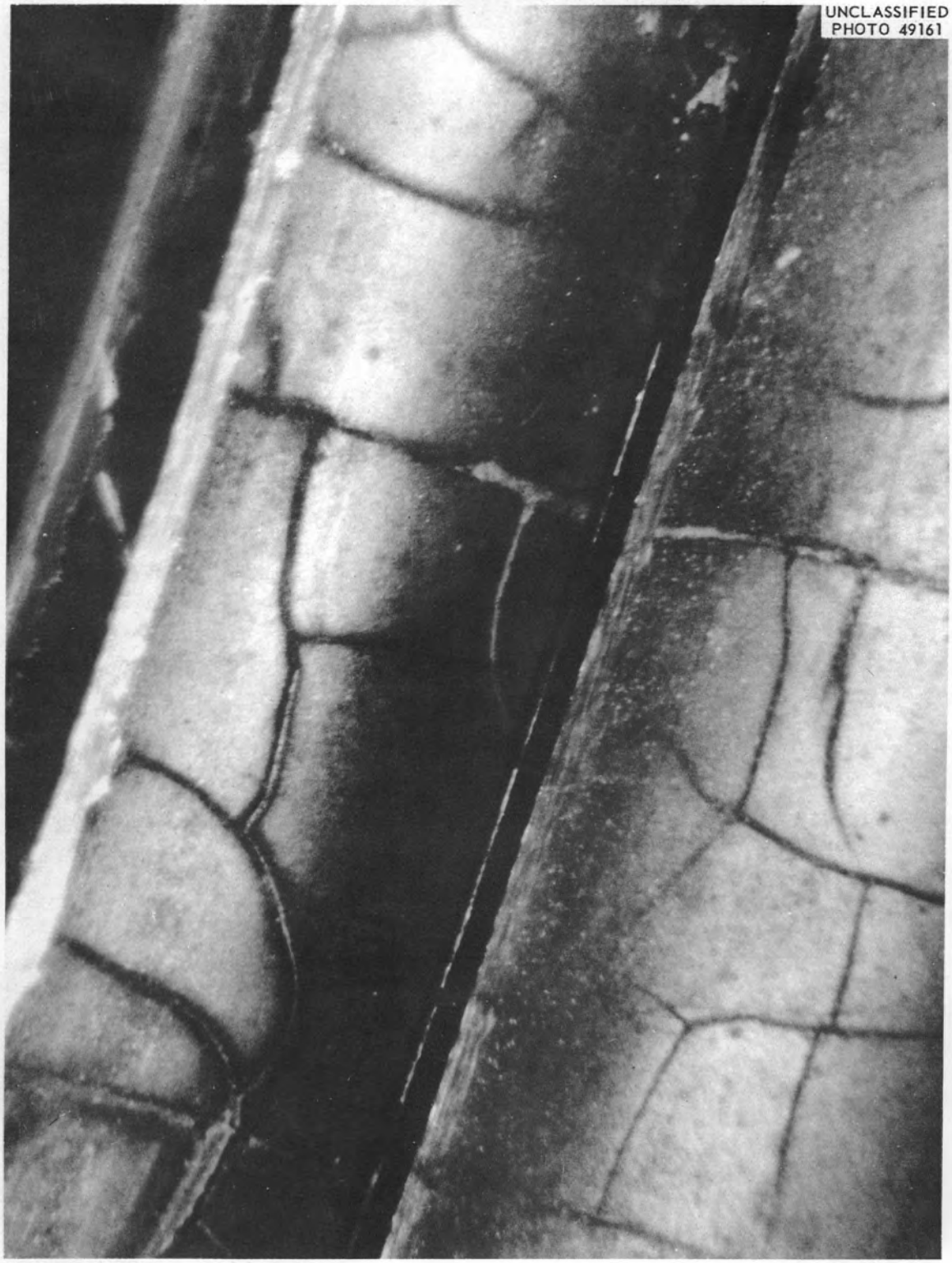

Fig. 5.16. Inner Surface of Capsule 1 of Stringer 1-3.

Table 5.10. History of Irradiation of Stringers in GETR

Stringer	Irradiation Period (1959)		Approximate Operating Temperatures (°F)	Capsule No.	Uranium Burnup (%)
	Inserted	Removed			
1-1	May 11	October 16	700–800	1	0.007
				2	0.010
				3	0.023
1-2	May 14	October 16	700–1000	1	0.014
				2	0.028
				3	0.064
1-3	May 4	October 16	700–900	1	Unknown
				2	0.050
				3	0.080
1-4	May 4	November 5	600–800	1	0.026
				2	0.048
				3	0.113
1-5	October 11	November 5	800–1000	1	0.014
				2	0.030
				3	0.051

pellets, it appears that the cracks occurred suddenly and did not progress with time. Because of the low burnup, no density measurements were made on the UO_2, and the stainless steel cans were not examined metallographically.

Instantaneous Fission-Gas-Release Experiment

Fission-Gas-Release Measurements

The experimental assembly now being irradiated in the ORR contains two thin plates of high-density UO_2 with thermocouples sandwiched between them and on the outer surfaces. The assembly is air-cooled, and the fission power is varied by inserting or withdrawing the assembly from the reactor lattice. Helium is passed over the fuel to entrain released fission gases. The experimental apparatus and procedures are described in detail in previous reports in this series. Modifications were being

made to the ORR offgas system during the period from December to February, and consequently only a few weeks operation has been possible this quarter.

The activity which reaches the counter of the experimental system is from three main sources: (1) fission gases, primarily xenon and krypton, that are evolved from the fuel during irradiation (a filter removes nongaseous products before they reach the counter tube); (2) daughter products that form after the gases pass through the filters and which plate the inside of the counter tube; (3) xenon formed from iodine which evolved from the fuel and plated somewhere along the line before reaching the counter tube. Typical spectra obtained with a 200-channel analyzer are shown in Fig. 5.17.

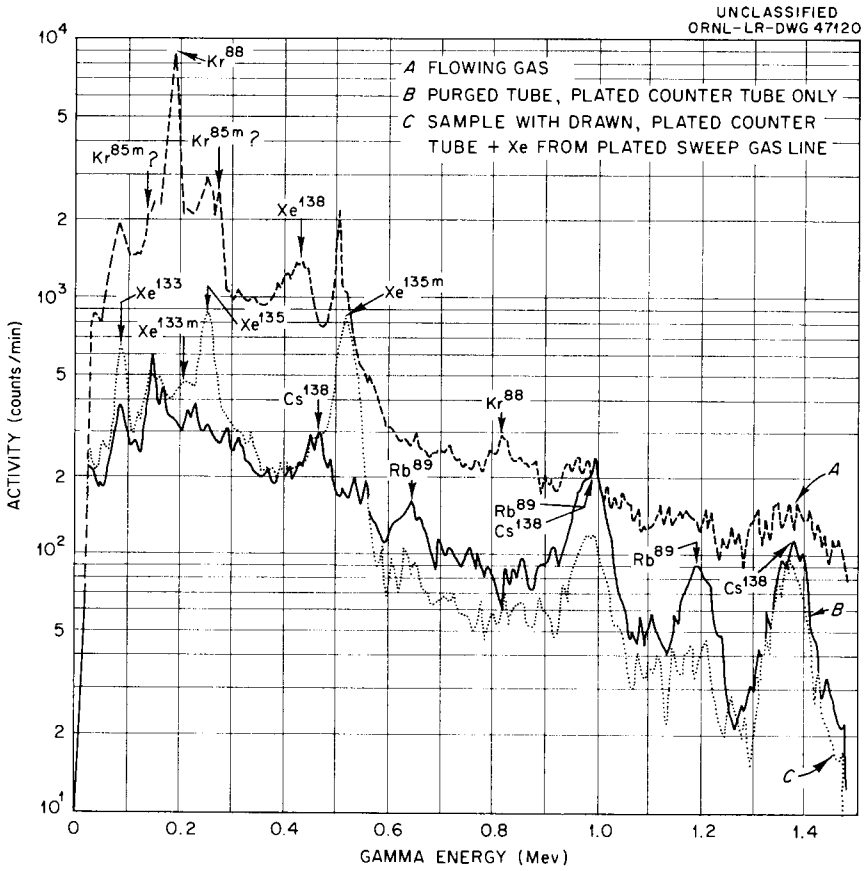

Fig. 5.17. Typical Fission-Gas Spectra Obtained in Instantaneous Fission-Gas-Release Experiment.

Curve A is a combination of all three sources. Curve B is from the second source only. This measurement is obtained by diverting the fission gas from the counter tube and then blowing the counter tube clear of radioactive gas with a blast of helium. The activity that still persists is from material plated in the counter tube. Curve C is a combination of sources 2 and 3. The data were obtained by withdrawing the fuel from the neutron flux and sweeping the carrier helium over the relatively cold specimen. Curve C was taken 45 min after curve B, so the background from the plated material of source 2 had decayed. Curve B was obtained 2 min after curve A.

Surface area measurements of the UO_2 plates (which have a density of about 97% of theoretical) were made with the use of krypton gas under pressure. The measurements indicated that the BET surface area is approximately twice the geometric surface area. In this case, the equivalent-sphere model is not particularly good for evaluating diffusion constants. Therefore the following "flat-plate model" time-dependent solution developed by Litz[4] for evolution of gaseous fission products from a thin plate was used in analyzing the data:

$$T = \frac{2}{A}\left\{\tanh\frac{A}{2} - \frac{4}{A}\sum_{n}^{\infty}\frac{1}{1+\left(\frac{\pi n}{A}\right)^2}\exp-\left[1+\left(\frac{\pi n}{A}\right)^2\tau\right]\right\}, \qquad (1)$$

where

T = fractional release rate,

$A = a(\lambda/D)^{1/2}$, dimensionless parameter,

a = plate thickness, cm,

λ = decay constant of species, sec^{-1},

D = diffusion constant, cm^2/sec,

[4]L. M. Litz, "Diffusion Equation for Radioactive Species in Thin-Plate Nuclear Reactors," p. 8, LRL-97 (March 1954).

$\tau = \lambda t$, a dimensionless parameter,

t = time of irradiation, sec,

n = odd integers from 1 to ∞.

The fractional release rate, T, was evaluated from Eq. (1) for values of A from 10^{-3} to 10^{-4} and values of λt from 10^{-3} to 10. It was found that T behaves as follows:

$$T \cong 1 \quad , \qquad \text{for } A \leqslant 0.01 \text{ and } \lambda t \geqslant 10^{-3} \quad ,$$

$$T \approx \frac{2}{A} E(\lambda t)^{1/2} \quad , \qquad \text{for } A \geqslant 10 \text{ and } \lambda t \geqslant 10^{-3} \quad ,$$

where

$$E(\lambda t)^{1/2} = \frac{2}{\pi} \int_0^{(\lambda t)^{1/2}} e^{-x^2} \, dx$$

and may be evaluated from the tables of Jahnke and Emde,[5] and

$$T \approx \frac{2}{A} \qquad \text{for } A \geqslant 10 \text{ and } \lambda t \geqslant 3 \quad .$$

The diffusion constants were then calculated on the basis that λt was greater than 3, that is, greater than four half-lives, and that $A > 10$; thus

$$D = \frac{a^2}{4} \lambda T^2 \quad .$$

The calculated diffusion constants of the various isotopes, with the exception of that for Xe^{135m} (the shortest lived isotope of those measured),

[5] E. Jahnke and F. Emde, "Tables of Functions with Formulae and Curves," 4th ed., p. 24, Dover, 1954.

were reasonably consistent, and hence they support the thesis that xenon and krypton have diffusion constants of the same order of magnitude.

The various dynamic gaseous fission-product yields and the calculated diffusion constants are presented in Table 5.11. The yields are based on "grab" samples taken during various runs. The data for a maximum plate temperature of 1945°F are the average of two measurements made two days apart under the same operating conditions. The individual results agreed to within 10%. The operating conditions under which the

Table 5.11. Dynamic Fission-Gas Yields and Calculated Diffusion Coefficients Based on the Flat-Plate Model

Maximum UO_2 Plate Temperature (°F)	Temperature Difference Across Plate (°F)	Isotope Released	Fraction Released	Calculated Diffusion Constant (cm^2/sec)
			$\times 10^{-4}$	
1945	195	Kr^{87}	3.5	4.1×10^{-15}
		Kr^{88}	8.4	10.8×10^{-15}
				7.4×10^{-15} average Kr
		Xe^{133}	30.3	3.1×10^{-15}
		Xe^{135}	9.8	4.5×10^{-15}
		Xe^{135m}	5.4	4.7×10^{-14}
		Xe^{138}	2.3	7.8×10^{-15}
				15.5×10^{-15} average Xe
				5.2×10^{-15} average Xe exclusive of Xe^{135m}
1890	200	Kr^{87}	2.7	2.3×10^{-15}
		Kr^{88}	4.6	3.3×10^{-15}
				2.9×10^{-15} average Kr
		Xe^{133}	20.0	1.3×10^{-15}
		Xe^{135}	6.5	2.0×10^{-15}
		Xe^{135m}	4.2	2.8×10^{-14}
		Xe^{138}	1.0	1.5×10^{-15}
				10.9×10^{-15} average Xe
				1.6×10^{-15} average Xe exclusive of Xe^{135m}

measurements were made for a maximum plate temperature of 1890°F were the same as for the measurements with a plate temperature of 1945°F, except for lower temperatures obtained by increased cooling.

Equipment Modifications

The gas-sampling system has been modified to avoid the complexities of backgrounds and short-lived compoents. A hypodermic needle with a three-way valve was installed in the gas line so that with a vaccine bottle pushed onto the needle the bottom may be evacuated and then filled with the active gas. The rubber stopper in the vaccine bottle seals gastight against the needle and remains leaktight when the needle is removed. The gas in the bottle is at a negative pressure at all times. After a short decay period, the gas in the bottle is analyzed for xenon and krypton.

UO_2 Thermal Conductivity Determinations

An inside and an outside thermocouple were connected for use as a differential couple with the voltage measured by a precision potentiometer, and the first several days of operation after the two-month shutdown period were devoted to thermal conductivity measurements. It was at once obvious that the temperature relations had changed from those existing before shutdown. Moreover it was noted that the relative temperatures were varying, that is, changing in abrupt steps and with always increasing temperature differentials.

From a study of these temperature relations it appears that one of the two plates had cracked and moved away from the thermocouple and that the other plate has retained its original position. No further thermal-conductivity measurements can be made on this sample. The plate either cracked during shutdown or during a low-power startup. The reason for the cracking is not known.

Radiation Effects on Structural Metals

Steel

Tests on the annealing of radiation-induced hardening as a function of annealing time are in progress, and specimen steels have been obtained to conduct an extensive study of irradiation temperature and neutron flux effects. Specimen preparation is now under way.

Irradiation experiment components used previously in the ORR poolside facility did not permit the exposure of an adequate number of specimens at uniform temperatures and neutron fluxes. Improved components are being developed, and mockup tests on these components are now being conducted.

Beryllium

As discussed previously,[6] a program has been established for determining the effect of neutron irradiation on the creep strength and permeability of beryllium. Specimen preparation for the high-temperature and low-temperature beryllium irradiation experiments has been completed, and analysis of preirradiation measurements is almost complete. The types of specimens that are being irradiated in both the high-temperature and low-temperature experiments are shown in Fig. 5.18. Notches were machined in the specimens to force the fracture, upon bend testing, to occur at the position of the notch so that the pieces may be used for subsequent experiments. The effects of the degree and type of preferred orientation on the properties of beryllium under irradiation are being investigated in both experiments by including specimens machined from hot-pressed block, extruded rod, unidirectionally rolled sheet, and cross-rolled sheet.

The specimens were annealed for 2 hr at 800 and 1100°C in order to vary the grain size. It was found, however, that these heat treatments produced recrystallization and that little grain growth occurred. In an

[6] "GCR Quar. Prog. Rep. Dec. 31, 1959," ORNL-2888, pp. 127–133.

UNCLASSIFIED
ORNL-LR-DWG 47121

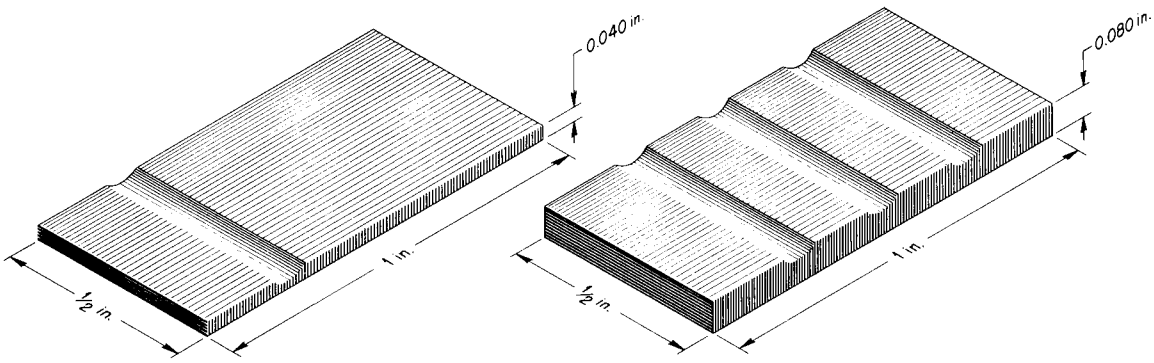

Fig. 5.18. Design of Beryllium Irradiation Test Specimens.

effort to produce a coarser grain size, a specimen was annealed at 1200°C, but, again, only a small amount of grain growth occurred. This inability to coarsen the grain size can probably be attributed to the oxide network around the original powder particles from which the beryllium was produced. The annealing treatment at 1100°C was chosen therefore because of the experimental difficulties encountered at higher temperatures and because it appeared that annealing at a higher temperature would not result in further grain coarsening.

Prior to operating creep experiments, it was necessary to determine the amount of helium gas that would be produced in the beryllium by the (n,α) and (n,2n) reactions and to study the mobility of the gas and the void formation in the metal as a function of crystal orientation, grain size, section thickness, and temperature. Two experimental assemblies have been installed in the ORR for the gas-evolution studies. One assembly, which contains 55 beryllium specimens mounted in an aluminum holder, was placed in core positon B-2. The specimens are cooled by reactor water with a maximum temperature of 130°F. The beryllium specimens mounted in the cooling channels of three aluminum plates and the exposure can which holds the plates and specimens after assembly may be seen in Figs. 5.19 and 5.20. The fourth plate shown in Fig. 5.19 is a blank, cover plate. The four plates are bolted together and fitted

UNCLASSIFIED
PHOTO 48819

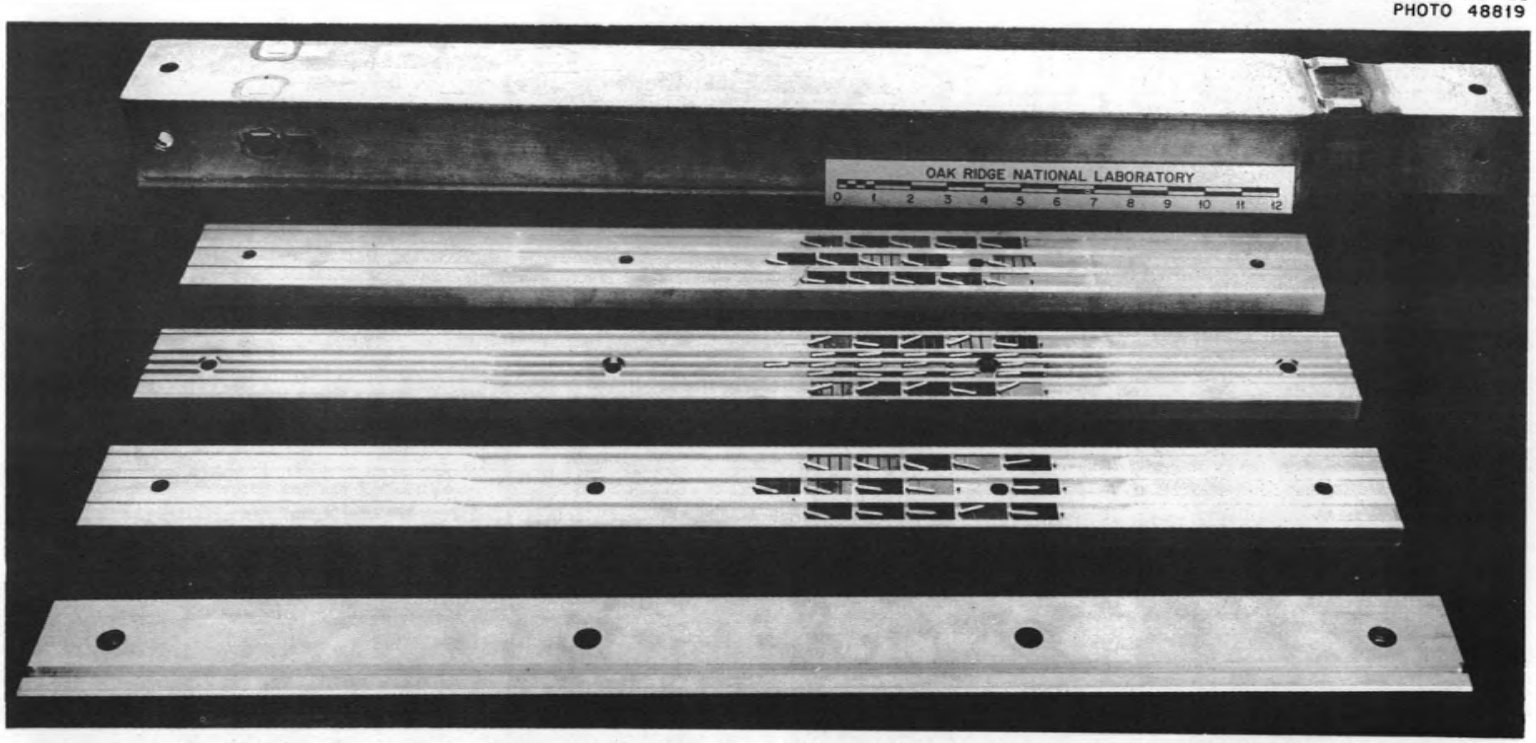

Fig. 5.19 Apparatus for Low-Temperature Irradiation of Beryllium Specimens.

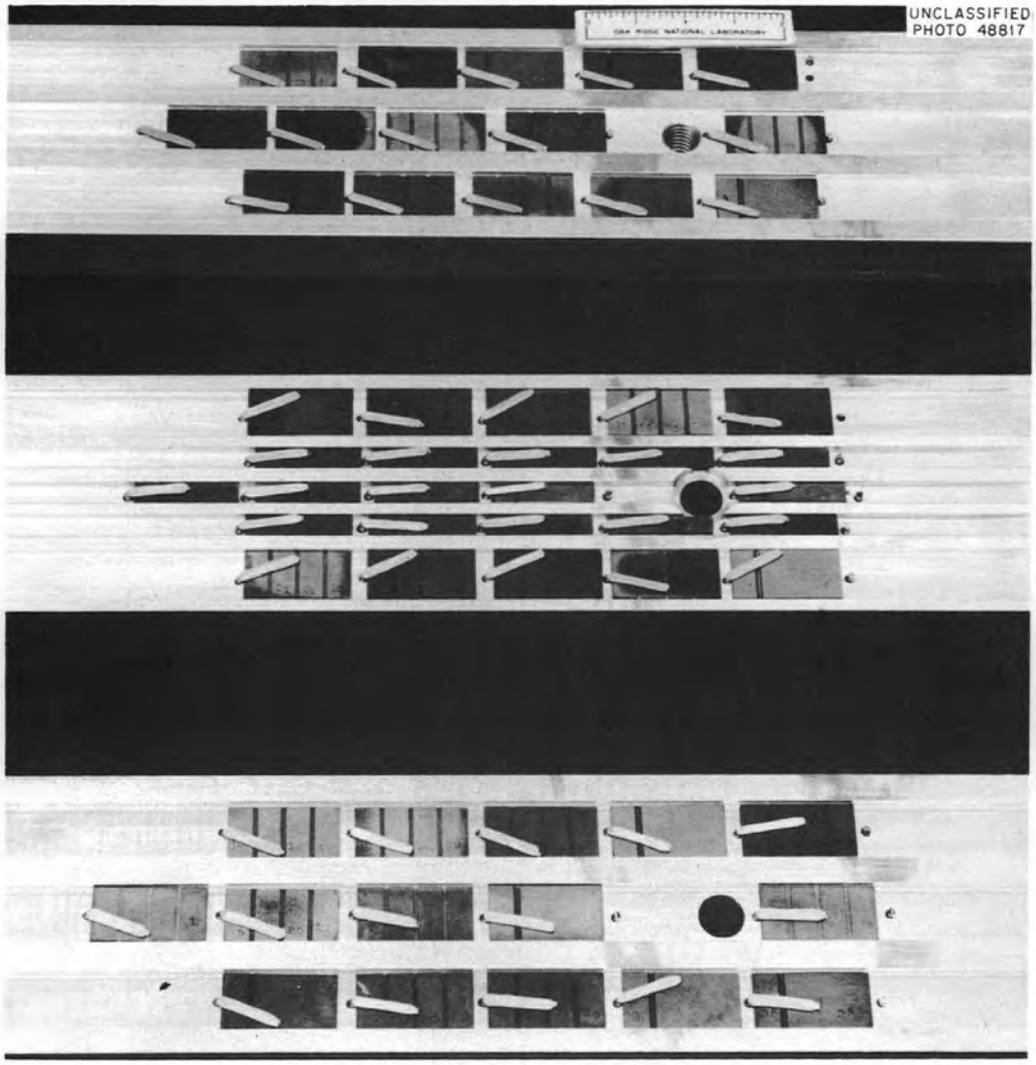

Fig. 5.20. Beryllium Specimens Mounted in Cooling Channels. The narrow specimens are 0.080 in. thick and the wide specimens are 0.040 in. thick. A bend test will be conducted at each notch after irradiation and, in some cases, thermal annealing.

into the exposure can. This experimental assembly was inserted in the reactor on January 1, 1960, and the reactor is now on its third subsequent cycle. This experimental assembly will remain in the reactor at least until July 1960.

The other assembly, which consists of 21 beryllium specimens contained in stainless steel capsules, is being irradiated at temperatures ranging from 500 to 700°C. The design of this experiment was discussed

previously.[6] The nearly complete assembly of the experimental system is shown in Fig. 5.21. The apparatus was inserted in core position B-8 of the ORR during the February shutdown, and, except for one capsule which had an open thermocouple, all capsules were operating satisfactorily when the reactor went to full power.

Approximately 3 hr after the reactor reached full power, the capsule furnaces began to burn out, and some thermocouples became detached from the capsules. Within 12 hr, 75% of the furnaces had burned out, and the capsules were operating on gamma heat only. Without the furnaces, the irradiation temperatures will be between 500 and 600°C.

Analyses of the furnace failures are in progress, but the cause of the failures can probably not be determined until the apparatus is removed from the reactor and opened in the hot cell for visual examination. Meanwhile, parts are being fabricated for a second experimental assembly, and design modifications are being discussed. It has been decided to irradiate the capsules without temperature control until a neutron dose of 10^{20} neutrons/cm^2·sec has been attained in one to two reactor cycles.

Both experimental assemblies are being monitored for neutron flux exposure. The flux monitors being used are CO, Np^{237}, U^{238}, and S^{32}. Because of the similarity of the fast-neutron threshold of neptunium and the 0.7-Mev threshold for the Be(n,α)Li reaction, neptunium is being used predominately, with uranium and sulfur added in order to determine the spectral distribution of the flux. The threshold energies of the monitors are given in the following tabulation:

Fig. 5.21. Apparatus for High-Temperature Irradiation of Beryllium Specimens.

Monitor	Threshold Energy (Mev)
Co	Thermal
Np^{237}	0.66
U^{238}	1.5
S^{32}	2.8

Inconel

A program for investigating the effect of fast-neutron bombardment on the creep properties of Inconel has been under way for some time as part of another study. The program has consisted of tube-burst-type stress-rupture tests in the LITR, MTR, and ORR. Details of the construction and operation of the experimental assembly and the data obtained have been reported.[7,8] A plot of stress versus the log of the time to rupture for irradiated and unirradiated specimens of the same heat tested in air at 1500°F is reproduced in Fig. 5.22 from the data reported

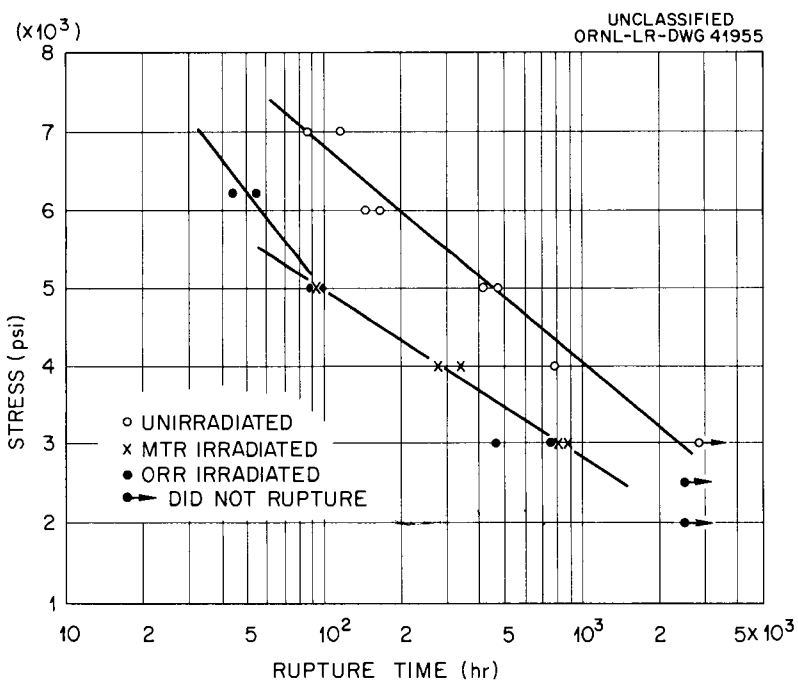

Fig. 5.22. Stress Versus Time to Rupture for Inconel in Air at 1500°F.

previously. The data obtained in more recent experiments are presented in Table 5.12.

An explanation for the shorter time to rupture under irradiation has been postulated.[8] Briefly, the hypothesis is that helium is being formed in the metal during irradiation by the neutron reaction $B^{10}(n,\alpha)Li^7$

[7]"Solid State Div. Ann. Prog. Rep. Aug. 31, 1958," ORNL-2614, pp. 106–08.

[8]"Solid State Div. Ann. Prog. Rep. Aug. 31, 1959," ORNL-2829, pp. 214–18.

Table 5.12. Effect of Neutron Bombardment in the ORR on the Time to Rupture of Inconel at 1500°F in Air

Specimen No.	Stress (psi)	Time to Rupture (hr)
Heat No. 1[a]		
9-4	5000[b]	117
11-5	5000[c]	173
11-6	5000	73[d]
11-7	5000[c]	141
11-8	5000	91
Heat No. 2		
7-5	4000	113[e]
7-6	4000	62
9-3	4000	18
14-1	5000	66
14-5	5000	70
14-10	4000	36

[a]Heat No. 1 is the material on which all previous data were obtained at the MTR and ORR; heat No. 2 is material of CX-900 quality which has passed nondestructive tests and has been approved for construction.

[b]Stress applied in the absence of irradiation after approximately 1000 hr of irradiation at 1500°F.

[c]Stress applied 48 hr before irradiation began.

[d]Excessive irradiation temperature suspected.

[e]Specimen ruptured during a high-temperature excursion.

and that the gas accumulates and creates voids in the grain boundaries which weaken the metal. In order to test this theory of failure, some of the Inconel specimens were irradiated for various periods of time at 1500°F prior to application of the stress. Other specimens were stressed for brief periods before irradiation began. In all the tests thus far, no major difference has been observed, that is, the time to rupture was about the same in all the in-pile tests. Another means of studying the mechanism of failure is to test other heats of Inconel. Therefore, tests on a second heat were begun. The results have thus far been inconsistent, but the times to rupture have all been less than for the first heat.

A number of experimental heats of Inconel are now available in which the boron content and the B^{10} enrichment have been varied. These are being made into tubing, and the next in-pile experiment will test speciemens of two of these experimental heats.

6. OUT-OF-PILE TESTING OF MATERIALS AND COMPONENTS

Materials Compatibility Tests

Isothermal Tests of Graphite and Structural Materials in Static Helium

The concentrations of the impurities in the helium coolant of the EGCR will, independently of the source, depend primarily on reactions of the impurities with graphite and with the structural metals of the reactor system. A review of the data from isothermal tests at 1100 and 1400°F in which the impurities were produced by the outgassing of graphite has shown an interesting effect of the interplay of these impurity reactions.

The outgassing rates and impurity concentrations measured when AGOT graphite was heated to 1100°F and to 1400°F in a static-helium atmosphere are presented in Figs. 6.1 and 6.2. It may be seen that at both temperatures impurity concentrations reach a maximum at the same time the vessel reaches the maximum test temperature. At this time the impurity level begins to decrease as a result of reaction with the metal, and, as shown, the decrease occurs much faster at 1400°F than at 1100°F. The changes in the CO_2 and $(CO + N_2)$ concentrations as a function of time at 1400°F, as shown in Fig. 6.3, and at 1100°F, as shown in Fig. 6.4, are also of interest. The CO concentrations which thermodynamic calculations indicate would be in equilibrium with graphite and the measured CO_2 concentrations are presented for comparison.[1] It may be seen that the gas mixture initially produced at 1400°F contains a considerably lower percentage of CO than the equilibrium CO calculated on the basis of the CO_2-graphite reaction. The concentrations of both $(CO + N_2)$ and CO_2 decline rapidly with time at 1400°F, and the concentration of CO becomes still lower than the equilibrium value. In contrast, at 1100°F the $(CO + N_2)$ concentration is at all times in approximately the ratio with respect to CO_2 that is predicted by the equilibrium calculations based on the CO_2-graphite reaction.

---

[1] L. S. Darken and R. W. Gurry, Phys. Chem. Metals, 219 (1953).

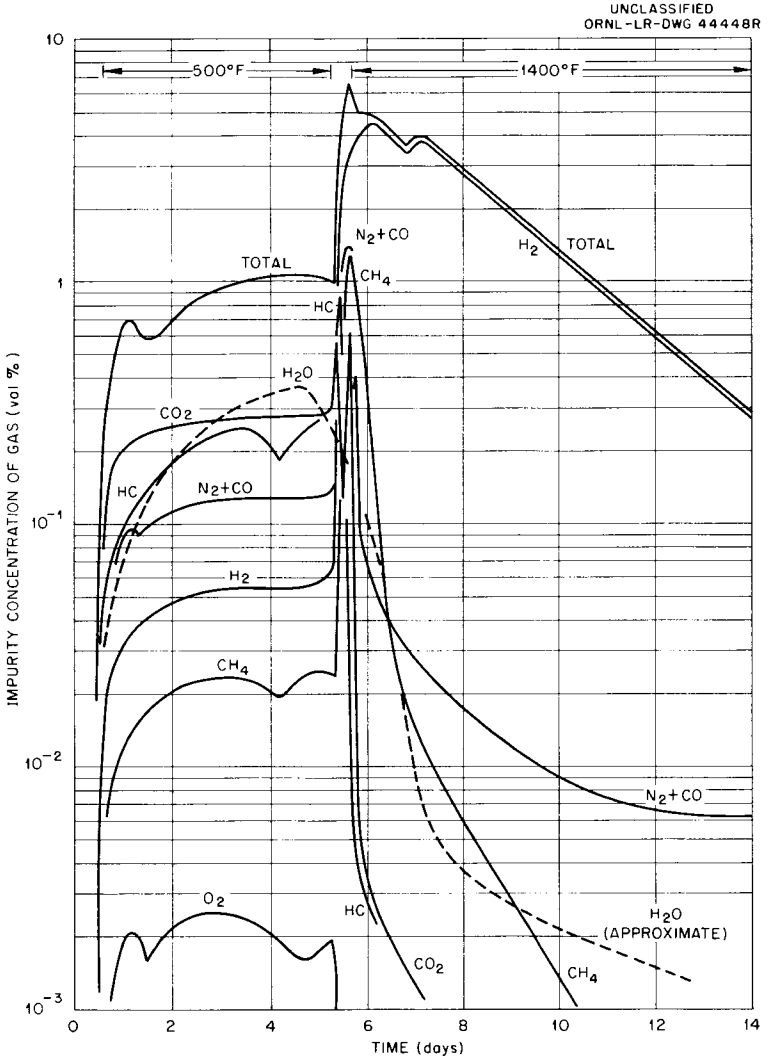

6.1. Impurity Concentration of Helium in Static Pot Test of AGOT Graphite at 1400°F.

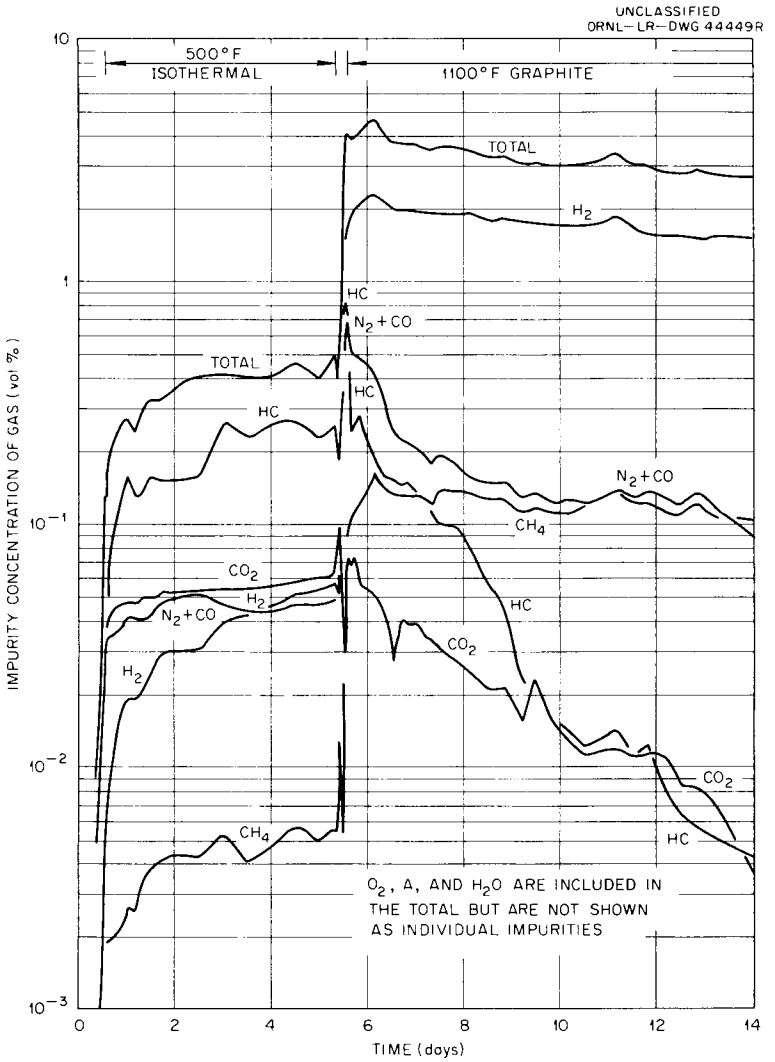

Fig. 6.2. Impurity Concentration of Helium in Static Pot Test of AGOT Graphite at 1100°F.

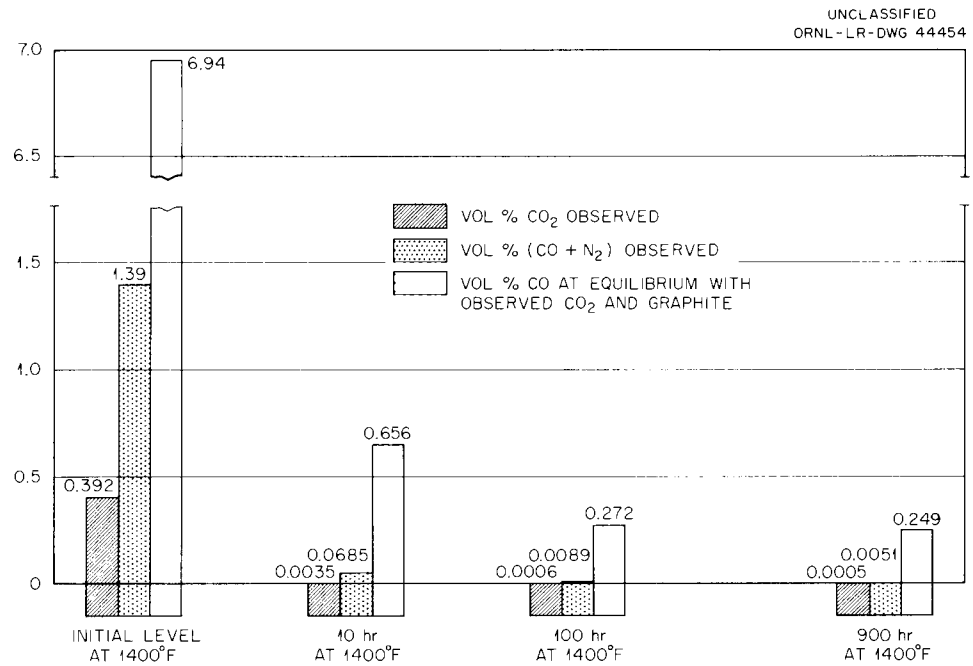

Fig. 6.3. Concentrations of (CO + N_2) and CO_2 Produced in Static Pots Containing AGOT Graphite at 1400°F.

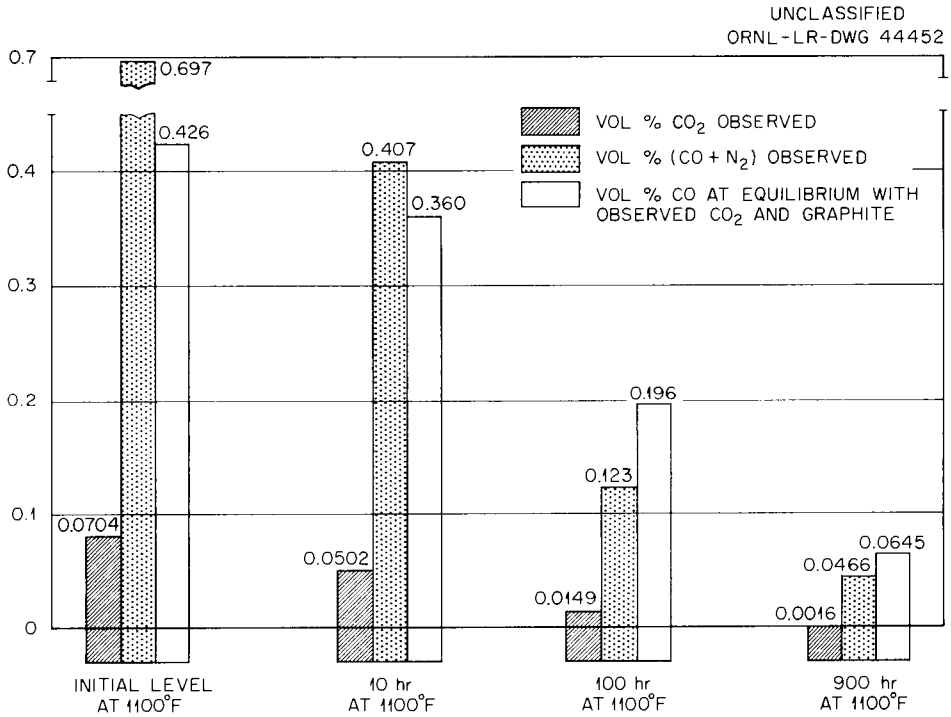

Fig. 6.4. Concentrations of (CO + N_2) and CO_2 Produced in Static Pots Containing AGOT Graphite at 1100°F.

Similar comparisons have been made of the methane and hydrogen concentrations with respect to the CO_2-graphite reaction equilibrium values. As shown in Figs. 6.5 and 6.6, the initial CH_4 concentrations measured both at 1100 and 1400°F are considerably above the levels in equilibrium with observed concentrations of hydrogen and graphite. The CH_4 concentration tends to decrease with time, however, and to approach the calculated equilibrium value.

The contrast in behavior of the oxygen-containing impurities at the two temperatures stems primarily from the effect of temperature on the rates of reaction of the oxidizing impurities with the metal in the system. At 1400°F, reaction of the outgassed contaminants with structural metals was extremely fast, as indicated by the rapid reduction in total impurity content. Accordingly, the ultimate concentrations of oxygen-containing impurities reflect the effects of metal reactions to a greater extent than reactions with graphite. At 1100°F, the gas impurities more closely approached concentrations in equilibrium with graphite. An over-all reduction of the impurities also occurred at 1100°F but at a much slower rate than at 1400°F.

The importance of these competing reactions is evidenced by the effects on the various metal samples tested at each temperature. As previously reported,[2] the decarburization of test specimens that occurred at 1400°F was unexpected because of the large quantities of graphite present in these test systems. Nevertheless, decarburization is consistent with the gas behavior discussed above. At 1100°F, specimens showed little effect of the test environment, although the gas conditions were strongly carburizing. It is known, however, that carburization is extremely slow at 1100°F, and, in the test times investigated, detectable carburization would not be expected.

Thermal-Convection Loop Tests of Graphite and Structural Materials in High-Pressure Helium

Test No. 2, conducted in a thermal-convection loop containing AGOT graphite, iron-base alloy specimens, and a dummy fuel element assembly,

[2] "GCR Semiann. Prog. Rep. Dec. 31, 1958," ORNL-2676, p. 139.

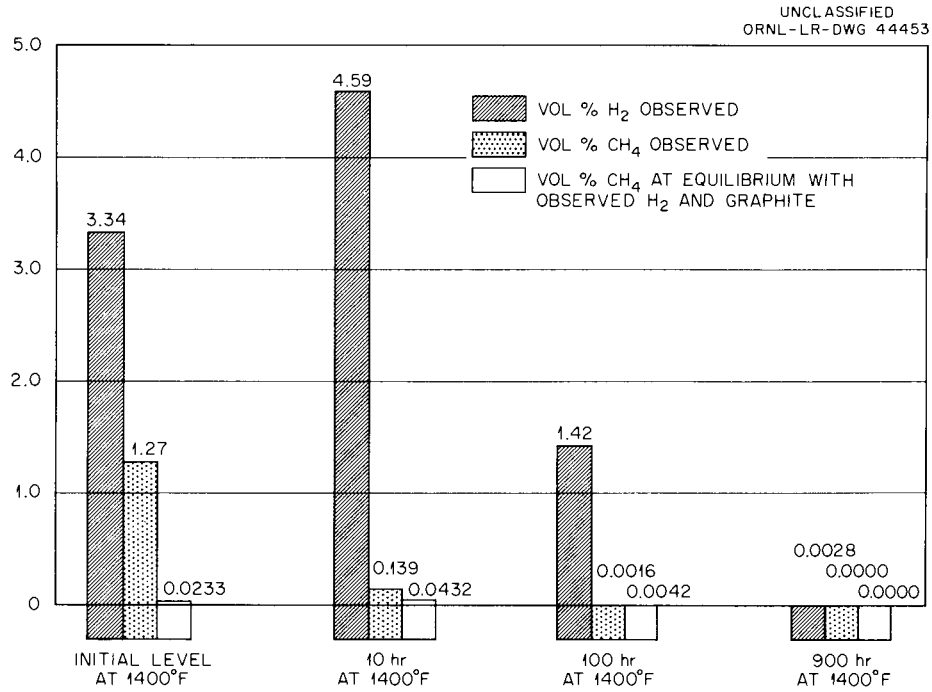

Fig. 6.5. Concentrations of Hydrogen and Methane Produced in Static Pots Containing AGOT Graphite at 1400°F.

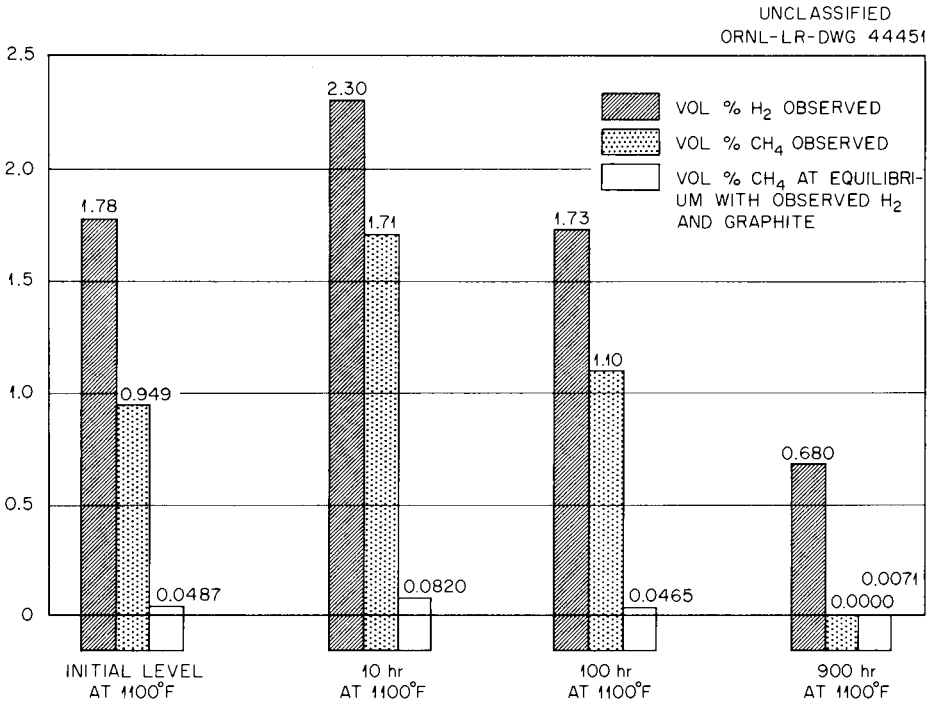

Fig. 6.6. Concentrations of Hydrogen and Methane Produced in Static Pots Containing AGOT Graphite at 1100°F.

was terminated after 5000 hr with a test section temperature of 1225°F and a system pressure of 325 psig. The appearance of the metal specimens after the test was similar to the appearance of the specimens exposed in high-pressure tests 1A and 3, which, as reported previously,[3,4] were of 1000 and 500 hr duration, respectively, under conditions identical to those of test No. 2. The weight changes of the specimens from the three tests are compared in Table 6.1. In all three tests, the stainless steel samples gained less than 1.0 mg/cm^2, whereas the low- and medium-alloy steels gained in excess of 6 mg/cm^2. The gains recorded after 500 hr were nearly as great as those recorded after 1000 and 5000 hr, indicating that most of the reaction with the impurities outgassed from the graphite took place within the first 500 hr. This result is in agreement with the observed impurity concentrations, which were reduced to relatively low levels after approximately 150 hr. The loop that was operated for 5000 hr was inspected for carbon mass transfer and, like the loops that

[3] "GCR Quar. Prog. Rep. Sept. 30, 1959," ORNL-2835, pp. 125–32.

[4] "GCR Quar. Prog. Rep. Dec. 31, 1959," ORNL-2888, pp. 151–52.

Table 6.1. Weight Changes of Metal Specimens Exposed for 500, 1000, and 5000 hr at 1225°F to High-Pressure Helium in Thermal-Convection Loops Containing AGOT Graphite

Specimen	Weight Gain (mg/cm^2)		
	In 500 hr, Test No. 3	In 1000 hr, Test No. 1A	In 5000 hr, Test No. 2
Type 304 stainless steel	0.06	0.09	0.10
Type 310 stainless steel	0.07	0.11	0.13
Type 316 stainless steel	0.06	0.12	0.35
Type 410 stainless steel	0.14	0.25	0.12
Croloy (2 1/4% Cr) steel	8.61	7.61	6.33
Croloy (3% Cr) steel	13.42	*	*
Type T-1 steel	6.24	8.13	6.76
DB-2 (Fe-Al-Cr alloy) steel	0.00	0.07	0.05

*Scale spalled off specimen.

were operated for 500 and 1000 hr, the cold leg showed no detectable carbon deposits. Another test is in progress in a loop containing AGOT graphite, various metal test specimens, and a dummy fuel element assembly. The maximum gas temperature is 1400°F, and the system pressure is 325 psig.

Effect of Gas Impurities on Metal Specimens

The surfaces of the T-1 and Croloy (2 1/4% Cr) steel specimens exposed to helium containing impurities produced by the outgassing of graphite in natural-convection systems at 1100 to 1200°F have characteristically exhibited relatively heavy, poorly adherent reaction films.[5,6] Visually, the films appear to be composed of a silver-colored outer layer and a black inner layer. Both layers are highly magnetic. Following spalling of the films, the specimens show weight losses as high as 24 mg/cm^2.

Initial studies were made of the scale in composite form with the use of electron and x-ray diffraction techniques. The patterns indicated were characteristic of Fe_3O_4. More recently, examinations were made of the silver-colored scale after physical separation from the black layer by agitation and ultrasonic methods. Electron diffraction examination of the silvery material gave patterns corresponding to a material indexed as "iron-graphite" (FeC). The lines for this compound are quite close to those for graphite, and it appears that the material consists of a solid solution of iron contained interstitially in the conventional graphite lattice. Compounds of similar structure have been formed following the penetration of graphite by liquid metals such as sodium or NaK.[7]

Further studies of the silver-colored scale included reacting it with dilute HCl solution. The reaction, which was quite vigorous,

---

[5] "GCR Quar. Prog. Rep. June 30, 1959," ORNL-2767, pp. 184–88.

[6] "GCR Quar. Prog. Rep. Sept. 30, 1959," ORNL-2835, pp. 131–32.

[7] L. M. Currie, B. C. Hamister, and H. G. MacPherson, "Production and Properties of Graphite for Reactors," pp. 451–75, Proceedings of Conference on Peaceful Uses of Atomic Energy, Vol. 8, 1956.

completely leached the iron from the scale. After reaction, segments of the scale produced patterns characteristic of pure graphite, and the lines common to the iron-graphite form were missing.

Examination of the black substrate layer revealed it to be composed predominantly of Fe_3O_4. This black material showed no visible reaction with HCl, and acid treatment of a composite of the silvery and black scales produced a residue containing both graphite and Fe_3O_4.

The atmospheres under which these scales have formed reflect the effects of reactions discussed in the preceding sections. The impurity concentrations which were measured at several time intervals in high-pressure test 1A are shown in Table 6.2. Thermodynamic calculations indicate that oxidation of the low-alloy T-1 material would have been possible only during initial stages of the test. Following this period, reactions of the contaminants with the graphite established conditions which favored carburization and deoxidation of these specimens. It is believed therefore that the silvery component of the film was formed subsequent to the buildup of the black oxide material and resulted from a combination of reduction of the iron oxide and the deposition of carbon at the gas-film interface. As indicated in Table 6.2, the ratios of CO

Table 6.2. Concentrations of Impurities in High-Pressure Test 1A Compared with Concentrations of CO and CH_4 In Equilibrium with Graphite at 1225°F

Time at 1225°F (hr)	Observed Impurity Concentrations (vol %)					Equilibrium Concentrations (vol %)	
	$CO + N_2$	CO_2	H_2O	H_2	CH_4	CO[a]	CH_4[b]
0	0.129	0.171	0.0029	0.382	0.0616	0.597	0.0068
8	0.278	0.237	0.0018	0.447	0.0616	0.702	0.0093
132	0.519	0.270	0.0040	0.461	0.0477	0.749	0.0098
468	0.796	0.134	0.0075	0.168	0	0.527	0.0013
900	0.542	0.0291	0	0.0158	0	0.246	0

[a]Based on reaction $C + CO_2$ (observed) $\rightleftharpoons 2CO$.

[b]Based on reaction $C + 2H_2$ (observed) $\rightleftharpoons CH_4$.

to CO_2 and CH_4 to H_2 were both sufficiently high to support carbon deposition.

Low-Pressure Thermal-Convection Loop Tests with Helium Containing Controlled Amounts of Impurities

Test No. 10 in a low-pressure thermal-convection loop that contained a type 304 stainless steel heated specimen at a temperature of 1500°F and AGOT graphite at a temperature of 1100°F was terminated after 900 hr of operation. The impurity concentration of the helium in the loop, which was monitored with an on-stream gas chromatograph, was controlled to 0.185 vol % CO. The concentration of all other impurities was low, with the exception of CO_2, which was present because of the CO-graphite equilibrium. The CO_2 concentration remained at a level of 0.132 vol % throughout most of the test period. This concentration of CO_2 is a factor of 10 greater than the equilibrium concentration predicted from the $CO_2 + C\ (g) \rightleftharpoons 2CO$ reaction at 1100°F.[1] It would be expected, however, that the equilibrium between the gas stream and the graphite in this test would be upset by the cold-leg section of the loop, in which a portion of the gas was cooled to 500°F. The equilibrium temperature for graphite and the observed CO-CO_2 mixture was calculated to be 960°F.

The heated specimen exposed in test No. 10 exhibited a thin, irridescent, tightly adherent film which was characteristic of the protective spinel-type oxides that commonly form on stainless steels. The unheated stainless steel coupons exposed at 1100°F also had protective films and quite low weight gains (1.0 mg/cm^2). Similarly exposed low-alloy steels were found to have rather heavy oxide films which had blistered during the test. The weight gains for these coupons were in excess of 1.0 mg/cm^2. More extensive analyses of the specimens used in this test are in progress.

Test No. 11 is in progress in a loop containing AGOT graphite at 1100°F and a type 304 stainless steel specimen heated at 1500°F. The H_2O content of the helium in the loop is being controlled at 0.122 vol % (±10% error). The observed concentrations of the other impurities in the loop are:

Impurity	Concentration (vol %)
CO	0.015–0.020
CO_2	0.040–0.050
H_2	0.090–0.100
CH_4	0.001–0.006

Forced-Convection Loop Test of Gas Purification System

A small-scale version of the gas purification system proposed for the EGCR[8] has been added to the forced-convection loop assembly. Evaluation of this purification system will get under way in conjunction with test No. 4 as soon as the process stream gas chromatograph (presently in operation with the low-pressure thermal-convection loops) becomes available.

Evolution of Gases from Graphite

The experimental techniques employed and the experimental results of studies of the degassing behavior of a large number of different graphite specimens have been reported previously.[9-12] Additional degassing studies of Great Lakes Corporation R-1HLM graphite have been made, and another reactor-grade graphite, Great Lakes R-6HLM, has been investigated. Samples of silicon–silicon carbide coated graphite received from the American Lava Corporation have also been studied.

The data presented previously[12] for the outgassing of R-1HLM graphite showed some rather large variations in the gas content of specimens cut from the same bar, as well as for specimens machined from different bars, when the specimens were degassed by heating from room temperature to 1000°C with the use of external-resistance heating. In contrast, the

[8]F. A. Anderson, "Proposed Helium Purification System for the Experimental Gas-Cooled Reactor," ORNL-2819 (Oct. 2, 1959).

[9]"GCR Semiann. Prog. Rep. Dec. 31, 1958," ORNL-2676, p. 147.

[10]"GCR Semiann. Prog. Rep. June 30, 1959," ORNL-2767, p. 190.

[11]"GCR Quar. Prog. Rep. Sept. 30, 1959," ORNL-2835, p. 133.

[12]"GCR Quar. Prog. Rep. Dec. 31, 1959," ORNL-2888, p. 153.

data included in Table 6.3 that were obtained by degassing R-1HLM graphite in the temperature range 30 to 1800°C by using induction heating show a fair degree of precision for specimens cut from four different bars. The total gas contents also are in fair agreement with those reported earlier[12] (1-D is a duplicate of 1-C, etc.). The ratio of the volume of H_2 to that of the combined volumes of CO and CO_2 is somewhat greater, however, for the D series than that reported earlier[12] for the C series. With the exception of sample 4-D, all samples gave a larger volume of $CO + CO_2$ than H_2. No explanation for the larger H_2 to $CO + CO_2$ ratio found in the D series can be given.

A 12-in. sample (4 × 4 in. in cross section) of R-6HLM was received from the Great Lakes Carbon Corporation for evaluation. Specimens 1 1/2 in. in diameter and 2 in. long were machined from this sample in such a manner that the long axis of the cylinder was either parallel or perpendicular to the extrusion axis. This sample also was used to provide specimens 1 1/4 in. in diameter and 1 in. long cut from the center and outside of the bar with the axis parallel to the extrusion axis.

The results obtained by degassing two of the 1 1/2-in. specimens are given in Table 6.3. Sample A-1 was cut perpendicular to the extrusion axis, and sample C-5 was cut parallel. Additional samples will have to be outgassed before any significant differences can be said to exist. Data for the outgassing of the 1 1/4-in.-diam, 1-in.-long specimens are also presented in Table 6.3. Samples B-1 and B-3 were cut from the outside of the bar and samples B-5 and A-5 were cut from the center. There are no significant differences in either the volume or composition of the gas evolved by the specimens cut from the different positions. The results obtained thus far indicate that the gas content of R-6HLM graphite is somewhat lower than that of R-1HLM. The evolved gas is characterized, however, by a rather large $CO + CO_2$ to H_2 ratio.

Silicon—silicon carbide coated specimens of two sizes, 1 1/2 in. in diameter and 2 in. long and 1 1/4 in. in diameter and 1 in. long, were received from the American Lava Corporation, and their degassing behavior was studied. The results obtained by heating the specimens from room

Table 6.3. Volume and Composition of Gas Evolved by Graphite Specimens

Sample Dimensions (in.)		Graphite Sample	Temperature (°C)	Time (hr)	Gas Volume (cm^3/100 cm^3 of graphite)	Gas Constituents													
						H_2		Hydrocarbons		H_2O		CO_2		N_2		CO		Mass 28	
Diameter	Length					Vol %	cm^3	Vol %	cm^3	Vol %	cm^3	Vol %	cm^3	Vol %	cm^3	Vol %	cm^3	Vol %	cm^3
1 1/2	2	Great Lakes	300	5	0.7	6		5		66	0.5	5		13	0.1	2			
		R-6HLM	600	11	3.3	14	0.5	4	0.1	20	0.7	38	1.3	4	0.1	19	0.7		
		No. A-1	1000	6.5	15.8	24	3.9	1	0.2	2	0.3	8	1.3	1	0.2	63	10.0		
			Total		19.8		4.4		0.3		1.5		2.6		0.4		10.7		
		Great Lakes	300	7	0.6	3		5		59	0.4	6		10	0.1	3			
		R-6HLM	600	5	3.3	5	0.2	13	0.4	36	1.2	25	0.8	3	0.1	16	0.5		
		No. C-5	1000	13	20.2	41	8.4	1	0.2	3	0.6	5	1.0	1	0.2	48	9.6		
			Total		24.1		8.6		0.6		2.2		1.8		0.4		10.1		
		American	300	3	(0.2)*														
		Lava	600	21	3.7	4	0.1	3	0.1	33	1.2	12	0.5	5	0.2	41	1.5		
		No. MMM-1	1000	24	8.8	50	4.4	11	1.0	2	0.2	3	0.3	1	0.1	33	2.9		
			Total		12.5		4.5		1.1		1.4		0.8		0.3		4.4		
		American	300	6	(0.2)*														
		Lava	600	17	2.2	34	0.8	3	0.1	20	0.4	10	0.2	3	0.1	28	0.6		
		No. MMM-2	1000	6	5.7	76	4.4	4	0.2	0.8		0.4		1	0.1	17	0.9		
			Total		7.9		5.2		0.3		0.4		0.2		0.2		1.5		
1 1/4	1	Great Lakes	1000	8	41.3	35	14.5	0.8	0.3	0.6	0.2	0.6	0.2	2	0.8	61	25.2		
		R-1HLM	1400	3.5	3.7	30	1.1	0.7				1.5	0.1	7	0.3	59	2.2		
		No. 1-D	1800	5	3.2	89	2.9	0.9				0.1		5	0.2	3	0.1		
			Total		48.2		18.5		0.3		0.2		0.3		1.3		27.5		
		Great Lakes	1000	3.5	39.4	29	11.5	0.7	0.2	0.4	0.2	0.3	0.1	3	1.2	67	26.4		
		R-1HLM	1400	8	7.6	40	3.0	0.7	0.1			1.4	0.1	9	0.7	48	3.8		
		No. 2-D	1800	9	7.5	83	6.2	1	0.1			0.2		7	0.5	8	0.6		
			Total		54.5		20.7		0.4		0.2		0.2		2.4		30.8		
		Great Lakes	1000	3.5	48.6	29	14.2	0.3	0.1	0.2	0.1	0.3	0.1	1	0.5	68	33.1		
		R-1HLM	1400	3.5	4.0	23	0.9	0.5				2.7	0.1	7	0.3	66	2.7		
		No. 3-D	1800	9	6.5	94	6.1	0.2				0.1		3	0.2	2	0.1		
			Total		59.1		21.2		0.1		0.1		0.2		1.0		35.9		

*Included in 600°C fraction.

Table 6.3. (continued)

Sample Dimensions (in.)		Graphite Sample	Temperature (°C)	Time (hr)	Gas Volume (cm^3/100 cm^3 of graphite)	Gas Constituents													
						H_2		Hydrocarbons		H_2O		CO_2		N_2		CO		Mass 28	
Diameter	Length					Vol %	cm^3	Vol %	cm^3	Vol %	cm^3	Vol %	cm^3	Vol %	cm^3	Vol %	cm^3	Vol %	cm^3
1 1/4	1	Great Lakes	1000	4	42.8	47	20.2	0.5	0.2	0.4	0.2	0.4	0.2	2	0.8	50	21.3		
		R-1HLM	1400	6.5	10.2	50	5.1	0.2				0.8	0.1	4	0.4	45	4.6		
		No. 4-D	1800	6.5	5.2	87	4.5	0.2						5	0.3	8	0.4		
			Total		58.2		29.8		0.2		0.2		0.3		1.5		26.3		
		Great Lakes	1000	4.8	43.3	31	13.5	0.3	0.1	0.1		0.4	0.2	1	0.4	67	29.0		
		R-6HLM	1400	2.5	4.8	15	0.7	0.3				2.7	0.1	4	0.2	78	3.7		
		No. B-1	1800	5	2.5	34	0.8	0.8				0.3						64	1.6
			Total		50.6		15.0		0.1				0.3						
		Great Lakes	1000	7	55.8	39	21.6	0.3	0.2	0.4	0.2	0.4	0.2					60	33.6
		R-6HLM	1400	2.3	3.5	31	1.1	0.5				1.4						63	2.2
		No. B-3	1800	3.3	2.3	54	1.2	1				0.4						33	0.8
			Total		61.6		23.9		0.2		0.2		0.2						36.6
		Great Lakes	1000	4	38.1	35	13.3	0.5	0.2			0.1		1	0.4	63	24.0		
		R-6HLM	1400	3	10.8	20	2.2	0.2				1.1	0.1	1	0.1	77	8.3		
		No. B-5	1800	6	1.0	34	0.3	0.4				0.2		20	0.2	41	0.4		
			Total		49.9		15.9		0.2				0.1		0.7		32.7		
		Great Lakes	1000	2	26.9	46	12.3	1	0.3	4	1.0	8	2.3	1	0.3	39	10.6		
		R-6HLM	1000	9.2	9.1	47	4.3	0.8	0.1	2	0.2	3	0.3	2	0.2	44	4.0		
		No. A-5	1400	2	11.9	26	3.1	0.2				1.5	0.2	1	0.1	68	8.0		
			1800	2.7	2.2	Sample lost													
			Total		50.1		19.7		0.4		1.2		2.8		0.6		22.6		
		American	1000	4	2.0	12	0.2	4	0.1			48	1.0	6	0.1	25	0.5	31	0.6
		Lava	1200	8.8	3.6	41	1.5	2	0.1			30	1.1	9	0.3	14	0.5	23	0.8
		No. MMM-3	1400	13.5	3.5	28	1.0	0.6				42	1.5					26	0.9
			1400	7	1.8	35	0.6					30	0.5					20	0.4
			1490	8	4.0	45	1.8	2	0.1			17	0.7					17	0.7
			Total		14.9		5.1		0.3				4.8						3.4

temperature to 1000°C with the use of external resistance heating are given in Table 6.3. The small volumes evolved at 300°C were not analyzed, but they are included in the 600°C samples. Previous experience has indicated that the gas evolved at 300°C is primarily water vapor.

As may be seen from the data, the coated specimens evolved surprisingly large volumes of gas. The composition of the evolved gas was similar to that evolved from some uncoated specimens, with significant amounts of CO and CO_2 present. These results suggest that the coatings of the specimens examined were imperfect, although they presumably were given the standard oxidation test before shipment. One of the degassed specimens was returned to the vendor for examination of the coating. Additional coated specimens prepared from better graphite stock are to be made available. The results obtained by degassing a coated specimen in the temperature range 30–1490°C by using induction heating are also given in Table 6.3. A rather small volume of gas was evolved at 1000°C, and it contained considerable quantities of CO and CO_2. Gas continued to be evolved at a rather slow rate over an extended period of time at 1200 and 1400°C. This behavior suggests that the rate of evolution was being affected by the process of diffusion through the coating. At 1490°C the rate of evolution was higher, as expected, since the coating was not intended to be protective in this temperature range. The specimen showed a large weight loss, and considerable silicon was deposited on the wall of the experiment tube. Failure of the coating was not characterized by any marked increase in the rate of gas evolution.

Modifications were made in the equipment used for outgassing with the use of induction heating in an attempt to provide lower pressures over the graphite specimens during the outgassing and to provide for measuring the pressures. A mercury diffusion pump and an ion gage were installed between the quartz tube and the Toepler pump, along with suitable connections for bypassing the gage and the diffusion pump. Operation of the ion gage was unsatisfactory, however, presumably because of the mercury vapor in the system. It appears that a cold trap will be required if the ion gage is to be used. Several runs were made

without the ion gage in which AGOT specimens were degassed. No marked difference in the degassing behavior was observed when the diffusion pump was used in comparison with earlier results obtained without it. There was, however, an indication that the time required to remove the bulk of the gas at any particular temperature was decreased slightly. The diffusion pump has not operated satisfactorily because of intermittent leakage, and it has been removed from the system for examination and repair.

Graphite samples manufactured from needle cokes by National Carbon Company, Speer Carbon Company, and Great Lakes Corporation have been received. Studies of the degassing behavior of some of these samples will be started shortly.

Transport of Gases Through Graphite

Permeability Studies

Further studies in the experimental program for the determination of the interdiffusion coefficients of noble gases in graphite[13] have included tests with AGOT graphite. The first experiments involved the determination of the open porosity and the permeability characteristics with helium. In the permeability determinations, difficulty was experienced in that nonlinear permeability curves were obtained at flow rates which had given satisfactory curves for Speer No. 1 graphite. It was immediately suspected that the forced-flow experiments for the permeability determinations were being conducted in turbulent flow regions, and use of the definitive gas permeability equations for isothermal steady-state flow,

$$Q_a P_a = \frac{k_a A \, (\Delta P) \, P_m}{\mu L} \tag{1}$$

and

$$Q_a P_a = K \frac{A}{L} \Delta P \tag{2}$$

[13] "GCR Quar. Prog. Rep. Dec. 31, 1959," ORNL-2888, pp. 158–62.

would not be valid under these conditions. In these equations Q_a is the volumetric flow rate (cm^3/sec) measured at pressure P_a (atm) when a pressure drop ΔP ($dynes/cm^2$) is imposed on a fluid of viscosity μ (poise) and the fluid flows through a porous medium of cross-sectional area A (cm^2), and length L (cm). In Eq. (1), P_m is mean pressure. The pressure drop is measured over L. Equations (1) and (2) emphasize that the gas velocity, $Q_a P_a/A$, must be linear with respect to P_m ($\Delta P/L$) or $(P_2^2 - P_1^2)/2L$, before values of k_a (cm) or K (cm^2/sec) can be determined.

Muskat[14] has shown that the Reynolds number, obtained by using the average grain diameter, at which turbulent flow might be expected is unity for porous media as compared with 2000 for a smooth circular conduit. Further, the transition from viscous to turbulent flow is not abrupt in porous media; rather, it occurs over a wide range of velocities, with only the large channels participating initially and the small channels becoming involved as the velocity increases. Uncertainties in estimating an average diameter for a grain indicated the need for an experimental determination[15] of the initial transition point (or critical velocity) so that meaningful permeability measurements could be obtained. Initial results of such experiments are presented in Fig. 6.7. The only linear curves are those for helium at $Q_a P_a$ values less than 125 cm^3/sec at 1 atm and 20°C. Since the Reynolds numbers for the two gases being used, argon and helium, should be equal at the transition point,

$$(Q_a P_a)_A = (Q_a P_a)_{He} \left(\frac{M_{He}}{M_A}\right)\left(\frac{\mu_A}{\mu_{He}}\right), \qquad (3)$$

where M is the molecular weight. Based on Eq. (3) and the helium transition value, an estimated argon transition value of 14.3 cm^3/sec was

---

[14] M. Muskat, "Physical Principles of Oil Production," p. 126, McGraw-Hill, New York, 1949.

[15] "Standard Procedure for Determining Permeability of Porous Media," API Code No. 27, 2nd Ed., American Petroleum Institute, Division of Production, Dallas, Texas, 1942.

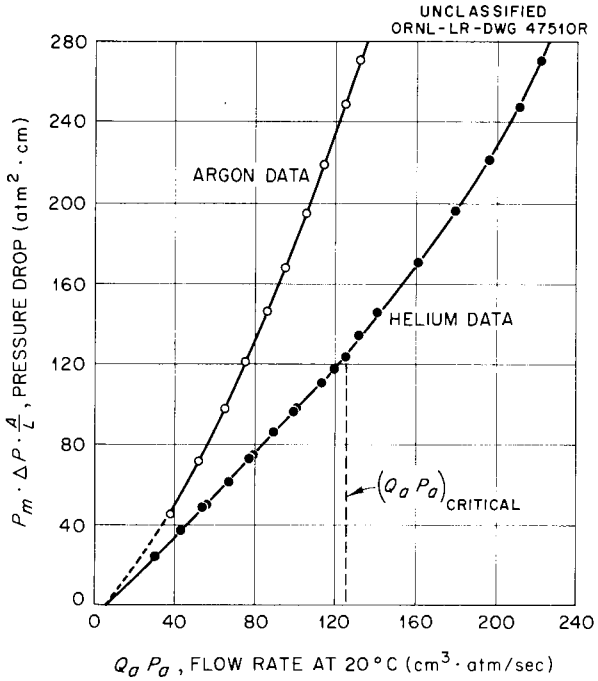

Fig. 6.7. Permeability Characteristics of AGOT Graphite at 20°C. See text for definition of terms.

obtained. Thus, it appears that all the argon data (corresponding to the points in Fig. 6.7) were obtained in the turbulent region. This discussion is pertinent from the standpoint of reactor technology, since room-temperature helium flow through this specimen at reactor pressures, for example, 30 atm, will be in the turbulent region, with pressure drops as low as 0.5 psi. If back flow of helium through graphite fuel elements is to be employed as an aid in fission-product retention, the possibility of the existence of turbulent flow within the graphite should not be overlooked.

It is currently believed that the permeability constants obtained from K versus P_m plots are of little value for estimating the absolute value of the Knudsen diffusion coefficients applicable to the relatively permeable graphites being studied to date. This conclusion intuitively results from considerations of pore-size distribution curves for AGOT

graphite (Fig. 6.8) that are based on published data.[16] The permeability values obtained thus far in experiments conducted at mean pressures above 1 atm could be governed by the contribution of a small percentage of large pores; however, values do verify the conclusion that Knudsen resistances will be negligible for AGOT graphite. Indeed, AGOT and Speer No. 1 graphite were selected for the initial experiments with the

[16]W. P. Eatherly et al., "Physical Properties of Graphite Materials for Special Nuclear Applications," A/CONF.15/P/708, Second United Nations International Conference on Peaceful Uses of Atomic Energy.

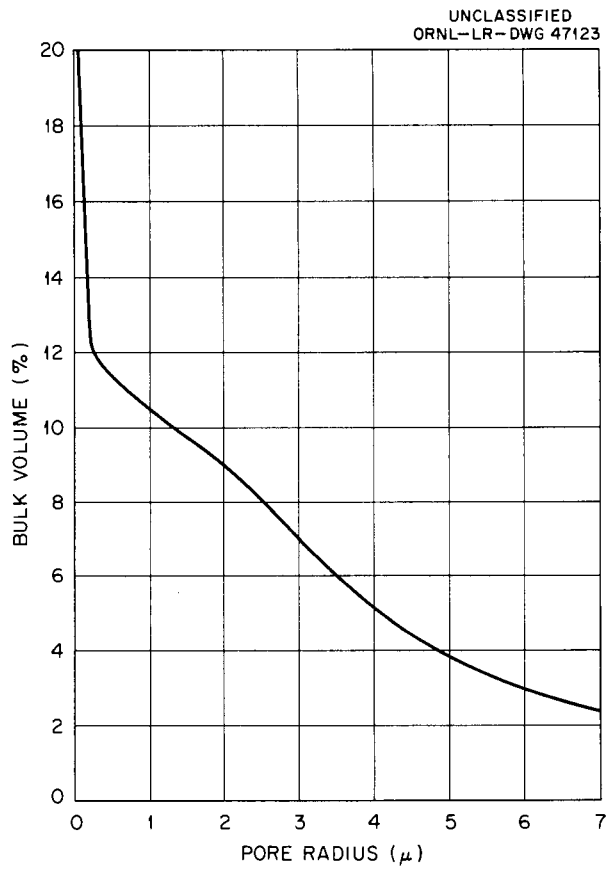

Fig. 6.8. Accessible Volume as a Function of Pore Radius for AGOT Graphite Based on Data of Ref. 4.

expectation that diffusion in these graphites would be essentially classical in nature and relatively independent of Knudsen effects. The permeability data are valuable, however, from the standpoint of graphite characterization and identification. Also, these data are necessary for future studies involving diffusion in forced-flow systems. The permeability data presented in Fig. 6.9 are based on k_0 $(cm)^2$ rather than K (cm^2/sec), as in Eq. (2), where

$$k_a = k_0 \left(1 + \frac{a}{P_m}\right) \tag{4}$$

and a is a measure of the well-known slip phenomenon.[17] As $1/P_m$ approaches zero, the gas tends to behave as a liquid, and k_a approaches k_0. The latter parameter is a property of the medium and does not contain contributions of P_m and μ, as does K. The results of the preliminary

[17]M. Muskat, op. cit., p. 137.

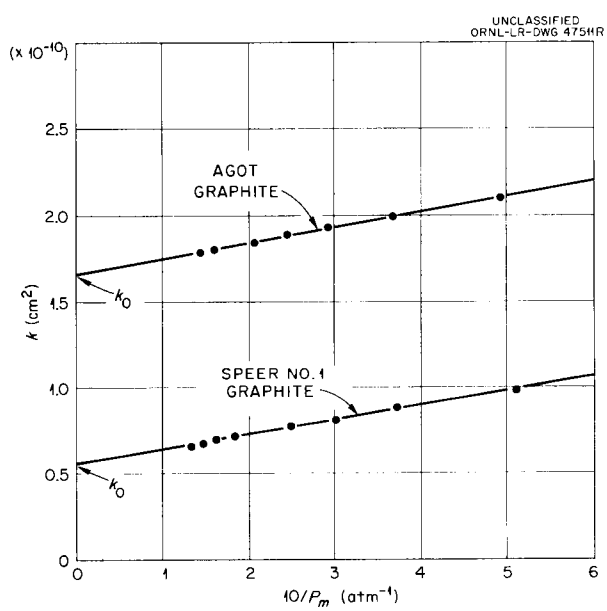

Fig. 6.9. High-Pressure Interpretation of Graphite Permeability Data at 20°C.

characterization experiments are presented below:

	Speer No. 1 Graphite	AGOT Graphite
Porosity to helium, vol %	17.8	22.0
Absolute permeability, k_0, cm^2	0.6×10^{-10}	1.7×10^{-10}

Constant-Pressure Diffusion Experiments

Interdiffusion coefficients of argon and helium have been obtained for AGOT graphite by using the procedures outlined previously.[13] The method being used differs from the methods described in the literature in that relatively large diffusion specimens (graphite cylinders rather than disks) are utilized and both the argon and the helium sweep streams are analyzed for diffused gas. The latter feature was incorporated to furnish a means of checking the data, since it was assumed that the rate of diffusion of each gas would be essentially equal in AGOT and Speer No. 1 graphite when the total pressure was maintained at the same value on each side of the diffusion septum. It was found, however, that the diffusion rates were not the same, as indicated by the data of Fig. 6.10, which present the apparent or effective diffusion coefficients for each gas as a function of reciprocal pressure. In the previous report,[13] it was mentioned that the presence of a mass-transfer film could be responsible for the low values obtained; however, estimates of film resistances at the sweep velocities employed indicate that film effects are negligible. This, coupled with the agreement between the ratios of the permeability constants, k_0, of the two graphites and, for example, the ratio of the argon diffusion coefficients at a pressure of 2 atm, has increased confidence in the reliability of the data.

During this quarter, attention has been focused on the net transfer of gas obtained in the diffusion experiments, as indicated by the data of Fig. 6.10. In an attempt to correlate the data, the following series model suggested by Carman[18] was studied:

[18]P. C. Carman, "Flow of Gases Through Porous Media," p. 79, Academic Press, New York, 1956.

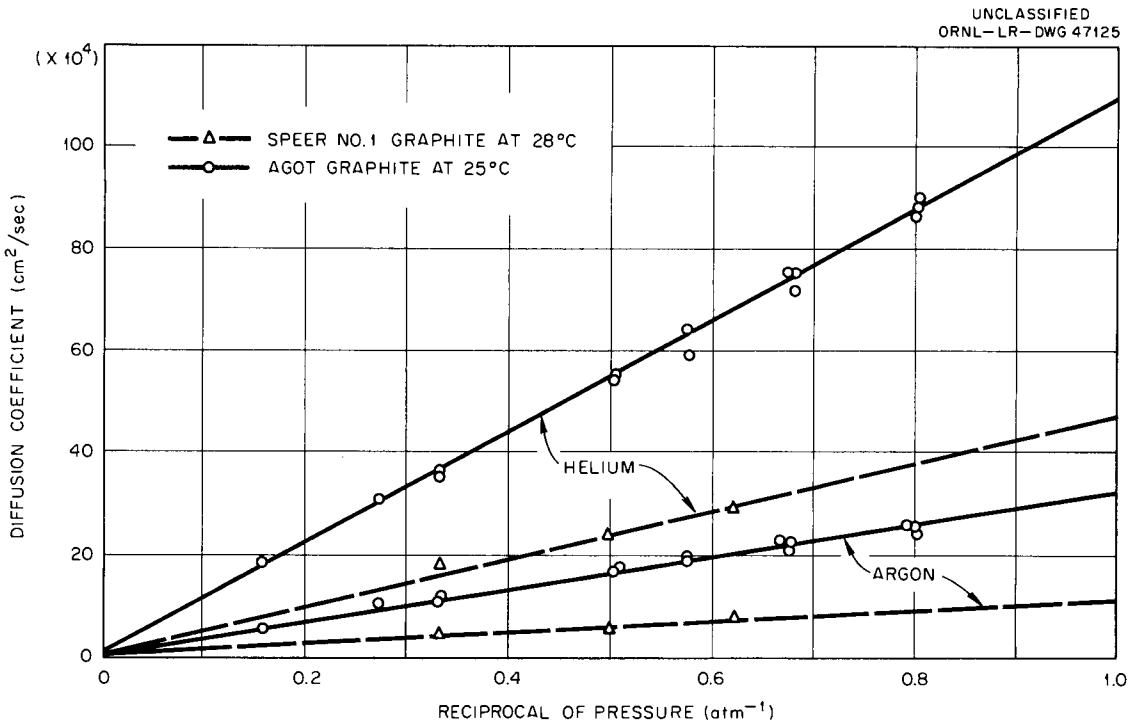

Fig. 6.10. Apparent Diffusion Coefficients for Argon and Helium in Graphite.

$$\frac{1}{D_{eff}} = \frac{1}{D_c} + \frac{1}{D_k} \quad , \tag{5}$$

where D_c refers to the classical diffusion coefficient and D_k refers to Knudsen coefficient. In terms of molecular weight and total pressure (maintained constant throughout the cell during a particular experiment), Eq. (5) may be written for either argon or helium as

$$\frac{1}{(D_{eff})_{He}} = B_1 P \left(\frac{2M_A M_{He}}{M_A + M_{He}}\right)^{1/2} + B_2 (M_{He})^{1/2} \quad , \tag{6}$$

where P is the gas pressure. The argon equation would be the same except that M_A would appear in the last terms.

Equations (5) and (6) refer to a single channel; however, conversion of these values to the gross value measured is not important here because the interest is in the form of the equation rather than the absolute value involved. From equation (6) it can be seen that $1/(D_{eff})$ should be linear with pressure for each gas. Also, the ratios of the intercepts should be given by the ratio of the square roots of the corresponding molecular weights, and the slopes should be essentially equal. A plot of this type is shown in Fig. 6.11, which indicates that the Knudsen effects are indeed small. Although both curves are linear and the intercepts are proportional to the square root of the molecular weights, the large differences between the two curves indicate that the model given by Eqs. (5) and (6) is not applicable to the present experiment.

A striking feature of the plots of Fig. 6.11 is that the ratio of the slope of the argon curve to the slope of the helium curve is precisely

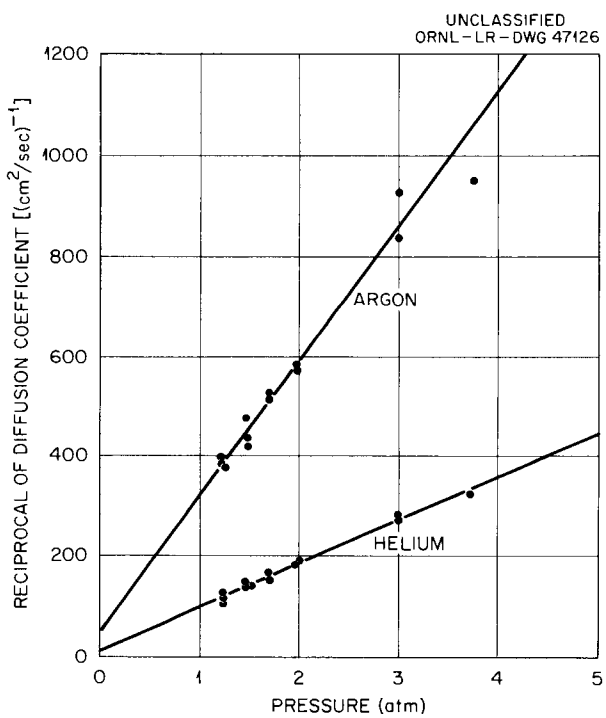

Fig. 6.11. Plot of Reciprocal of Apparent Diffusion Coefficients for Argon and Helium in AGOT Graphite at 25°C.

3.16, which is the ratio of the square root of the argon molecular weight to that of helium. This suggests that a viscosity relationship similar to that given by Dushman[19] may be applicable, rather than a classical diffusion term, as originally anticipated. Another point under consideration is the fact that the net flows result in nonlinear concentration profiles which have not been accounted for in the calculation of the apparent coefficients presented. A more meaningful approach would involve equations of the form[20]

$$G_i = N_i G_T - D_{12} A \frac{P}{RT} \frac{\partial N_i}{\partial L} ,$$

where G_i is the flow of component i, G_T is the net flow, and the last term represents the diffusive component. This approach appears to be valid, since the pressure-dependence relationships obtained indicate that nearly all types of flow present are common to all the pores. Rather than specifying two apparent coefficients, it would then be possible to specify a single coefficient and the net flow.

It should be pointed out that previous investigators have been concerned with diffusion rates of only one component of the binary mixtures studied; that is, only one of the two sweep streams employed was analyzed for diffused gas. Thus, little information regarding the net transfer effect (at $\Delta P = 0$) can be obtained from the literature. Attempts to correlate the data will be continued.

Chemical Behavior of Fission Products in Fissioning UO_2

Important properties, such as vapor pressure, diffusion rates, and chemical reactivity, of fission-product species depend on the state of

---

[19] S. Dushman, "Scientific Foundations of Vacuum Techniques," p. 40, John Wiley, New York, 1949.

[20] A. J. de Bethune, W. G. Pollard, and R. D. Present, "Flow of Gases Through Barriers," p. 80, Technical Information Service, USAEC, Oak Ridge, Tenn., NNES-II-3 (1952).

chemical combination in which the fission product comes to equilibrium. The necessity for the fissioning medium to maintain cation-anion equivalence (charge balance) and for thermodynamic equilibrium to be maintained among the possible chemical species should dictate the state of combination for each element. The expected state of combination at equilibrium, estimated from available thermodynamic data,[21] for all products of fission of $UO_{2.00}$ with yields above 0.1 atom per 100 fissions is shown in Table 6.4.

It is known that SrO, BaO, ZrO_2, Nd_2O_3, and Y_2O_3 dissolve to form solid solutions with UO_2. Considerations of the cation radii lead to the confident prediction that the trioxides of lanthanum and the rare earths form similar solutions. Europium and samarium may form divalent oxides, and they should, in that case, form solid solutions with UO_2, as do BaO and SrO. The available literature does not permit prediction of the phase behavior of MoO_2, so this compound is being prepared in order to determine, in a simple experiment, its solubility in UO_2.

The basic reasons why Cs, Rb, Tc, Ru, Rh, Pd, and Te do not form oxides are that the oxide formers listed in Table 6.4 form more stable oxides and are present in sufficient quantities to react with all

[21] J. P. Couglin, "Heats and Free Energies of Formation of Inorganic Oxides," U.S. Bureau of Mines Bulletin 542 (1954).

Table 6.4. Molecular Form of UO_2 Fission Products

Oxides	Elemental Gases	Solid Metal	Liquid Metal	Anions of Cs, Rb, Ba, and Sr
Zr	Kr	Tc	Cs	I
Mo	Xe	Ru	Rb	Br
La	Cs	Rh		Se
Rare earths	Rb	Pd		Te
Y				
Sr				
Ba				

oxygen that is a byproduct of fission. Cesium and rubidium would distill away from the UO_2 pellets to cooler portions of the fuel capsules, probably at the bottom of each capsule, except that the temperatures will be sufficiently high for them to exert a high vapor pressure (~1 atm), and therefore they will be in the gas phase in high concentration, along with krypton and xenon.

The four metals, Tc, Ru, Rh, Pd, will be present as a separate metal phase (or phases) which will have a liquidus temperature greater than 4000°F. Palladium, which melts at 2830°F, may be present as liquid but will tend to migrate and form a solid solution phase with either ruthenium or rhodium. The basis for these predictions lies in the known phase behavior of Ru, Rh, and Pd.[22]

The four fission products which are best treated as nonmetals, I, Br, Se, and Te, form stable compounds with the alkali and alkaline earth elements. However, the exact fraction of the alkalis and alkaline earths that would react with the nonmetals is not certain because important thermodynamic data are unavailable. From molecular size considerations and the lack of similarity to UO_2, it is safe to say that these compounds will not form solid solutions in the fuel pellets. Furthermore, the alkali halides formed will volatilize to some extent, condense in the cooler portions of the element, and probably dissolve in the free alkali-metal phase.[23]

Measurement of High Temperatures

Measurement of Surface Temperatures in High-Velocity Cooling Gas

The investigation of factors influencing the accuracy of thermocouples attached to metal surfaces in high-velocity cooling gas was continued. When thermocouples are used to measure the temperatures of

---

[22] M. Hansen, "Constitution of Binary Alloys," McGraw-Hill, New York, 1958.

[23] M. A. Bredig, H. R. Bronstein, and W. T. Smith, Jr., J. Am. Chem. Soc. 77, 1454 (1955).

gas-cooled surfaces, corrections must be made for the cooling action of the gas on the thermocouple. The cooling gas removes heat from the surfaces of the thermocouple leads and induces the flow of heat outward through the thermocouple. Consequently a thermal gradient is set up in the region between the original surface and the junction of the thermocouple inside the thermocouple bead. The magnitude of the resulting error in the temperature measurement is proportional to the distance separating the thermocouple junction from the original metal surface and is also proportional to the thermal gradient in this region. The distance separating the thermocouple junction from the original metal surface, which will be called the height of the junction, is fixed at the time the thermocouple is fabricated. The thermal gradient through the thermocouple depends upon the various geometrical factors and gas flow conditions which affect the heat transfer through the thermocouple and the lead wires. These factors include the diameters and exposed lengths of the thermocouple lead wires, the composition and pressure of the cooling gas, the dimensions of the cooling channel, the velocity of the cooling gas, and the thermal conductivity of the thermocouple metals.

Methods of fabricating bare-wire thermocouples which have reproducible cooling corrections have been developed.[24] A section through a thermocouple bead at a point displaced toward the end of the thermocouple wires about 0.005 in. from the center of the bead is shown in Fig. 6.12. Sections taken near the center of the bead show the Alumel region resting above the Chromel region. The location of the thermocouple junction in a thermocouple of this type cannot be determined by examination. Various points of contact between the Chromel and Alumel contribute in differing degrees to the electrical junction. The effective location may be at any point along the Chromel-Alumel boundary.

Methods for experimentally determining cooling corrections for attached thermocouples are available.[24] Briefly, a metal specimen is

---

[24]W. E. Browning and H. L. Hemphill, "Solid State Div. Semiann. Prog. Rep. Feb. 28, 1955," ORNL-1851, p. 19.

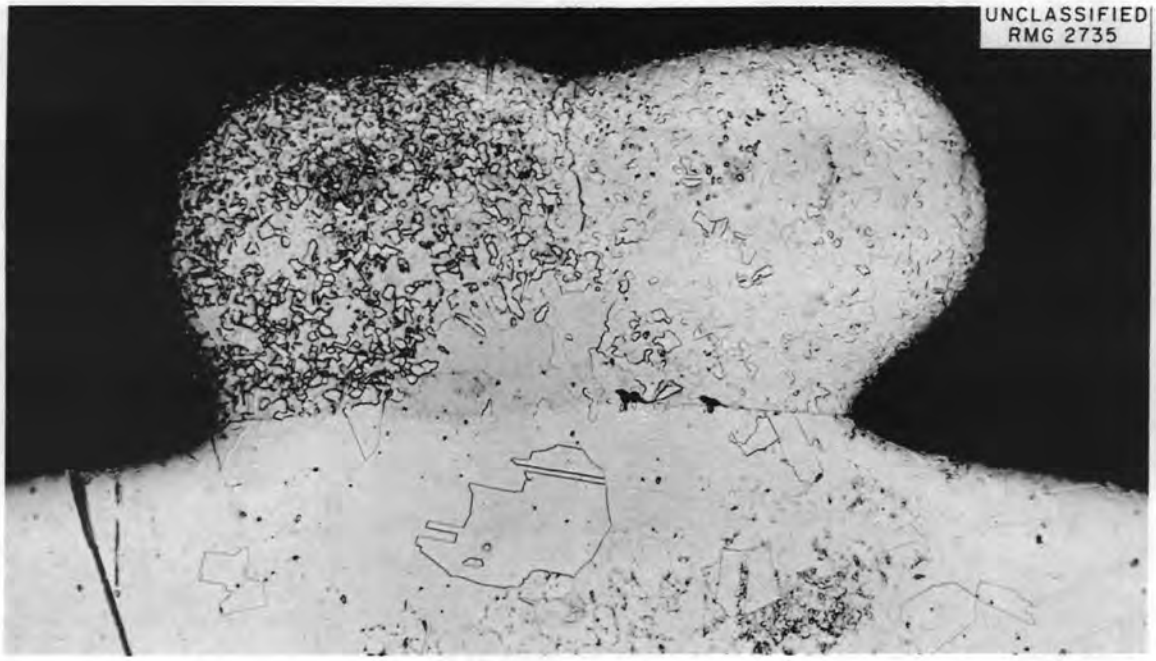

Fig. 6.12. Section Through Chromel-Alumel Thermocouple Bead.

heated electrically while being cooled by gas passing through a cooling annulus defined by a quartz tube. The metal surface temperature is determined by viewing through the quartz with an optical pyrometer, and the actual temperature is compared with the temperatures indicated by attached thermocouples to determine the required correction.

Since it would be desirable to be able to predict the cooling corrections for thermocouples under a variety of cooling conditions based on tests conducted under a limited number of cooling conditions, a procedure has been developed for using the Oracle to make the calculations required to predict the variations of cooling corrections with the cooling conditions surrounding the thermocouples. The results of these theoretical calculations are being used to correlate cooling correction data obtained under a variety of cooling conditions.

The ideal model shown in Fig. 6.13 was used for the calculation of heat transfer within an attached thermocouple exposed to a coolant stream. The thermocouple is represented as two isolated wires whose ends are attached to the surface whose temperature is to be measured. It was desired to calculate the temperature at a point within the thermocouple

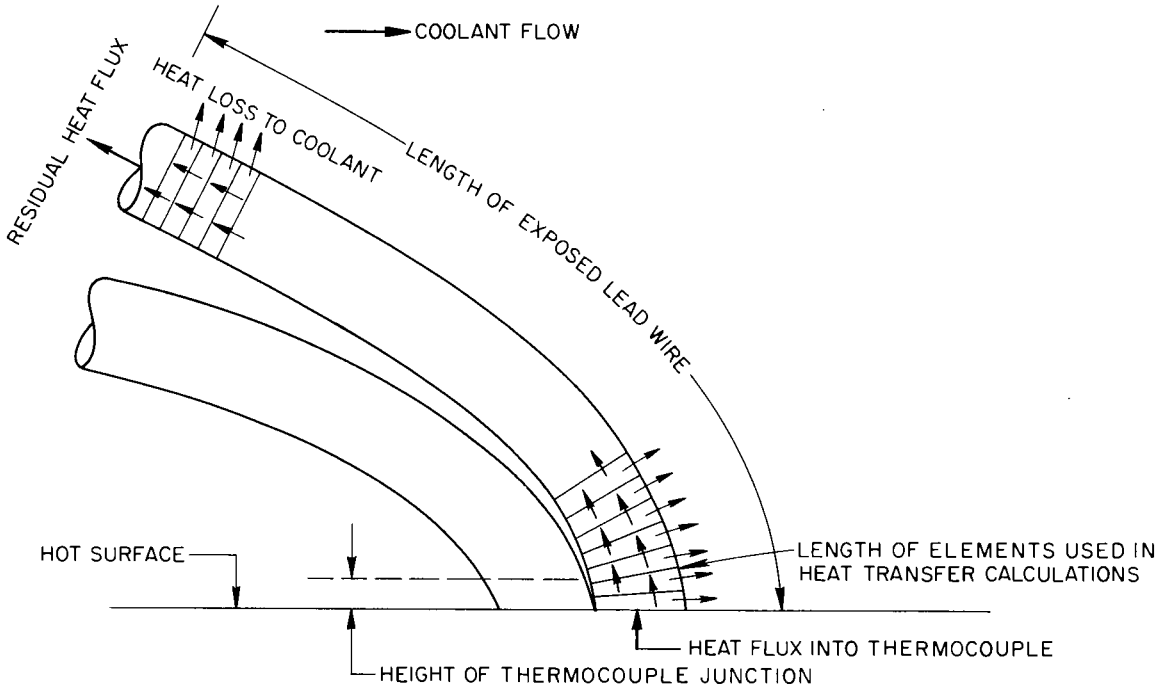

Fig. 6.13. Thermocouple Model for Heat Transfer Calculations.

at the location of the thermocouple junction. To perform this calculation, it was necessary to evaluate the heat flux profile and temperature distribution throughout the thermocouple. The exposed thermocouple lead wire was divided into 100 elements of length for this calculation, and a heat flow balance was established for each element. An initial estimate was made of the heat flux into the base of the thermocouple from the hot surface, and the calculation of the temperature of the first element was based on the heat flux estimate and the thermal conductivity of the thermocouple metal. The convective heat losses from the element to the coolant were calculated from the temperature of the element and the heat transfer film coefficient determined from the cooling conditions for the case being calculated. The convective heat losses were subtracted from the heat flux entering the element to yield the heat flowing from the first element to the second element. The temperature of the second element was then calculated, and the process

was repeated for each of the 100 heat transfer elements. If the initial estimate of the heat flux into the base of the thermocouples had been correct, the residual heat flux remaining at the end of the thermocouple lead wire would have been zero. Actually, it was necessary to use the magnitude of the residual heat flux to construct a revised estimate of the heat flux at the base of the thermocouple and to repeat the calculations until the residual heat flux was sufficiently close to zero. The calculation usually converged after only two or three iterations.

The calculations yielded a temperature profile in the thermocouple that could be used to predict the temperature cooling correction if the height of the thermocouple junction inside the thermocouple were known. Since the height of a thermocouple junction cannot be observed directly, but is presumably fixed for each thermocouple, it was of interest to express the results of these calculations in terms of the thermal gradient near the base of the thermocouple. This thermal gradient should be proportional to the cooling correction for each thermocouple and should vary with cooling conditions in the same way, as far as the thermocouple cooling correction is concerned.

Some of the results of the calculations are presented in Figs. 6.14 and 6.15. The thermal gradient at the base of the thermocouple versus the Reynolds number of the coolant for various lengths of exposed thermocouple leads is shown in Fig. 6.14. The calculations were made for 0.010-in. Chromel-Alumel wires with air at atmospheric pressure passing through a 0.050-in.-thick annular channel. As may be seen, the thermal gradient increases with the Reynolds number and is quite sensitive to the length of exposed lead wire for lengths of less than 0.100 in. The calculated thermal gradient is plotted versus the length of exposed lead wire for two values of the Reynolds number in Fig. 6.15.

Thermocouple cooling corrections were also determined experimentally for a series of thermocouples under the conditions used in the calculations. The results of these tests, together with the information presented in Fig. 6.14, were used to evaluate an effective height of the thermocouple junction for each individual thermocouple. The effective

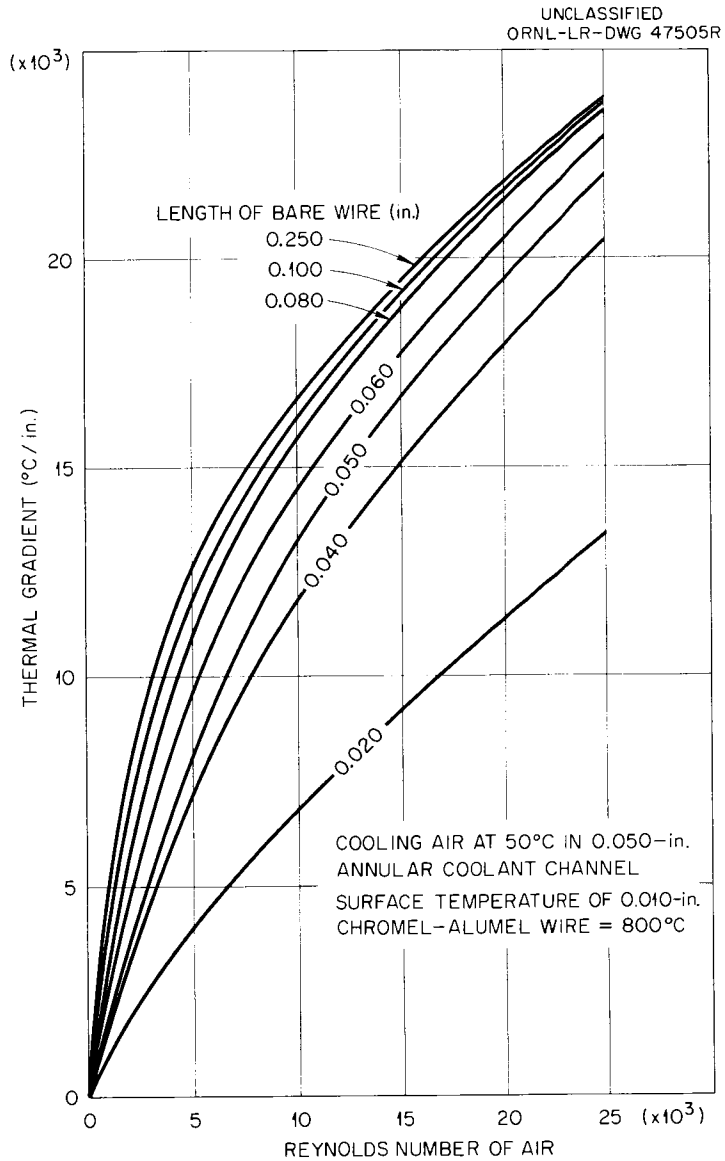

Fig. 6.14. Calculated Thermal Gradients in Thermocouples Versus Reynolds Number of Coolant.

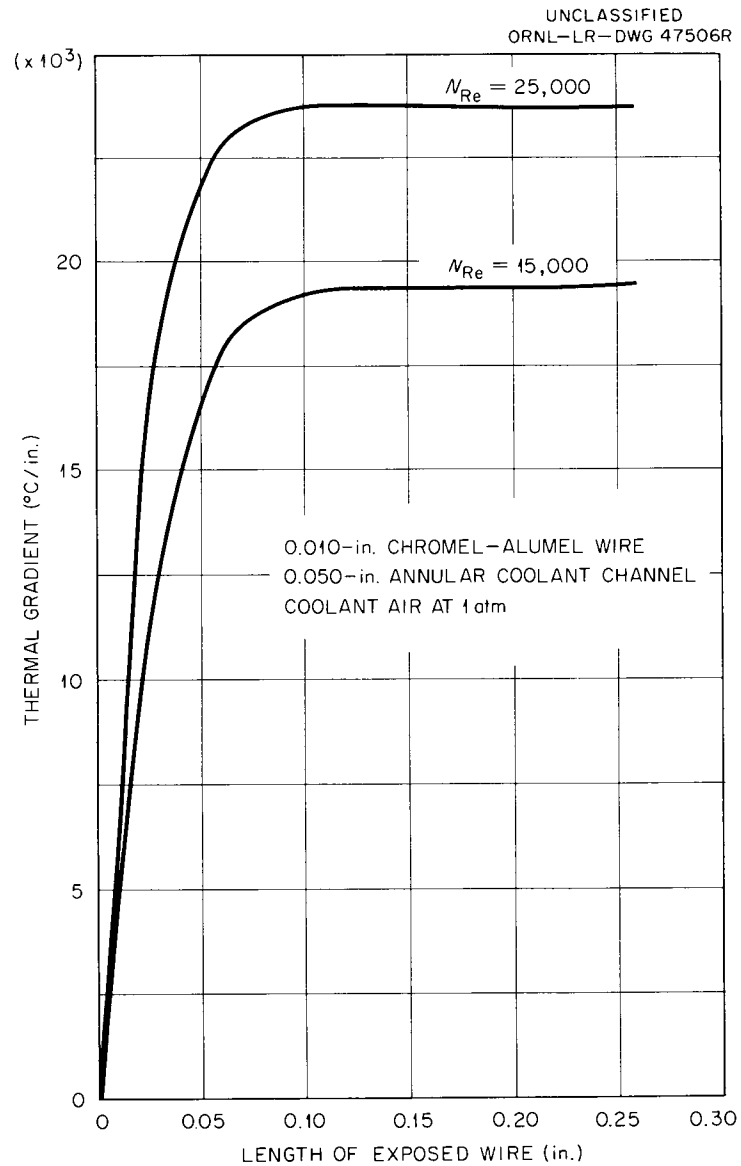

Fig. 6.15. Calculated Thermal Gradients in Thermocouples Versus Length of Exposed Lead Wire.

heights so obtained were used, together with the information of Fig. 6.14, to calculate the theoretical thermocouple cooling corrections as functions of Reynolds numbers. The theoretical values are presented in Fig. 6.16 and compared with the experimentally determined cooling corrections. It may be seen that the theoretical heat transfer calculations successfully predict the variation of the thermocouple cooling correction with the Reynolds number.

Stability of Rhenium-Tungsten Thermocouples

Tests were continued on rhenium-tungsten thermocouples at temperatures from 1000 to 2000°C. Thermocouples of these materials are of interest for measurement of central temperatures in UO_2 fuel elements. Studies are being made of the effects on calibration of various factors, including aging at high temperature, thermal cycling, and atmospheric impurities.

Effects of Radiation on Thermocouples

Calculations of the amounts of impurities produced in thermocouple materials by transmutation reactions were continued. Five platinum-rhodium thermocouples and one rhenium-tungsten thermocouple irradiated in the LITR are on hand for postirradiation calibration. Calibration curves will be determined for these thermocouples in the hot cells.

Tests of Chromel-Alumel Thermocouples in Various Atmospheres

Chromel-Alumel thermocouples have been tested under various conditions because of evidence of abnormally high drift rates in the presence of certain contaminants.[25] Negative drifts of 10 to 40°C in 24 hr had been noted for thermocouples in stagnant air at 1040°C in the presence of chromium and Inconel powders. In stagnant helium atmospheres, negative drifts of 15 to 35°C in 40 hr had been noted for thermocouples in the presence of chromium and Inconel. The thermocouples were in

[25] J. L. Potts and D. L. McElroy, ORNL, personal communication to W. E. Browning, ORNL.

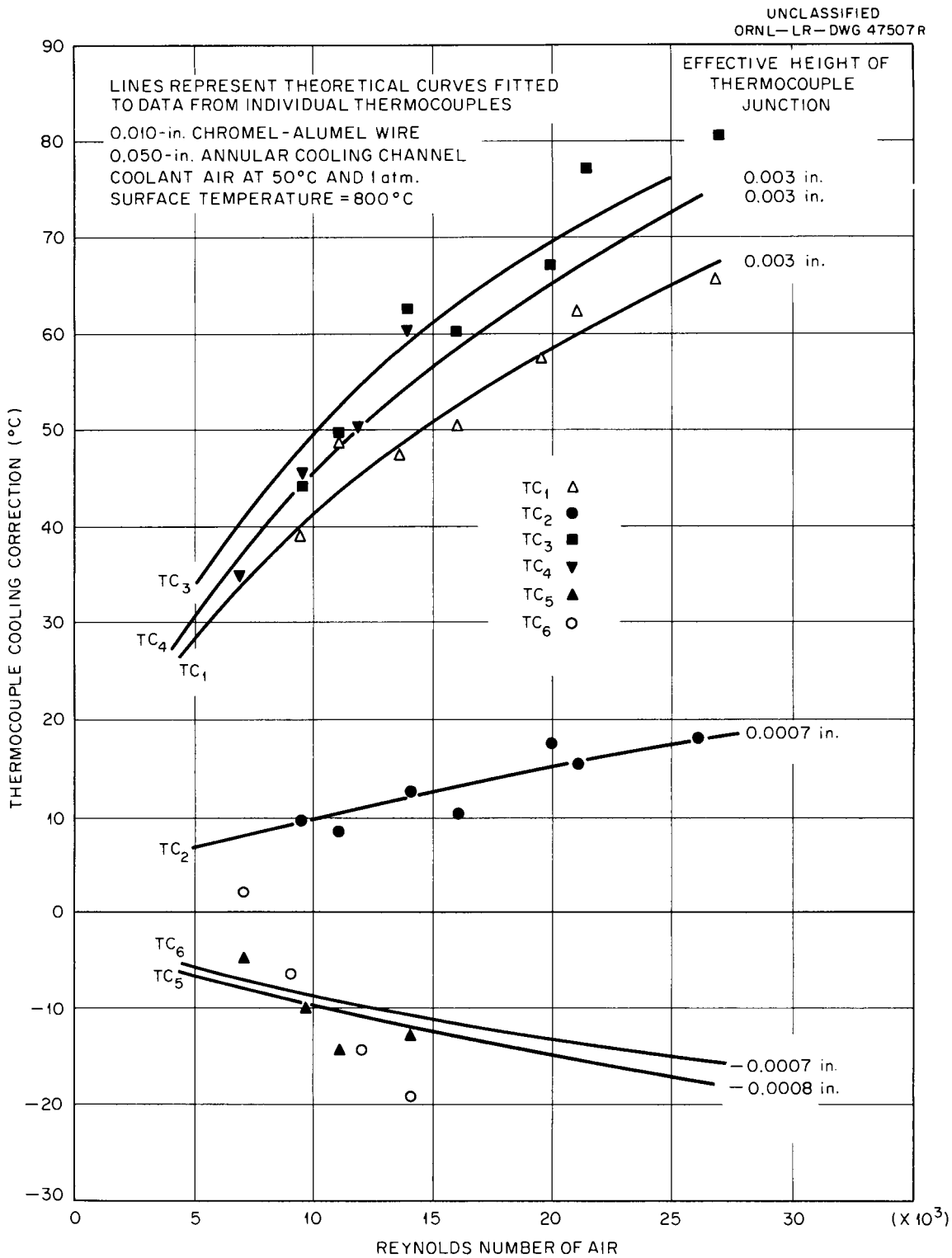

Fig. 6.16. Comparison of Experimental and Theoretical Cooling Corrections for Thermocouples in Cooling Gas Streams.

quartz tubes in the thermal-gradient region and had long alumina protection tubes. Uncontaminated Chromel-Alumel thermocouples drifted 2 to 4°C in a positive direction under similar conditions.

Studies made under carefully controlled conditions have resulted in only one example of an abnormal drift. It should be pointed out, however, that no tests have been made under exactly the conditions that gave the abnormal results reported above. The studies reported herein were made with 12-in. quartz protection tubes in place of the 36-in. alumina tubes used by previous investigators. The one case of abnormal drift resulted from the use of chromium powder and a stagnant helium atmosphere with the thermocouple insulating tube broken at 0.75-in. intervals and with 0.25 in. of metal exposed between the breaks throughout the length of the tube. The protection tube was not purged of air before a helium pressure of 3 psi was applied with no flow. The drift rate was almost linear during 24 hr at a rate of -2.0 mv in 24 hr; the rate of drift subsequently decreased.

In stagnant air at 1000°C the measurements obtained during a 100-hr period for 18 thermocouples showed a maximum difference between thermocouples of 4°C. The data showed no significant differences between thermocouples with broken or solid insulators, and all drifts were positive. The Chromel leg measurements drifted 3°C ± 1°C, and the drift tended to level off. The Alumel leg measurement drifted 6°C ± 1°C and continued to increase in error.

In flowing helium the results were approximately the same. Specially purified helium gave the same results as cylinder helium. After 140 hr of helium flow, the helium lines were replaced with air lines, and air was passed through the tubes for 60 hr. There was no change in rate of drift of any of the thermocouple measurements.

The measurements of thermocouples in broken insulators in the presence of chromium and Inconel powders tested with a flowing helium atmosphere showed no greater drift than those of control thermocouples tested without metallic contaminants. The insulators used in these tests were broken by cracking the ceramic into approximately 0.75-in.

lengths, and no gaps were larger than 0.10 in.; therefore only very narrow sections of the wires in the thermal-gradient region were exposed to contamination. The wires fitted snugly into the ceramic insulation, so there was only a slight chance of diffusion up the hole, particularly after slight oxidation of the wire caused swelling and completely blocked the hole. Therefore, the results from these tests should not necessarily have been intermediate between the results of tests with solid insulators and broken, spaced insulators.

As a further check on the oxidation changes that take place in the wires, accurate resistance measurements were made on the individual thermocouple legs during the tests in helium. The presence of metallic contaminants had no significant effect on resistance changes. In general, the sections of Alumel wire in the high-temperature zone in helium increased in resistance by approximately 50% during 200 hr. The resistance of the Chromel wires increased only 5% during 200 hr. When the helium flow was replaced by air flow, the rate of change in the resistance of the Alumel wire increased by a factor of 4. The Chromel wires showed no appreciable changes. The measured resistance changes agreed with predicted values. As the cross sectional areas of the wires were reduced by oxidation, the resistance increased. No correlation between emf drift and resistance change was found. This was expected, since any oxidation could cause resistance changes, but only oxidation that resulted in changing the metal composition could cause emf changes.

It is interesting to note that no appreciable changes were found in the resistances of either the Chromel or Alumel legs in the one instance of abnormal emf drift. The slight increases in resistance measured were much less than the usual changes in helium.

The results obtained thus far indicate that Chromel-Alumel thermocouples in the presence of chromium, Inconel, and quartz insulation in a flowing helium atmosphere show no abnormally fast emf drifts when there is limited access of the helium to the wires in the thermal-gradient range; however, abnormal drifts may occur under similar conditions in stagnant atmospheres. The tests are not complete, but the

data are significant and are as accurate and reproducible as necessary for this program.

Purification of Cooling Gases

Methods of removing impurities, particularly fission gases, from the coolants of gas-cooled reactors are being investigated. The effect of helium carrier gas pressure on the dynamic adsorption of krypton by charcoal at 25°C has been studied experimentally, preliminary tests have been made of a number of samples of commercially available activated carbons with respect to fission-gas retention, and the adsorbers designed for GCR-ORR loop No. 1 have been evaluated.

In the design of adsorbers for the removal of noble gas fission products from high-pressure helium, it is highly desirable to have information regarding the effect of helium pressure on retention times and on N, the number of theoretical plates. These factors were studied by obtaining krypton elution curves for helium carrier gas pressures up to approximately 420 psia with Columbia G activated carbon at 25°C as the adsorbent and with Kr^{85} as the tracer. The general techniques employed and the gas-solid chromatographic theory involved were discussed previously.[26] Results of the study are presented in Fig. 6.17, where the dynamic adsorption coefficient k and N are plotted versus helium pressure. The k values were determined from the expression

$$k = \frac{t_{max} F}{m} ,$$

where t_{max} is the time (min) for buildup of the maximum fission gas partial pressures in the effluent gas, F is the volumetric flow rate measured at the carrier gas pressure in the adsorber (cm^3/min), and m is the mass of adsorbent (g). The N values were obtained with the use of an abbreviated form of the theoretical equation previously developed.[26]

---

[26]W. E. Browning and C. C. Bolta, "Measurement and Analysis of the Holdup of Gas Mixtures by Charcoal Adsorption Traps," ORNL-2116 (July 27, 1956).

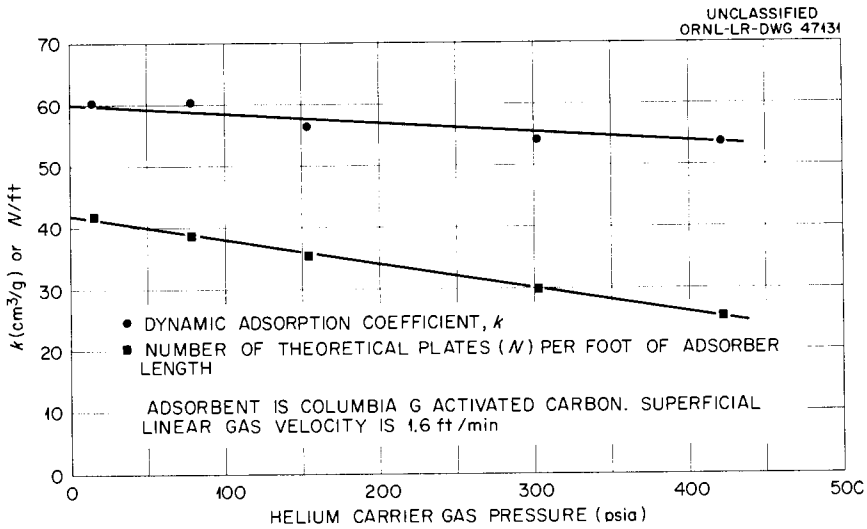

Fig. 6.17. Effect of Helium Pressure on Dynamic Adsorption of Krypton from the Helium Stream on Charcoal at 25°C.

The N values obtained in this manner agreed well with those obtained by using the calculation method customarily employed in gas-liquid chromatography. This suggests that the same process is rate determining in the two techniques. As may be seen, k is only slightly reduced by the helium pressures considered; also, although the decrease in N with pressure is appreciable, this effect does not appear to be serious from the standpoint of adsorber efficiency. (The behavior of k was to some extent predictable, since interference from helium adsorption at 25°C would be negligible, even at 420 psia.)

Fourteen additional samples of activated carbon in a variety of mesh sizes from five different manufacturers were tested for krypton retention at room temperature with helium as the carrier gas. The results of these preliminary tests indicated that most of these materials would be suitable for certain applications.

The activated charcoal traps designed for use with GCR-ORR loop No. 1 were evaluated.[27] The maximum quantity of fission products that

[27]R. E. Adams and W. E. Browning, "Evaluation of Activated Charcoal Fission Gas Adsorbers Designed for the GCR-ORR Loop Experiment No. 1," ORNL CF-60-1-24 (March 16, 1960).

could be expected to be released was calculated, and the resulting hazard was examined on the basis of probable radiation doses to laboratory personnel from exposure to the gas cloud. The release was postulated to have occurred during adverse meteorological conditions when the efficiency of the gas disposal stack was low. Even with these assumptions which were intended to make the estimate maximal, the probable total-body radiation dose was determined to be only 0.55 mr. Therefore, the consequences of atmospheric disposal of fission products, mainly krypton, passing through the charcoal traps do not appear to be serious.

Determination of Impurities in Helium

The Greenbrier Chroma-matic 112 process dual-column gas chromatograph, which has been described in previous reports,[28,29] has been operated throughout its first application on the low-pressure thermal-convection test loop and is now being used to provide analyses for a similar test run on the same loop. The maintenance required by the unit has been negligible. The accumulated experience during approximately three months of operation and calibration runs during periods between tests has served to demonstrate that the reproducibility of the chromatograph results is somewhat better than was reported earlier.[29] On the basis of 36 analyses over a 12-hr period on a sample containing 0.1 to 0.2% of each contaminant, the coefficient of variation is about 3% for H_2, 1% for CO, and less than 1% for CO_2, N_2, and CH_4. The stability of the instrument over extended periods is illustrated in Table 6.5.

The calibration analyses were performed periodically on synthetic samples that were substituted for the samples from the test loop. A catalytic combustion detector assembly has been received that is expected to improve the sensitivity of the determination of hydrogen. It will be installed during the next period in which the chromatograph is not in use.

---

[28] "GCR Quar. Prog. Rep. Sept. 30, 1959," ORNL-2835, p. 151.

[29] "GCR Quar. Prog. Rep. Dec. 31, 1959," ORNL-2888, p. 178.

Table 6.5. Calibration Analyses on Greenbrier Chroma-Matic 112 Process Chromatograph

Analytical Instrument	Date	Analytical Results (ppm by volume)						
		H_2	CO_2	O_2	N_2	CH_4	CO	N_2 + CO
Process chromatograph	2/8/60	1100	1110	11	950	1010	1010	
	2/10/60	1060	1060	10	940	1010	980	
	2/12/60	1100	1120	11	950	1010	1000	
	2/15/60	1120	1060	13	950	1000	1000	
	2/18/60	1070	1060	12	935	995	990	
	2/24/60	1090	1085	12	945	980	1040	
	2/26/60	990	1060	9	925		1040	
	3/1/60	1090	1080	11	935	980	1035	
		1080 av	1080 av	11 av	940 av	1000 av	1010 av	1950 av
Laboratory chromatograph		1100	1110		950	1010	1010	1960
Mass Spectrometer		1090	1280			984		1950

The Consolidated Electrodynamics moisture monitors have not, as yet, been completely satisfactory. The basic component in these instruments is the electrolytic cell, which consists of two platinum-wire electrodes closely wound in a double helix on the inner surface of a glass tube. These electrodes are coated with a thin film of phosphorus pentoxide that quantitatively absorbs the moisture from a stream of sample gas which flows at a regulated rate of 20 cm^3/min. A potential is applied across the electrodes to effect electrolysis of the absorbed water. Since the resistance of the electrolyte film increases as water is removed, the cell approaches a steady state in which the concentration of the water remains constant. The current is then equal to that required by Faraday's law for the electrolysis of the moisture from the gas stream. A microammeter in series with the cell is calibrated to read concentration directly in ppm by volume. Attenuator circuits are provided to extend the concentration range to 20 000 ppm. The instrument is specified to provide a measurement of moisture concentration, accurate to ±5% in all gases except those that react with P_2O_5, such as ammonia, hydrogen fluoride (which is electrolized), and

hydrogen (which promotes recombination of the oxygen that results from electrolysis).

The proposed applications of these instruments included the measurement of concentrations of water up to 2000 ppm in the loop atmosphere, which may contain hydrogen concentrations up to 5%, and the measurement of water in a saturated helium stream which is used for the controlled injection of water into the test loop. During initial operations the cells in instruments used in both applications failed by shorting after a few hours of use.

Examination of the cells used for the analysis of the loop atmosphere revealed that they had become shorted by metallic particles from the tubing in the sample system or by liquids distilled from the graphite in the test loop. After the cells were cleaned and recoated, the instruments were found to provide accurate measurements at concentrations up to 3000 ppm and to give satisfactory service for periods of several weeks. The accuracy has been established by calibration in the laboratory with helium equilibrated with water at reduced temperatures and by comparison of analyses of loop samples with those obtained by dew-point measurements. In agreement with reports from the manufacturer, negligible errors of 10 to 30 ppm are introduced by the addition of 10% hydrogen to the samples. The magnitude of these errors appears to be independent of the concentration of water in the sample, but the magnitudes differ for each cell.

The monitors have not been found to be dependable for the measurement of concentrations of water near 1%. Cell failures have occurred after periods from a few hours to several days. A metallic connection between the electrodes appears to be responsible for the failure because the shorts are removed only by washing with nitric acid or nitric acid followed by hydrochloric acid. Microgram quantities of copper have been found in the nitric acid washing solution, and iron, chromium, nickel, and copper are present in the hydrochloric acid washing solution. Because metallic particles have been carefully eliminated from sample lines and cell failures have been observed to occur slowly, shorting is believed to result from electrolytic deposition of metallic dendrites

on the cathodes. Significant positive errors and more rapid failure of cells are brought about by the addition of 10% of hydrogen to the samples. These phenomena may be the result of a catalytic effect of the metallic deposits on the recombination of hydrogen and oxygen and a mass action effect of the hydrogen. Current efforts are directed toward finding the source of the metallic contaminants and eliminating them.

Determination of Oxygen-to-Uranium Ratios in UO_2 Pellets

An investigation has been undertaken to develop a method for the determination of UO_3 in UO_2 fuel pellets by reduction in a hydrogen atmosphere. Since higher oxides are reduced to UO_2, the water produced by this reaction would be proportional to the oxygen present in excess of a 2:1 mole ratio. In the proposed method a powdered sample of UO_2 will be placed in a heavy gage platinum boat in a quartz combustion tube which will be evacuated to remove adsorbed oxygen. The sample will then be ignited with an induction furnace in a stream of rapidly flowing hydrogen which will subsequently pass through a liquid nitrogen cold trap. When the water produced by the reaction,

$$UO_3 + H_2 \rightarrow UO_2 + H_2O \quad ,$$

has been collected in the cold trap, the trap will be connected to a stream of dry helium that will pass through the cell of a modified Consolidated Electrodynamics moisture monitor. The trap will then be warmed to transfer the water to the cell of the moisture monitor in which it will be absorbed and quantitatively electrolyzed. The excess oxygen will then be calculated from the integrated current-time product of the current required for the electrolysis. The use of the coulometric method for the measurement of water is, of course, dependent on the resolution of the problems mentioned above in the use of the mositure monitor for the determination of high concentrations of moisture.

Alternate methods for the determination of the trapped water include tensiometric measurement or conversion to acetylene, which can be determined by a gas chromatographic technique.

7. DEVELOPMENT OF TEST LOOPS AND COMPONENTS

ORR Gas-Cooled In-Pile Loops

GCR-ORR Loop No. 1

Design work is nearing completion on GCR-ORR loop No. 1, the ORR installation layout, the auxiliary services, and the instrumentation and controls. Fabrication of all main loop components, that is, the in-pile section, transfer station, heater, regenerator, cooler, and compressor vessel, is also nearly complete. Installation of the loop in the ORR was started during the March reactor shutdown.

In the ORR building, off-gas piping to the vacuum pump has been installed beneath the basement floor and through the pool standpipe. Installation of wireways and service piping is under way. Fabrication of the three charcoal adsorbers is complete, and the shielded compressor cubicle is being installed on the lower pool balcony. The motor-generator sets for the compressor drive motors and the vacuum pump have been set.

A flux-monitoring test was run in the B-1 lattice position during the January ORR shutdown. The test elements have been disassembled, and the data are being analyzed. The thermocouple calibration test was completed, and a preliminary examination of results indicates that the cooling gas stream has little effect on the fuel element cladding thermocouples at any velocity or temperature. An underwater test of the transfer station and fuel element insertion and removal system was started.

The fabrication of instrument panels and racks is well advanced, and remote tools for underwater maintenance at the ORR are being assembled. Components for the first fuel element assembly are being machined.

GCR-ORR Loop No. 2

Design of the loop No. 2 components, such as the evaporators, condenser, charcoal adsorbers, etc., is approximately 70% complete. Design studies of the loop cell enclosure and the required building services have been initiated. Existing equipment adjacent to the ORR-HS beam

hole has been removed. The design of a new facility plug and liner for the beam hole is approximately 80% complete.

Gamma-ray heating calculations were made for the liner area adjacent to the reactor core. A maximum value of 2.7 w/g was found for the particular core loading chosen at a reactor power level of 45 Mw.[1]

A full-stream coolant filter was designed for installation between the cooler and compressors at a point in the loop where the gas temperature will be approximately 600°F. The design specifies a commercially available pleated-glass-paper filter element suitable for use at temperatures up to 1000°F that has a rated dioctyl phthalate (smoke) efficiency of 99.9% for 0.3-μ particles.

A redesign of the charcoal adsorber traps has been made in an attempt to reduce the total weight of the trap and shield. Cooling the traps to -50°F is expected to make possible the desired weight reduction.

A preliminary investigation of cell ventilation requirements has been made. An existing duct will handle the required gas volume, but an auxiliary blower will be needed to provide adequate head to operate the filter, scrubber, and charcoal bed needed in the cell exhaust gas system and to maintain a negative pressure in the cell.

A compact, extended-surface type of regenerator has been ordered. The helium buffer region in the original heater design has been replaced with an atmospheric air containment region in order to minimize the problem of arcing across electrical leads because of ionization of helium at the expected temperatures. A test was conducted to determine whether any difficulties would be encountered in welding the heater cartridges to the header. The test welds were satisfactory, and it was decided to make the header of Inconel so that the many welds between header and cartridge would not be made between dissimilar metals.

Although it was determined that the use of a reflective type of insulation for the loop piping would result in only slightly less heat

---

[1]P. H. Pitkanen, "Gamma-Ray Heating in the South Facility of the ORR," ORNL CF-60-2-40 (February 9, 1960).

loss than the use of ordinary insulation, the advantages of easy removal, replacement, and cleaning make the reflective type a desirable choice.

Data required for a proposed analog simulator study of loop operation have been assembled.

Design conditions were determined for tests of graphite-clad fuel elements consisting of uranium dispersed in graphite, and loop temperature profiles were established. The zero power design conditions have been revised to keep the maximum loop piping temperature below 1470°F.

The design of the cell shielding walls has been changed from 3 ft of dry-packed magnetite ore to 4 ft of barytes concrete in order to obtain the required neutron shielding.

It has been decided that direct viewing of remote operations within the cell will be accomplished with a single, lead-glass, zinc-bromide window located opposite the beam hole plus one or more optical viewing devices along the length of the cell. A dummy plug will be required to permit access to the cell at times when the loop is not operating, the test plug is withdrawn, and the reactor is at power. The handling and storage problems connected with the relatively long concrete dummy plug considered earlier have been eliminated by a design which provides the necessary shielding by a combination of filling and 10-ft-long test plug opening with circulating reactor coolant water plus a 6- to 12-in.-thick lead end cap.

EGCR Experimental Loops

Design Status

Criteria have been developed for the helium- and carbon dioxide-cooled experimental loops in the EGCR. Each loop is to be capable of dissipating 1.5 Mw of power with inlet and outlet temperatures of 600 and 1050°F, respectively, and is to be capable of operating at a maximum inlet temperature of 950°F at a reduced power output. Outlet coolant temperatures of above 1050°F from the test element may be achieved by attemperation of the exit gas. The normal loop pressure was set at 500

psia, with maximum capability of 1000 psia. Conceptual designs of the loops are being prepared. Prime consideration was given to those features that affect the reactor design, that is, loop power requirements, nozzle design, utility requirements, experimental cell penetrations, cell shelter, and crane design.

Design studies of the main loop components are under way, and, in some instances, they have progressed to the point where experimental investigations are required to verify some of the design assumptions. The components being studied consist primarily of the main-line filters, gas coolers, gas heater, and auxiliary equipment, such as storage tanks, the charcoal adsorber bed, and the transfer pumps. In addition, a survey of vendors was undertaken to find suitable valves for the service conditions in the loops. Preliminary layouts of the equipment and piping in the experimenter's cell are being made in order to determine a suitable arrangement consistent with ease of maintenance and minimum piping stress. With the new symmetrical cell layout furnished by the architect-engineer, one equipment layout will suffice for all cells that contain helium- and carbon dioxide-cooled loops.

Experimental Fuel Element Handling. A study of handling problems associated with experimental fuel elements was initiated. Methods of final inspection, handling the fuel assembly in the EGCR vapor container, and preparing irradiated specimens for shipment to examination sites were defined, with particular emphasis placed on areas of interference with the present design.

A revised design of the reactor servicing machine indicates that the maximum length of experimental stringer that can be handled has been increased from 33 1/2 to 38 ft. In order to utilize the full height of the core for instrumented fuel stringers, however, stringers 47 ft long would be required. Therefore a study was made of methods of inserting and removing experimental fuel assemblies from the through tubes. Three schemes are being considered. In one scheme a service machine capable of winding a portion of the length of the instrument leads onto a large-diameter revolving drum would be used. This concept results in a machine

having an over-all height of 41 1/2 ft and weighing approximately 88 tons. In another scheme a service machine would be used that had sufficient length to receive a 47-ft experimental assembly without coiling or otherwise collapsing the instrument leads. This machine would have an over-all height of about 57 ft and would weigh approximately 80 tons. In the third scheme the present EGCR service machine would be modified to permit it to handle experimental fuel assemblies. The modified machine would have an over-all height of about 57 ft. Cost estimates were presented for each of these concepts.

Cooling Water for Experimental Facilities. An examination of the demineralized cooling water requirements for the experimental facilities was made. A sufficient supply will be available to remove 15 Mw of heat with a permissible temperature rise from 100 to 130°F.

An estimate of the heat loss from the equipment in the experimental cells has been made based on 4 in. of Thermobestos insulation on the equipment. The calculations gave a heat loss of approximately 30 kw, which will be removed by the heating and ventilation system and by other supplementary cooling means, such as river water.

Loop Kinetics. Three kinetic problems concerning the loops were investigated by numerical methods. This work was preliminary to the analog simulator study. The numerical results were used primarily in establishing specification for long-lead-time items, such as compressors. Three problems were considered: the complete loss of power upon failure of the emergency power system; the loss of one loop blower in a set, along with no compensating speed increase of the remaining blowers; and a reactor scram without a loop scram, that is, with the loops continuing to operate. Several cases were run on each problem. The total of 16 cases studied included variations in test specimens, number of blowers, reactor scram time, blower coastdown time, and test section attemperation. Both helium and carbon dioxide were considered as coolants.

The maximum rates of change of the test specimen surface temperatures were found to be as much as 60°F/sec under some conditions. With blower and blower motor-generator coastdown times of the order of 30 sec, it was

found that approximately 1 min could be used to establish emergency power. The calculations indicated that, upon failure of a blower, the surface temperature of the test specimen would rise 400°F in 10 sec. With a reactor scram and no adjustment in the loop, the cooling gas temperature would drop as much as 400°F in 8 sec. There would be essentially no natural-convection cooling in the loops.

Process Analysis

Flowsheet. A flowsheet for the primary experimental system components is presented in Fig. 7.1, and Fig. 7.2 shows a proposed auxiliary gas-handling system.

The primary experimental system flowsheet indicates the components, piping, and arrangement required to remove the heat generated in a test fuel element. The equipment consists of a set of three compressors, the fuel element test section in one of the eight through tubes in the reactor,

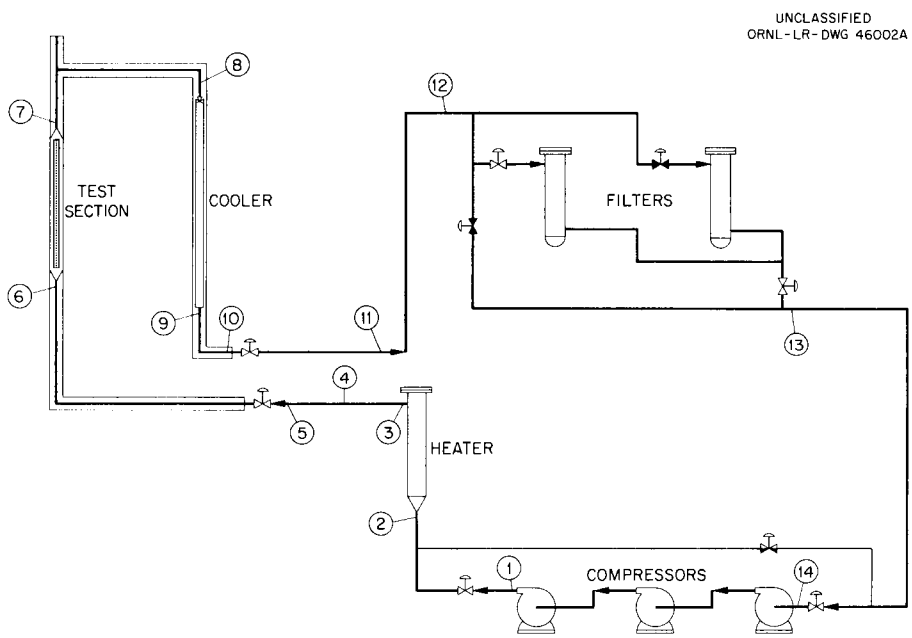

Fig. 7.1. Primary Coolant System Flowsheet for EGCR Experimental Loops. Numbers refer to entries in Table 7.1.

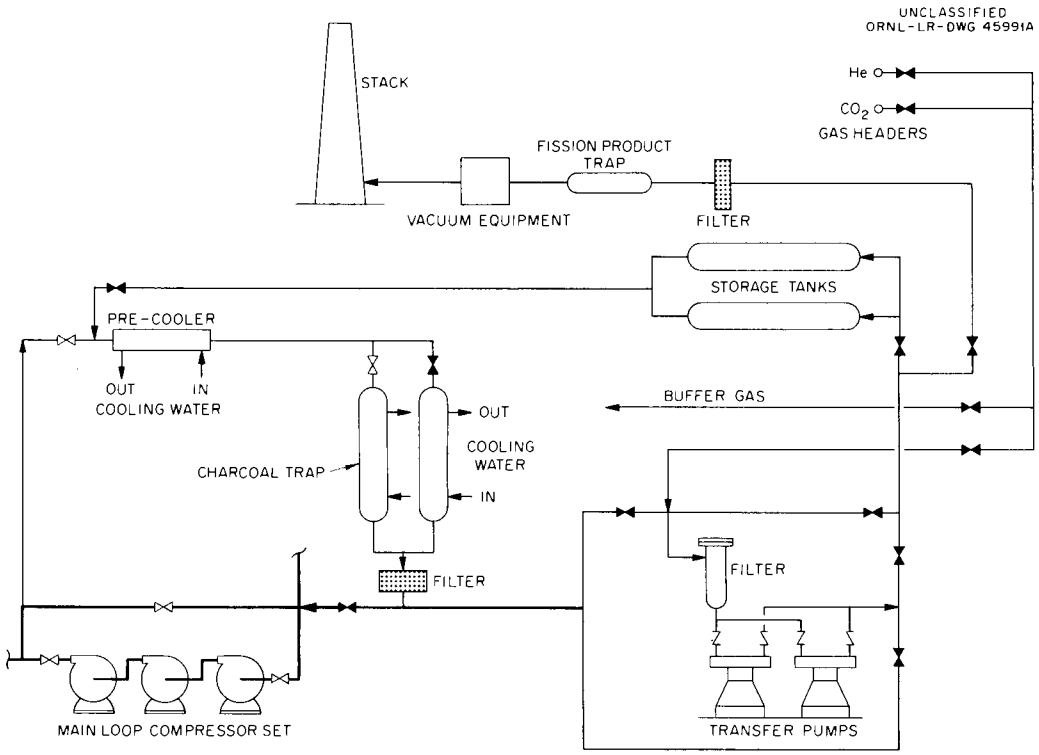

Fig. 7.2. Auxiliary Gas-Handling System Flowsheet for EGCR Experimental Loops.

a cooler to remove the heat generated, a set of parallel filters, a heater to regulate the gas temperature, and flow control valves. Conditions corresponding to the appropriate points on the flowsheet are shown in Table 7.1 for helium and CO_2 as the cooling gases.

The primary functions of the gas-handling system are to store the gas (He or CO_2) when it is not in use in the primary loops and to remove radioactive contamination from the gas by decay or by circulating the gas through the cleanup system before returning it to the in-pile loops or before discharging it from the stack. The basic components of the gas-handling system are shown in Fig. 7.2. All components that will contain high-pressure gas and those that may become contaminated with radioactivity are located in a special shielded compartment within the experimenter's cell space.

Tanks are provided for storing the gases required to fill the experimental loops. A loop will be filled by bleeding gas directly into

Table 7.1. Coolant Flow Conditions at Various Points for Four Operating Conditions of the EGCR In-Pile Experimental Loops With Helium and With CO_2

Nominal Operating Conditions

	I	II	III	IV
Loop power generation, kw	1500	1500	334	334
Gas pressure, psia	500	1000	500	1000
Inlet gas temperature, °F	600	600	950	950
Outlet gas temperature, °F	1050	1050	1050	1050

Point in System	I		II		III		IV	
	Pressure (psia)	Temperature (°F)	Pressure (psia)	Temperature (°F)	Pressure (psia)	Temperature (°F)	Pressure (psia)	Temperature (°F)
	Operation with Helium at a Flow Rate of 9190 lb/hr							
1	481.00	550	975.00	550	489.00	900	991.00	900
2	481.00	550	975.00	550	489.00	900	991.00	900
3	481.00	600	975.00	600	489.00	950	991.00	950
4	481.00	600	975.00	600	489.00	950	991.00	950
5	481.00	600	975.00	600	489.00	950	991.00	950
6	500.00	600	1000.00	600	500.00	950	1000.00	950
7	500.00	1050	1000.00	1050	500.00	1050	1000.00	1050
8	500.00	1050	1000.00	1050	500.00	1050	1000.00	1050
9	500.00	534.3	1000.00	534.3	500.00	888	1000.00	895
10	500.00	534.3	1000.00	534.3	500.00	888	1000.00	895
11	500.00	534.3	1000.00	534.3	500.00	888	1000.00	895
12	500.00	534.3	1000.00	534.3	500.00	888	1000.00	895
13	500.00	534.3	1000.00	534.3	500.00	888	1000.00	895
14	500.20	534.3	1000.50	534.3	500.00	888	1000.40	895
	Operation with CO_2 at a Flow Rate of ~41 000 lb/hr							
1	500.50	550	1000.00	550	500.00	900	1000.00	900
2	499.62	550	999.49	550	500.00	900	1000.00	900
3	497.12	600	998.24	600	500.00	950	1000.00	950
4	496.78	600	998.13	600	500.00	950	1000.00	950
5	496.58	600	997.95	600	500.00	950	1000.00	950
6	496.24	600	997.73	600	500.00	950	1000.00	950
7	469.94	1050	945.13	1050	500.00	1050	1000.00	1050
8	469.26	1050	944.80	1050	500.00	1050	1000.00	1050
9	466.76	533	943.45	536	500.00	890	1000.00	890
10	466.42	533	943.23	536	500.00	890	1000.00	890
11	466.22	533	943.05	536	500.00	890	1000.00	890
12	465.88	533	942.94	536	500.00	890	1000.00	890
13	464.08	533	941.69	536	500.00	890	1000.00	890
14	463.00	533	941.00	536	481.00	890	980.00	890

the system until an equilibrium pressure has been reached. The transfer compressor set will then be used to produce the desired pressure. The transfer compressors will also be used to transfer gas from the loop back into the storage cylinders. The storage cylinders will have separate connections to the transfer compressor suction and discharge so that a portion of contaminated coolant can be temporarily stored and then recirculated through the cleanup equipment.

Estimated System Pressure Drops. Based on the loop design criteria summarized in the previous report,[2] estimates of the pressure losses in the proposed loop systems have been made. The total pressure drop through the system includes: (1) the pressure drop through the in-pile test section, which was proportioned so that the pumping power allocated to this portion of the loop would not exceed 2% of the maximum loop power of 1.5 Mw; (2) the pressure loss through the loop piping; and (3) pressure losses through the loop equipment, which was assumed to consist of a cooler, six valves in series, hot gas filters, and a heater in the primary circuit. Since equipment designs have not been completed, the estimated pressure drops through the equipment were based on data derived from other loops.

The total estimated system pressure drops were determined as a function of mass flow rate for both helium and carbon dioxide at 500 and 1000 psia, respectively. Analyses were made for maximum power operation at 1.5 Mw with the gas inlet temperature at 600°F and the outlet temperature at 1050°F. Also, since the loops are to be capable of operating at a maximum inlet temperature of 950°F at a reduced power, an analysis was made of the mass flow rates and corresponding pressure drops under these conditions in order to determine the maximum anticipated loop power at elevated temperatures. In all cases, it was assumed that the exit gas from the test section would be attemperated to 1050°F. Representative graphs of the individual and total system pressure drops under the nominal basic design conditions of 500 psia and 600°F inlet temperature to the test section are shown for helium and CO_2, respectively, in Figs. 7.3 and 7.4.

Gas Cooler. The gas cooler for the loops must meet the four conditions specified in Table 7.2 for operation with helium and with CO_2. The water flow to the gas cooler will remain constant at a given power setting. The inlet water temperature will be 120°F and the outlet water temperature will be 150°F.

---

[2]"GCR Quar. Prog. Rep. Dec. 31, 1959," ORNL-2888, p. 186.

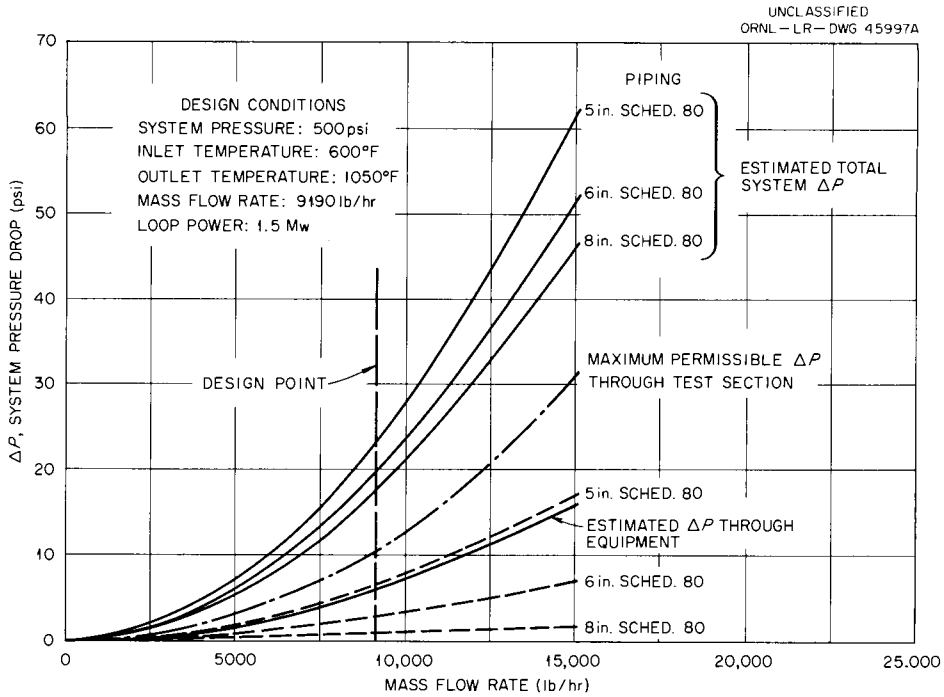

Fig. 7.3. Estimated Pressure Drop in Experimental Loop System with Helium as the Coolant.

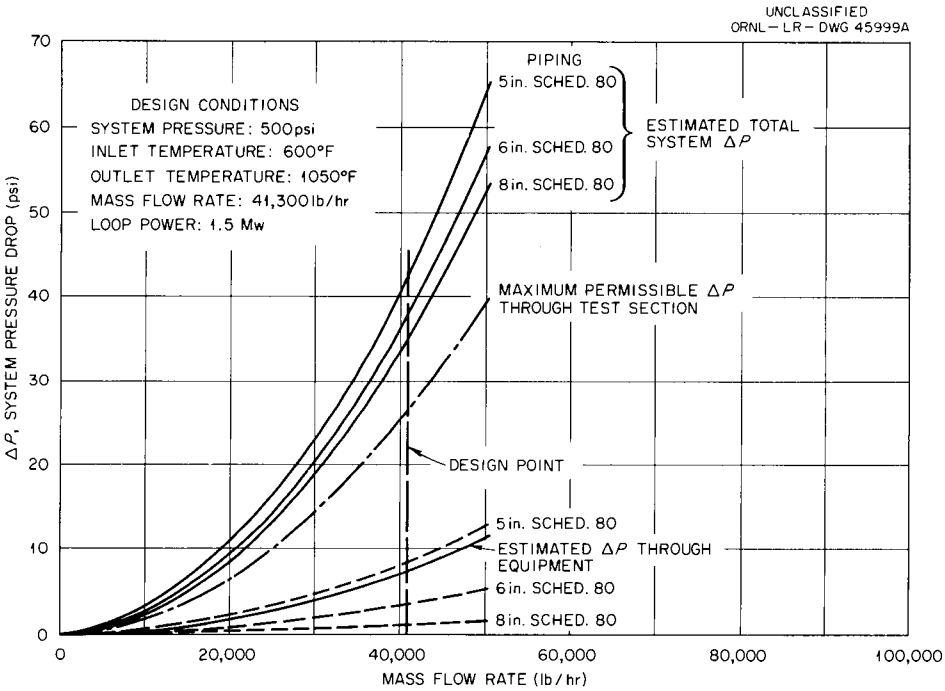

Fig. 7.4. Estimated Pressure Drop in Experimental Loop System with CO_2 as the Coolant.

Table 7.2. Nominal Gas Cooler Requirements

	Operating Conditions			
	I	II	III	IV
	Helium			
Heat removal rating, kw				
Heat generated in test specimen	1500	1500	334	334
Heat generated in 50°F rise through heater	166.7	166.7	166.7	166.7
Heat added by compressor	52.2	34.2	39.8	16.6
Total	1718.9	1700.9	540.5	517.3
Inlet gas temperature, °F	1050	1050	1050	1050
Outlet gas temperature, °F	534.3	539.7	888	895
Total gas flow to and from cooler, lb/hr	9190	9190	9190	9190
Nominal gas pressure, psia	500	1000	500	1000
	CO_2			
Heat removal rating, kw				
Heat generated in test specimen	1500	1500	334	334
Heat generated in 50°F rise through heater	157	159	167	169.5
Heat added by compressor	49.7	47.2	30.7	16.9
Total	1706.7	1706.2	531.7	520.4
Inlet gas temperature, °F	1050	1050	1050	1050
Outlet gas temperature, °F	534.2	535.2	890.8	895
Total flow to and from cooler, lb/hr	41 300	40 700	41 000	41 000
Nominal pressure, psia	500	1000	500	1000

The two principal components of the proposed design for the cooler, as shown in Fig. 7.5, are the valve assembly and the heat exchanger section of the cooler. The valve assembly is made up of a three-way valve and an actuator located at the top of the cooler. The valve and actuator must be within the primary containment vessel for the process gas and secondary containment vessel surrounding the complete assembly. Either a canned-motor actuator or a conventional actuator with a bellows-sealed shaft surrounded by a second containment shell may be used.

The heat exchanger consists of three concentric tubes that form an insulated center channel for the bypass stream, an annulus for the main gas stream, and an outer annulus for the cooling water. The heat transfer section is a counterflow heat exchanger, and the coolant in the outer tube is demineralized water. The cooling water flow is maintained constant and is determined by the maximum heat removal rating of the cooler. The heat removal is controlled by passing gas down the center tube as required to maintain its desired temperature.

Gas Filters. A preliminary design study of the main-line filter units has been completed. It appears that a suitable filter can be designed to fit within a 24-in. sched.-80 stainless steel pipe section which is capable of a maximum allowable working pressure of 1380 psi at 1050°F if fabricated from type 347 stainless steel according to the 1956 ASME Unfired Pressure Vessel Code. The filter can be assembled with Fiberfrax, a commerically available material which is capable of filtering 1-μ particulates at greater than 99% efficiency at temperatures up to 2000°F for prolonged periods. Also, manufacturers have available, as standard items, corrugated asbestos—ceramic paper filters that are claimed to filter 99.95% of all particles greater than 0.3 μ in size at temperatures in the range of 1600 to 1800°F. Several alternate designs have been prepared that are based on both types of filters. Two of the designs are presented in Figs. 7.6 and 7.7.

In order to facilitate maintenance, it is presently planned to install two joints on the filters. One plan for servicing the filter units requires a remotely operable 24-in. mechanical joint or closure. Leak

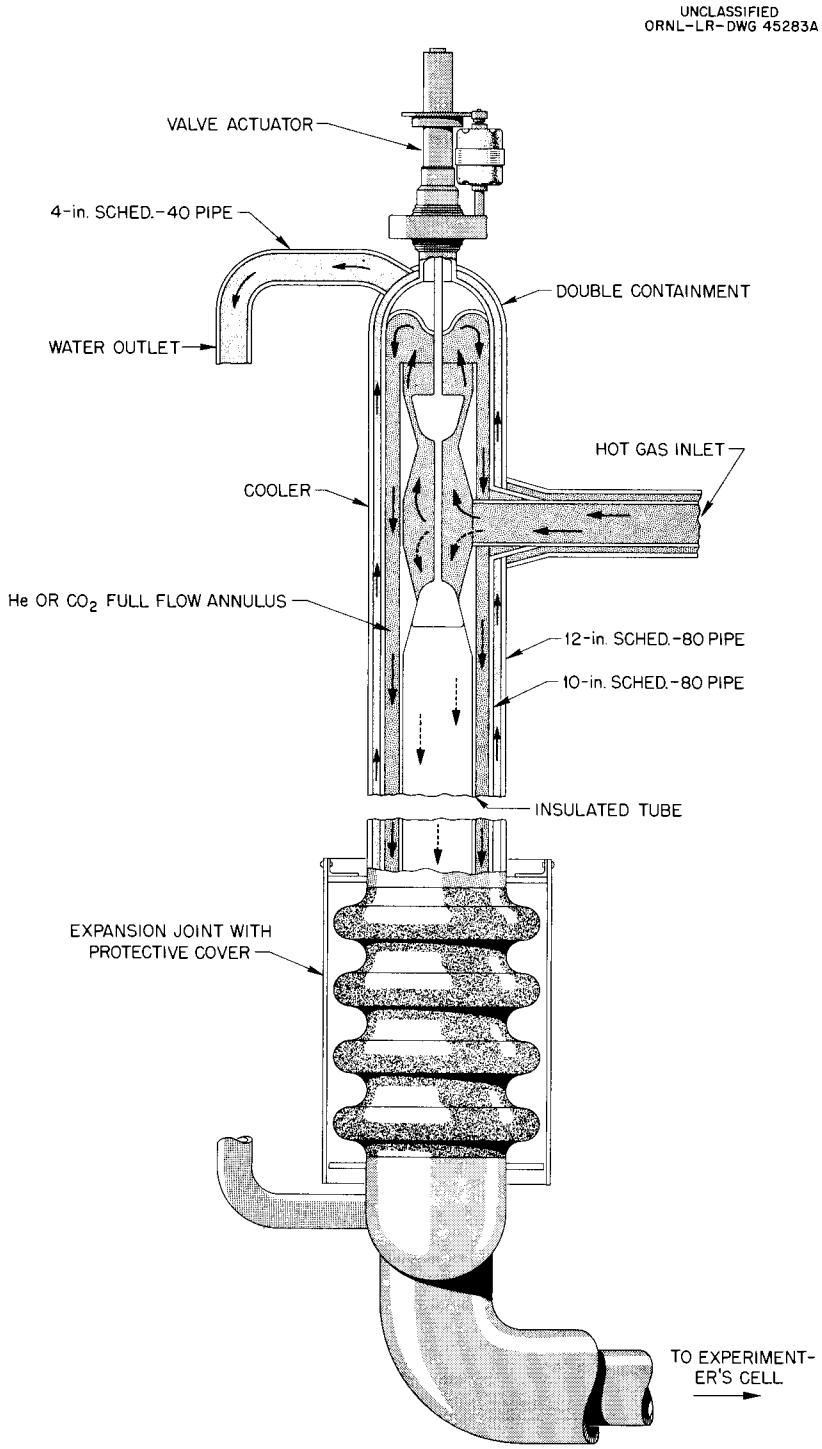

Fig. 7.5. Cooler of Primary Coolant System for EGCR Experimental Loops.

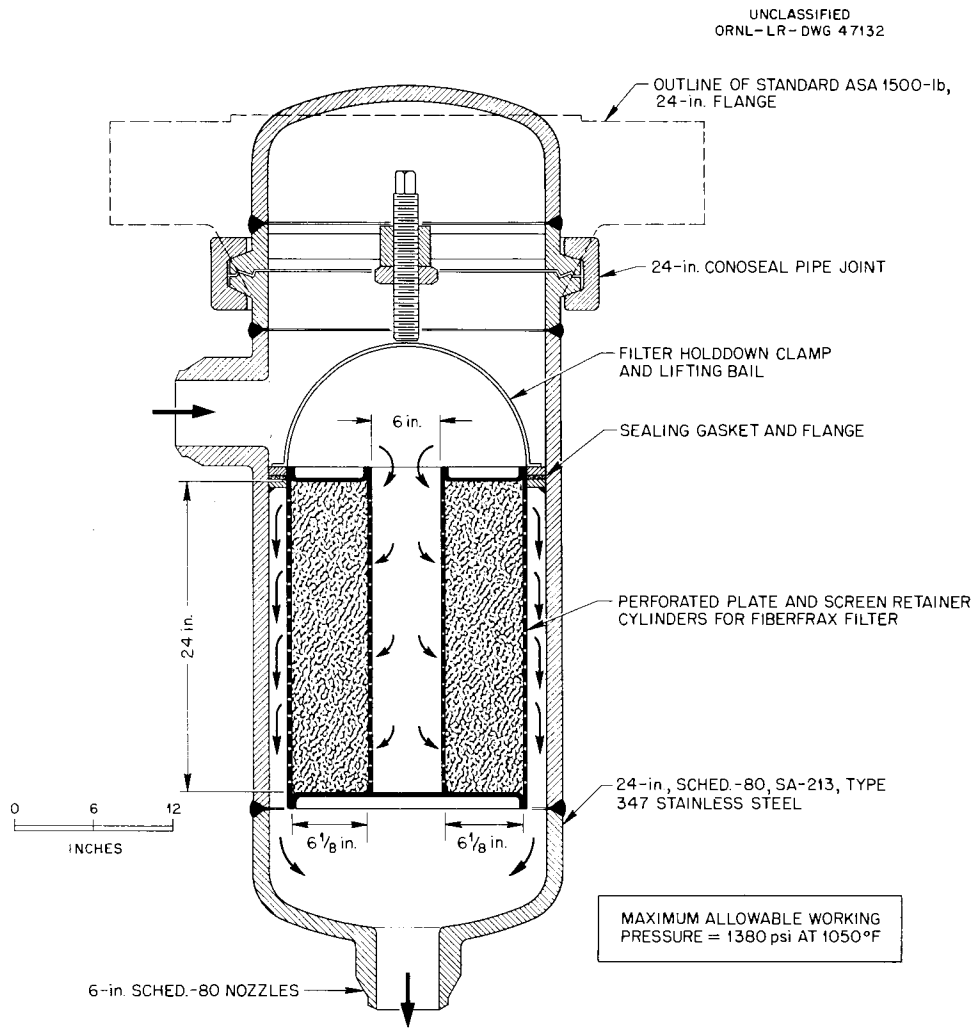

Fig. 7.6. Hot-Gas Filter for EGCR Experimental Loops Using Fiberfrax as the Filter.

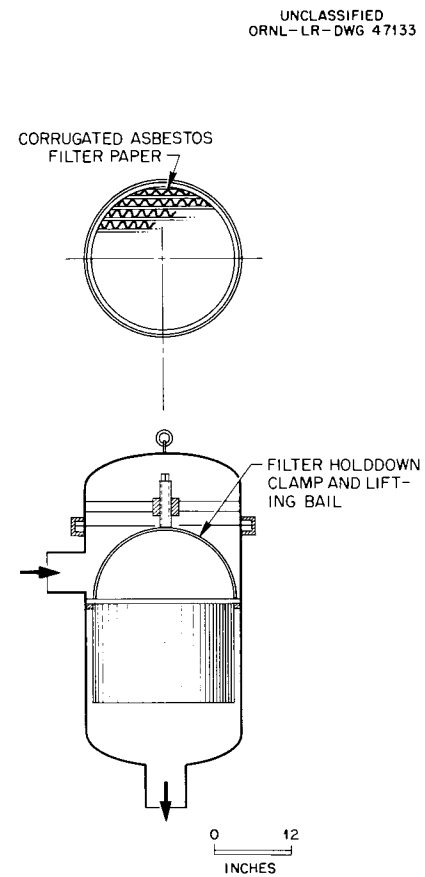

Fig. 7.7. Alternate Hot-Gas Filter for EGCR Experimental Loops Using Corrugated Asbestos Paper as the Filter.

tightness and accessibility are the main criteria. A method of mounting the filter for remote removal of the filter element into a shielded transfer cask is shown in Fig. 7.8.

Gas Heater. The electric heater design study has been completed. The criterion for the study was that sufficient electric heat be provided in the inlet to each through tube to raise the inlet gas temperature a maximum of 50°F to provide for heat losses and other contingencies. The design power of the heater will be ~200 kw.

A "Radi-Fin" heater element appears to have the combination of low pressure drop, ease and accuracy of control of exit gas temperature, compactness, and reliable high-temperature operation required. Because of the high pressure (500 to 1000 psia) and temperature (600 to 950°F) of the gas, some difficulty is anticipated in designing and/or procuring suitable electric lead-in bushings for supplying power to the heater elements. A concept of the heater with a proposed method of conducting the heater leads through the pressure vessel closure in buffered hermetic seals is shown in Fig. 7.9.

Gas Sampler. An important function in the operation of an experimental loop is the ability to extract safely representative samples of gas from strategic points in the loop system for analysis. A system for performing this operation is shown in Fig. 7.10. The sample bomb and mechanism which make the operation possible are shown in Fig. 7.11. The sampling system is complicated by the high pressure and high temperature of the gas and the fact that the gas may be radioactive. The sampler shown by Fig. 7.11 is based on a design proposed by the British that was modified to suit conditions in the EGCR loops.[3]

Gas-Handling System Components. The gas-handling system components shown in Fig. 7.2 consist essentially of the cleanup equipment (charcoal traps), the transfer pumps, and the storage tanks. A study of the requirements for removal of fission products from the gas stream is currently

---

[3]R. R. Bell et al., "H.T.G.C. Pluto Loop 'A'," p. 20, U.K.A.E. Research Group, HTRDC-P.25 (November 1958).

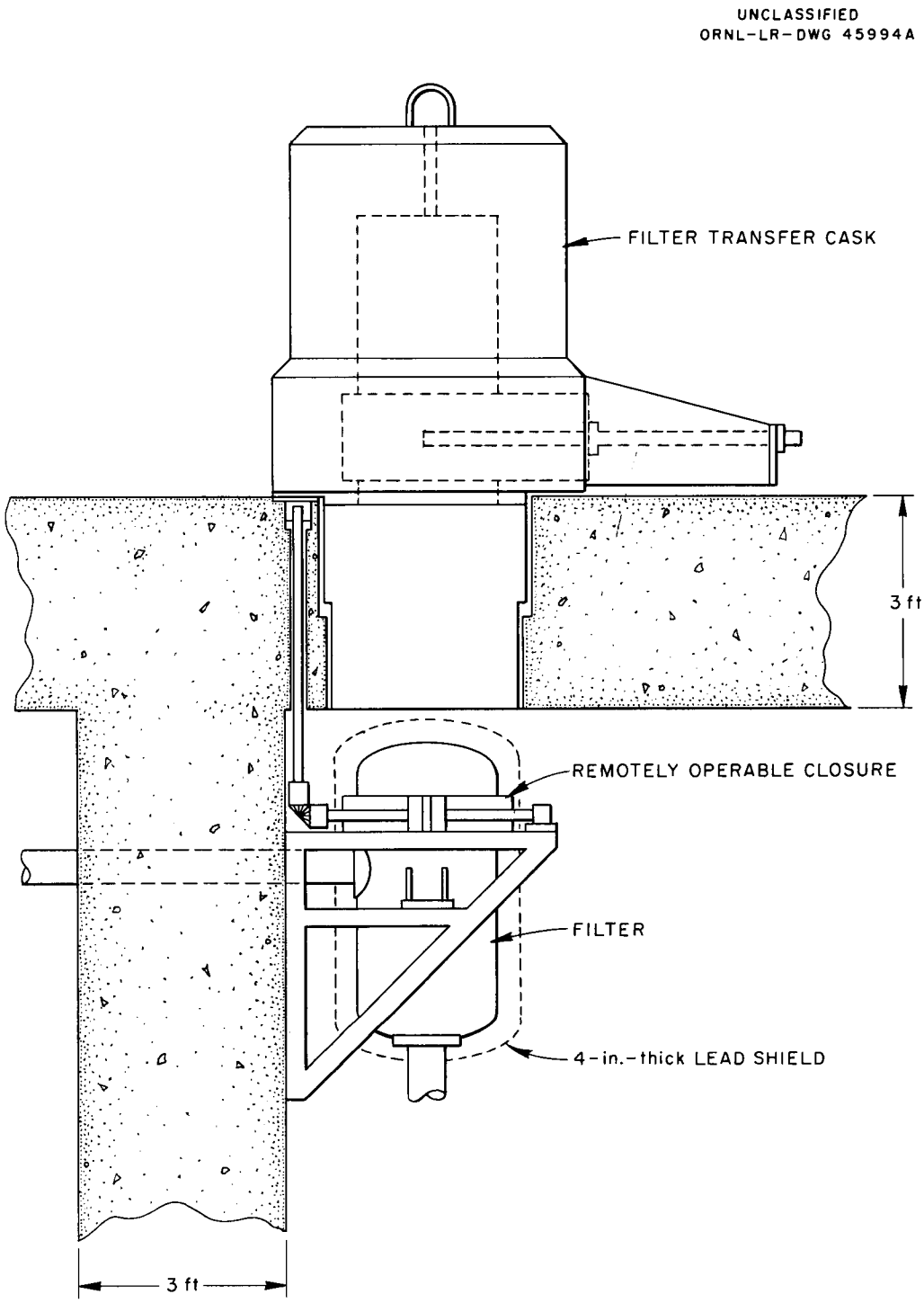

Fig. 7.8. Equipment for Remotely Controlled Removal of Hot-Gas Filter.

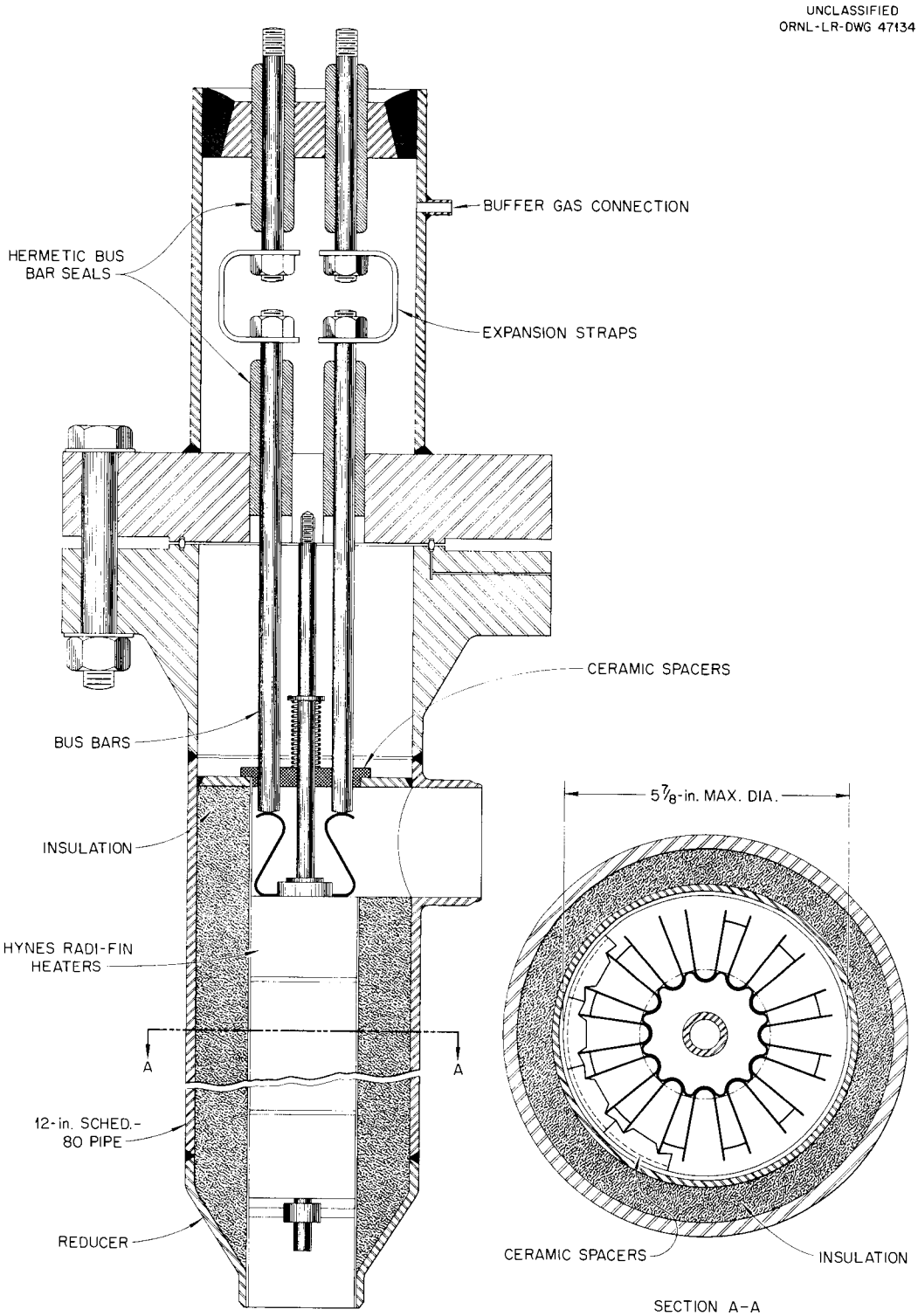

Fig. 7.9. Gas Heater for EGCR Experimental Loops.

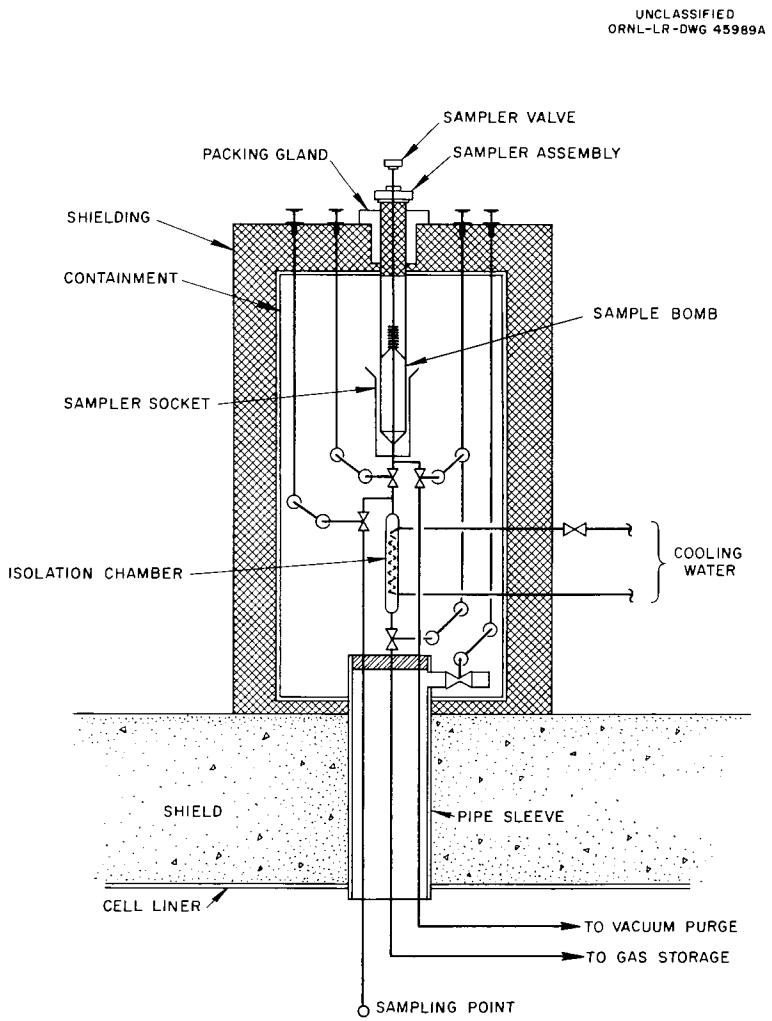

Fig. 7.10 Gas-Sampling System for EGCR Experimental Loops.

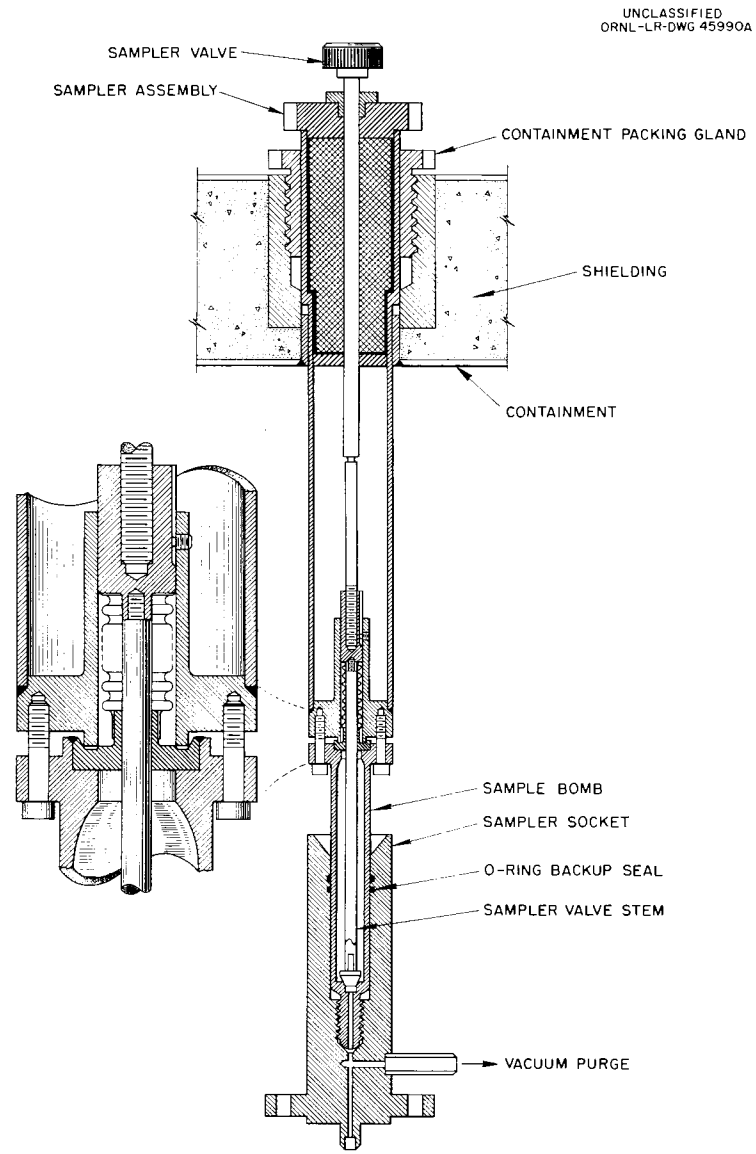

Fig. 7.11. Gas Sampling Device.

under way. The transfer pumps will be low-capacity, high-head, hermetically sealed compressors probably similar to the Corblin diaphragm compressors used at the Amarillo, Texas, helium processing plants. A survey of vendors is currently being made to locate suitable pumps. The storage tanks have not yet been designed. The volume and pressure conditions for these tanks will probably be determined on the basis of space allocations.

Mechanical Joint Service Testing

Five 2 1/2-in. and two 10-in. sched.-40 standard Conoseal mechanical joints were received from the Marman Division of Aeroquip Corporation. One of these joints is shown disassembled in Fig. 7.12. Tests on the 2 1/2-in. joints are under way, and fabrication of the thermal cycling apparatus for testing the 10-in. joints is essentially complete.[4] An

[4]"GCR Quar. Prog. Rep. Dec. 31, 1959," ORNL-2888, p. 195.

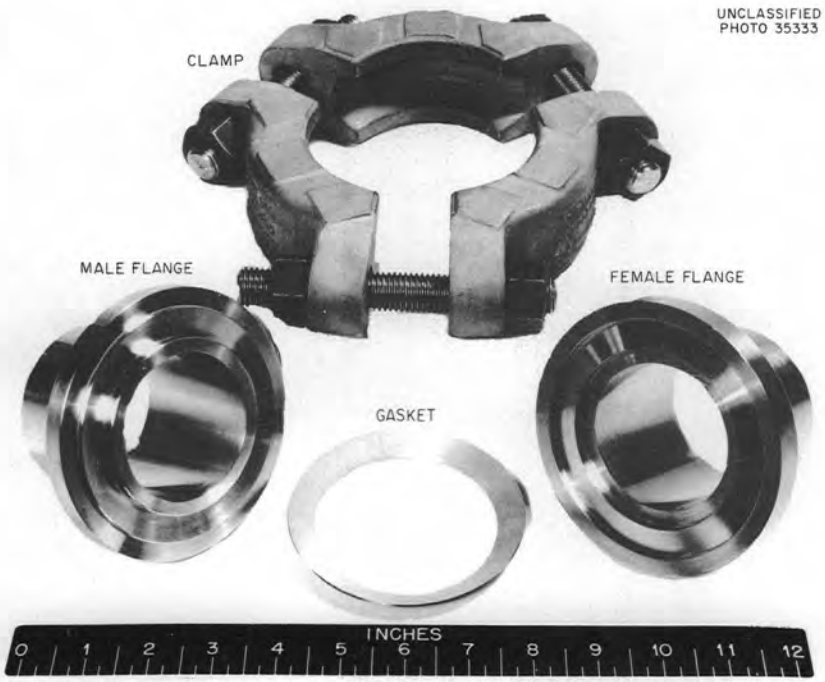

Fig. 7.12. Unassembled Conoseal Mechanical Joint.

apparatus was designed for imposing bending moments and axial loads on mechanical joints in pipe sizes from 2 1/2 to 12 in. operating at temperatures and pressures up to 1000°F and 400 psig, respectively. Fabrication of this apparatus is under way. A 10-in. Conoseal joint will be tested initially.

The tests conducted on 2 1/2-in. joints are described in Table 7.3. The thermal cycling tests were carried out with the joint mounted in an electric furnace. The tabulated temperatures represent the average temperature of the entire joint, including the clamping mechanism. In this respect the test condition is more severe than that which would be present in a typical high-temperature gas line application where the bolts and clamps would normally be at lower temperatures than the body of the joint.

Double-gasketed, gas-buffered, mechanical joints are being evaluated for use in experimental loops which will operate with gases containing radioactive fission products. Orders were placed with DSD Manufacturing Company, Marman Division of Aeroquip Corporation, and Hydrodyne Corporation for 2 1/2-in. sched.-80 joints of this type. The joints must be suitable for operation at 1500°F with an internal pressure of 300 psig and a buffer pressure of 400 psig. Specified maximum helium leakages are 1×10^{-6} cm^3/sec from the buffer zone to the system and 1×10^{-2} cm^3/sec from the buffer zone to the atmosphere.

Three double-gasketed joints of the type shown in Fig. 7.13 were received from DSD Manufacturing Company. These were leak tested at room temperature, and each joint exhibited leakage rates greater than the maximum values which can be measured with a helium leak detector ($\sim 2 \times 10^{-4}$ cm^3/sec). A nitrogen supply was therefore connected to the buffer zone through a flowmeter, and the total leakage was measured at various buffer zone pressures. The leak rates obtained in this manner are presented in Table 7.4.

The joints were furnished with a surface finish of 125 rms on the flat flange face. In an effort to lower the leakage rate, the flange face of joint 3 was lapped to a 16 rms finish before testing. The

Table 7.3. Results of Tests of 2 1/2-in. Stainless Steel Conoseal Mechanical Joints

Joint No.	Gasket No.	Description of Test	Maximum Helium Leakage Rate (std cm^3/sec)	Remarks
1	1	Torque increased from 40 ft-lb to 120 ft-lb and then decreased to 10 ft-lb in 20 ft-lb increments; joint pressurized to 400 psig at each torque condition and then evacuated and helium leak checked	8.0×10^{-7}	Joint will seal with a torque of about 10 ft-lb applied to the bolts, and the quality of the seal is not substantially improved at higher torque; the leakage rate did not substantially increase until the torque was reduced to below 10 ft-lb
	2	Same as for gasket 1 except that leak checks were started at a torque of 10 ft-lb	2.7×10^{-5}	
	3	Same as for gasket 2 except that the maximum torque applied was 50 ft-lb	3×10^{-6}	
	4	The joint was made up with a 10 ft-lb torque applied to the bolts, placed in an electric furnace, and pressurized to 375 psig; leakage rates were measured at each of the following temperatures:		Bolt torques higher than that required to seal the joint are necessary to prevent excessive leakage under thermal-cycling conditions
		Room temperature	4×10^{-9}	
		500°F	4×10^{-10}	
		1000°F	1.9×10^{-10}	
		1200°F	4×10^{-10}	
		500°F	Excessive ($>2 \times 10^{-4}$)	
	5	The joint was made up with a 60 ft-lb torque applied to the bolts, loosened, and retightened to 50 ft-lb torque; it was then exposed to the following thermal cycling and pressure cycling program:		The joint will remain tight under thermal-cycling conditions with 1000°F maximum temperatures but may leak under thermal-cycling conditions if the maximum temperature is increased to 1200°F
		a. 111 thermal cycles between room temperature and 500°F and 14 pressure cycles between atmospheric pressure and 375 psig	5.9×10^{-10}	
		b. 106 thermal cycles between 500 and 1000°F and 12 pressure cycles between atmospheric pressure and 375 psig	5.1×10^{-10}	
		c. 23 thermal cycles between 700 and 1200°F and 6 pressure cycles between atmospheric pressure and 375 psig	Excessive ($>2 \times 10^{-4}$)	
	6	The joint was made up with an initial 85 ft-lb bolt torque and a final torque of 50 ft-lb; it was thermally cycled 12 times between 700 and 1200°F, and the following leakage rates were measured:		Efforts to reseal gaskets 5 and 6 by retightening without replacing the gaskets were unsuccessful
		Before cycling	2.75×10^{-7}	
		After first cycle	$<1.1 \times 10^{-10}$	
		After 12 cycles	$>2 \times 10^{-4}$	

Table 7.3. (Continued)

Joint No.	Gasket No.	Description of Test	Maximum Helium Leakage Rate (std cm^3/sec)	Remarks
2		The joint was made up 10 times with a new gasket each time and was leak checked at room temperature; an initial torque of 60 ft-lb and a final torque of 50 ft-lb was applied for each closure; leakage rates measured for each closure are shown below:		
	1		1.0×10^{-8}	
	2		1.0×10^{-7}	
	3		$<1.1 \times 10^{-10}$	
	4		$<1.1 \times 10^{-10}$	
	5		1.3×10^{-7}	
	6		6.6×10^{-8}	
	7		1.3×10^{-8}	
	8		$<1.1 \times 10^{-10}$	
	9		$<1.1 \times 10^{-10}$	
	10		$<1.1 \times 10^{-10}$	

Fig. 7.13. Unassembled Gas-Buffered Mechanical Joint.

excessive leakage of all the joints at room temperature and low pressures indicates, however, that this type of joint is not suitable for helium service without further improvement.

Table 7.4. Leakage Rates of Double-Gasketed, Gas-Buffered, Mechanical Joints

N_2 Pressure in Buffer Zone (psig)	N_2 Leakage Rate (cm^3/min)		
	Joint 1	Joint 2	Joint 3
10	16	14	6
20	35	27	8
30	60	41.5	10
40	90	69	13
50	110	85	17.5

Special Gas Compressors and Electric Motors

Grease-Lubricated Centrifugal Compressors

A grease-lubricated centrifugal compressor has satisfactorily completed a 3000-hr endurance test while operating at 12 000 rpm with helium at 590°F and 400 psig (suction conditions). The total operating period was accumulated without shutdown, except for repairs to the gasoline-driven electric generator sets. During this report period, the compressor has been operated intermittently at 12 000 rpm with helium at 400 psig and 600°F to suit the requirements of the thermocouple calibration test that is now being conducted.

Regenerative Compressors

A prototype regenerative compressor unit has been operated continuously in the high-temperature test loop for approximately 150 hr at 9000 rpm with helium at 385 psig and 600°F (suction conditions). Compressor performance data were taken at several speeds, and curves of head versus flow are presented in Fig. 7.14. Several tests were made

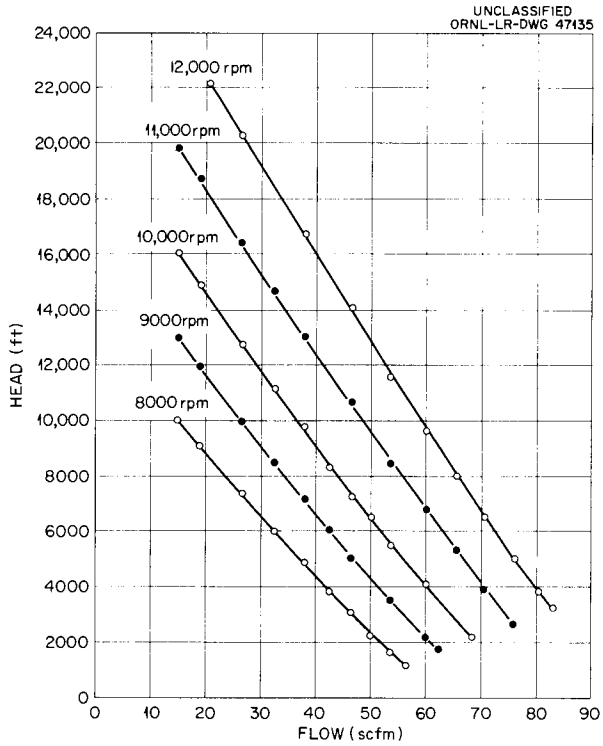

Fig. 7.14. Performance Characteristics of Prototype Regenerative Compressor (HECT-2) Operating with Helium at 385 psig and 600°F.

to determine the effects of sudden pressure loss and temperature drop on compressor performance, and it was deduced that there were no deleterious effects.

A compressor unit for GCR-ORR loop No. 1 was assembled and installed in the test loop for proof-testing. After 100 hr of operation at 9000 rpm with helium at 385 psig and 600°F (suction conditions), the compressor failed while performance data were being taken. Prior to failure, the vibration and noise level of the compressor were thought to be above normal. The unit was disassembled, and it was found that the impeller had rubbed against the outboard housing. Further inspection of the rotary element revealed a faulty bearing at the impeller end of the compressor. A close scrutiny of the damaged grease-lubricated bearing showed that one ball was missing (14 balls were found instead of the 15 required). Weight comparisons with other identical bearing assemblies

and the lack of debris indicated that the missing ball had probably not been installed at the factory. Two other compressor units are being assembled.

Compressors with Gas-Lubricated Bearings

A gas-lubricated test bearing having a length-to-diameter ratio of 0.5 and a diametral clearance of 0.0054 in. was operated for 1 hr and 18 min with a maximum load of 18 lb at a maximum speed of 12 000 rpm. This load represents a unit loading of 4 psi. Testing was stopped for repairs to the capacitance-gage equipment. During subsequent test runs with this bearing and with two other bearings, rubbing noises were evident. Reducing the unit loading did not remove the rubbing. The journal surface was therefore measured, and it was found to have a taper of 400 μin. and a total indicator runout of 200 μin., which may have contributed to the rubbing. A new journal 1.5 in. in diameter has been fabricated, and two bearings with a length-to-diameter ratio of 1 are being made. Testing will be resumed with these bearings.

All components of the loop for testing the Bristol-Siddeley compressor are being fabricated. The loop will be assembled prior to receipt of the compressor, which is still undergoing testing at the factory. The compressor has been tested at the full operating speed (15 050 rpm) at temperatures up to 750°F, and tests at the design operating temperature of 1000°F are under way.

Compressor for High-Temperature Electric-Motor Test System

In order to be able to vary the static loading on the GABE I compressor journal bearings, the loop stand is being designed to permit tilting from horizontal to vertical. This requirement places a limit on the size of the loop and heat exchanger configuration. The available area for the heat exchanger will provide for steady-state operation at compressor suction temperatures between 225 and 800°F.

The compressor design was modified to include a tachometer pickup capable of operation to 800°F. The flowmeter has been received, and the

throttling valve, pressure vessel, heat exchangers, and motor-generator set are on order. The electrical and gas control designs were completed.

Compressors for ORR In-Pile Loop No. 2

A specification for two centrifugal-type compressors having gas-lubricated bearings to be operated in series was submitted to 11 compressor manufacturers. Four bids were received, and the proposals are being evaluated. In particular, each manufacturer's promised delivery date is being weighed against an estimate of the time required to develop rotary assemblies supported on gas-lubricated bearings. In order to meet the loop construction schedule, a backup design that consists of a modification of the centrifugal compressor is being considered.

Compressors for EGCR Experimental Loops

Head and flow requirements for operation of the EGCR loops with both helium and carbon dioxide were established. A study of various compressor arrangements was then made, and a set of three compressors operating in series was chosen to meet the specified wide range of operating conditions. A primary consideration was that the same compressors must meet all loop test conditions when operating on either helium or carbon dioxide at compressor inlet conditions of 550 to 900°F and 500 to 1000 psia. In the event of failure of one compressor, the design coolant flow rate will be re-established by increasing the speed of the remaining operational compressors rapidly enough to prevent an excessive temperature rise in the test fuel element. In the event of failure of a second compressor, it is required that the remaining compressors provide sufficient cooling for an orderly shutdown of the reactor. A specification for centrifugal compressors supported on gas-lubricated bearings was prepared. Based on preliminary information from a number of compressor manufacturers, the specifications were submitted to five firms, and two additional sources requested that the inquiry be sent to them.

Study of Back Diffusion Through Labyrinth Seals

Test apparatus has been completed for a study of back diffusion of buffer oil or water vapor against the flow of helium through labyrinth-type seals. The initial studies and tests are being conducted with water as the buffer fluid and dry air as the coolant gas at a temperature of about 500°F and a pressure of about 100 psig. The dry-air tests will be conducted for a range of pressures up to about 300 psig prior to using helium.

Previous reports in this series are:

ORNL-2500	Parts 1-4, issued April 1, 1958
ORNL-2505	Issued June 19, 1958
ORNL-2510	Issued September 18, 1958
ORNL-2676	Period Ending December 31, 1958
ORNL-2767	Period Ending June 30, 1959
ORNL-2835	Period Ending Sept. 30, 1959
ORNL-2888	Period Ending Dec. 31, 1959

INTERNAL DISTRIBUTION

1. G. M. Adamson
2. J. W. Allen
3. S. A. Beall
4. M. Bender
5. D. S. Billington
6. E. P. Blizard
7. A. L. Boch
8. C. J. Borkowski
9. W. F. Boudreau
10. G. E. Boyd
11. E. J. Breeding
12. J. C. Bresee
13. R. B. Briggs
14. C. E. Center (K-25)
15. R. A. Charpie
16. T. E. Cole
17. J. H. Coobs
18. J. A. Conlin
19. W. B. Cottrell
20. J. A. Cox
21. F. L. Culler
22. H. N. Culver
23. J. H. DeVan
24. L. M. Doney
25. D. A. Douglas
26. L. B. Emlet (K-25)
27. E. P. Epler
28. R. B. Evans
29. D. E. Ferguson
30. J. Foster
31. A. P. Fraas
32 J. H. Frye, Jr.
33. G. A Garrett (K-25)
34. J. M. Googin (Y-12)
35. B. L. Greenstreet
36. W. R. Grimes
37. E. Guth
38. R. F. Hibbs (Y-12)
39. T. Hikido
40. M. R. Hill
41. H. W. Hoffman
42. A. Hollaender
43. A. S. Householder
44. H. Inouye
45. W. H. Jordan
46. P. R. Kasten
47. C. P. Keim
48. M. T. Kelley
49. J. J. Keyes
50. R. B. Korsmeyer
51. P. Lafyatis
52. J. A. Lane
53. S. A. Levin (K-25)
54. R. S. Livingston
55. H. G. MacPherson
56. W. D. Manly
57. E. R. Mann
58. H. E. McCoy
59. H. C. McCurdy
60. W. B. McDonald
61. H. F. McDuffie
62. C. J. McHargue
63. F. R. McQuilkin
64. H. J. Metz
65. A. J. Miller
66. R. S. Miller
67. J. G. Morgan
68. K. Z. Morgan.
69. J. P. Murray (Y-12)
70. F. H. Neill
71. M. L. Nelson
72. L. G. Overholser
73. N. Ozisik
74. P. Patriarca
75. F. S. Patton (Y-12)
76. A. M. Perry
77. D. Phillips
78. C. A. Preskitt
79. M. E. Ramsey
80. P. M. Reyling
81. T. K. Roche
82. M. W. Rosenthal
83. A. F. Rupp
84. G. Samuels
85. H. W. Savage
86. A. W. Savolainen

87. J. L. Scott
88. O. Sisman
89. E. D. Shipley
90. M. J. Skinner
91. G. M. Slaughter
92. A. H. Snell
93. E. Storto
94. R. D. Stulting
95. J. C. Suddath
96. C. D. Susano
97. J. A. Swartout
98. E. H. Taylor
99. D. F. Toner
100. D. B. Trauger
101. E. Von Halle (K-25)
102. C. S. Walker
103. J. L. Wantland
104. A. M. Weinberg
105. M. E. Whatley
106. J. R. Weir
107. J. C. White
108. E. A. Wick
109. G. C. Williams
110. C. E. Winters
111. J. Zasler
112-115. ORNL — Y-12 Technical Library Document Reference Section
116-185. Laboratory Records Department
186. Laboratory Records Department, ORNL R. C.
187-189. Central Research Library

EXTERNAL DISTRIBUTION

190-192. W. F. Banks, Allis-Chalmers Mfg. Co.
193-195. P. D. Bush, Kaiser Engineers
196. E. Creutz, General Atomic
197. T. Jarvis, Ford Instrument Co.
198. Richard Kirkpatrick, AEC, Washington
199-200. H. Lichtenburger, General Nuclear Engineering Corp.
201. J. P. McGee, Bureau of Mines, Appalachian Experiment Station
202. S. G. Nordlinger, AEC, Washington
203. H. B. Rahner, Savannah River Operations Office
204. Corwin Rickard, General Atomic
205. S. T. Robinson, Sanderson & Porter
206. M. T. Simnad, General Atomic
207. Donald Stewart, AEC, Washington
208. Philip L. Walker, Pennsylvania State University
209. R. E. Watt, Los Alamos Scientific Laboratory
210-211. W. L. Webb, East Central Nuclear Group, Inc.
212. Division of Research and Development, AEC, ORO
213-789. Given distribution as shown in TID-4500 (15th ed.) under Reactors — Power category (75 copies — OTS)